DYNAMIC CONTROL OF AERODYNAMIC FORCES ON A MOVING PLATFORM USING ACTIVE FLOW CONTROL

A Thesis
Presented to
The Academic Faculty

by

Daniel P. Brzozowski

In Partial Fulfillment
of the Requirements for the Degree
Doctor of Philosophy in the
School of Mechanical Engineering

Georgia Institute of Technology
December 2011

DYNAMIC CONTROL OF AERODYNAMIC FORCES ON A MOVING PLATFORM USING ACTIVE FLOW CONTROL

Approved by:

Professor Ari Glezer, Committee Chair
School of Mechanical Engineering
Georgia Institute of Technology

Professor Anthony J. Calise
School of Aerospace Engineering
Georgia Institute of Technology

Professor Anthony Leonard
School of Aerospace Engineering
California Institute of Technology

Professor Marc K. Smith
School of Mechanical Engineering
Georgia Institute of Technology

Bojan Vukasinovic, Ph.D.
School of Mechanical Engineering
Georgia Institute of Technology

Date Approved: 11 November 2011

To my parents,

Mary Beth and Paul Brzozowski,

who have given me every opportunity in life.

ACKNOWLEDGEMENTS

I would first like to thank my thesis and research advisor, Prof. Ari Glezer, who provided me with the opportunity, funding, and support to pursue Ph.D. research in experimental fluid dynamics. Prof. Glezer constantly encouraged me, with his example driving my hard work and desire for quality results. On a personal level, Ari and his family have been wonderful friends during my time at Georgia Tech. From sharing Thanksgiving dinner to a post-appendectomy hospital visit, his and Maggie's kindness has been invaluable to me and my wife.

My dissertation committee members have each provided much-needed technical expertise and advice. For his expansive knowledge of control systems and multi-disciplinary cooperation throughout the course of the AVOCET project, I would like to thank Prof. Anthony Calise. I am deeply grateful to Prof. Tony Leonard for his guidance on unsteady aerodynamic theory, as well as his patience, effort, and mathmatical inspiration during our many telephone and email discussions about the ROM. Prof. Marc Smith has provided a wonderful outside perspective on my thesis project, and I have appreciated his demand for science, especially during the Committee's closed-door sessions. Finally, many thanks to Dr. Bojan Vukasinovic for his time and knowledge as a mentor during my early years at Georgia Tech and his constant example of impeccable academic and experimental integrity.

To my friends and colleagues in the Fluid Mechanics Research Lab, I truly value the time I spent in your company and will sincerely miss you. My years with you yielded no shortage of intellectual resources and taught me that “team environment” and “working together” weren't things I should avoid.

I would like to thank Scott Driscoll (FMRL honorary member) for his assistance with electronics, creative inspiration, and cool head during so many midnight crises. Most importantly, thank you for an invitation to tag along to a birthday party – a night that changed my life forever.

Without the incredible organizational skills and top notch lab management provided by Abe Gissen, completion of this project would have been a much more painful process. I look forward to a long and productive relationship over the years.

Many thanks to John Culp for intoducing me to software engineering and creating (what I know will be) a life-long passion for computer programming. The "apprenticeship" in such practical skills as creating shop drawings and tracking down problems in electrical and mechanical systems will no doubt be critical throughout my career. Additionally, his relentless pursuit of his dream is refreshing and inspiring to me as a friend and an engineer.

I am deeply grateful on so many levels for the friendship and technical assistance provided by George Woo. In the lab he has constantly challenged me with complex questions about my work and his, and I very much appreciate all the exercise (and bug identification) he has given my data processing codes. Plus, our discussions about career paths and life goals have been eye-opening; I wish him all the success he aspires to and deserves.

During my seven years in the FMRL I was fortunate to work with so many other talented students. The early years with Pierre Gerardin, Dave Garth (whose SLA skills were essential) and others helped me find my way in a challenging new setting. The middle period with Michael DeSalvo, Ashok Rajendar, Philip Abramson, Hanif Hunter, Chris Rinehart, Donavon Gerty, Pablo Hidalgo, and Brett Warta was when I fully realized the wonderfully stimulating environment I was lucky to enjoy each day. Finally, these last years with the "younger generation" of FMRL students have been both incredibly fun and insanely productive. Mark Simpson and John Kearney (often together and always wonderful collaborators), as well as Tom Lambert, Tom Boziuk, and Taylor Jones - thank you so very much. I look forward to future collaboration and continued friendship with all of you.

I owe a great debt of gratitude to my many collaborators over the years. I very much appreciate the hard work of my friends in Prof. Calise's control system group, Drs. Ali Kutay and Jonathan Muse and Rajeev Chandramohan, which made my flow control experiments possible and allowed us to demonstrate the utility of flow control in achieving closed-loop flight control. I appreciate the critical evaluation of the experimental data provided by Drs. Omar Lopez and Sol Keun Jee (working under Prof. Bob Moser). They always

asked the “tough questions” about my research, and the work is immensely better because of it. Thank you also to Dr. Andrew Tchieu for his guidance on and editing of the ROM chapter. Collaboration with these talented colleagues opened my eyes to the crucial value of multidisciplinary teams in solving engineering problems.

I am incredibly grateful for the patience and assistance of Judy Diamond for making sure I didn’t miss deadlines with the finance office (despite my frequent delinquency in this area). She consistently went above and beyond what I would have expected - and probably deserved.

Thank you to Robbie Ouzts for her incredible dedication during my job search. Georgia Tech students are lucky to have such an energetic and knowledgeable powerhouse in their corner.

I would like to thank the amazing staff of NASA’s Scientific and Technical Information office for more than once digging up 100-year-old articles in less than a day.

I am deeply indebted to many who contributed to my knowledge and passion prior to arriving at Georgia Tech. Thanks to Brother Phillip DiMarchi, my high school physics and calculus teacher, who always reminded us that Sir Isaac Newton only invented calculus so he could do more physics. At Johns Hopkins, thank you to Profs. Shiyi Chen and Charles Meneveau (my M.S. thesis adviser), whose undergraduate fluid dynamics courses inspired me to pursue the research I did. Also thanks to Prof. Allison Okamura who provided me with my first research opportunity.

I would like to acknowledge and thank the sponsoring agencies for my research: the Air Force Office of Scientific Research, NASA, and The Boeing Company.

I appreciate the patience of my new boss - Dr. Bill Bower - during the completion of my thesis work.

This dissertation is dedicated to my parents, Paul and Mary Beth, for their unconditional support and encouragement for over 30 years. My parents identified early that I was destined to be an engineer and cultivated that dream with years worth of Construx Christmas presents and weekend afternoons spent launching model rockets. I couldn’t have asked for a happier childhood or a more supportive family; without their love, none of this would be possible.

A huge thank you also to my sister, Maureen, and her husband, Peter. They have always encouraged me in my studies and were there to offer valued advice and support. More importantly, they dragged me away from work every once in a while to have some fun.

To Sammy and Yodel, whose unfailing love is one of the greatest blessings in my life. We are the luckiest cat owners in the world. (Thanks also to George, Scott, John, and all the others who helped take care of them.)

Finally, I'd like to thank my wife, Amanda, who has supported me through the dissertation process as both a loving companion as well as an academic colleague. Whether it was having a midnight (or 4am) snack waiting for me after many hours of experiments or a consultation on statistical analysis, she was there with whatever I needed at the moment. During those long nights in lab, she would often visit to share dinner or a walk through campus and was always available to loan an extra pair of hands in the lab. On more than one occasion, my wind tunnel model would have held up the next tunnel entry if it were not for her assistance in lifting some very heavy pieces of metal. Then there was the editing... every word of this thesis passed through her hands where it was scrutinized for grammar and style (although responsibility for all errors remains solely with me). Unlike your average copy editor, however, she actually took the time to understand enough about vortex dynamics and flow control to catch technical errors as well! Her passion for academic research and teaching are an inspiration to me and she never let me discount the value of a doctoral degree or academia. I'm truly fortunate to have found someone who shares my passion for learning and intellectual curiosity.

To all of you, I am truly grateful.

Contents

List of Tables

List of Figures

SUMMARY

The unsteady interaction between trailing edge aerodynamic flow control and airfoil motion in pitch and plunge is investigated in wind tunnel experiments using a two degree-of-freedom traverse which enables application of time-dependent external torque and forces by servo motors. The global aerodynamic forces and moments are regulated by controlling vorticity generation and accumulation near the trailing edge of the airfoil using hybrid synthetic jet actuators. The dynamic coupling between the actuation and the time-dependent flow field is characterized using simultaneous force and particle image velocimetry (PIV) measurements that are taken phase-locked to the commanded actuation waveform. The effect of the unsteady motion on the model-embedded flow control is assessed in both trajectory tracking and disturbance rejection maneuvers. The time-varying aerodynamic lift and pitching moment are estimated from a PIV wake survey using a reduced order model based on classical unsteady aerodynamic theory. These measurements suggest that the entire flow over the airfoil readjusts within 2-3 convective time scales, which is about two orders of magnitude shorter than the characteristic time associated with the controlled maneuver of the wind tunnel model. This illustrates that flow-control actuation can be typically effected on time scales that are commensurate with the flow's convective time scale, and that the maneuver response is primarily limited by the inertia of the platform.

Chapter I

INTRODUCTION AND LITERATURE REVIEW

1.1 Motivation

In a recent report commissioned by the US Congress and NASA, the National Research Council (2006) defined four high priority strategic objectives necessary to ensure national leadership in civil aeronautics. The objectives were (i) increase capacity, (ii) improve safety and reliability, (iii) increase efficiency and performance, and (iv) reduce energy consumption and environmental impact. The report goes on to outline 51 high-priority research objectives necessary to achieve these goals, four of which are directly related to aerodynamic flow control, notably "aerodynamic performance for V/STOL and ESTOL" and "aerodynamics and vehicle dynamics via closed-loop flow control". The experimental research presented in this thesis was conducted as part of an AFOSR-MURI project tasked with implementing closed-loop flow control as described in the aforementioned report.

The specific aim of the MURI project was the implementation of closed-loop flow control on a one-meter scale unmanned aerial vehicle (UAV). Because of their small size and ease of deployment, these aircraft are particularly suited for operation in urban environments. The ability of these aircraft to maneuver rapidly is currently limited by the characteristic time scale of the control surfaces. Active flow control can enable direct manipulation of the aerodynamic forces on a flight platform with minimal input delay and a central theme of the project was to investigate the dynamic interaction between the flow control actuation and the unsteady flow field of the moving vehicle.

The MURI project consisted of a number of parallel cooperative efforts. The central element of the project was a series of wind-tunnel experiments using a 2D wing model mounted on a 2DOF traversing mechanism which involved close coordination of aerodynamic flow control testing (e.g., Brzozowski & Glezer, 2009) and controller development (Muse *et al.*, 2008*b*,*a*). In addition to the wind tunnel investigations, two separate low order modeling approaches were pursued for flight controller enhancement as well as to elucidate the underlying physical mechanisms of the flow control approaches. Tchieu *et al.* (2008) developed a reduced order model (ROM) based on discrete vortex elements. Ben-Dov *et al.* (2009) used separate approach, decomposing the experimental data into vorticity POD modes which were then correlated with unsteady pressure measurements and used for real-time control. High order numerical simulations of the open- and closed-loop flow control experiments using Delayed Detached Eddy Simulation (Lopez *et al.*, 2009; Jee *et al.*, 2009) were used to aid in experiment planning and validation of the low order models. In parallel with these efforts, Aiyar *et al.* (2009); Song *et al.* (2009) explored possible MEMS sensors for integration into the skin of a UAV to provide distributed shear stress measurements over the wing planform. Another important component of the MURI project was a flight demonstration of aerodynamic maneuvering using a Dragon-Eye UAV.

1.2 Thesis Objectives and Organization

The overarching goal of the present dissertation is to demonstrate aerodynamic flow control of unsteady forces and moments on a moving airfoil model. This is accomplished through the following objectives:

- Investigation of the fundamental interaction mechanisms between quasi-steady flow control actuation and the cross flow over a static airfoil, and characterization of the ensuing aerodynamic forces and moments.
- Investigation of the dynamic response of the flow field over the airfoil, and the resulting aerodynamic forces and moments to transitory actuation.
- Demonstration of closed-loop feedback control of pitch and plunge motions of the airfoil that are effected exclusively by aerodynamic flow control.
- Connection of the experimental investigations with reduced order modeling and unsteady aerodynamic theory.

The remainder of the present chapter includes a literature survey of synthetic jet flow control (§1.3) and unsteady aerodynamics (§1.4). This is followed with a description of the experimental setup and procedure (Chapter 2) and the closed-loop control system (Chapter 3) which regulates the airfoil's position using either electromechanical or flow control actuators. The experimental results commence in Chapter 4 with characterization of the static performance of the actuators over a range of angles of attack, actuator position and actuation strength. Following this analysis, investigations of the unsteady flow field resulting from transient actuation (i.e., a step input in actuation amplitude) is described in Chapter 5. Closed-loop aerodynamic flow control of the wind tunnel model is demonstrated for both pitch-only and pitch/plunge maneuvers in Chapter 6. Finally, the experimental results are compared with reduced order model predictions in Chapter 7. The conclusions and contributions of this thesis work are summarized in Chapter 8.

1.3 Flow Control

1.3.1 Formation and Evolution of Synthetic Jets

In recent years, "synthetic" (zero net mass flux) jets have emerged as versatile actuation technology tool for a broad range of aerodynamic flow control applications. The jets are formed by the advection and interactions of trains of discrete vortical structures that are formed by actuators integrated in the boundary of a cross flow. The jets are formed entirely from the working fluid of the flow system in which they are deployed and thus can transfer linear momentum to the flow system without net mass injection across the flow boundary. The vortices that synthesize the jet are formed by alternate suction and blowing of the ambient fluid through an orifice in the flow boundary by the motion of a diaphragm that is built into one of the walls of an otherwise sealed cavity below the surface. These attributes of synthetic jets coupled with the development of actuators that can be integrated into the flow surface without the need for complex piping and fluidic packaging make them attractive fluidic actuators for a broad range of flow control applications. In fact, by exploiting inherent instabilities of the base flow, synthetic jets can effect significant global modifications on scales that are one to two orders of magnitude larger than the characteristic length scales of the jets themselves.

The formation and evolution of isolated synthetic jets in the absence of a cross flow have been the subject of a number of investigations with emphasis on the near field formation, evolution, and advection of the jet vortices and on scaling of the time-averaged flow. These works included numerous experimental investigations (*plane jets*: Smith & Glezer, 1998; Yao *et al.*, 2004; Yehoshua & Seifert, 2006; *round jets*: Cater & Soria, 2002; Shuster & Smith, 2007), and numerical investigations (*plane jets*: Rizzetta *et al.*, 1999; Lee & Goldstein, 2002; Kotapati *et al.*, 2007). Modeling has included compressibility effects (Tang & Zhong, 2007), reduced order models (Yamaleev & Carpenter, 2006), and lumped element models of the actuator (Gallas *et al.*, 2003).

The interaction of a synthetic jet (or jet arrays) with an external cross flow over the surface in which they are mounted has been of significant interest in light of their application to flow control. Zhong *et al.* (2005) considered the interaction of a round synthetic jet with a flat plate laminar boundary layer, and the evolution of the jet vortices (stretching and penetration) for different Reynolds numbers, velocity ratios, and formation frequencies. In a related investigation Liddle & Wood (2005) investigated the interactions of clusters of round synthetic jets with the boundary layer and considered both streamwise-symmetric and -asymmetric interactions. This work was extended by Jabbal & Zhong (2008) who investigated the effects of spanwise arrays of round synthetic jets on the flow over a 2D circular cylinder and concluded that hairpin vortices and stretched vortex rings played a role in delaying separation. In a recent paper, Jabbal & Zhong (2010) investigated the impact of these vortical structures on cross-stream velocity distributions within a laminar boundary layer and reported that trains of stretched vortex rings would be most effective for separation control. The evolution of synthetic and conventional jets having the same orifice and velocity ratio was compared by Milanovic & Zaman (2003) in a flat plate boundary layer who showed that for several orifices global features (velocity, streamwise vorticity, turbulence intensity, and penetration) are similar. Smith (2002) investigated the interaction between arrays of rectangular jets and a flat plate turbulent boundary layer and found that downstream of the jets a streamwise array resulted in wake-like flow while a spanwise array led to the formation of longitudinal, counter-rotating vortex pairs. The interaction of a synthetic jet with a turbulent boundary layer was also investigated numerically (the computation domain included the cavity) by Dandois *et al.* (2006) who provided detailed information about the alteration of the velocity field within the boundary layer and the structure of the jet in the vicinity of the orifice. The utility of a spanwise array of synthetic jet actuators for active control of the near-wall region of a turbulent boundary layer was investigated by Rathnasingham & Breuer (2003) who used transfer functions to predict the downstream characteristics of the streamwise velocity fluctuations and reported up to a 30% reduction in the streamwise velocity fluctuations and 23% reduction in the bursting frequency within a domain of influence measuring about 50 x 150 viscous lengths in the wall-normal and spanwise directions, respectively.

1.3.2 Separation Control at "Low" Actuation Frequencies

Flow control strategies for external aerodynamic surfaces have mostly focused on mitigation of flow separation which is typically precipitated by an adverse pressure gradient (e.g., on a lifting surface) or by a sharp discontinuity in the flow boundary (e.g., a cavity or a bluff trailing edge). Attempts to manipulate and ultimately control separation over stalled airfoils have typically relied on the narrow band receptivity of the separating flow to external actuation. The separation is simultaneously affected by *two* instability mechanisms namely, a local instability of the separating shear layer and, more importantly, a wake instability that ultimately results the formation and shedding of large-scale vortical structures into the wake (e.g., Wu *et al.*, 1998). Because the nominally time-periodic vortex shedding into the wake is accompanied by global changes in circulation, it strongly affects the evolution of the separating shear layer near the leading edge. In fact, this coupling appears to dominate the rollup of the shear layer whose natural ("most unstable") frequency is typically higher than the global shedding frequency. Since the characteristic scale of the wake is typically commensurate with the scale of the separated flow domain, earlier work on separation control over fully- or partially-stalled airfoils has emphasized actuation frequencies that are on the order of the shedding frequency. This corresponds to a Strouhal number $St_{\mathrm{act}} = \frac{LU_{\mathrm{c}}}{T_{\mathrm{act}}}$ of $O(1)$ where the actuation period T_{act} is nominally on the same order as the convective time scale T_{conv}, or time of flight over the separated flow domain (L and U_{c} are the characteristic advection length and speed, respectively).

This approach to control of separation has been applied with varying degrees of success since the early 1980s to restore aerodynamic performance of stalled airfoils and flaps (e.g., Ahuja & Burrin, 1984; Hsiao *et al.*, 1990; Neuberger & Wygnanski, 1987; Seifert *et al.*, 1993). Seifert *et al.* (1993) argued that the actuation is most effective when the "reduced frequency" F^+ (which is essentially the actuation Strouhal number St_{act}) is $O(1)$ indicating that *the actuation frequency couples to, and in fact drives the shedding in the near wake.* Actuation at these frequencies leads to the formation of vortical structures that scale with the length of the separated flow domain and the ensuing changes in the rate of entrainment result in a Coanda-like deflection of the separating shear layer towards the surface of the stalled airfoil such that the layer vortices are effectively advected downstream in close proximity to the surface as discussed for example by Amitay & Glezer (2002*b*), Glezer *et al.* (2005), and Greenblatt (2006).

It might be argued that the fundamental flow mechanisms of separation control using synthetic jet actuation at "low" frequencies whose period is commensurate with the convective time scale of the flow, are probably similar in many aspects to the mechanisms of associated with "conventional", time periodic (or pulsed) jet actuation at the same frequency (for example, Neuberger & Wygnanski, 1987; Seifert & Pack, 1999). Furthermore, the primary advantages of synthetic jets for flow control implementation are that excessive actuation mass flux at high forcing amplitudes may adversely affect flow attachment, there is no need for an external fluid source, and integration and packaging are simplified. A number of experimental and numerical investigations have utilized synthetic jet actuators for separation control at "low" actuation frequencies. Experimental investigations have included Greenblatt & Wygnanski who used synthetic jet actuation to improve the stall characteristics of an MAV airfoil (2001), and to assess the effect of leading edge curvature on separation control on NACA 0012 and NACA 0015 airfoils (2003), Margalit *et al.* (2005) who used low-frequency modulation of piezoelectrically-driven synthetic jet actuators to control stall on a delta wing model reported that modulation of the high-frequency actuation signal at reduced modulation frequency $O(1)$ increased the normal force generated by the delta wing most effectively. The numerical simulations of Raju *et al.* (2008) considered synthetic jet flow control of separation over a stalled NACA 4418 airfoil. The authors identified three characteristic frequencies that, in addition to the separating shear layer and the wake also include a separation bubble that may form if the flow reattaches upstream of the trailing edge (but may still undergo periodic release of vortices). It is found that actuation frequencies that are close to the separation bubble frequency are most effective in diminishing separation and improving aerodynamic performance while actuation frequencies that are commensurate with the separating shear layer tend to enhance separation. You *et al.* (2008) used large-eddy simulation to investigate turbulent separation over a NACA 0015 airfoil ($Re_c = 896,000$). When the flow separates around a midchord, the LES in the presence and absence of synthetic jet actuation agree well with the measurements of Gilarranz *et al.* (2005) which demonstrated separation delay and a significant increase in the lift. When the flow separates near the leading edge, the same actuation is marginally effective.

"Low" frequency synthetic jet actuation has also been applied with some degree of success to flaps with emphasis on high-lift systems. Smith *et al.* (2006) investigated the application of low-frequency [$St\ O(1)$] synthetic jet control to enhance the high-lift characteristics of a SSTOL aircraft using voice-coil driven actuators on a powered model of a SSTOL. They reported lift increments of 0.2 for takeoff (flap deflection 40°) and 0.5 for landing (50°). In 2D testing, a similar system using a slat and a 40° flap yielded a $20 - 40\%$ increase in lift (depending on angle of attack), at $Re_c = 7.5 \cdot 10^5$. Comparable results were achieved by Nagib *et al.* (2006) who used externally driven low frequency synthetic jets an demonstrated how the lift can be increased by manipulating the flow near the suction surface juncture between the main element of the airfoil and the deflected single-element flap. Schatz *et al.* (2004) mitigate separation from the leading edge of a deflected flap using an externally driven synthetic jet, resulting in a significant increase in lift that was observed both in CFD and an experimental study. Shmilovich & Yadlin (2006) demonstrate how the improvement of flow attachment on the flap results in an increase in suction over the main element that also contributes to increased lift and found that with multiple chordwise injection points flow reattachment to the flap trailing edge can be achieved at high flap deflections, leading to near-inviscid lift levels. More recently, Greenblatt & Washburn (2008) investigated synthetic jet actuation at the leading edge and at the flap juncture of a semispan wing model that could be tested in unswept and swept configurations. The authors reported that control at the flap yielded an increase in lift in the absence of sweep, but was significantly less effective in the presence of sweep.

1.3.3 Aerodynamic Control at "High" Actuation Frequencies

A different approach to the control of flow separation on lifting surfaces emphasizes fluidic modification of the "apparent" aerodynamic shape of the surface upstream of separation with the objective of altering the streamwise pressure gradient to achieve complete or partial bypass (or suppression) of separation. The control of aerodynamic flows by modifying the apparent shape of aero-surfaces in order to prescribe the streamwise pressure distribution and therefore influence their aerodynamic performance is not new and was addressed in a substantial body of work in the 1940s and 50s. For example, Perkins & Hazen (1953) used a stationary, trapped vortex to alter the apparent local surface curvature and therefore the direction of the external flow near the trailing edge of an airfoil to increase the lift at zero angle of attack. Trapped vorticity is effected by forming a controlled interaction domain of between a surface-mounted fluidic actuator (e.g., a synthetic jet) and the cross flow above the surface. As demonstrated by Honohan *et al.* (2000) and Honohan (2003) on a two-dimensional cylinder, the trapped vorticity interaction domain between a high-frequency synthetic jet and the cross flow over the surface displaces the local streamlines of the cross flow and thereby induces a 'virtual' change in the shape of the surface (measuring roughly $2 - 4$ actuation wavelengths). The resulting change in the streamwise pressure gradient alters the evolution of the boundary layer and leads to a delay in separation. Natural formation of a small, closed separation bubble on the surface of a cylinder near the critical Reynolds number ($Re_{\mathrm{Dcrit}} \approx 3.2 \cdot 10^5$) allows the boundary layer to withstand higher than normal pressure rise and thus *flow separation moves farther downstream* and the cylinder base pressure increases (Roshko, 1993).

In contrast to control approaches that rely on global manipulation of the coupled instability of the separating shear layer and the wake where the characteristic actuation wavelength scales with the affected flow domain, "virtual" surface shaping is based on actuation having a characteristic wavelength that is at least an order of magnitude smaller than the relevant local or global length scale of the flow. Therefore, the corresponding actuation frequencies for these two approaches are at least an order of magnitude apart, typically $O(T_{\mathrm{conv}}^{-1})$ and $O(10T_{\mathrm{conv}}^{-1})$ for "low" and "high" actuation frequencies, respectively. In fact, "virtual" surface shaping utilized an actuation frequency that is high enough so that the interaction between the actuator and the cross flow is essentially time-invariant on the global time scale of the flow (e.g., of vorticity shedding) and therefore is effectively *decoupled* from the actuation frequency in the sense that once the actuation frequency is high enough, its effect becomes frequency-independent.

This approach has been demonstrated in several previous works on separation control at "high" actuation frequencies where control authority was achieved over a broad range of St_{act}. Amitay & Glezer (2002*b*) demonstrated high-frequency actuation on an unconventional airfoil and showed that the aerodynamic forces become almost invariant as the actuation frequency increases. Timor *et al.* (2004) used synthetic jet actuation to investigate 3D effects on a cropped NACA 0018 airfoil. Actuation led to a significant increase in lift pitch-down moment particularly when the actuation phase was varied along the span. Watson *et al.* (2007) used high frequency actuation to control the separating shear layer over highly swept wings and thereby to mitigate vortex breakdown and the resulting unsteady dynamic loading using actuation frequency that was selected to be an order of magnitude higher than the characteristic vortex bursting frequencies. The actuation led to a reduction of about 40% in the unsteady pressures near the trailing edge. In a numerical investigation of the control effectiveness of a synthetic jet on a stationary and a pitching NACA 0015 airfoil ($Re_c = 360,000$) Rehman & Kontis (2006) reported that the actuation yielded an increase in lift at angles of attack within the range 10°–20°. The authors noted that the increase in lift was accompanied by an increase in drag, but if the jet is placed close to separation drag can be reduced. A single synthetic jet did not suppress vortex formation and shedding on a pitching airfoil, but the overall airfoil performance was enhanced. As shown by Amitay & Glezer (2002*b*) and by Glezer *et al.* (2005), at "high" frequencies the actuation is effectively decoupled from the wake instability and therefore the modified aerodynamic forces tend to be virtually time-invariant.

Trapped vorticity flow control can also be effective when the baseline flow is fully attached, at low angles of attack (e.g., at cruise conditions). Chatlynne *et al.* (2001) and Amitay *et al.* (2001) showed that the formation of a stationary trapped vortex above an airfoil at low angles of attack leads to pressure drag reduction that is comparable to the magnitude of the pressure drag of the baseline configuration with minimal lift penalty. This approach was expanded by DeSalvo *et al.* (2002) and later by DeSalvo & Glezer (2004) to manipulate the Kutta condition of an airfoil using controlled concentrations of trapped vorticity near the trailing edge using a miniature $O(0.01c)$ hybrid actuator similar to a Gurney flap. The changes in the flow near the trailing edge result in significant global aerodynamic effects over a broad range of angles of attack ($\alpha < 10°$) that include a substantial reduction in pressure drag (and therefore an increase in L/D_{p}) and a significant increase in the pitching moment that can be continuously adjusted by varying the strength of the actuation or the momentum coefficient. DeSalvo & Glezer (2005) realized an even higher decrease in pressure drag with virtually no loss in lift or significant change in skin friction drag by trapped vorticity concentrations on the pressure surface near the leading edge. More recently DeSalvo & Glezer (2007) reported bi-directional changes in the pitching moment at low angles of attack that are effected without the presence of moving control surfaces using controllable, nominally-symmetric trapped vorticity concentrations on both the suction and pressure surfaces near the trailing edge. The pitching moment is varied continuously by alternate operation of the actuators, and the actuation is effective with minimal lift and drag penalties over a broad range of angles of attack.

1.3.4 Aerodynamic Control using Pulsed Jets and Transitory Actuation

Several investigators have considered anharmonic actuation to exploit transitory flow mechanisms that are associated with time-dependent flow evolution such as during separation and attachment. In the present investigation such actuation is implemented by amplitude modulation of the time harmonic actuation waveform by a closed-loop control system such that the resulting actuation is at times transient in nature. Amitay and Glezer (1999, 2002*a*, 2006) investigated flow transients associated with the onset and termination of high-frequency actuation that leads to flow attachment over a stalled airfoil, and noted the similarity to the transients that accompany separation and attachment during dynamic stall. In particular, Amitay & Glezer (2006) demonstrated that the separated flow is extremely susceptible to transitory actuation and showed that when the actuation input was applied on time scales that are significantly shorter than the characteristic advection time over the separated flow domain, the resulting aerodynamic forces are larger than the forces realized by conventional, continuous time-harmonic actuation. The onset and termination of continuous actuation over a flat-plate flap configuration were investigated by Darabi & Wygnanski (2004*a*,*b*) who reported close characteristic attachment and separation times for "optimal" actuation momentum coefficient C_μ and dimensionless frequency F^+. More recently, Siauw *et al.* (2009) investigated the transient attachment and separation on a NACA 0015 airfoil using fluidic vortex generators, and similarly Mathis *et al.* (2009) considered transient attachment and separation by pneumatic disruption of an actuation jet which effects separation over a splitter plate when active.

The utility of pulsed actuation for separation control was demonstrated by Crittenden et al. (2001, 2004, 2006) and Funk *et al.* (2002) who used time-periodic, momentary [$O(1\text{ ms})$] high-impulse actuation jets produced by combustion-powered actuation (COMPACT). This work was later extended by Brzozowski *et al.* (2010) to the investigation of the transitory response of the flow over a stalled NACA 4415 airfoil to actuation by a single pulse having a characteristic time scale of $0.05T_{\text{conv}}$. These authors showed that the momentary actuation leads to a partial collapse of the separated flow domain, coupled with a momentary increase in circulation magnitude on a time scale that is nearly $10T_{\text{conv}}$. In subsequent investigations Woo *et al.* (2008, 2009) and Woo & Glezer (2010) demonstrated that successive actuation by single pulse or short actuation bursts results in a rapid buildup of circulation that can extend the streamwise domain of attached boundary layer towards the trailing edge. The fast dynamic response associated with the reattachment process, combined with the relatively long relaxation process, allows low duty cycle pulsed actuation bursts to prevent full stall between bursts.

1.4 Flow Control on Moving Airfoils

Following the demonstration of the utility of active flow control for regulation of aerodynamic forces on static airfoils, attention has begun to shift toward aerodynamic control on moving platforms. A substantial body of literature discusses flow control efforts for mitigation and control of dynamic stall. A number of numerical (Wu *et al.*, 1998, Wake & Lurie, 2001, Duraisamy & Baeder, 2002, and Florea & Wake, 2003) and experimental (Lorber *et al.*, 2000, 2002, Greenblatt & Wygnanski 2001, and Pinier *et al.*, 2007) investigations employed time-periodic actuation in an effort to manipulate dynamic stall on oscillating airfoils and have shown that the actuation can increase the unsteady stall angles and post-stall lift. Woo & Glezer (2010) expanded on the steady-airfoil work of Brzozowski *et al.* (2010) and demonstrated dynamic stall control on a pitching NACA 4415 using pulse-combustion actuators. More recently, Colonius & Williams (2011) used pneumatic actuation at the leading edge of a low aspect ratio wing to regulate the lift force in the presence of an unsteady free stream. A related area research is the stabilization of bluff bodies. Zhang *et al.* (2004) demonstrated control of vortex shedding on a spring-mounted rectangular cylinder using an active surface perturbation when the system was in resonance.

Investigations of aerodynamic flow control on static and moving platforms have primarily focused on separated flows and little or no attention has been paid to control of fully attached flows at low angles of attack where the effected aerodynamic forces and moments are relatively small. Applications of flow control to fully attached flows include minimization of cruise drag, optimization of lift distribution, trim for varying flight conditions, etc. The primary objective of the present work is investigation of flow control mechanisms that enable maneuvering. The application of forces induced by flow control occur on time scales in which the actuator dynamics coupled with the unsteady aerodynamic characteristics of the platform which are briefly reviewed here.

Classic aerodynamic theory (Milne-Thomson, 1973, Abbott & von Doenhoff, 1959) has focused primarily on static airfoils in a steady free stream. Investigations of unsteady aerodynamic theory began in earnest after WWI and were initially derived from inviscid flow theory as extensions to thin airfoil theory. Wagner (1925) studied the problem of the lift generation on an airfoil following a step change in the bound circulation ($L_{\mathrm{qs}}(t) = L_0$ for $t > 0$) around an airfoil which may be induced, for example, but a sudden change in α. By modeling the wake vorticity as a function of time and streamwise distance from the trailing edge, Wagner was able to compute the lift induced on the airfoil by the wake. The result of this analysis is Wagner's function $\phi(t)$ (Figure 1.1a) which is equal to the unsteady circulatory lift as a function of time $L(t)$ divided by the quasi-steady lift L_0. Note that $L(t)$ here represents the circulatory part of the lift (i.e., the lift due to bound circulation and the lift due to wake vorticity). The non-circulatory part of the unsteady lift force arises from the apparent mass effect (see discussion in Chapter 7) and is readily modeled with momentum conservations (Fung, 1993). Immediately following the discontinuity, $L(t)$ is equal to half the steady-state value. For $t > 0$, $L(t)$ asymptotically approaches L_0. At $t = 30T_{\mathrm{conv}}$, $L = 0.99L_0$. By applying Duhamel's integral, Wagner's result may be generalized to an arbitrary variation in quasi-steady lift:

$$L(t) = \frac{1}{2}L_{\mathrm{qs}}(t) + \int_{-\infty}^{t} L_{\mathrm{qs}}(t')\,\phi'(t-t')\,dt' \tag{1.1}$$

Note that the early investigators measured time in semichords s traveled by a particle moving with the free stream speed U_0. Their results have been recast here in terms of $t/T_{\mathrm{conv}} = s/2$ for consistency with the remainder of the thesis.

While Wagner adopted a time-domain approach to the unsteady airfoil problem, researchers in the United States made progress with frequency-domain analysis. Motivated by the problem of wing flutter, Theodorsen (1935) studied the unsteady lift and pitching moment on a thin airfoil undergoing harmonic oscillations in pitch and plunge. Theodorsen's lift-deficiency function $C(k)$ is effectively a transfer function relating the magnitude and phase of L and L_{qs} as a function of reduced frequency $k \equiv \frac{\pi f c}{U_0}$ where f, c, and U_0 are the oscillation frequency, airfoil chord, and free stream speed, respectively. Figure 1.1b shows

$C(k)$ plotted in the complex plane. In the absence of oscillation ($k = 0$), $C = 1$ since $L = L_{\text{qs}}$. As k increases, the wake vorticity exhibits a lowpass filtering effect in that L is increasingly diminishes in amplitude and is delayed in phase with respect to L_{qs}. The maximum phase delay of 16° occurs at $k = 0.36$ and corresponds to an amplitude ratio of $|L|/|L_{\text{qs}}| = 0.66$. In the limit of large k, the phase shift decays back to zero and $L = 0.5L_{\text{qs}}$. Application of the Fourier transform enables computation of $L(t)$ for a general periodic motion (with corresponding periodic L_{qs}):

$$\widehat{L}(k) = \widehat{L}_{qs}(k)\, C(k) \tag{1.2}$$

where $\widehat{L}(k)$ and $\widehat{L}_{\text{qs}}(k)$ are the Fourier transforms of $L(t)$ and $L_{\text{qs}}(t)$. Since both Wagner's and Theodorsen's results are derived from thin airfoil theory, they yield equivalent estimations of $L(t)$ and $L_{\text{qs}}(t)$. Indeed by combining Equations 1.1 and 1.2, it is possible to derive an explicit relationship between $\phi(t)$ and $C(k)$ (Fung, 1993).

Other important early contributions were made by Küssner (1936) who gave a more elegant derivation of Wagner's result and treated the problem of an airfoil encountering a sudden gust acting normal to the free stream. Jones (1940) extended the results of these three authors to finite span elliptic wings, in the process deriving exponential approximations to Wagner's function and wake vortex distribution. Von Kármán & Sears (1938) and Sears (1940, 1941) compiled these results and recast the equations in a more concise form which avoided much of the difficult mathematical derivations of the earlier authors. In addition, they derived the response of a thin airfoil to a sinusoidal gust, where the primary result became known as Sears' Function. Later authors extended unsteady theory to thick airfoils (Woods, 1954) and finite wings with general planform shapes (Dore, 1966).

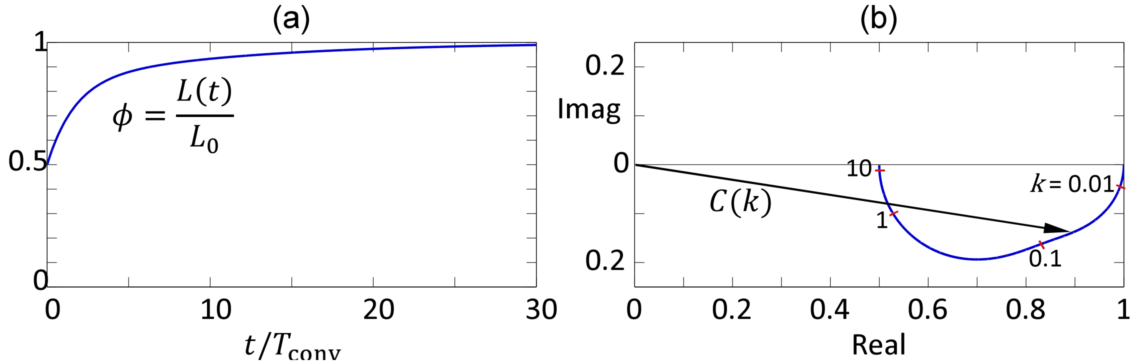

Figure 1.1: The relationship between the quasi-steady and the total circulatory lift on a thin airfoil in unsteady motion. (a) Wagner's function: time response to a step change in quasi-steady lift, $L_{\text{qs}}(t) = L_0$ for $t > 0$. (b) Theodorsen's function: frequency response for an airfoil undergoing harmonic motion with reduced frequency k.

Chapter II

EXPERIMENTAL PROCEDURE

This section describes the experimental methods and apparatus employed for the present research. First the airfoil and fluidic actuators are described. Following that, a brief overview is given of the wind tunnel facility and particle image velocimetry (PIV) system. The post-processing procedure for the PIV records is laid along with an overview of the computer processing employed to process the data. The chapter concludes with a description of the traverse which enables the model to move in two degrees-of-freedom (2DOF) in the tunnel, and direct measurements of the dynamic pitching moment and lift force on the model.

2.1 Airfoil Model

The present experiments were conducted in an open-return low-speed wind tunnel having a square test section measuring 92 cm on the side and 3 m long. The tunnel test section is driven by a 1.1 kW (150 hp) blower through a diffuser (area ratio 1 : 3.8), a turbulence manipulation section, a plenum, and a contraction (area ratio 8.9 : 1). The upper and lower walls of the test section may be adjusted to correct for model blockage, or to specify a desired streamwise pressure gradient. In the present experiments, the model is moving in pitch and plunge and the pressure gradient could not be adjusted dynamically, therefore the walls were set parallel to each other.

The airfoil model has a constant cross-section and is based on a NACA 4415 (Figure 2.1) with a chord of $c = 457$ mm and maximum thickness to chord ratio of $t/c = 0.15$. The model, which spans the entire width of the wind tunnel test section, is comprised of multiple sections, each constructed of a five-layer fiberglass skin wrapped over an aluminum frame (Figure 2.1). A stereo-lithographed (SLA) segment is located between adjacent sections approximately at the midspan and includes 73 static pressure ports and several high-frequency pressure sensors (Figure 2.2). The entire model is assembled around hollow shaft (outer diameter $D_\mathrm{o} = 41.3$ mm, inner diameter $D_\mathrm{i} = 31.8$ mm, length $L = 1.96$ m) and installed in the test section with the ends of the shaft protruding through vertical slots in the side walls. The airfoil model is integrated with arrays of fluidic actuators described in §2.2 and is mounted on a two degrees-of-freedom traverse described in §2.4.

2.2 Fluidic Actuators

Bi-directional pitching moments on the airfoil model are effected by spanwise arrays of hybrid synthetic jet actuator modules located just upstream of the trailing edge on the pressure-side (*PS*) and suction-side (*SS*) of the airfoil as shown in Figures 2.3a,b. Each actuator module has a characteristic height of $0.017c$ above the airfoil surface and the jets emanate from a rectangular spanwise slot $b_{\mathrm{j}} = 0.4$ mm high and 33 mm long (parallel to the airfoil's trailing edge). The jets are generated by a spanwise array of 17 equally-spaced piezoelectric actuators, each integrated into a separate cavity. The piezoelectric actuators (Thunder TH-5C manufactured by FACE International, see Mane *et al.*, 2008) are driven off-resonance by an external high voltage AC amplifier (up to 100 V_{RMS}) at $f_{\mathrm{act}} = 2050$ Hz.

Each of the *SS* and *PS* actuator arrays are individually operated by a flight control system (described in Chapter3) such that all the actuators on each side are driven synchronously. When the model is driven in closed-loop using the fluidic actuators, the actuators are operated such that only the *SS* or *PS* array is operated at any given time. Therefore, from a control perspective, the actuators may be thought of as traditional control surfaces (at low maneuvering frequencies), where, as discussed in Chapter 4, *SS* and *PS* operation correspond to downward and upward flap deflections, respectively.

Although a detailed discussion of the effect of the flow control mechanism will be delayed until the later chapters, the net effect of actuation on the flow is depicted schematically in Figure 2.3c. In the absence of actuation the flow separates between the downstream edge of each actuator and the trailing edge, forming a recirculation region. Operation of either actuator manipulates the vorticity concentration downstream of the actuator which results in changes in pressure distribution and therefore in pitching moment.

Since the operation of the SS and PS actuators is mutually-exclusive in these experiments, it is convenient to introduce a single dimensionless parameter to describe the actuation state:

$$u_{\mathrm{f}} = \mathcal{E}'\delta_{\mathrm{act}} \quad \text{where} \quad \delta_{\mathrm{act}} = \begin{cases} -1 & PS \text{ actuation} \\ 0 & \text{no actuation} \\ +1 & SS \text{ actuation} \end{cases} \tag{2.1}$$

where $\mathcal{E}'$ is the fraction of the maximum operational voltage so that $-1 \leq u_{\mathrm{f}} \leq 1$ with $u_{\mathrm{f}} = -1$ and $u_{\mathrm{f}} = 1$ corresponding to full PS and full SS actuation, respectively. Hot-wire measurements shown in Figure 2.4a indicate that the RMS jet speed U_{j} at the actuator's orifice scales approximately linearly with the driving voltage. The corresponding jet momentum coefficient $C_\mu = \frac{U_{\mathrm{j}}^2 b_{\mathrm{j}}}{U_0^2 c}$ is show in Figure 2.4b. Since the RMS jet speed varies linearly with $\mathcal{E}'$, the momentum coefficient varies quadratically, from $C_\mu = 2x10^{-4}$ at $\mathcal{E}' = 0.2$ to $C_\mu = 2x10^{-3}$ at $\mathcal{E}' = 1$.

The flow control signal generation is depicted schematically in Figure 2.5. The controller splits the actuation command u_{f} into two separate commands for the SS and PS actuators:

$$\begin{aligned} u_{\mathrm{f},SS}(t) &= \min\{0, u_{\mathrm{f}}(t)\} \\ u_{\mathrm{f},PS}(t) &= \min\{0, -u_{\mathrm{f}}(t)\} \end{aligned}$$

Each of these signals is used for amplitude modulation of the actuation waveform. Two external signal generators are used to drive the piezoelectric actuators at a carrier frequency of $f_{\mathrm{act}} = 2050$ Hz. The amplitude of each carrier is varied by $u_{\mathrm{f},SS}$ and $u_{\mathrm{f},PS}$ respectively. The modulated waveforms are amplified by a gain of 20 to yield the desired disk driving voltage range of 0 to $100\,V_{RMS}$.

2.3 Particle Image Velocimetry

2.3.1 System Overview

The wind tunnel is equipped with a high-speed particle image velocimetry (PIV) system (LaVision) which allows for the characterization of the flow over the airfoil. The flow is seeded with micron-sized smoke particles which are generated by the heating of an aqueous glycol solution in a commercial fog generator. The fog is injected into the tunnel through the trailing edge of a symmetric airfoil within the tunnel's plenum that is aligned vertically with the midspan plane $z = 0$. The open segment along the trailing edge of the fog airfoil can be adjusted for a sheet of fog of desired cross-stream extent above and/or below the airfoil model in the test section. The cross-stream width of the fog sheet is also selected to minimize light attenuation.

The chordwise position of the laser sheet, its thickness and its streamwise extent can be varied using the transmitting optics on top of the tunnel. Typical laser sheet dimensions are 200 mm in the streamwise direction and a thickness of 2–3 mm in the spanwise direction. The high-speed laser (Quantronix Darwin Duo) is comprised of a pair of Nd:YLF units each capable of a maximum repetition rate of 10 kHz. The nominal pulse energy is 60 mJ at 1 kHz. The timing of the laser pulses with respect to each other and to the camera exposure is controlled by a programmable timing unit.

PIV images are aquired using a Photron FASTCAM 1024PCI which is based on a 1024×1024 pixel CMOS imager having a pixel spacing of $17\,\mu$m in both dimensions. At full resolution, the camera can record images at 1000 fps which gives a maximum double-frame PIV sample rate of 500 Hz. The camera can record reduced-resolution images at rates up to $109,500$ fps. In the present experiments the camera is operated from 200 fps to 1000 fps. The number of images recorded in a single burst is limited by memory on the frame grabber PCI card which interfaces the camera to the computer. The present system has 12 GB of memory which corresponds to 6400 full resolution images (or 3200 PIV pairs).

After each recording, images are transferred from the frame grabber memory to an array of hard disks configured in RAID Level 0 (a configuration in which data is "striped" across several disks to reduce storage time). In the present experiments the image download rate was 10 pairs of full resolution images per second or 13 pairs of half-resolution images per second.

The camera and laser are synchronized with a LaVision High-Speed Controller which is programmed with the DaVis software package. In addition to supporting simple interactive PIV sessions, DaVis features a command language (with syntax similar to the C language) through which the user has programmable access to all major system functionality as well as system resources (e.g., serial ports) which may be used to synchronize data acquisition with other systems (for example, the Simulink-based control system discussed in Chapter 3).

2.3.2 PIV Data Processing

Typically sets of 200 image pairs each are recorded for time-averaged measurements or for each phase point in phase-averaged measurements. Initial 2D velocity vector fields are computed using an interrogation window (or "spot size") of 32×32 pixels with 50% overlap. For an image recorded with the camera's imager parallel to the imaging plane (i.e., without off-axis imaging), a 1024×1024 pixel image yields a 63×63 vector array. When off-axis imaging is used to avoid obstructions in the optical path, the array's dimension varies slightly once an image de-warping algorithm is applied. For configurations in which the imaging sensor is parallel to the image plane, a calibration is obtained from an image of a ruler aligned with the laser sheet. For off-axis imaging, the mapping from the image coordinates to laboratory coordinates, which in general is not a linear, isotropic mapping, calibration is achieved using a calibration target consisting of a square grid of dots that is aligned with the laser sheet and imaged. The DaVis software computes a two-dimensional mapping function from the image coordinates to the corresponding laboratory coordinates. For either type of calibration, the appropriate mapping is applied to the vector fields during the initial vector field computation.

The initial vector field computed from the cross-correlation typically contains a number of spurious vectors which can result from low local seeding concentration. It is important to reject these outliers because they may degrade time-averaged quantities and bias second-order statistics (such as the Reynolds stresses and the turbulent kinetic energy). The DaVis software package includes a number of user-configurable built-in image- and vector-processing routines designed to minimize spurious vectors.

The present processing procedure includes several steps. First, the number of spurious vectors is reduced using an algorithmic mask computed on the original image pair. The mask is a binary representation of the input image pair which is constructed using a sequence of image processing operations in such a manner that the mask has a value of 0 in regions where there is inadequate seeding and a value of 1 everywhere else. Using this mask, vector validation proceeds as follows. If more that a certain fraction of the pixels within each interrogation region in the source image pair are marked as "bad" in the mask, the vector resulting from that interrogation region is discarded.

After the application of the algorithmic mask a median filter is applied to each of the remaining vectors by computing the median magnitude deviation of its neighbors. If the magnitude of the center vector deviates from the median by a predetermined fraction, the vector is rejected. Furthermore, if any of the next four highest peaks in the processing cross-correlation (which are recorded) are within a second predetermined fraction of the median deviation, this vector is inserted to replace the rejected vector.

Time-averaged and phase-averaged quantities are estimated from the set of instantaneous vector fields. The procedure for computing phase-averaged quantities is computational identical to that of time-averaged quantities, except that the calculations are repeated at each phase point of the reference signal. Because each instantaneous vector field typically contains a small number of missing vectors, the time-averaged velocity at each point $\left(\overline{U}, \overline{V}\right)$ is estimated as the sample mean of the available instantaneous velocity measurements at that point (U_i, V_i) where $i = 1, ..., N_i < N$. Similarly the Reynolds stress components are estimated as the sample variance and covariance of the available data:

$$\begin{aligned}
\overline{U'U'} &= \frac{1}{N_i} \sum \left(U_i - \overline{U}\right)^2 \\
\overline{V'V'} &= \frac{1}{N_i} \sum \left(V_i - \overline{V}\right)^2 \\
\overline{U'V'} &= \frac{1}{N_i} \sum \left(U_i - \overline{U}\right) \left(V_i - \overline{V}\right)
\end{aligned}$$

The time-averaged 2D estimate of the turbulent kinetic energy is computed from the trace of the 2D Reynolds stress tensor as $k = \frac{1}{2}\left(\overline{U'U'} + \overline{V'V'}\right)$. Finally, the time-averaged vorticity is computed from the time-averaged velocity components of the 8 neighboring points, following the circulation method of Raffel *et al.* (2007):

$$\begin{aligned}
\overline{\omega}_z &= \frac{\overline{U}^{\mathrm{SW}} + 2\overline{U}^{\mathrm{S}} + \overline{U}^{\mathrm{SE}}}{8\Delta y} + \frac{\overline{V}^{\mathrm{SE}} + 2\overline{V}^{\mathrm{E}} + \overline{V}^{\mathrm{NE}}}{8\Delta x} \\
&\quad - \frac{\overline{U}^{\mathrm{NE}} + 2\overline{U}^{\mathrm{N}} + \overline{U}^{\mathrm{NW}}}{8\Delta y} - \frac{\overline{V}^{\mathrm{NW}} + 2\overline{V}^{\mathrm{W}} + \overline{V}^{\mathrm{SW}}}{8\Delta x}
\end{aligned}$$

where $(\Delta x, \Delta y)$ is grid spacings of the vector array.

2.4 Pitch/Plunge Traverse

The airfoil model is moved dynamically in pitch and plunge using a programmable, 3DOF (pitch, plunge and roll) traverse that is constructed in a frame around the wind tunnel test section as shown in Figures 2.6 and 2.7.

2.4.1 Mechanical Design

The airfoil model is mounted on hollow rotating shaft which is coupled to a pitch servo actuator at one end, and an air bearing at the other. The pitch servo motor effects rotational motion over the range ±25° (Figure 2.7a). A bearing allows both rotational and axial motions (the latter enables the wind tunnel model to bank slightly since the two plunge drives are controlled independently). Both the pitch servo actuator and air bearing are coupled to plunge carriages through gimbals that act as universal joints. Vertical motion of each carriage is effected by a servo motor, using a 20 mm pitch ball-screw mechanism and a linear slide (Figure 2.7b). It should be noted that the model shaft moves in plunge through vertical slots in the side walls of the wind tunnel test section. An electromagnetic release brake prevents load on the carriage when the traverse is not in operation and the travel of each linear slide is constrained by adjustable stops and limit switches. The traverse motion is controlled by a dedicated feedback control system, which is discussed in detail in Chapter 3.

In the present work, the linear motion of the model is limited to speed and acceleration of up to 0.5 m/s and $2g$, respectively (the maximum design speed and acceleration in the present configuration are 2.5 m/s and $5g$, respectively). The pitch servo motor can produce a peak torque of 42.6 Nm and a continuous stall torque of 14.2 Nm.

2.4.2 Sensors

The traverse is instrumented with a number of sensors which allow for measurement of positions, velocities, and accelerations, as well as forces and moments. The pitch angle is measured using a high-resolution optical encoder which is mounted to the pitch servo. Since this encoder does not contain an absolute position reference, a secondary angle measurement from an angular resolver (integrated into the servo actuator) is used to obtain the initial offset in pitch angle measurement. Angular acceleration of the model is measured by an angular accelerometer which is mounted to the end of the rotating shaft, immediately adjacent to the air bearing. The accelerometer (Columbia Research Labs) is configured to measure ± 50 rad/s^2 and has resolution of 0.01% of the full range. The torque applied to traverse by the pitch servo is computed from the voltage command to the servo amplifier using a dynamic model generated in an offline calibration (discussed in §2.5.1).

Sensors on each plunge axis measure the carriage position $y_{c,i}$, spring deflection δ_i, and force F_i applied to the pitch axis assembly by the plunge servo actuator. The carriage position is measured using a rotary optical encoder integrated into the plunge servo actuator. The spring deflection is measured with a compact laser range finder which is moves rigidly in plunge with the carriage and measures the distance to a flat surface that moves rigidly with the gimbal. These position measurements are augmented by acceleration measurements at several spanwise locations along the length of the support shaft. The linear accelerometers (Measurement Systems) have a range of 49 m/s^2 ($\pm 5g$), a resolution of 0.1% of the full range, and responds to frequencies up to 300 Hz. The vertical force applied by the carriages on the pitch axis assembly is measured using a load cell mounted between the carriage and gimbals on either side of the tunnel.

Finally, time-resolved surface pressure is measured at four points on the airfoil circumference at midspan using piezoresistive pressure senors (Honeywell) having high frequency response. These sensors have a range of ± 1 kPa and a resolution of ± 10 Pa and are located at the leading edge, the trailing edge, on the suction surface ($x/c = 0.39$), and on the pressure surface ($x/c = 0.4$).

2.4.3 Dynamic Sensor/Actuator Calibration

Dynamic models for the angular accelerometer and pitch servo motor, obtained through offline bench tests, were used to account for the non-ideal behavior of the sensor and actuator. The servo torque T_{servo} and angular acceleration $\ddot{\alpha}$ were computed from these models based on the servo command u_{m} and the angular accelerometer output $\ddot{\alpha}_{\mathrm{accel}}$, respectively. The bench tests were conducted using a steel disk of known inertia that was mounted on the servo motor, along with the angular accelerometer and a high resolution digital encoder (cf. §2.4.2). This digital encoder was used as the standard measure of position α_{enc} against which the pitch servo and angular accelerometer were calibrated. The servo motor was actuated with a series of time-harmonic torque inputs (both in open-loop and in closed-loop feeding back on the digital encoder) over a frequency range $1 < f < 20$ Hz with increments of $\Delta f = 0.25$ Hz. The resulting angular acceleration was measured with the angular accelerometer and (twice-differentiated) encoder. For each driving frequency f_n, the Fourier coefficient corresponding to f_n was extracted from the time histories of α_{enc}, $\ddot{\alpha}_{\mathrm{accel}}$, and u_{m}:

$$\begin{aligned} \hat{\alpha}_{\mathrm{enc},n} &= \mathcal{F}\left[\alpha_{\mathrm{enc}}(t)\right]_n \\ \hat{\ddot{\alpha}}_{\mathrm{accel},n} &= \mathcal{F}\left[\ddot{\alpha}_{\mathrm{accel}}(t)\right]_n \\ \hat{u}_{\mathrm{m},n} &= \mathcal{F}\left[u_{\mathrm{m}}(t)\right]_n \end{aligned}$$

The complex gains $H_{\mathrm{servo},n}$ and $H_{\mathrm{accel},n}$ corresponding to f_n were then computed:

$$H_{\mathrm{servo},n} = \frac{\text{realized torque}}{\text{commanded torque}} = \frac{-\left(2\pi f_n\right)^2 I_z \hat{\alpha}_{\mathrm{enc},n}}{\hat{u}_{\mathrm{m},n}} \tag{2.2}$$

$$H_{\mathrm{accel},n} = \frac{\text{measured acceleration}}{\text{"true" acceleration}} = \frac{\hat{\ddot{\alpha}}_{\mathrm{accel},n}}{-\left(2\pi f_n\right)^2 \hat{\alpha}_{\mathrm{enc},n}} \tag{2.3}$$

The measured gains H_{servo} and $1/H_{\mathrm{accel}}$ are plotted in Figures 2.8 and 2.9, respectively (red symbols). The response of the pitch servo (Figure 2.8) is remarkably flat; even at $f = 20$ Hz the gain is 1.07 and the phase delay is only 12°. The accelerometer's response exhibits a reasonably flat magnitude but a substantial linear phase shift which reaches 45° by $f = 13$ Hz (Figure 2.9).

A pair of continuous gain functions $H_{\mathrm{servo}}(f)$ and $1/H_{accel}(f)$ were generated using a spline fit to the measured data (solid line in Figures 2.8 and 2.9). In order to prevent high-frequency artifacts (ringing) in T_{servo} and $\ddot{\alpha}$, it was necessary for the gain functions be smooth and continuous up to the Nyquist frequency of 500 Hz. For the range $20 < f < 500$ Hz, the splines were constrained to enforce continuity and first derivative existence at $f = 20$ Hz and to decay rapidly to zero at higher frequencies. Although the spline fit is clearly not unique beyond 20 Hz, its values in this domain do not significantly affect the calculations.

The functions $H_{\mathrm{servo}}(f)$ and $1/H_{accel}(f)$ computed from the bench tests allowed for estimation of $T_{\mathrm{servo}}(t)$ and $\ddot{\alpha}(t)$ during arbitrary maneuvers of the airfoil model in the wind tunnel. These estimates were computed from the measured values, $u_{\mathrm{m}}(t)$ and $\ddot{\alpha}_{\mathrm{accel}}(t)$ by applying the gain functions in Fourier space:

$$\begin{aligned} T_{\mathrm{servo}}(t) &= \mathcal{F}^{-1}\left[H_{\mathrm{servo}} \cdot \mathcal{F}\left[u_{\mathrm{m}}(t)\right]\right] \\ \ddot{\alpha}(t) &= \mathcal{F}^{-1}\left[\frac{1}{H_{\mathrm{accel}}} \cdot \mathcal{F}\left[\ddot{\alpha}_{\mathrm{accel}}(t)\right]\right] \end{aligned}$$

2.5 Dynamic Force Measurement

This section describes the procedure used to estimate the dynamic (unsteady) lift $L(t)$ and pitching moment $M_{c/4}(t)$ about the quarter chord on the moving airfoil. These forces are computed using several sensors including dynamic load cells, linear and angular accelerometers and torque sensing using the servo actuator.

2.5.1 Pitching Moment

The aerodynamic pitching moment about the axis of rotation M_a is computed from a balance of torques about the axis shown in Figure 2.10a:

$$M_a = I_z \ddot{\alpha} - T_{\mathrm{servo}} - mgr_{\mathrm{cm}} \cos(\alpha) \tag{2.4}$$

where T_{servo} is the torque provided by the pitch servo, I_z is the moment of inertia about the pitch axis, m is the mass of the airfoil model, g is the gravitational acceleration and r_{cm} is the distance from the axis of rotation of the center of mass. The parameters I_z and r_{cm} are computed respectively from dynamic and static tunnel-off measurements. Note that the pitching moment is initially computed about the axis of rotation and then shifted to quarter chord $M_{c/4} = M_a + Lr_a$ where r_a is the chordwise distance from the axis of rotation to the quarter-chord point. Application of the dynamic sensor/actuator models (§2.4.3) is depicted in the form of a block diagram in Figure 2.10b.

Figure 2.11 shows the servo torque, angular acceleration and calculated aerodynamic pitching moment following a step change in pitch angle in the absence of air flow when the aerodynamic pitching moment is zero. Figure 2.11a shows the estimated servo torque with and without application of the dynamic servo model discussed in §2.4.3 (Equation 2.8). The actual servo torque is delayed slightly with respect to the torque command. Similarly, the estimated angular acceleration with and without application of the dynamic accelerometer model is shown in Figure 2.11b. It is evident that the model corrects the substantial phase shift present in the accelerometer. Figure 2.11c shows the terms of the torque balance: $I_z\ddot{\alpha}$, T_{servo}, and M_a (gravitational effects are negligible for this maneuver). Using the corrected torque and angular acceleration measurements, the measured aerodynamic moment- which, in the absence of air flow, represents the residual error- is limited to ±1.1 Nm (7%). Note that if the angular accelerometer and torque measurements are *not* corrected using the dynamic models discussed in §2.4.3, the residual error is nearly 100% as shown in Figure 2.11d.

2.5.2 Plunging Force

Estimation of the dynamic plunging force is complicated by the spanwise elastic bending of the pitch axis assembly (the airfoil model, support shaft, pitch servo and gimbals) which is suspended on the vertical spring set. In the present wing model, the fiberglass skin of the airfoil model is protected by minimizing the stress between the airfoil and the traverse. This was achieved by securing the airfoil model to the support bar only at the (spanwise) edges of the model. However, while the airfoil model (and actuators) add substantial mass to the pitch axis assembly (about 20 kg of the total 65 kg), the model adds minimal stiffness to the system and therefore can aggravate bending. This section discusses the procedure used to estimate the plunging force while accounting for the bending motion.

The motion of the pitch axis in the $y-z$ plane is modeled as a thin elastic beam that is free to plunge, roll (about the x-axis), and bend (Figure 2.12a). The spanwise distribution of vertical acceleration is $\ddot{y}(z,t)$. The forces acting on the beam are the weight mg, the aerodynamic lift $L(t)$ which is modeled as a concentrated force acting at the pitch axis center of mass, and the forces applied by the plunge actuators at each end of the beam

$F_1(t)$and $F_2(t)$ (measured by the load cells). In addition, the spanwise mass distribution of the system $\rho(z)$ along the span ($0 < z < l$) is such that the total mass is $m = \int_0^l \rho(z)dz$. A balance of forces in the (normal) y-direction for this system yields:

$$L(t) = \underbrace{mg - F_1(t) - F_2(t)}_{-F(t)} + \underbrace{\int_0^l \rho(z)\ddot{y}(z,t)dz}_{I(t)} \tag{2.5}$$

In the present experimental setup, it is not practical to measure the spanwise distribution of mass and acceleration. Instead, $I(t)$ is estimated using a sum of weighted accelerations $a_i(t)$ measured at six discrete locations along the span where the weights w_i are chosen to minimize an error $\epsilon(t)$ defined below. The weights are computed using measurements in the absence of air flow (i.e., where $L(t) = 0$). In this case the total external force $F_{U=0}(t)$ should balance the inertia term:

$$F_{\text{tunnel off}}(t) = \sum_{i=1}^{N} w_i a_i(t) + \epsilon(t)$$

and the weights w_i are chosen to minimize the error $\epsilon(t)$. A block diagram of the sensor arrangement is given in Figure 2.12b.

The calibration procedure was conducted as follows. In the absence of air flow, the model is driven in a sinusoidal plunge trajectory using the vertical servo motors. The plunge frequency is varied from 1 Hz to 20 Hz in increments of 0.25 Hz. For each frequency, the load cells and linear accelerometers are sampled. Note that in order to prevent transient accelerations in plunge, the plunge amplitude is slowly ramped up from zero at each discrete frequency before the acquisition starts and ramped back down when the acquisition is completed. All of the data from these runs are then concatenated into a single data matrix and a set of weights that minimize the mean squared error

$$\min \overline{\epsilon^2(t)} = \min \overline{\left[F_{\text{tunnel off}}(t) - \sum_{i=1}^{N} w_i a_i(t)\right]^2}$$

is computed. By including a wide range of frequencies in the calibration process, the intention is to compute a set of globally applicable weights w_i which may be applied during an arbitrary maneuver.

Although it is not possible to validate this method without an independent measure of unsteady force, an indication of its fidelity is shown in Figure 2.13. Using the coefficients computed from the calibration procedure described above (which is based on a series of harmonic plunge trajectories), the inertia term $I(t)$ was computed for a case in which the airfoil executed a nearly step change in plunge position in the absence of air flow (Figure 2.13). The system is given a plunge down command at $t = 0$ upon which the carriages immediately begin to accelerate (Figure 2.13a). This sudden acceleration of the endpoints of the pitch axis assembly sets the support bar into bending oscillations at $f_{\text{bend}} \sim 9$ Hz. The bending is evident both in the load cells (Figure 2.13b) and the spanwise distributed accelerometers (Figure 2.13c). In particular it is clear from the individual accelerometer traces that the system does not exhibit simple bending of the first mode, but in fact contains several bending modes as is evidenced by the higher frequencies present in both the load cell an accelerometer signals. The load cell measurements (Figure 2.13b) indicate that the forces are not spanwise-symmetric because of the presence of the pitch servo motor that is mounted on the left side of the pitch axis assembly. The bending oscillations decay exponentially until $t = 2T_{\text{conv}}$, when the system is given a step plunge up command which once again excites the bending modes.

The terms $F(t)$ and $I(t)$ in Equation 2.5 are plotted in Figure 2.13d. Recall that in the absence of air flow, the aerodynamic lift force is essentially zero, so it is expected that $F(t) = I(t)$. Indeed the two quantities are nearly identical over the 4-second record shown. In fact while these quantities vary over a range of$\pm$200 N, the difference between them shown in green is bound by $|F(t) - I(t)| < 8$ N or 4%. Once the weights are computed from the above calibration in the absence of air flow, Equation 2.5 may be used to estimate the lift force during maneuvers in the presence of air flow.

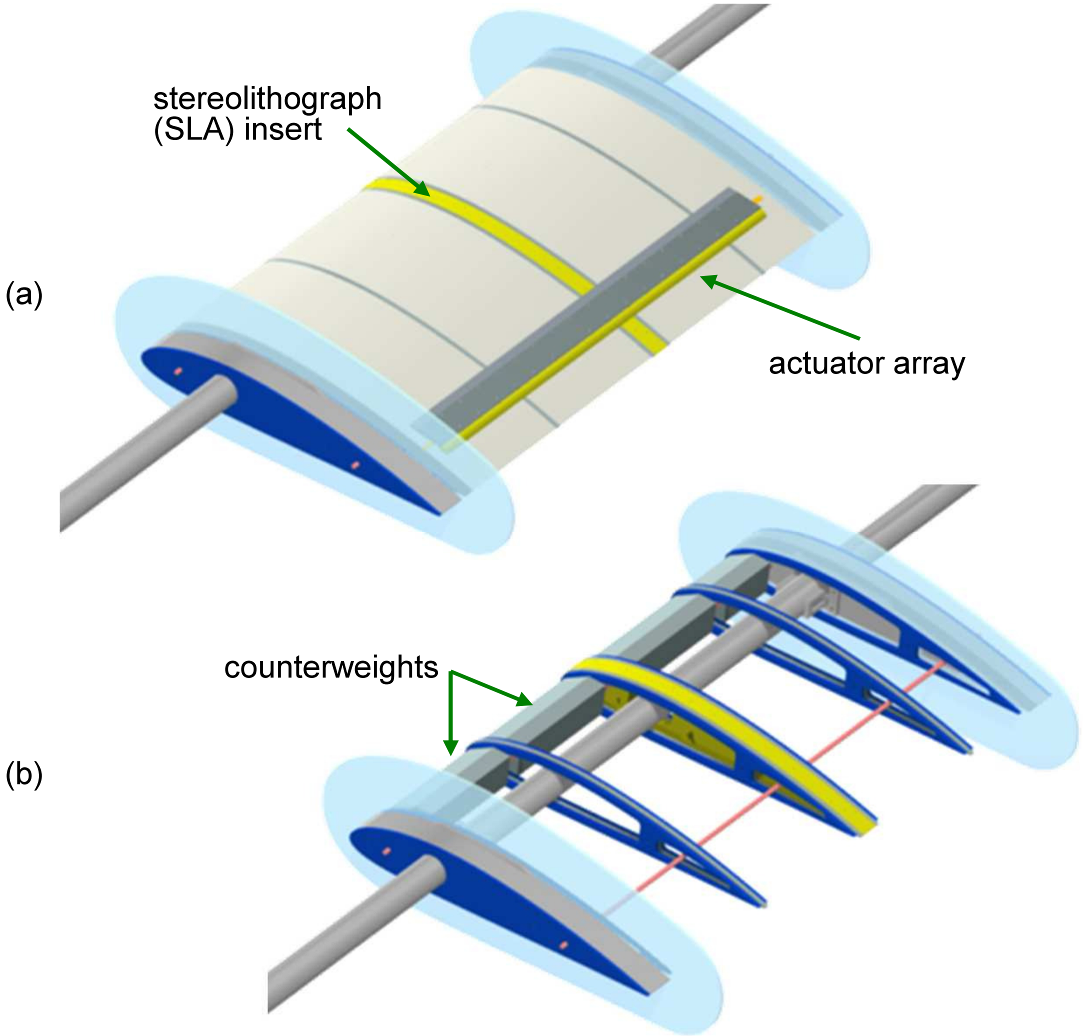

Figure 2.1: The NACA4415 airfoil model (a) assembled and (b) with the actuators and fiberglass skin removed.

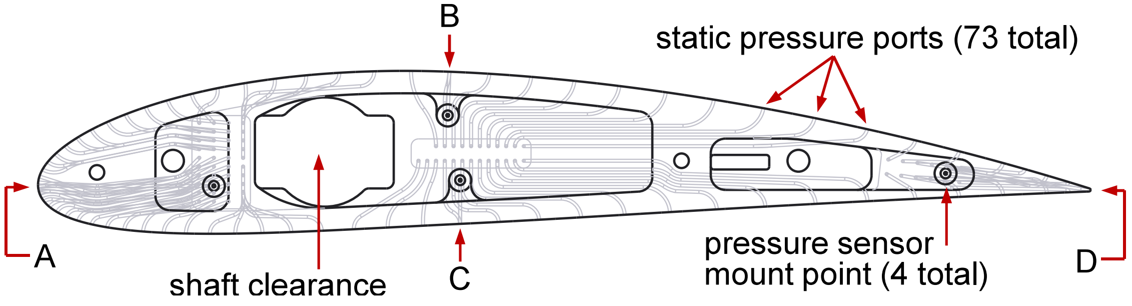

Figure 2.2: The stereolithograh insert includes 73 static pressure ports and four high-frequency pressure sensors located (A) at the leading edge, (B) on the suction surface at $0.39c$, (C) on the pressure surface at $0.4c$, and (D) at the trailing edge.

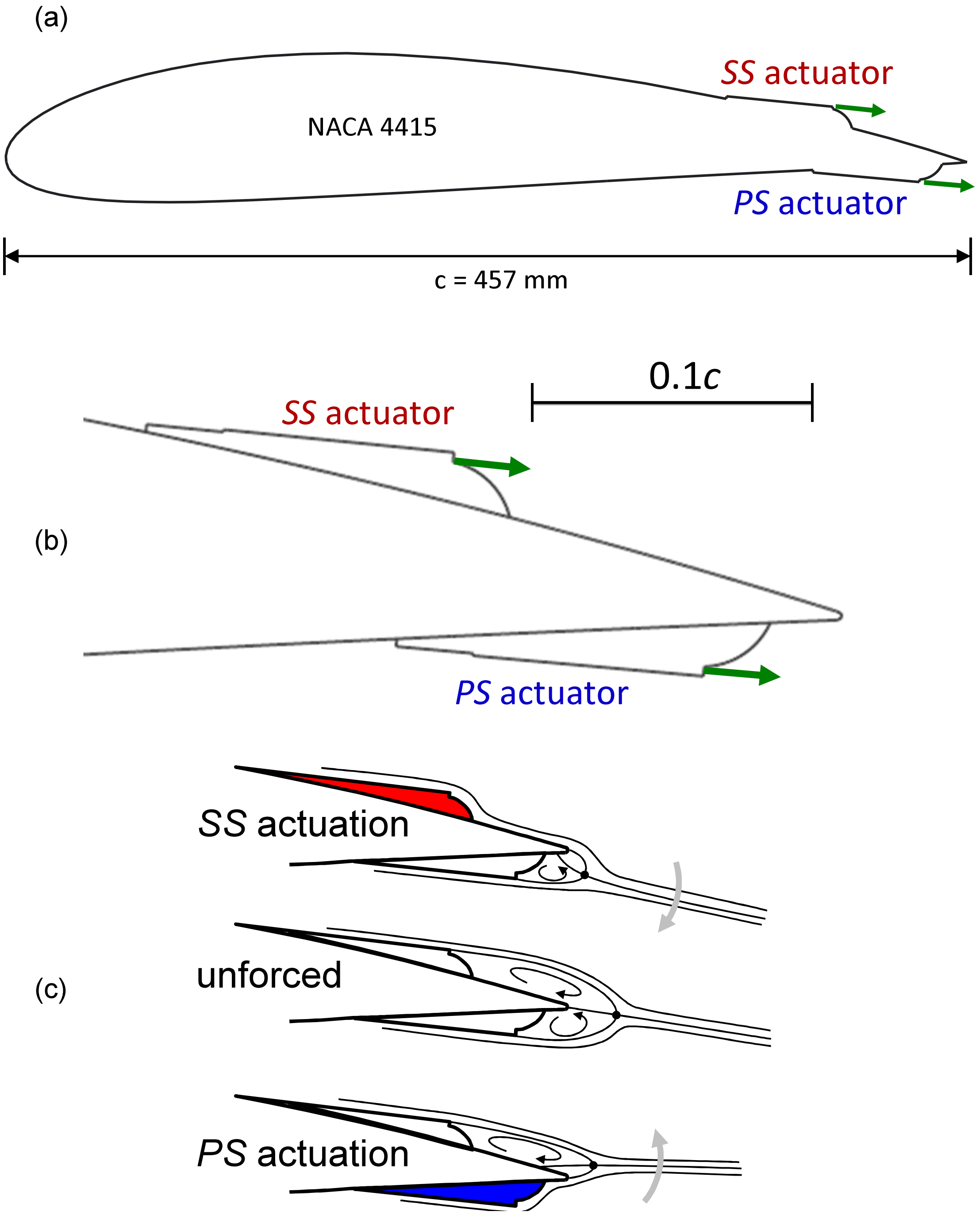

Figure 2.3: (a) Profile of the modified NACA4415 and (b) close-up of trailing edge region. (c) Schematic representation of bi-directional control of pitching moment.

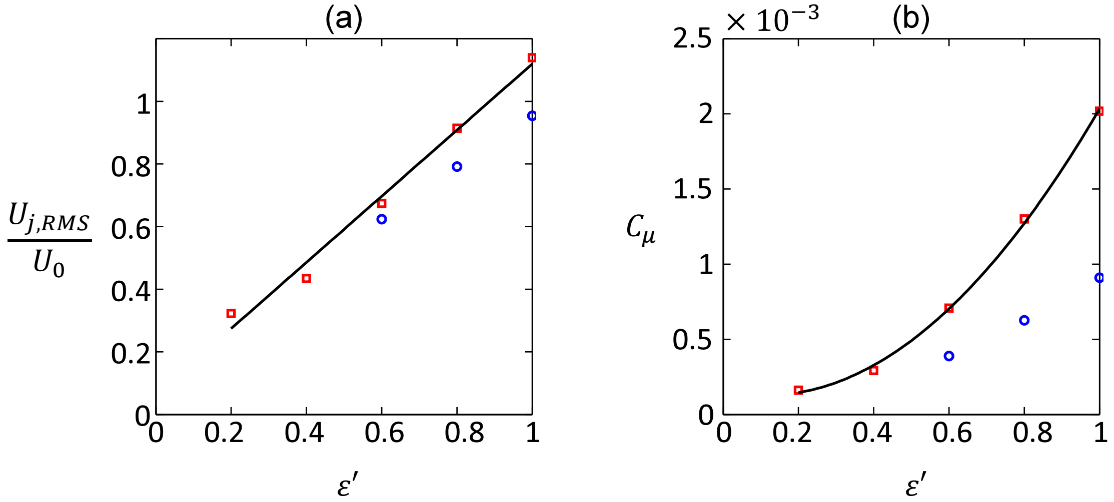

Figure 2.4: Synthetic jet calibration in quiescent flow: variation of (a) RMS jet velocity and (b) jet momentum coefficient at the center of the jet orifice for slow heights of 457 µm (blue symbols) and 711 µm (red symbols).

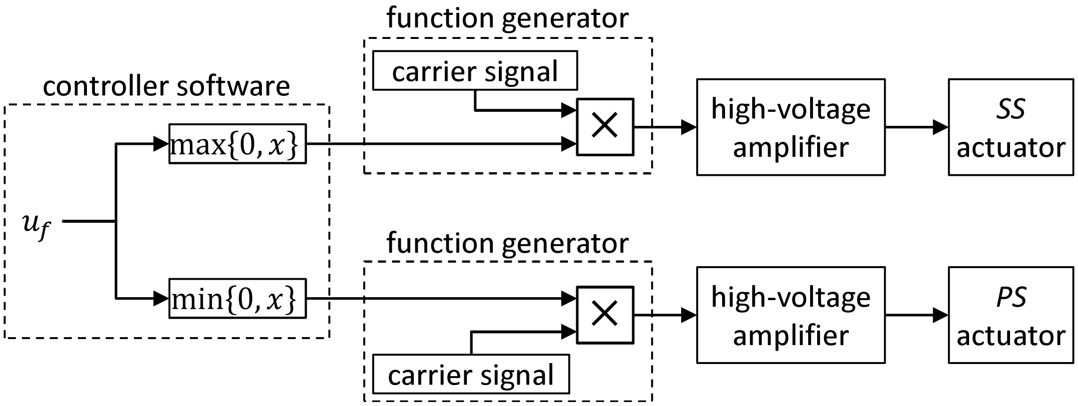

Figure 2.5: Schematic representation of signal generation for the flow control actuators.

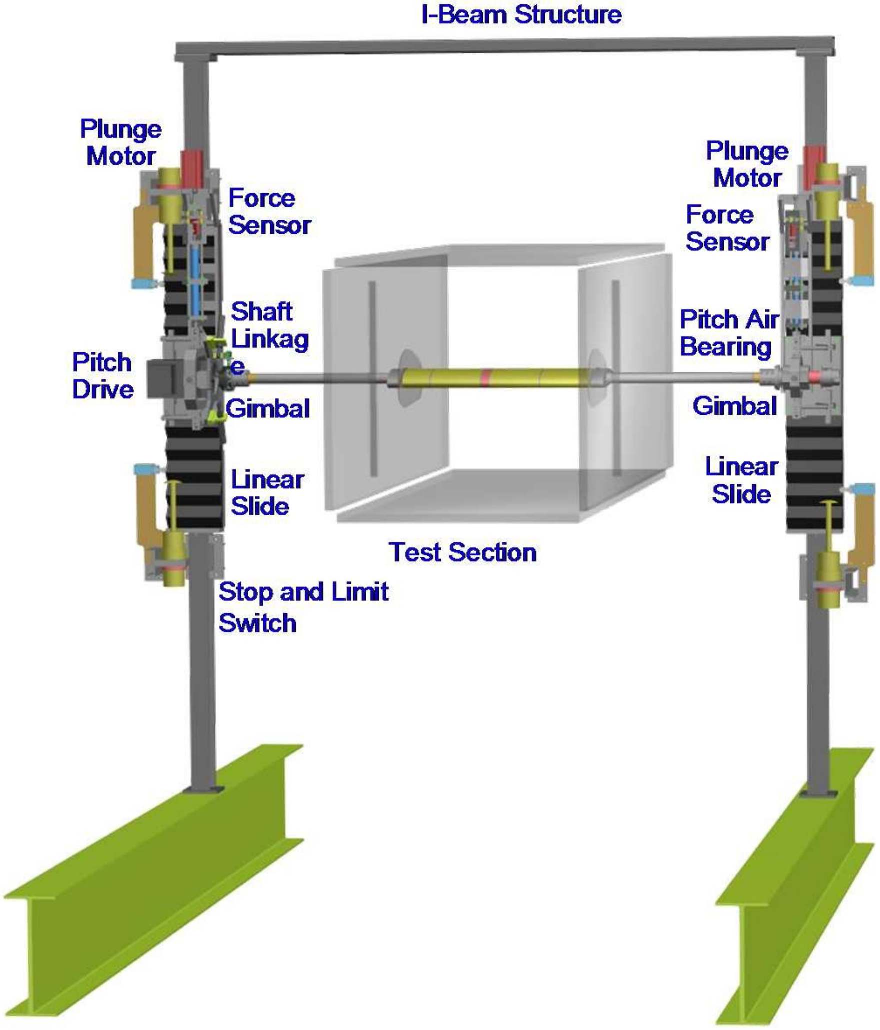

Figure 2.6 The pitch/plunge traverse

Figure 2.6: The pitch/plunge traverse

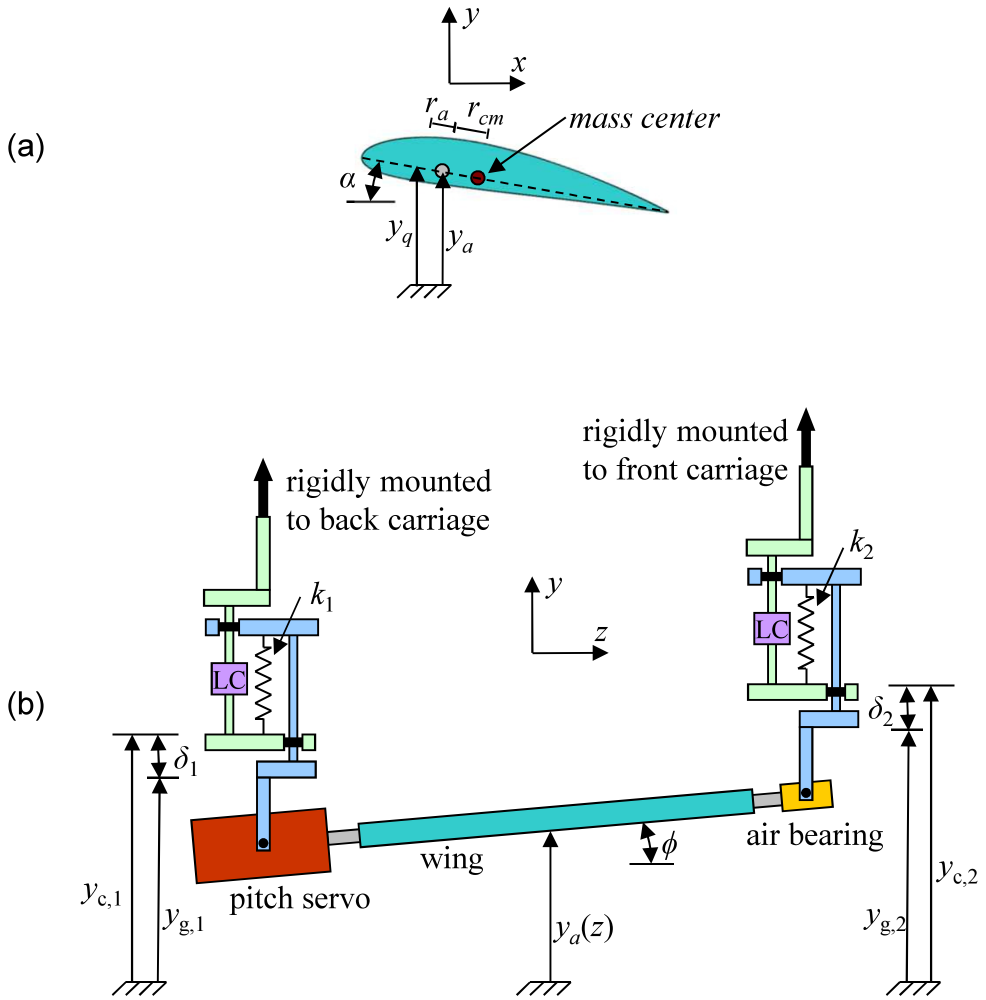

Figure 2.7 Schematic diagram of the (a) pitch and (b) plunge axis showing major components and degrees of freedom.

Figure 2.7: Schematic diagram of the (a) pitch and (b) plunge axes showing major components and degrees-of-freedom.

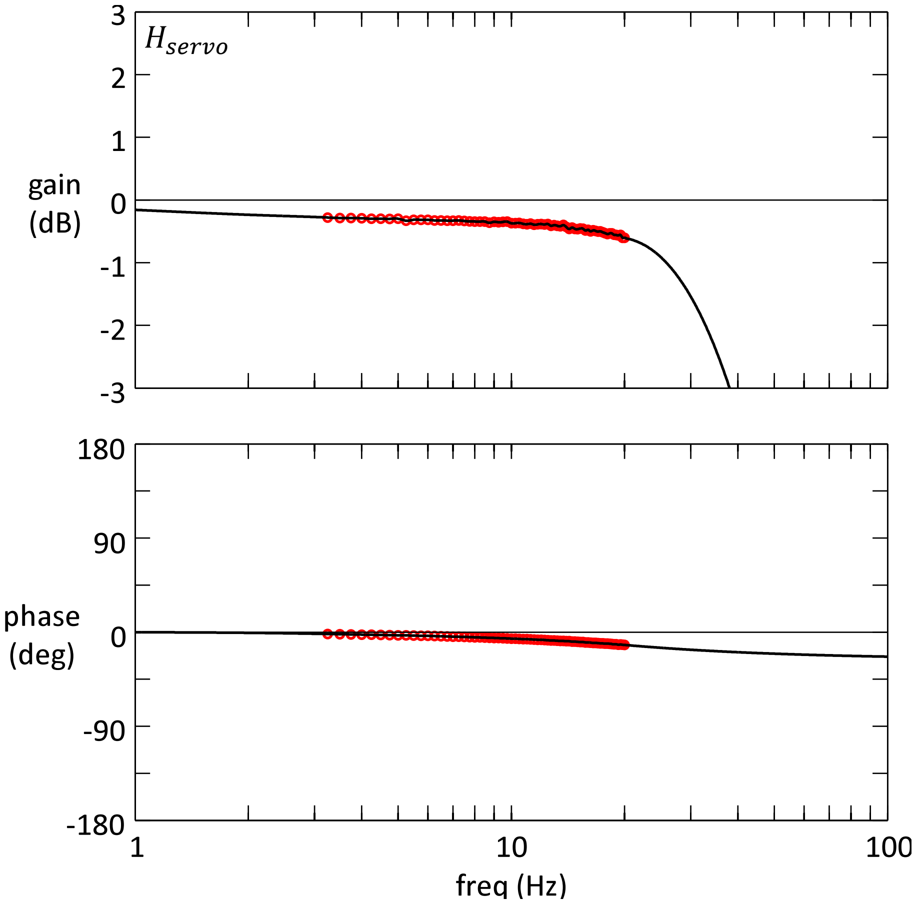

Figure 2.8: Dynamic response of the pitch servo: measured (○) and modeled (—).

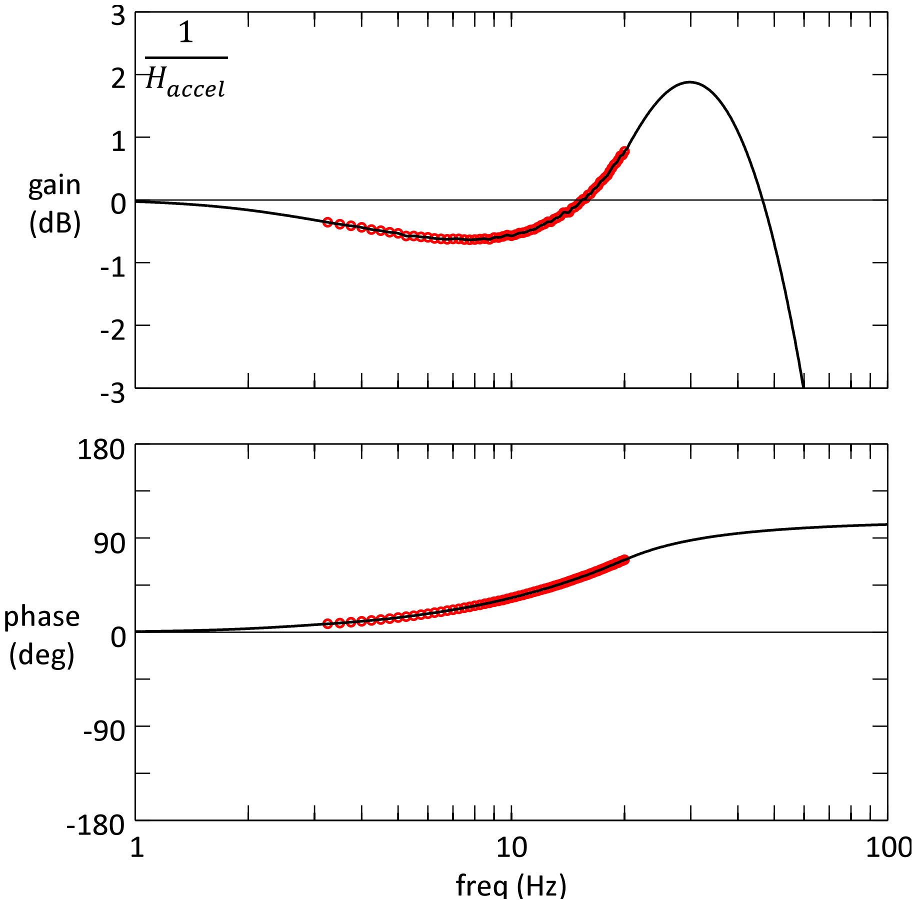

Figure 2.9: Dynamic response of the angular accelerometer: measured (○) and modeled (—).

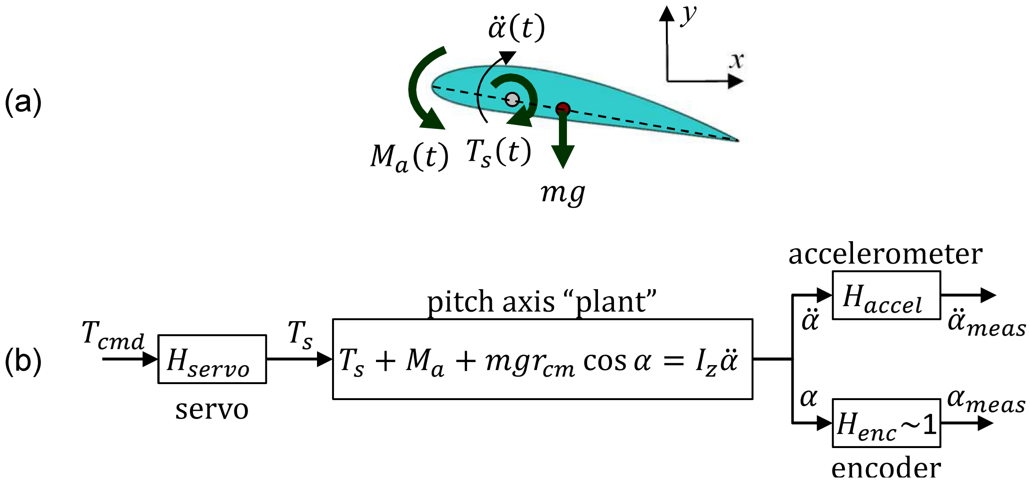

Figure 2.10: (a) Balance of torques in the pitch axis. (b) The pitch axis plant as seen by the control system.

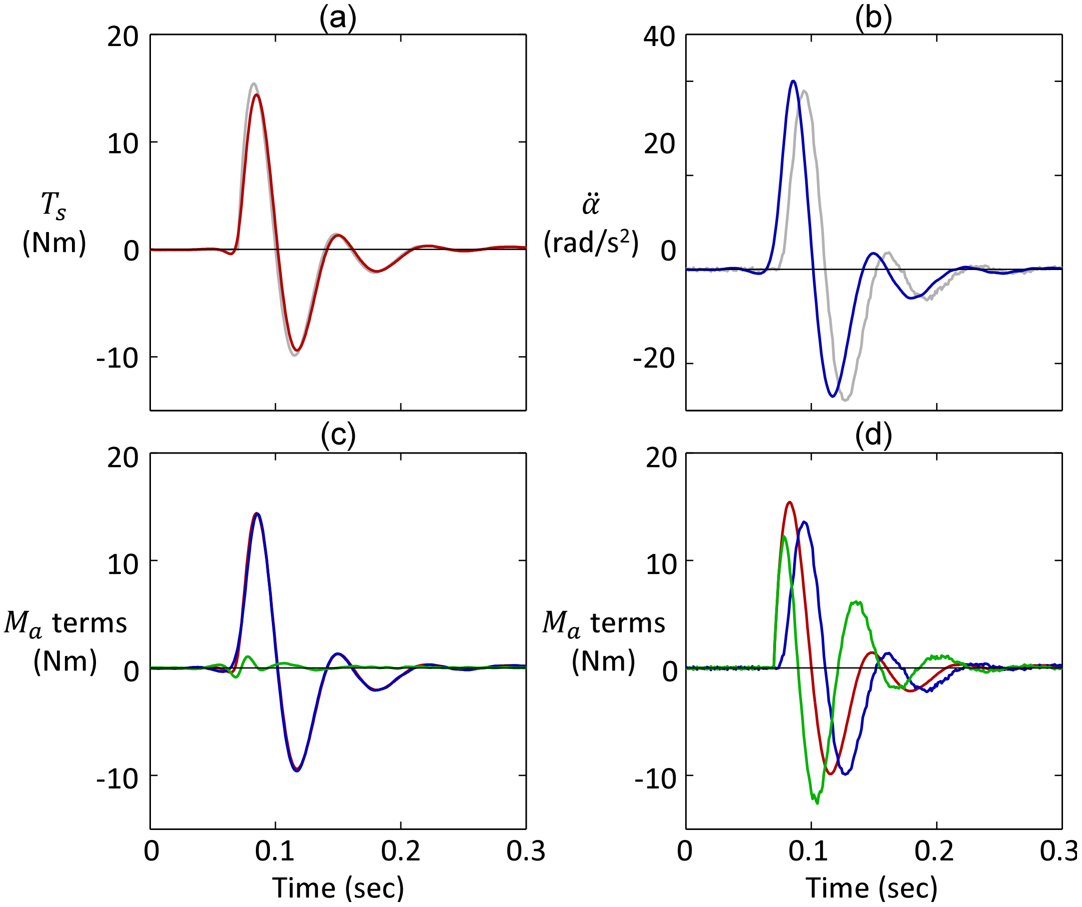

Figure 2.11: Time history of (a) pitch servo torque (b) angular acceleration following a step change in pitch when the tunnel is off. The raw servo and accelerometer measurements are show in (gray) and the colored traces reflect application of the inverse transfer functions. The time-history of torque balance between the applied torque and the resulting angular inertia (c) with and (d) without application of the transfer functions.

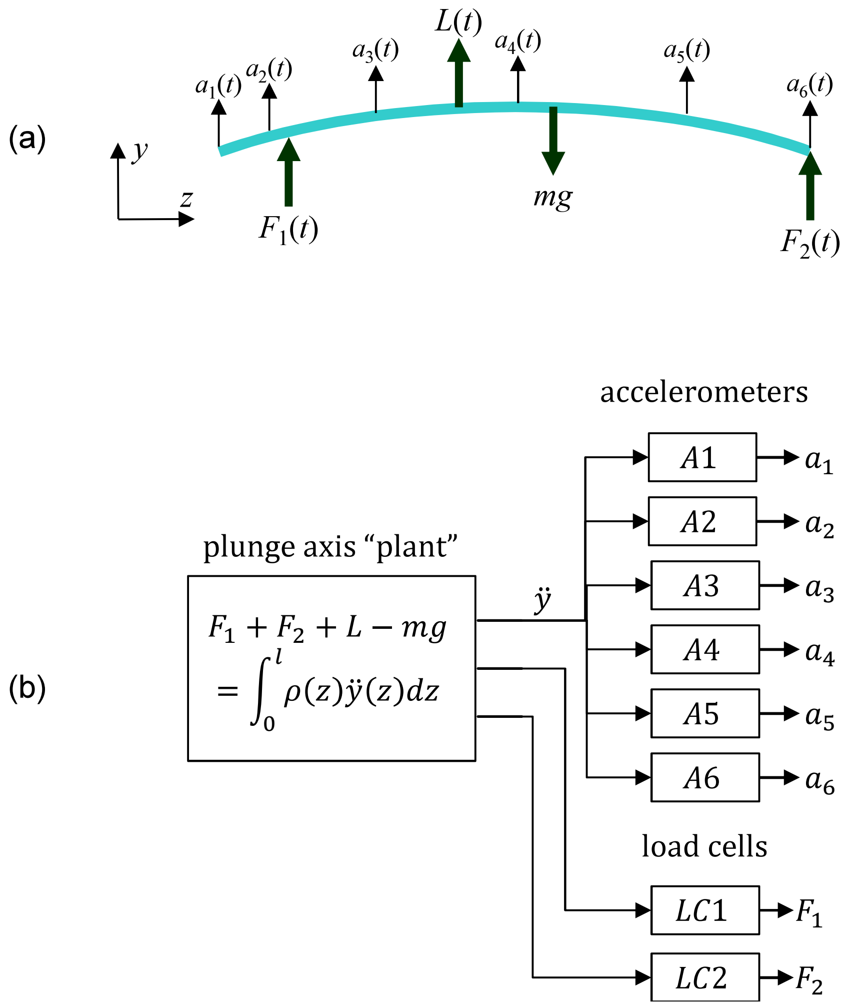

Figure 2.12: (a) Force balance in plunge. (b) Plunge axis plant as seen by the control system.

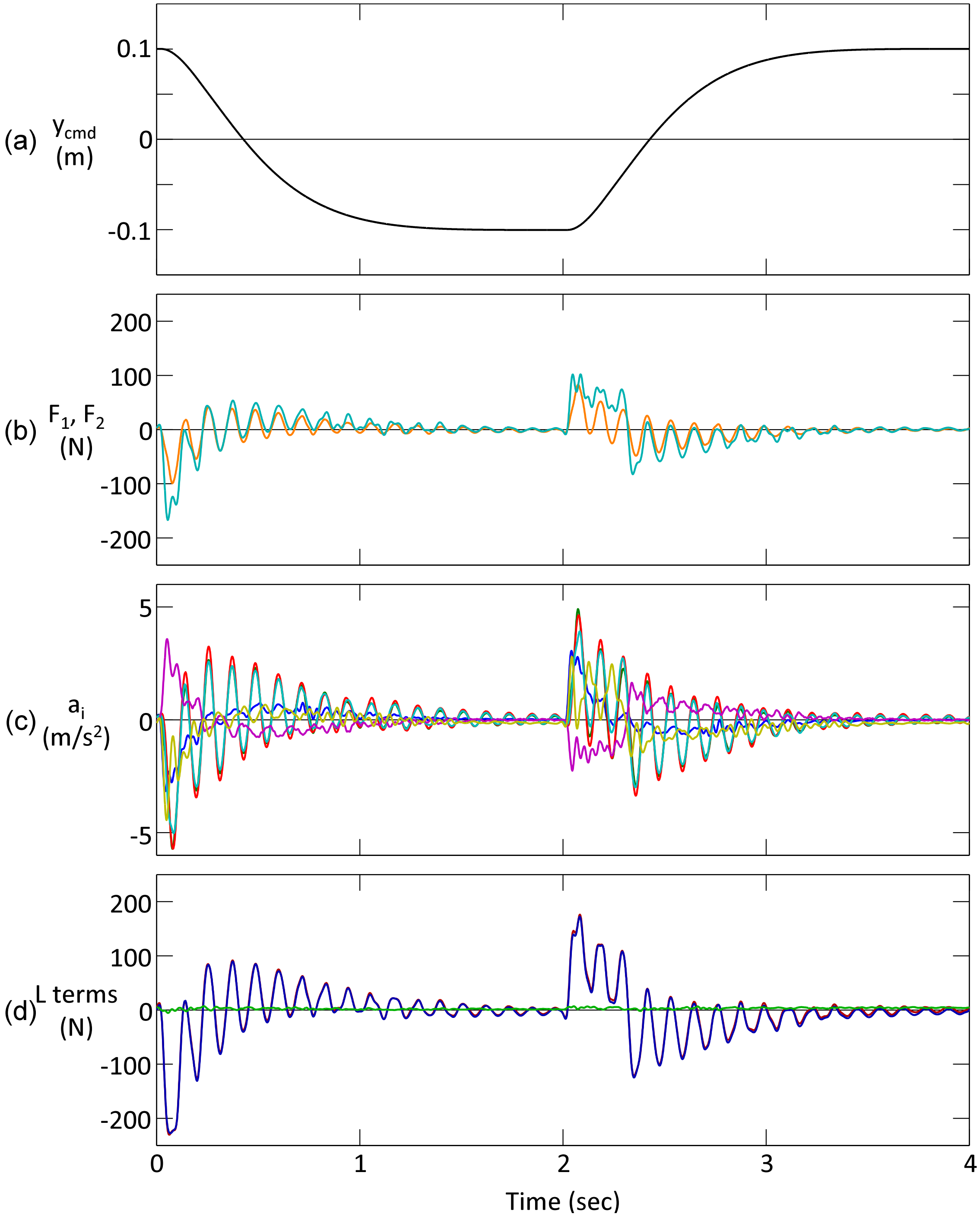

Figure 2.13: Time history of (a) plunge command, (b) load cell forces, and (c) linear acceleration measurements during a plunge maneuver when the tunnel is off. (d) The time-history of force balance between the load cell forces and weighted accelerometer measurements.

Chapter III

CLOSED-LOOP CONTROL SYSTEM

3.1 Control System Overview

This chapter describes various closed-loop systems that are used in maneuvering the model during the present dynamic wind tunnel experiments. The motion of the 2DOF traverse is controlled by a dedicated feedback control system that removes the effect of parasitic mass and rotational inertia of the dynamic support system. The controller can also prescribe stability characteristics to mimic the behavior of a range of "virtual" air vehicles, all having the same wing as the wind tunnel model but with static margins that can be adjusted by the controller, including unstable configurations for high maneuverability.

The feedback control system for operating the 2DOF traverse and flight maneuvers under active flow control was developed by Dr. Ali Kutay, Dr. Jonathan Muse and Mr. Rajeev Chandramohan under the supervision of Prof. Anthony Calise. The system is operated by a feedback controller built in the Simulink environment (Barnard, 2005) which executes in real time on a laboratory computer running the QNX operating system (Hildebrand, 1992). The flow of information between the controller and the various subsystems is shown schematically in Figure 3.1 including the various sensor outputs and actuation commands. The controller communicates with three primary subsystems - the pitch axis, the plunge axis, and the airfoil model which is maneuvered using flow control actuation. In order to minimize electronic noise, all sensor information is amplified and digitized as close to the sensors as possible before it is transmitted to the controller via Ethernet communication.

The control system has three distinct modes of operation. In *servo control* mode, the motion of the model is completely regulated by the pitch and plunge servos without flow control actuation. This mode is used for open-loop actuation experiments as well as system characterization. In the *1DOF pitch tracking* and *2DOF plunge tracking* modes, the motion of the model is completely regulated with the flow control actuators. In 1DOF pitch, the airfoil's vertical position is invariant and actuation is used to track a pitch command. In 2DOF plunge, a vertical force control system is used to allow the model to maneuver in pitch and plunge in the wind tunnel and the actuators are used to by regulate the pitch angle thereby varying the lift. Each of these modes of operation will be described in detail.

3.2 Servo Control Mode

In *servo control mode*, the trajectory of the model in pitch, plunge and roll is effected with the servo actuators and the commands to the flow control actuators are issued in open-loop with minimal effects on the airfoil's position. The block diagram for this mode of operation is shown in Figure 3.2. In servo control mode, the pitch and plunge controllers act independently from each other. While the three degrees-of-freedom are indeed coupled through the aerodynamic and inertial forces, in general the gain on both the pitch and plunge servos is high enough that this coupling is negligible. Also in this configuration, the pitch axis assembly is connected to the carriages with rigid links with embedded load cells unlike the implementation of the force controller which uses a system of springs (as discussed in §3.4).

Consider first the pitch axis which is controlled by a PID controller (Figure 3.2a). The current pitch state $(\alpha \;\; \dot{\alpha})$ is computed from the outputs of the angular encoder and angular accelerometer using a Kalman filter (Kutay *et al.*, 2006). This state estimate is subtracted from the pitch command $(\alpha \;\; \dot{\alpha})_{\mathrm{cmd}}$ to give the state error that is minimized by the PID controller. The controller issues a servo command $u_{\mathrm{m,p}}$ to the pitch servo actuator which in turn generates a torque $T_{\mathrm{s,p}}$ to effect the necessary motion of the airfoil in pitch.

Control of wing in plunge and roll in servo control mode (Figure 3.2b) is only slightly more complicated due to the independent motion of the two vertical actuators at the spanwise edges of the model (which allows for rolling motion). The plunge/roll command takes the form $\left(y \;\; \dot{y} \;\; \phi \;\; \dot{\phi}\right)_{\mathrm{cmd}}$ where y is the plunge position measured midway between the two vertical actuators and ϕ is the model's roll angle measured relative to the horizontal $x - z$ plane. First the plunge/roll command is converted to plunge commands for the two vertical actuators according to:

$$\begin{aligned}
y_1 &= y + \frac{d}{2}\sin\phi \\
\dot{y}_1 &= \dot{y} + \frac{d}{2}\dot{\phi}\cos\phi \\
y_2 &= y - \frac{d}{2}\sin\phi \\
\dot{y}_2 &= \dot{y} - \frac{d}{2}\dot{\phi}\cos\phi
\end{aligned}$$

where $d = 2.324$ m is the spanwise distance between the vertical actuators. The individual carriage commands $(y_1 \;\; \dot{y}_1)_{\text{cmd}}$ and $(y_2 \;\; \dot{y}_2)_{\text{cmd}}$ are then fed into the corresponding carriage controllers. Each carriage controller consists of a simple high gain PID controller. Each carriage state $(y_i \;\; \dot{y}_i)$ is estimated from the encoder reading and its derivative. The controller issues a servo command $u_{\text{m},i}$ based on the carriage state error and the plunge servo actuators in turn rotate the ball screws which drive the carriages. For pitch-only experiments, the plunge axis cab be locked by engaging the carriage brakes to prevent accidental plunge motion and reduce strain on the plunge servo actuators.

As noted above, flow control commands issued in servo control mode are issued exclusively in open-loop (Figure 3.2c). Measurements using continuous and transient flow control actuation (Chapters 4 and 5, respectively), are conducted with the controller in this mode. While the airfoil may move slightly as a result of the flow control actuation, its desired position is controlled (in closed-loop) by the servo actuators.

3.3 1DOF Pitch Tracking Mode

In *1DOF pitch tracking mode* the wind tunnel model is held rigidly fixed in plunge and roll and the pitch angle is regulated exclusively with the flow control actuators. The block diagram for this mode of operation is shown in Figure 3.3. As in the servo control case, the pitch command takes the form $(\alpha \;\; \dot{\alpha})_{\text{cmd}}$ and the pitch state $(\alpha \;\; \dot{\alpha})$ is estimated by the Kalman filter using the resolver and angular accelerometer outputs. However, unlike the servo control case, the pitch state error is fed to a a PID controller which regulates the flow control actuators (as opposed to the pitch servo). This pitch controller is designed based on steady-state flow control actuator measurements in which increasing levels of *SS* actuation yielded increasing levels of nose-down pitching moment, whereas increasing levels of PS actuation yielded increasing levels of nose-up pitching moment (Kutay *et al.*, 2006). To simplify the control law formulation, the dimensionless parameter u_{f} is used as an analog to the pitch servo command $u_{\mathrm{m,p}}$.

While the pitch command is only fed to the flow control actuators that operate in what is referred to hereafter as the *outer loop*, the pitch servo actuator operates in an *inner loop* for the purpose of providing a static trim torque as well as optionally feeding back on the pitch state and the model's angular acceleration thereby altering its dynamic characteristics. In general, in 1DOF pitch tracking mode, the servo torque takes the form:

$$T_{\mathrm{s}} = T_{\mathrm{s},0} + k_{\mathrm{p}}\alpha + k_{\mathrm{d}}\dot{\alpha} + k_{\mathrm{a}}\ddot{\alpha} \tag{3.1}$$

The constant $T_{\mathrm{s},0}$ is the trim torque at which the servo actuator is frozen when the flow control tracking mode is first engaged. It should be noted that servo tracking mode is always necessary in order to start the experiment and as the wind tunnel is brought up to speed since the flow control actuators require a cross flow in order to operate. Therefore, flow control tracking always begins with servo tracking. The parameter k_{p} may be set to alter the static margin of the wing $\frac{\partial C_M}{\partial \alpha}$ and the the parameter k_{d} may be used to simulate aerodynamic damping. In the present work, both k_{p} and k_{d} were set to zero. However, a nonzero acceleration feedback gain k_{a} is used to implement acceleration feedback and thereby change the apparent rotational inertial of the airframe within the bandwidth of the controller. In particular, setting this parameter to some value in the range $0 < k_{\mathrm{a}} < I_z$, effectively reduces the apparent rotational inertia to $I_z' = I_z - k_{\mathrm{a}}$ to enable rapid maneuvering of the present heavily-instrumented wind tunnel model.

3.4 2DOF Plunge Tracking Mode

The third mode of operation of the control system is *2DOF plunge tracking mode*. In plunge tracking mode, the plunge servo actuators are regulated by a *force controller* which effectively allows the model to "float" or "fly" in the wind tunnel. The force controller does this by applying a prescribed vertical force to the model (which in the simplest case is just a constant force to balance the weight of the model). The trajectory of the model is then regulated by a *longitudinal flight controller* which operates independently of the force controller. The force and longitudinal controllers are independent from a control perspective, and are discussed briefly in the following sections (see also Muse, 2010, Chapter 8).

3.4.1 Force Controller

Applying a constant torque to the pitch axis is almost trivial due to the extremely low rotational friction in the pitch axis. In contrast, the ball screw mechanisms driving the carriages on either side of the tunnel inherently have static and sliding friction. For this reason is impossible to treat the servo/ball screw assembly as a linear motor. In order to directly control the force applied to either side of the wing model special hardware and control system considerations were necessary. When operating the plunge axis in force control mode, the rigid links connecting the gimbals at either end of the pitch axis assembly are replaced with the spring sets (cf. §2.4). The spring sets act as a compliant element between the ball screw drive and the wing model. Each spring set contains an integrated load cell which allows the time-dependent force applied to the model to be monitored. This force measurement also acts as the input to the force controller which aims to maintain the total vertical force applied to the model to a prescribed (possibly time-varying) input force.

The design of the force controller is depicted in the block diagram of Figure 3.4. The current force state is estimated from the sum of the load cell forces F_1 and F_2 and their time derivatives. This force state is subtracted from the force command $\begin{pmatrix} F & \dot{F} \end{pmatrix}_{\text{cmd}}$ to yield the force error. The force controller computes a carriage state command with the objective of minimizing the force error (Muse *et al.* (2008*b*)). The carriage command computed by the force controller is fed into both carriage position controllers described in §3.2. The plunge servo actuators accelerate the carriages as necessary to regulate the force state on the model.

To simulate free flight, the force controller is commanded to maintain a constant force which balances the weight of the wind tunnel model. While it is possible to program arbitrary pitch/plunge dynamics by feeding back on α, y and their derivatives, this feature was not used in the present experiments. However, the ability to apply time-dependent force inputs was used to apply a momentary disturbance simulating a sudden wind gust. Experiments that demonstrate the ability to recover from such disturbances are presented in §7.3.4.

It is important to note that when the force controller alone is operational, the wind tunnel model can drift to either the upper or lower travel limit of the the traverse. This is particularly important in the presence of air flow where vortex shedding to the near wake can cause the model to diverge rapidly- as most aircraft would without any flight control. For this reason, the force controller is almost exclusively used in conjunction with the longitudinal flight controller (§3.4.2). As with the 1DOF pitch tracking, all 2DOF plunge tracking experiments are started in servo control mode as the wind tunnel is brought up to speed. Once the flow reaches steady state, the force controller and longitudinal flight controller are engaged simultaneously.

3.4.2 Longitudinal Flight Controller

The longitudinal fight controller uses the flow control actuators to regulate the pitch angle thereby effecting changes in lift which allow for active plunge tracking (Figure 3.5). As in the servo control mode, the pitch state is estimated from the pitch encoder and angular accelerometer by a Kalman filter and the plunge state of each carriage is computed from the plunge encoders. The carriage states are converted to plunge (estimated at midspan) and roll:

$$\begin{aligned} y &= \frac{1}{2}\left(y_1 + y_2\right) \\ \dot{y} &= \frac{1}{2}\left(\dot{y}_1 + \dot{y}_2\right) \\ \phi &= \arctan\frac{y_1 - y_2}{d} \\ \dot{\phi} &= \frac{\left(\dot{y}_1 - \dot{y}_2\right) d}{\left(y_2 - y_1\right)^2 + d^2} \end{aligned}$$

The roll state is actively driven to zero by the force controller and is not fed back to the longitudinal flight controller (which assumes zero roll). The pitch state, plunge state and plunge command are fed into a flight controller which computes an actuation input u_{f} to achieve the desired plunge trajectory. This flight controller is based on a low order vortex model (Tchieu *et al.*, 2008 and Muse *et al.*, 2009). The flow control input effects changes in the pitching moment of the model to regulate the pitch angle. Changes in pitch angle cause changes in lift which are used to drive the model in plunge to track the desired plunge trajectory.

As for 1DOF pitch tracking mode, the pitch state and angular acceleration can be fed back to the pitch servo to trim the model and prescribe arbitrary system dynamics. The modification of system dynamics through the pitch servo acts as a *torque controller* in pitch analogous to the *force controller* in plunge.

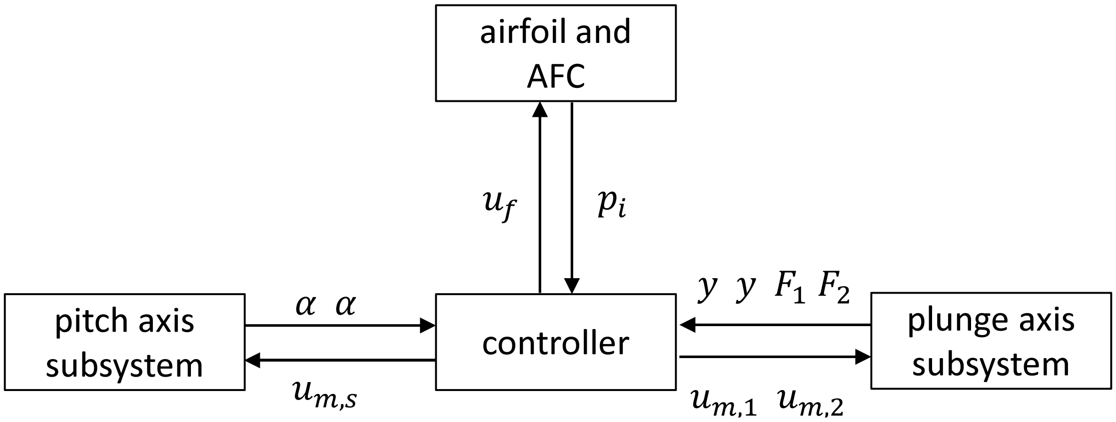

Figure 3.1: Information flow in the 2DOF experiment

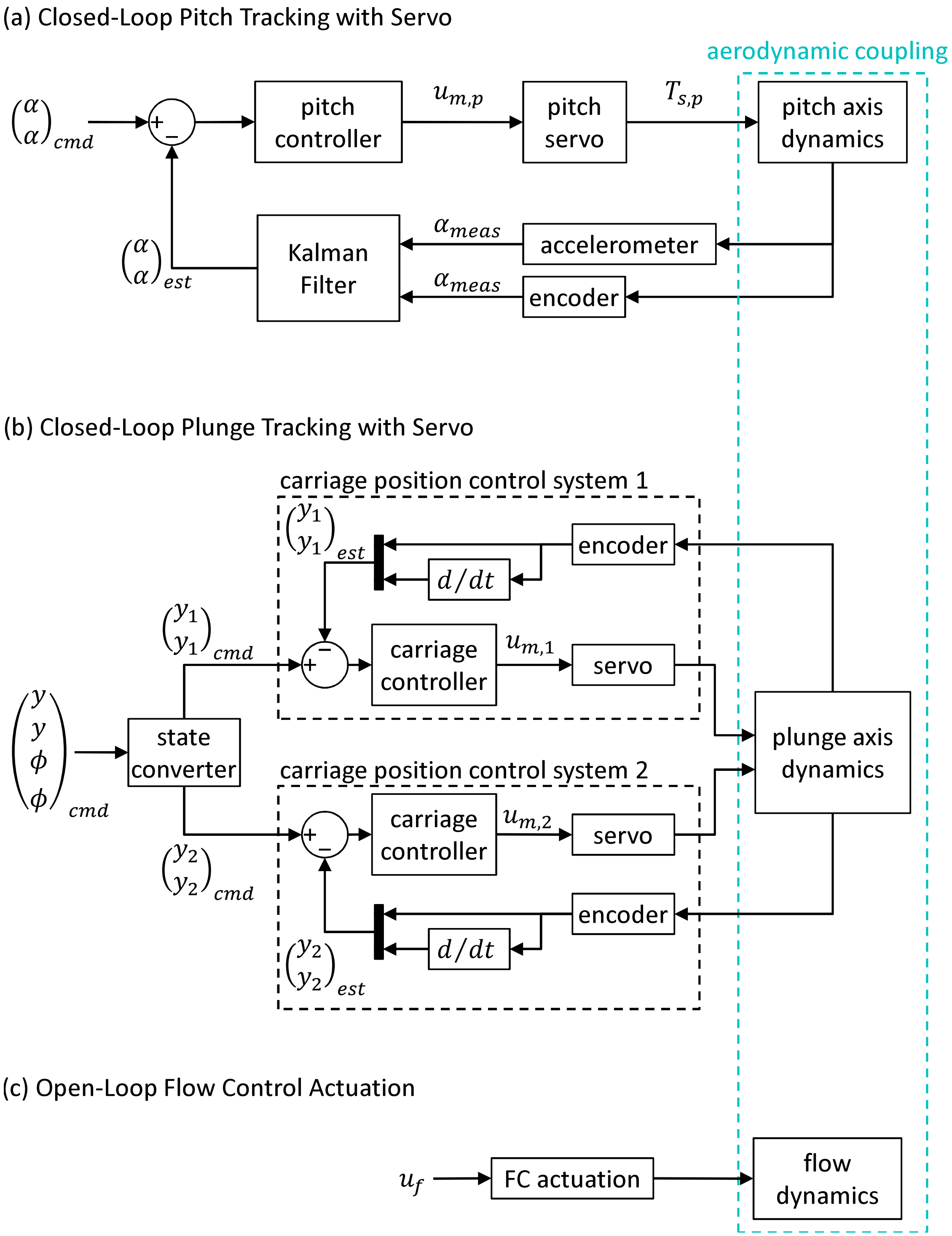
(a) Closed-Loop Pitch Tracking with Servo

(b) Closed-Loop Plunge Tracking with Servo

(c) Open-Loop Flow Control Actuation

Figure 3.2: Servo control mode

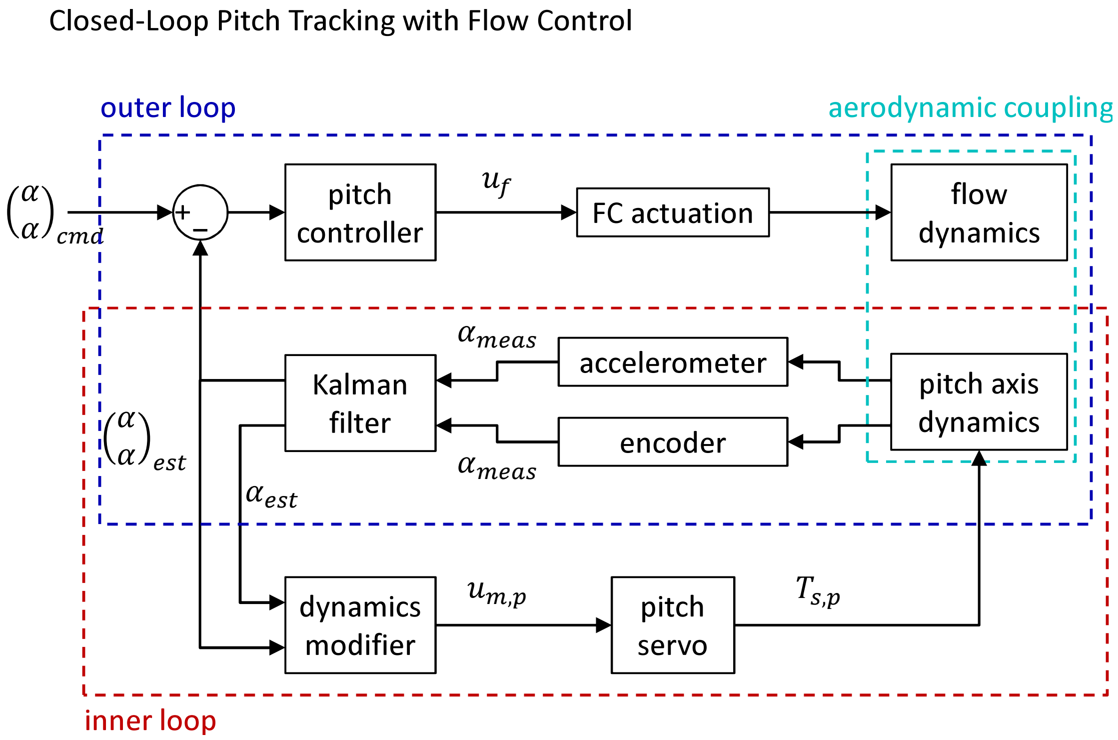

Figure 3.3: 1DOF pitch tracking mode

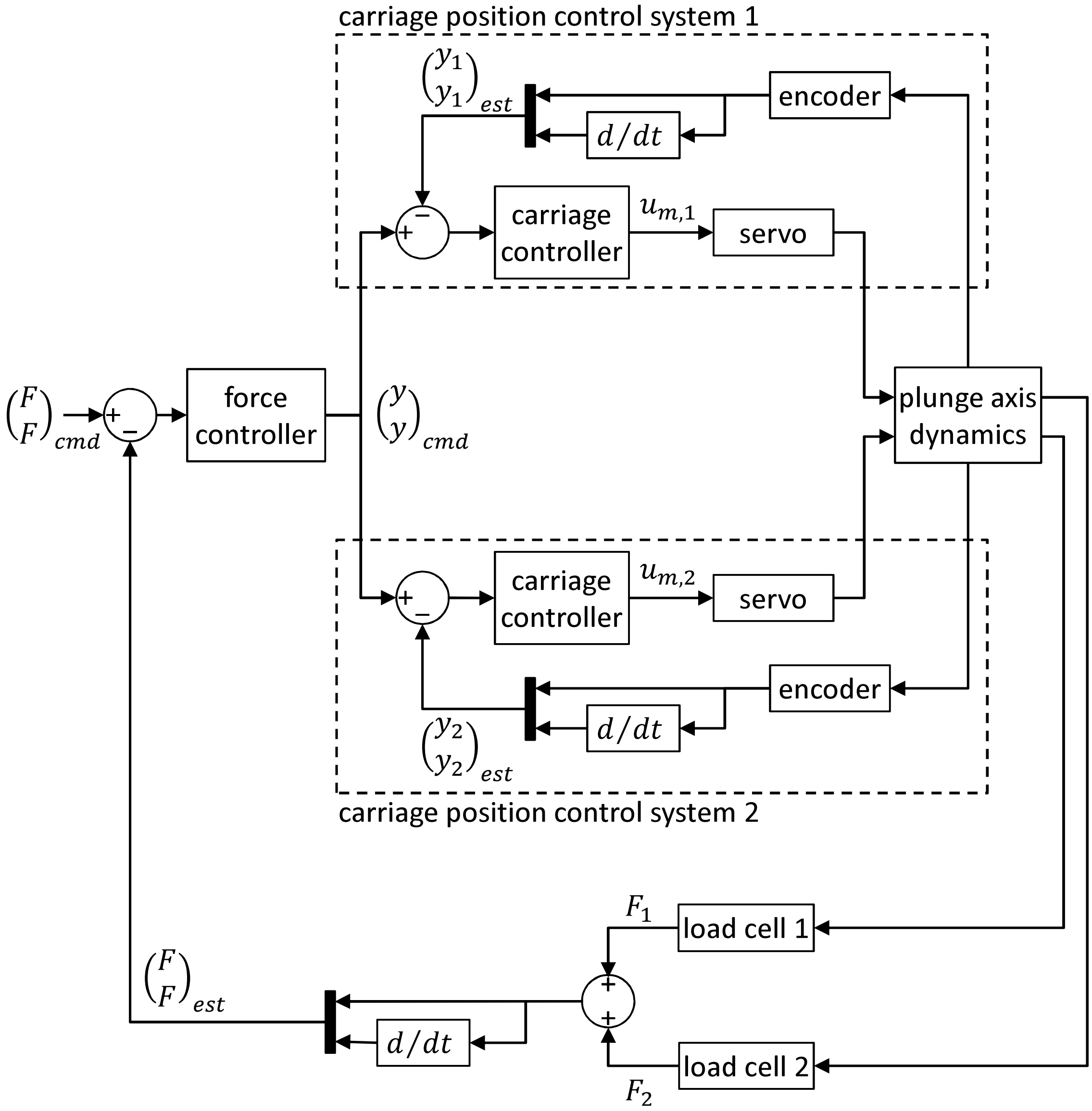

Figure 3.4: The vertical axis force controller

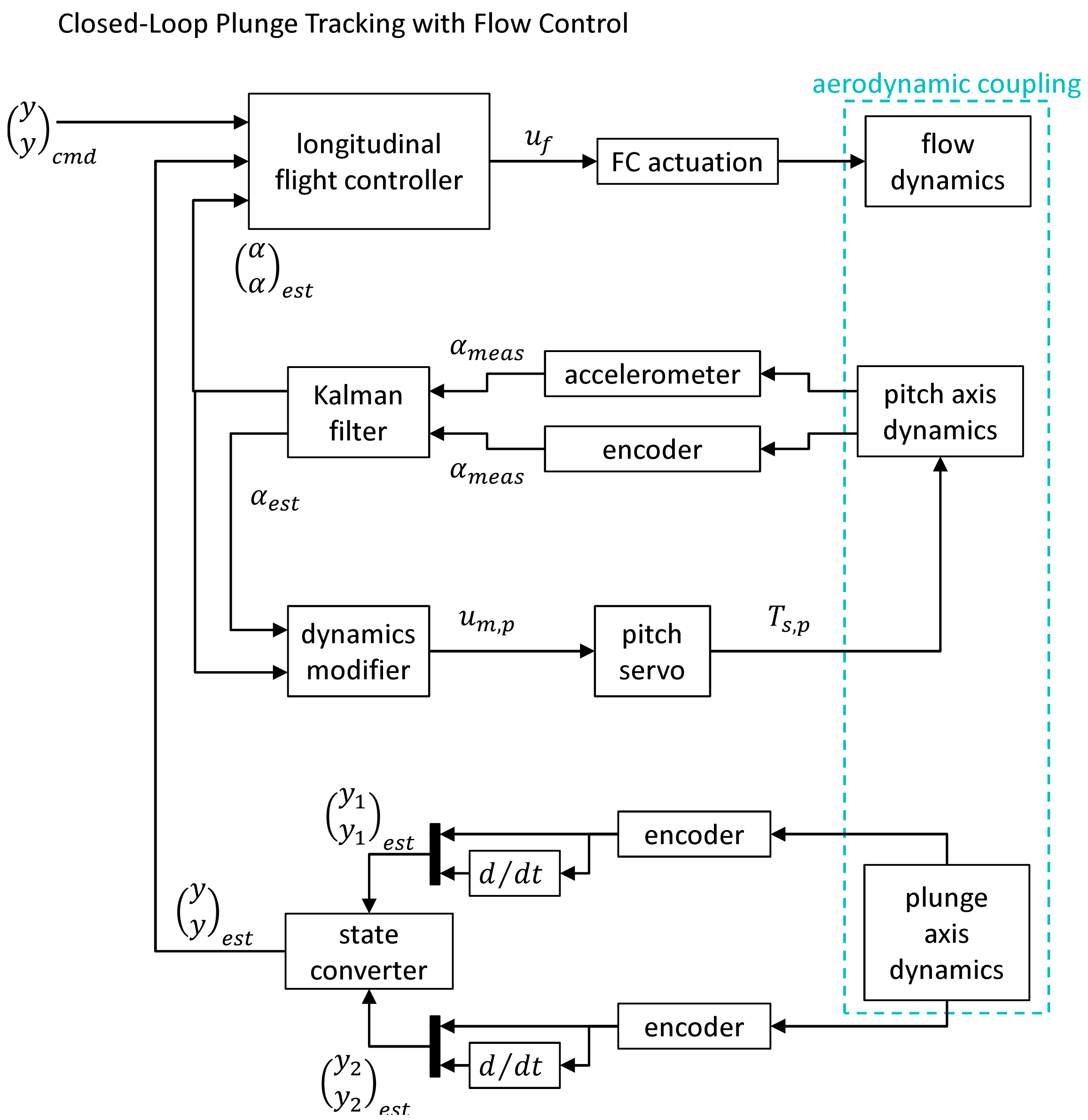

Figure 3.5: 2DOF plunge tracking mode

Chapter IV

CONTINUOUS ACTUATION

This chapter discusses *quasi-steady* flow control actuation. While the actuator jet velocity is nominally time-harmonic with a characteristic period of 0.5 ms, this time scale is more than an order of magnitude shorter than the convective time scale of the flow $T_{\mathrm{conv}} \approx 15$ ms. Therefore from the standpoint of the control system, the effects of the actuation may be regarded as nominally steady.

The first three sections of this chapter consider only the effect of the actuation on the time-averaged flow field $\overline{\mathbf{u}}(\mathbf{x})$ and surface pressure $\overline{p}_{\mathrm{s}}(\mathbf{x})$. In particular, §4.1 gives an overview of the actuation effect on the time-averaged surface pressure distributions and aerodynamic forces. The effects of actuator location and different actuation configurations are discussed in §4.2. The modifications of the time-averaged flow field induced by the actuation are presented in §4.3. Finally, the flow field in the vicinity of the actuators measured phase-locked to the actuation cycle is discussed in §4.4.

4.1 Time-Averaged Effects

4.1.1 Static Pressure

Distributions of surface pressure around the circumference of the airfoil at midspan are measured when the *SS* and *PS* actuation jets are located at $x/c = 0.86$ and 0.95, respectively. These measurements were obtained over a broad range of angles of attack $-5° < \alpha < 15°$ when the actuators are inactive and when each of the *SS* and *PS* actuators is operating at full power ($u_{\mathrm{f}} = 1$ and -1, respectively). For comparison, pressure distributions over the smooth (baseline) airfoil were also measured. Figures 4.1a-d show the pressure distributions for $\alpha = -3°$, $3°$, $9°$, and $15°$.

Consider first $\alpha = 3°$ (Figure 4.1b). On the baseline airfoil, the flow over the suction surface accelerates to a suction peak of $C_{\mathrm{p}} = -1.17$ at $x = 0.17c$, followed by pressure recovery to $C_{\mathrm{p}} = 0.08$ at the trailing edge. On the pressure side, the flow accelerates over

$0 < x/c < 0.05$ where the surface pressure exhibits a slight suction relative to the ambient and remains relatively flat (with a very gradual pressure rise) over $0.05 < x/c < 1$.

The presence of the actuators results in a substantial modification of the baseline pressure distribution. On the top surface of the airfoil upstream of the SS actuator, the suction level decreases up to the leading edge and the suction peak decreases by 5% to $C_{\mathrm{p}} = -1.11$. Upstream of the actuator ($0.5 < x/c < 0.7$), the pressure rises faster than on the smooth airfoil due to blockage followed by reversal in the pressure gradient along the actuator ramp $0.7 < x/c < 0.85$ (i.e., upstream of the synthetic jet exit) from $C_{\mathrm{p}} = -0.27$ to $C_{\mathrm{p}} = -0.35$. At $x = 0.85c$, the flow separates from the actuator which results in a nearly invariant pressure domain between the actuator exit and the trailing edge. Perhaps the most notable feature of the modified airfoil is the substantial decrease in trailing edge pressure ($C_{\mathrm{p}} = -0.34$) relative to the smooth airfoil. This increase in suction pressure is due to a recirculation domain between the jet exit and the trailing edge ($0.85 < x/c < 1$) which is discussed further in connection with the corresponding time-averaged PIV measurements (§4.3).

On the pressure side within the domain $0 < x/c < 0.5$, the pressure distribution is similar to the smooth airfoil with a slightly stronger adverse gradient which increases as the flow approaches the upstream edge of the actuator ($0.5 < x/c < 0.79$) to a peak value of $C_{\mathrm{p}} = 0.18$. The pressure gradient reverses sign as the flow accelerates along the actuator's ramp ($0.79 < x/c < 0.95$) to a suction of $C_{\mathrm{p}} = -0.25$ just upstream of the jet exit followed by a rapid decrease across the jet exit to $C_{\mathrm{p}} = -0.33$ and remains invariant to the trailing edge.

The presence of the inactive actuators has similar effects on the pressure distributions at $\alpha = -3°$, $9°$, and $15°$ (Figures 4.1a, c, and d, respectively) with a few notable exceptions. At $\alpha = -3°$ (Figure 4.1a), the pressure rise upstream of the SS actuator ramp is more noticeable due to the lower overall suction levels at this low angle and the larger (relative) ramp angle with respect to the free stream. At $\alpha = 15°$ (Figure 4.1d), the presence of the actuator appears to slightly enhance the lift on the airfoil and results in an increase in the suction peak ($x/c = 0.004$) from $C_{\mathrm{p}} = -4.26$ to $C_{\mathrm{p}} = -4.59$. At this angle the trailing edge pressures of the smooth and modified airfoils exhibit a slight suction ($C_{\mathrm{p}} = -0.27$ and

-0.25 respectively) that is associated with recirculating flow near the trailing edge. These observations are qualitatively consistent with the findings of DeSalvo & Glezer (2006, 2007) on a swept airfoil configuration.

Operation of the SS actuator has several prominent effects on the pressure distribution. For $-3^\circ < \alpha < 9^\circ$, the local region of low pressure induced by the synthetic jet at $x/c = 0.86$ leads to stronger flow acceleration along the ramp of the SS actuator ($0.69 < x/c < 0.86$) compared to the unactuated flow. Downstream of the actuator, the flow remains attached to the Coanda surface and the pressure recovers to $C_p = -0.12$, -0.12, and -0.14, respectively for $\alpha = -3^\circ$, 3°, and 9°, a level between the unactuated and baseline airfoils. This modification of the trailing edge flow field induces changes along the chord that extend up to the leading edge where suction pressure returns to or exceeds suction over the smooth airfoil. On the pressure side of the airfoil, the pressure level is slightly higher compared to the unactuated and baseline airfoils. Clearly these effects are associated with an increase in lift compared to the unactuated configuration (cf. §4.1.2). It is noteworthy that at $\alpha = 15^\circ$ (Figure 4.1d), operation of the SS actuators has minimal effects on the pressure distribution. At this high angle of attack, the flow in the vicinity of the actuator is close to separation and the local boundary layer is quite thick which impedes the effectiveness of the SS actuator.

The effects of the PS actuator are similar to the SS actuator in that the synthetic jet leads to acceleration of the local flow upstream of the jet and to its attachment downstream of the actuator. The acceleration along the actuator ramp ($0.79 < x/c < 0.95$) due to PS actuation is evident at all four angles (Figure. 4.2) and is followed by strong suction peaks just upstream of the jet exit corresponding to pressure changes (relative to the unactuated case) of $\Delta C_\mathrm{p} = -0.49$, -0.61, -0.70, and -0.75 for $\alpha = -3^\circ$, 3°, 9°, and 15°, respectively. While the trailing edge suction pressure increases with respect to the unactuated flow, for the three lower angles, the increase is less than for the SS actuation (e.g., 30% less at $\alpha = 3^\circ$).

The data in Figure 4.1 demonstrate that operation of the PS actuator effects global changes in the pressure distribution and results in a moderate to substantial decrease in the suction level along the entire upper surface of the airfoil. On the lower surface of the airfoil, the pressure upstream of the PS actuator exhibits a slight increase in suction relative to the unactuated case as a result of the acceleration induced by the actuation. Clearly this combination of decreased suction on the suction surface and decreased pressure on the pressure surface results in a reduction in aerodynamic lift. However, as demonstrated in §4.1.2, the lift penalty is accompanied by a significant modification of the pitching moment which is leveraged for flight control.

4.1.2 Modification of Aerodynamic Forces

At each angle of attack and actuation condition the pressure distribution is integrated to obtain the lift, pitching moment and pressure drag. As noted in Section §2.4.2, the sensors integrated into the 2DOF traverse yield the global lift and pitching moment, which include various $3D$ effects that are not captured by the sectional pressure measurements. The forces derived from both measurements are compared in Section §4.1.3. The variations of the force coefficients C_L, C_M and C_Dp with α are plotted in Figures 4.2a, b, and c, respectively, for the baseline, unforced, and full SS/PS actuation. The aerodynamic efficiency based on pressure drag $C_\mathrm{L}/C_\mathrm{Dp}$ is plotted in Figure 4.2d. The variation of the change in these quantities (relative to the unforced flow) with actuation level u_f plotted in Figures 4.2e-h $\alpha = -5°$, $0°$, $3°$, and $15°$.

For the fully-attached flow ($-5° \leq \alpha < 10°$), the presence of the inactive actuators results in a slight decrease in lift with a maximum penalty of $\Delta C_\mathrm{L} = -0.04$ (5%) at $\alpha = 5°$ (Figure 4.2a). This decrease in lift is accompanied by an increase in pressure drag which ranges from $\Delta C_\mathrm{Dp} = 0.018$ (230%) at α=$-5°$ to $\Delta C_\mathrm{Dp} = 0.015$ (27%) at $\alpha = 10°$ (Figure 4.2b). At $\alpha = 5°$ (the operating point with the maximum decrease in lift), the drag increase $\Delta C_\mathrm{Dp} = 0.015$ is a 60% increase over the smooth airfoil drag. Furthermore, the maximum aerodynamic efficiency (L/D_p) is reduced from 51 to 29 occurring respectively at $\alpha = 0°$ and 5°(Figure 4.2d). The presence of the actuators has very little effect on the pitching moment over the attached flow range (Figure 4.2c). For $\alpha \geq 10°$, the flow of the smooth airfoil begins to separate from the suction surface starting at the trailing edge as evidenced by the gradual decrease in $\partial C_\mathrm{L}/\partial\alpha$ in this range (Figure 4.2a). As noted §4.1.1, the presence of the actuators appears to enhance the lift in this regime by re-accelerating the flow towards the trailing edge. Also, for $13^\circ \leq \alpha \leq 15^\circ$ the rate of pressure drag increase $\partial C_{\mathrm{Dp}}/\partial\alpha$ is smaller for the modified airfoil than for the smooth airfoil (Figure 4.2b). In fact, at $\alpha = 15^\circ$ the aerodynamic efficiency for the smooth and actuated airfoils is nearly identical ($\frac{L}{D} = 13$, Figure 4.2c). Finally, the pitching moment about $c/4$ for the modified airfoil remains nearly invariant for $\alpha \geq 10^\circ$, whereas the pitching moment of the smooth airfoil begins to decrease in magnitude (become less nose-down, Figure 4.2b). This further indicates that separation on the modified airfoil is delayed separation compared to the smooth airfoil.

Operation of the SS actuator at full power ($u_{\mathrm{f}} = 1$) results in an increment in lift relative to both the baseline and the modified airfoils over all angles of attack (Figure 4.2a). The magnitude of the increase is nearly invariant ($\Delta C_{\mathrm{L}} = 0.1$) over the attached regime, but begins to decrease for $\alpha \geq 10^\circ$. This lift increase is accompanied by an increase in the magnitude of the nose-down pitching moment which ranges from $\Delta C_{\mathrm{M}} = -0.030$ at $\alpha = -5^\circ$ to $\Delta C_{\mathrm{M}} = -0.007$ at $\alpha = 15^\circ$ (Figure 4.2c). For $\alpha \leq 5^\circ$, full operation of the SS actuators mitigates some of the drag introduced by the installation of the actuators as the actuation reattaches the flow downstream of the SS actuator (Figure 4.2b). However for $\alpha > 5^\circ$ the lift-induced drag nullifies this effect.

As discussed in Chapters 2 and 3, the actuation amplitude can be continuously varied using amplitude modulation with the actuation parameter u_{f}. Interestingly, for small values of SS actuation ($0 < u_{\mathrm{f}} < 0.2$), the actuation effect is *reversed* at all angles. Pressure distributions (not presented here) indicate that for such low levels of actuation, the changes in surface pressure are almost entirely confined to $x/c > 0.8$. Given that the changes in pressure do not propagate around the airfoil for $0 < u_{\mathrm{f}} < 0.2$, it is not surprising that the lift-enhancement effect is not observed at these low actuation levels. For larger SS actuation inputs $0.2 < u_{\mathrm{f}} < 1$, the changes in lift, pressure drag and pitching moment vary nearly monotonically with u_{f}. This continuous (monotonic) variation of ΔC_{M} with u_{f} forms the basis of the present flight control strategy.

Operation of the PS actuator at full power ($u_{\mathrm{f}} = -1$) results in lift decrement relative to both the baseline and the modified airfoil over all angles of attack (Figure 4.2a). The magnitude of the decrease varies from $\Delta C_{\mathrm{L}} = -0.18$ at $\alpha = -5°$ to $\Delta C_{\mathrm{L}} = -0.21$ at $\alpha = 3°$ and remains invariant over $3° \leq \alpha \leq 15°$. This decrease in lift is accompanied by a substantial change in pitching moment across all angles (Figure 4.2c), with the largest increment occurring at the higher angles ($\Delta C_{\mathrm{M}} = 0.067$ at $\alpha = 12°$). Note that even the smallest increment ($\Delta C_{\mathrm{M}} = 0.058$ occurring at $\alpha = -5°$) is larger than the changes effected by the SS actuator over the same range of angles surveyed.

For all angles and actuation levels surveyed, PS actuation results in a decrease in pressure drag relative to the unactuated airfoil (although it is noteworthy that at the lowest angle, $\alpha = -5°$, the drag is almost the same for the unactuated and full PS airfoils) (Figures 4.2b and f). This decrease may be attributed to two effects. First, operation of the PS actuator attaches the flow downstream of the actuator, thereby eliminating the separated domain, which for the unforced airfoil, extends from the downstream edge of the actuator to the trailing edge. Second, the decrease in lift effected by the PS actuation is also accompanied by a decrease in induced drag. As a result of these effects for $\alpha \geq 3°$ the pressure drag for full PS actuation is actually smaller than for the smooth airfoil. Furthermore, for $\alpha \geq 8°$, the aerodynamic efficiency (based on pressure drag) is greater for the PS-actuation than for the smooth airfoil.

Similar to the SS actuator, the jet exit velocity of the PS actuator can be continuously varied by adjusting the (dimensionless) actuation parameter $-1 \leq u_{\mathrm{f}} < 0$. The variation of aerodynamic forces with PS actuation is shown in the left half of Figures 4.2e-h for $\alpha = -5°$, $0°$, $3°$, and $15°$. For $\alpha = -5°$, $0°$, and $3°$, C_{L}, C_{Dp}, and C_{M} vary monotonically and almost linearly with u_{f}. However, the variation for $\alpha = 15°$ is significantly different. The nearly linear variation is evident for $-0.5 < u_{\mathrm{f}} < 0$, however for $u_{\mathrm{f}} < -0.5$ the actuation effect appears to be saturated (although the drag coefficient continues to decrease slowly with increasing actuation input). This suggests that for this type of hybrid actuator, a critical jet speed is necessary to fully attach the flow, but it is unclear whether the critical parameter is the jet speed or momentum (both of which are mapped relative to the actuation input u_{f}).

The drag polar (C_{L} vs) for this configuration is shown in Figure 4.3. At the point of minimum drag ($\alpha = -3^\circ$, =0.006), the smooth airfoil has a lift $C_{\mathrm{L}} = 0.2$. The angle of max aerodynamic efficiency ($\alpha = 0$, cf. Figure 4.2d) corresponds to $C_{\mathrm{L}} = 0.45$ and =0.009. As noted in connection with Figure 4.2c, installation of the actuators results in a drag penalty for $-5^\circ < \alpha < 12^\circ$ as evidenced by a shift of the C_{L}- curve to the right in Figure 4.3. For $\alpha > 12^\circ$, the increased drag is offset by the even larger increase in lift due to the presence of the inactive actuators. When either the SS or PS actuators are operated, the drag penalty is mitigated as shown by the shifting of the C_{L}- to the left such that for a given C_{L}, the drag penalty associated with an operating actuator is approximately 50% of the corresponding ΔC_{D} for the inactive actuators.

4.1.3 Three-Dimensional Effects

The static pressure measurements are taken in a single spanwise plane and therefore yield only sectional force coefficients. The force measurements computed from the load cells and pitch servo actuator, however, measure the total lift and pitching moment. Figure 4.4 shows comparisons of the sectional lift and pitching moment with the corresponding global (or three-dimensional) distributions for the smooth and modified (unactuated) airfoil. The sectional and global C_{L} for the smooth airfoil (Figure 4.4a) are in good agreement for $-5^\circ < \alpha < 3^\circ$. However, for $\alpha > 3^\circ$, the sectional values exhibit a slightly lower slope $\partial C_{\mathrm{L}}/\partial\alpha$ such that at $\alpha = 15^\circ$, the sectional and local C_{L} are 1.47 and 1.59, respectively. Woo & Glezer (2010) observed the same divergence in the sectional and global values on a very similar NACA4415 wind tunnel model. These authors demonstrated that the presence of the fences at either end of the airfoil (cf. Figure 2.1) effectively delayed separation towards either edge of the span. Since the sectional measurements derive from the pressure distribution at midspan (where the flow separates first), the result is a lower sectional C_{L} at higher α. The sectional and global C_{M} for the smooth airfoil (Figure 4.4b) are in much closer agreement overall. For $-5^\circ < \alpha < 5$, both the sectional and global C_{M} have nearly constant slope with the latter exhibiting a slightly ($< 5\%$) lower magnitude. For $5^\circ < \alpha < 12^\circ$, the two measures track very closely before diverging again at $\alpha > 12^\circ$. At $\alpha = 15^\circ$, the sectional and global C_{M} are -0.067 and -0.059, respectively.

As previously noted in connection with the sectional C_{L} measurements in Figure 4.2, installation of the actuators results in a lift penalty for $\alpha < 10^\circ$ and a slight augmentation in C_{L} for $10^\circ < \alpha < 15^\circ$ as the presence of the actuators appears to delay flow separation (Figure 4.4a). Nonetheless, the sectional and global C_{L} for the modified airfoil exhibit the same trend observed for the smooth airfoil where the global C_{L} increases more rapidly than the sectional C_{L} for higher α. Interestingly, at $\alpha = 15^\circ$ the global and sectional C_{L} are 1.72 and 1.59, respectively, which are in equal proportion (0.92) to the smooth airfoil values. The global and sectional C_{M} for the modified airfoil (Figure 4.4b) follow the same trend as the corresponding C_{L} (cf. Figure 4.4a). The constant ratio between both the global and sectional C_{L} and C_{M} suggest that (chordwise) center of pressure remains constant both at the midspan as well as in the global sense throughout the range $-5^\circ < \alpha < 15^\circ$.

A comparison of the sectional and global measurements of C_{L}, ΔC_{L}, C_{M}, and ΔC_{M} are shown in Figures 4.5a, b, c and d, respectively where the incremental quantities ΔC_{L} and $\Delta C_{\mathrm{L}}$are plotted as a function of u_{f} as in Figure 4.2. The unactuated airfoil curves from Figures 4.4a and b are included in Figures 4.5a and c for reference.

The sectional and global $C_{\mathrm{L}}$for full SS/PS actuation ($u_{\mathrm{f}} = \pm 1$) follow very similar trend to the unactuated airfoil (i.e., higher global C_{L}at higher α, Figure 4.5a). Because the discrepancy between the sectional and global lift curves is manifested as a constant shift which is only a function of α but not actuation level, this difference all but disappears in the ΔC_{L} curves (Figure 4.5b) which are measured with respect to the unactuated case.

The sectional and global C_{M} are compared in Figure 4.5c. When the SS actuators are operated at $u_{\mathrm{f}} = 1$, the magnitude of the total pitching moment is moderately smaller than the sectional moment for all α, where the decrement increases with α. At higher α, the difference between total and sectional pitching moment for $u_{\mathrm{f}} = 1$ is more pronounced than the difference for the unactuated airfoil ($u_{\mathrm{f}} = 0$). This indicates that the SS actuation accentuates the absence of the actuators in the outboard sections. When PS actuators are operating at $u_{\mathrm{f}} = -1$, the sectional and global C_{M} values agree well at the high α but not for $\alpha < 5^\circ$. In particular, the global C_{L} does not exhibit the same diminished magnitude evident in either the $u_{\mathrm{f}} = 0$ or $u_{\mathrm{f}} = 1$ cases. This seems to suggest that operation of the PS

actuators effectively mitigates the inherent three-dimensionality of the modified airfoil.

The increment in sectional and global moment ΔC_{M} with respect to the unactuated case is shown in Figure 4.5. The most notable feature of this plot is the range $-1 < u_{\mathrm{f}} < -0.5$ for $\alpha = 15°$. First, as noted in connection with Figure 4.2f, the actuation effect appears to be saturated over this range. Also, because of the three-dimensionality which is present for $u_{\mathrm{f}} = 0$ case but not $u_{\mathrm{f}} = -1$ (cf. Figure 4.5c), the sectional ΔC_{M} is moderately (16%) larger than the corresponding global increment. As both the actuation saturation and "two-dimensionalization" phenomena are only evident for this small portion of the α-u_{f} domain, it would seem that these two effects are related.

In the following section, only the global (3D) lift and pitching moment are reported. Despite the non-negligible three-dimensional effects discussed above, the overall trends in C_{L} and C_{M} for various α and u_{f} are the same whether sectional or global forces are considered. Furthermore, the global forces are the relevant parameters for flight control, when the aerodynamic forces are unsteady.

4.2 Effect of Actuator Location

The investigations of DeSalvo & Glezer (2007) indicate dependence of the actuation effect on the streamwise (or chordwise) location of the actuators. In light of this finding, the sensitivity of the aerodynamic performance to the streamwise position of the SS and PS actuators was investigated. The measurements were conducted first with either actuator followed by several combinations of both SS and PS actuators to identify an optimal actuation position that maximizes the control authority as measured by ΔC_{M}.

4.2.1 Actuator Installed on Suction Surface Only

A series of experiments was conducted when the SS actuator was installed such that the synthetic jet orifice was located at $x/c = 0.98$, 0.95, and 0.83. Pressure distributions were measured over a range of angles of attack and the distributions for $\alpha = -3°$, $3°$, $9°$, and $15°$ for each of the three configurations are shown in Figure 4.6. The corresponding C_{L}, C_{Dp}, and C_{M}, computed from the pressure distributions, are shown in (Figure 4.7).

Consider first the configuration in which the actuator is mounted so that its downstream edge is flush with the trailing edge (Figures 4.6a-d). For $\alpha = 3°$ (Figure 4.6b), the pressure distribution over the suction surface of the airfoil is similar to the pressure distributions discussed in §4.1.1. The presence of the actuator results in a reduction in peak suction relative to the smooth airfoil case (from $C_\mathrm{p} = -1.17$ to -1.09 at $x/c = 0.17$). As the flow approaches the upstream edge of the actuator ramp, the pressure increases faster than over the smooth airfoil until reaching a local peak $C_\mathrm{p} = -0.090$ at $x/c = 0.83$ (compared to $C_\mathrm{p} = -0.27$ for the same location on the smooth airfoil). The pressure decreases slightly as the flow accelerates near the upstream edge of the ramp, but for $0.88 < x/c < 1$ the pressure remains nearly constant as the flow approaches the trailing edge where there is slight suction ($C_\mathrm{p} = -0.14$). The overall decrease in suction (due to the installation of the actuator) is also accompanied by a decrease in pressure on the pressure surface. The effects of actuator installation at other angles (Figures 4.6a, c, and d) are similar to $\alpha = 3°$ although they are less prominent at $\alpha = 9°$and 15°.

When the actuator is active, the flow accelerates along the actuator ramp ($0.83 < x/c < 0.98$) resulting in local changes in pressure around both sides of the airfoil where the pressure changes towards the levels of the smooth airfoil. It is noteworthy that immediately across the synthetic jet exit ($0.976 < x/c < 0.986$), the surface pressure increases from $C_\mathrm{p} = -0.18$ to $C_\mathrm{p} = 0.02$, ostensibly as a result of the interaction with and partial impingement on the Coanda surface.

The variation of C_L, C_Dp, and C_M with α is shown in Figures 4.7a-c. The presence of the actuator is accompanied by a small penalty in lift for $-5° \leq \alpha < 11°$, and a slight increase in lift for $11° < \alpha \leq 15°$. This change in lift is accompanied by as slight drag penalty for $-5° \leq \alpha < 3°$ but not at higher angles. The presence of the actuator has the most prominent impact on the pitching moment which decreases in magnitude relative to the smooth airfoil for $-5 \leq \alpha \leq 11°$particularly at low α. Whereas the smooth airfoil has a negative static margin ($\partial C_\mathrm{M}/\partial\alpha > 0$), the modified configuration has a positive static margin.

Operation of the *SS* actuator results in changes to C_L, C_Dp, and C_M (relative to the modified, unactuated airfoil) which are on the same order of magnitude as the changes induced by installation of the actuator. For all angles surveyed, operation of the actuators results in an increase in lift which varies from $\Delta C_{\mathrm{L}} = 0.08$ to 0.01 at $\alpha = -5°$ and 15° respectively. In fact, for $\alpha \geq 10°$, the lift of the actuated airfoil, exceeds the lift of the smooth airfoil. The effect of actuation on the pressure drag is less prominent. For $\alpha < 3°$, actuation reduces the drag about halfway to the smooth airfoil level, which is likely a result of reducing the separated flow domain downstream of the actuator. At higher α, however, the pressure drag increases slightly relative to the modified airfoil as a result of the increase in lift (i.e., this is the induced drag).

The most prominent changes resulting from operation of the SS actuator are manifested in the pitching moment. For the entire range of α the actuation increases the nose-down pitching moment which varies from $\Delta C_{\mathrm{M}} = -0.024$ to -0.003 at $\alpha = -5°$ and 15° respectively. The increment in pitching moment is correlated with the lift increment for the attached flow with $\Delta C_{\mathrm{M}}/\Delta C_{\mathrm{L}}$ bound between 0.31 and 0.34 over the range $-5° < \alpha < 10°$. It is also noteworthy that at $\alpha = 10°$ $\partial C_M/\partial\alpha$ changes its sign. This slight increase in C_{M} for $\alpha > 10°$ results from the weakened actuation effect at higher angles. In this flow regime, the actuators are unable reattach the flow downstream of the actuator to the same extent as is evident for lower α and the result is a smaller change in C_{M} at these higher angles.

When the actuator is moved upstream from the trailing edge such that the jet orifice is located at $0.95c$ the features of the pressure distribution that are associated with the actuator geometry (such as the acceleration over the ramp) are shifted upstream (Figure 4.6e-h). However, there are two notable differences compared to the configuration in which the actuator is flush with the trailing edge. First, installation of the actuator upstream of the trailing edge induces larger changes relative the smooth airfoil (e.g., the decrease in the peak suction at $\alpha = 3°$ to $C_{\mathrm{p}} = -1.076$). Second, the pressure rise immediately upstream of the actuator ramp is more pronounced, even reaching a positive value $C_{\mathrm{p}} = 0.062$ at $x/c = 0.83$ for $\alpha = -3°$. The changes in the pressure distribution induced by operation of the actuator in this case are consistent with the changes observed when the actuator is flush with the trailing edge as are the distributions of C_{L}, C_{Dp}, and C_{M} for this case (Figures 4.7d-f). Therefore, it may be concluded that for an isolated SS actuator (i.e., no PS actuator present) near the trailing edge ($0.97 < x_{SS}/c > 1$), the effect of actuator placement and operation is not very sensitive to the precise distance between the downstream edge of the actuator and the airfoil's trailing edge.

However, when the actuator is moved farther upstream to $x_{SS}/c = 0.85$ (Figures 4.6i-l) there is a longer separated domain downstream of the actuator in the absence of actuation. For example, at $\alpha = 3°$, the peak suction on the upper surface is lower than when the actuator is closer to the trailing edge (Figure 4.6j). Following the acceleration of the flow over the actuator ramp ($0.7 < x/c < 0.83$), the pressure continues to drop from $C_\mathrm{p} = -0.27$ just downstream of the synthetic jet ($x/c = 0.84$) to $C_\mathrm{p} = -0.30$ at $x/c = 0.98$, indicating the presence of a longer recirculation domain between the actuator and the trailing edge. The trailing edge pressure ($C_\mathrm{p} = -0.23$) as well as the pressure along the entire length of the pressure surface of the airfoil exhibits higher suction than either of the actuator locations closer to the trailing edge. This increased trailing edge suction is evident at $\alpha = -3°$, $9°$, and $15°$ as well (Figures 4.6i, k, and l).

When the *SS* actuator is operated in this configuration there are significant changes in the pressure distribution in the vicinity of the trailing edge. The flow acceleration over the ramp appears to be strengthened compared to previous configurations. For example, at $\alpha = 3°$, the pressure on the ramp at $x/c = 0.78$ decreases from $C_\mathrm{p} = -0.27$ to -0.48 as a result of the actuation. Downstream of the actuator, pressure recovery is observed from the downstream edge of the Coanda surface ($x/c = 0.85$, $C_\mathrm{p} = -0.29$) to the trailing edge where the pressure is slightly positive ($C_\mathrm{p} = 0.03$). The flow reattachment downstream of the actuator and the corresponding pressure recovery lead to substantial changes in the pressure distribution about the entire airfoil.

The corresponding changes in the forces and moment are overall larger than those observed when the actuator is closer to the trailing edge. To begin with, installation of the actuator results in a decrease in lift for all but the highest α. At $\alpha = 3°$, the lift is reduced by $\Delta C_\mathrm{L} = -0.20$ (28%) with respect to the smooth airfoil, compared to $\Delta C_\mathrm{L} = -0.17$ (17%) when the actuator is flush with the trailing edge. The pressure drag now exceeds the drag of the smooth airfoil for all but the highest α. The pitching moment for the modified, unactuated airfoil is less nose-down than in the previous two configurations but the static margin is nearly zero for $\alpha < 5°$. For $\alpha > 5°$, the pitching moment becomes slightly more nose-down until it coincides with the data for the smooth airfoil for $13° < \alpha < 15°$.

The modifications to the pitching moment effected by the actuation in this configuration are larger in magnitude than when the actuator is close to the trailing edge. In particular, $\Delta C_{\mathrm{M}} = -0.027$ and -0.009 for $\alpha = -5°$ and $15°$, respectively, indicating a strong control authority.

4.2.2 Actuator Installed on Pressure Surface Only

To complement the measurements in the previous section, pressure distributions were measured when the PS actuator was installed at three streamwise locations, with the jet at $x/c = 0.98$, 0.95, and 0.83.

When the PS actuator is flush with the trailing edge the pressure distribution around the airfoil is significantly altered (Figures 4.8a-d). Both the suction, on the top surface of the airfoil, and the pressure, on the bottom surface of the airfoil, increase compared to the smooth airfoil. For example, at $\alpha = 9°$ the suction peak ($x/c = 0.016$) increases from $C_{\mathrm{p}} = -2.20$ to -2.46 (Figure 4.8c). In this respect, the presence of the inactive actuator acts like a Gurney flap (Liebeck, 1978) increasing both the lift, drag, and nose-down pitching moment (Figure 4.9a-c). In particular, the pitching moment is altered substantially with respect to the smooth airfoil (Figure 4.9a), given by $\Delta C_{\mathrm{M}} = -0.040$ (38%), -0.054 (53%), -0.056 (60%), and 0.044 (60%) for $\alpha = -3°$, $3°$, $9°$, and $15°$, respectively.

Operation of the actuator also results in significant changes in the pressure distribution (Figures 4.8a-d). For all α the flow is accelerated over the actuator resulting in a substantial suction peak just upstream of the synthetic jet ($x/c = 0.97$). The largest pressure decrease along the ramp is visible for $\alpha = 9°$ where C_{p} varies from 0.30 at the upstream edge of the ramp ($x/c = 0.83$) to -0.61 just upstream of the actuator, a change of $\Delta C_{\mathrm{p}} = -0.91$ (Figure 4.8c). The effect of this pressure decrease on the lower surface of the airfoil propagates about its circumference. Over much of the pressure and suction surfaces, the pressure levels return to the values observed for the smooth airfoil, largely nullifying the increased lift induced by the installation of the actuator (Figure 4.9a), but also reducing the associated induced drag (Figure 4.9b). This change is also evident in the magnitude of the pitching moment (Figure 4.9c) which is reduced over all angles to levels below the smooth airfoil values. From a flight control perspective, continuous variation of the synthetic jet input allows for continuous variation of the pitching moment over all α.

When the actuator is moved upstream to $x_{PS}/c = 0.97$, the lift is slightly decreased over all angles with respect to the previous configuration (Figure 4.9d), while the drag is almost unchanged (Figure 4.9e). This seems to indicate that the drag increase associated with the presence of the actuator is not lift-induced drag but form drag owing to the low pressure recirculation region present downstream of the actuator (which is present in all configurations when the actuator is not operational). The increase in nose-down pitching moment (Figure 4.9f) is slightly less than what was observed when the actuator is flush with the trailing edge (e.g., $\Delta C_{\mathrm{M}} = -0.037$ or 93%), which is consistent with the slightly decreased lift (refer to the discussion of Figure 4.13 concerning the relationship between ΔC_{L} and ΔC_{M}).

When the actuator is operated, the changes in lift, drag, and pitching moment are larger than for the trailing-edge flush configuration. In fact, for $\alpha = 10^\circ$ the actuation changes the pitching moment by $\Delta C_{\mathrm{M}} = 0.071$ (68% of the magnitude of the pitching moment in the absence of actuation).

As the actuator is moved farther upstream to $x_{PS}/c = 0.085$ (Figure 4.8i-l), the airfoil's performance becomes more complex. Specifically, the pressure distributions and C_{L}, C_{Dp}, and C_{M} exhibit different characteristics for $\alpha < 5^\circ$ and $\alpha > 5^\circ$. For $\alpha < 5^\circ$ the pressure distributions (Figures 4.8i and j) follow similar trends to the previous two configurations, with the pressure rising upstream of the actuator ramp ($0.5 < x/c < 0.69$) followed by flow acceleration along the ramp to the jet exit ($x/c = 0.83$). Downstream of the jet, the pressure level remains fairly constant in the recirculation region behind the actuator. Unlike previous configurations however, the suction in the recirculation region is so large that near the trailing edge, the pressure on the suction surface is actually higher than the pressure on the pressure surface. Therefore, the pressure gradient would tend to drive the flow around the trailing edge in a clockwise direction (from the upper to lower surface). This flow is associated with a slightly increased levels of both lift and drag compared to the smooth airfoil (Figures 4.9g and h). The increase in drag is expected due to the recirculation region downstream of the actuator (which results in lower pressure on the downstream face of the actuator and Coanda), but the cause of the lift increase is more subtle. The most likely explanation is that the reversed pressure gradient near the trailing edge causes an increase in the overall circulation about the airfoil (similar to the Gurney flap effect associated with the previous two configurations).

At higher angles such as $\alpha = 9^\circ$ and 15° (Figures 4.8k and l, respectively), the suction in the recirculation region becomes so strong that it reduces the total lift (Figure 4.9g). The drag decreases as well in this regime a result of the loss in lift. The most prominent feature at the higher values of α, however, is the pitching moment which increases (becomes less nose-down) almost to the point of reversing to a positive (nose-up) level. For example, for $\alpha = 10^\circ$, the pitching moment increases from $C_\mathrm{M} = -0.072$ in the smooth case to -0.015 as a result of the actuator installation.

Operation of the actuator leads to flow attachment downstream of the actuator for all α where the acceleration on the actuator ramp is amplified by the active synthetic jet resulting in attachment along the Coanda surface and in the region between the actuator and the trailing edge.

As a result of the actuation, the lift distribution, which is modified by the installation of the actuators, “relaxes” towards the distribution of the smooth airfoil (Figure 4.9g). Interestingly, for $\alpha < 5^\circ$, the lift for the actuated airfoil is almost identical to the lift of the smooth airfoil, yet the underlying pressure distributions are different (Figures 4.8i and j). This is primarily due to the increased pressure on the lower surface upstream of the actuator ($0 < x/c < 0.75$) and increased suction along the ramp and over the Coanda surface ($0.75 < x/c < 0.9$) which effectively balance out resulting in nearly the same total force acting on the pressure side of the actuated airfoil as for the smooth airfoil. For $\alpha < 8^\circ$ the actuation causes a reduction in drag compared to the unactuated airfoil as a result of the pressure recovery downstream of the actuator (Figure 4.9h). For $\alpha > 8^\circ$, however, the drag begins to increase relative to the unactuated airfoil as a result of the increased lift caused by actuation.

The pitching moment increases for $\alpha < 3^\circ$ compared to both the unactuated and smooth airfoils (Figure 4.9h). While the actuated and smooth airfoils have the same lift within this range, there is an increase in C_M for the actuated airfoil is apparently caused by upstream motion of the center of pressure as a result of the actuation. For $\alpha > 3^\circ$, the pitching moment of the actuated airfoil is lower (more nose-down) than for the unactuated airfoil, but has nearly the same slope $\partial C_M/\partial\alpha$ as the smooth airfoil. At these higher values of α, the reduced pitching moment magnitude is accompanied with a slightly decreased lift with respect to the smooth airfoil (e.g., $\Delta C_\mathrm{L} = -0.075$ at $\alpha = 10^\circ$).

4.2.3 Both Actuators Installed Flush with Trailing Edge

A particularly interesting configuration is one in which the actuators are both mounted flush with the trailing edge. Unlike the two-actuator configuration presented in §4.1, when both actuators are flush with the trailing edge, there is no recirculation region present over the surface of the airfoil. Instead, both low pressure recirculation regions resulting from installation of the actuators are completely located in the wake. As in previous configurations, operation of either the SS or PS synthetic jets reattaches the flow along the respective corresponding Coanda surface. However, unlike the case in which the actuators are located (i.e., the Coanda surfaces terminate) upstream of the trailing edge, the present configuration affords the possibility for the flow to remain attached past the end of the Coanda surface, across the trailing edge and onto the Coanda surface of the opposite actuator.

This configuration is very similar to the circulation control airfoils first proposed by Englar (1975) for the purpose of enhancing lift on a STOL (short takeoff and landing) aircraft. Englar's design consists of a thick airfoil with a circular trailing edge and a slot jet located just forward of the trailing edge on the suction surface. A continuous jet of air emanating from the slot keeps the flow attached around the trailing edge, dramatically increasing the lift (as well as induced drag which in this case is useful for aircraft landing approach). The present configuration differs from this classical circulation control airfoil in two important aspects. First, the mechanism employed to effect flow reattachment over the rounded trailing edge is a synthetic jet (as opposed to steady blowing). Second, in the present configuration, the trailing edge does not have a smooth- or even continuous radius- but rather a discontinuity in slope where the two actuator Coanda surface meet at $(x, y) = (c, 0)$. As discussed in the experimental results below, it is possible that this discontinuity prevents the continuation of attachment around the trailing edge.

The pressure distributions for the unactuated configuration, full SS actuation, and full PS actuation are plotted in Figure 4.10 for $\alpha = -3°$, $3°$, $9°$, and $15°$ with the smooth airfoil case included for comparison. Installation of the actuators results in changes the the pressure distribution similar to previous two-actuator configuration shown (Figure 4.1). Upstream of either actuator, the pressure rises before rapidly decreasing as the flow accelerates up the ramp towards the jet exit. In this configuration the SS and PS jets are located at $x/c = 0.981$ and 0.976, respectively. (Although the actuators are manufactured to identical specifications and both have their downstream edges flush with the trailing edge, the SS actuator is rotated- pitched up- slightly due to the slope of the suction surface of the airfoil which results in the slight downstream displacement of the jet ext.) The presence of the actuators results in a positive shift in the pressure drag curve $\Delta C_{\mathrm{Dp}} \approx 0.13$ for $-5° \leq \alpha \leq 5°$ with respect to the smooth airfoil (Figure 4.2b) with little associated change in lift (Figure 4.2a). At higher angles, the lift for the modified airfoil is augmented with respect to the smooth case and the drag is comparably larger for these angles as well indicating. As in various SS-actuator-only cases, installation of the actuators causes the static margin to become positive with the pitching moment decreasing from $C_{\mathrm{M}} = -0.079$ at $\alpha = -5°$to $C_{\mathrm{M}} = -0.105$ at $\alpha = 15°$.

When the actuators are operated, the changes in lift, drag and pitching moment are qualitatively similar to those observed in the previous two-actuator case although in the present case, the changes in all parameters are smaller in magnitude. This suggests that the flow control mechanism is the same regardless of whether the actuators are flush with the trailing edge or located at some upstream location. Moreover, unlike in the circulation control airfoils, it appears that the flow does not turn smoothly around the trailing edge in the present case- a fact indicated by the sharp discontinuity in all pressure distributions at $x/c = 1$. The possible explanations for this are (i) the trailing edge radius is too aggressive in this case to achieve such attachment (ii) the slope discontinuity at the trailing edge somehow trips the attached flow or (iii) the circulation control cases, the steady blowing momentum coefficient is an order of magnitude larger than in the present case.

4.2.4 Pseudo-Optimal Actuator Location

It is clear from the results presented in the previous section, that the changes in aerodynamic coefficients resulting from actuator installation and actuator operation depend at least partly on the streamwise position of the actuator on the airfoil. Also, in all cases except the furthest upstream PS location, it was demonstrated that operation of the SS and PS actuators respectively effect an increase and decrease in nose-down pitching moment which may be varied continuously with the actuation input u_{f}. Additionally, the previous results of DeSalvo & Glezer (2007) demonstrate that it is possible to use both a SS and PS actuator in tandem to effect bidirectional control over the pitching moment. In light of this, several combinations of SS and PS actuator location were investigated with the goal of identifying a locally-optimal (or *pseudo-optimal*) actuation position with respect to the objective of maximizing the control authority $\Delta C_{\mathrm{M}}|_{u_{\mathrm{f}}=1}$ - $\Delta C_{\mathrm{M}}|_{u_{\mathrm{f}}=-1}$ at $\alpha = 3°$ (an arbitrarily selected operating point).

First, keeping the PS actuator as in the reference configuration of DeSalvo and Glezer ($x_{PS} = 0.98c$), the SS actuator position was varied from $x_{SS} = c$ (i.e., flush with the trailing edge) to $x_{SS} = 0.83c$. Figure 4.12a shows the pitching moment for the unforced, full SS actuation, and full PS actuation cases as a function of streamwise SS actuator location. As the SS actuator is moved upstream from the trailing edge, the baseline pitching moment decreases almost monotonically (i.e., becoming more nose-down). The change in pitching moment (Figure 4.12b) effected by operation of the SS actuators is nearly invariant for all but the farthest upstream locations, where the change is less than half that achieved for the downstream locations.

Interestingly, moving the SS actuator affects not only its own performance but that of the PS actuator. As the SS actuator is displaced upstream from the trailing edge, the baseline flow conditions seen by the PS actuator are modified such that the net nose-up pitching moment brought about by the PS actuators increases with the upstream motion of the SS actuators, highlighting the coupling of the actuation effect across the trailing edge. For this location of the PS actuators, the maximum control authority is found at $x_{SS} = 0.88c$.

A similar sensitivity investigation was performed keeping the SS actuators at this location and moving the PS actuators. The corresponding absolute and relative values of pitching moment are shown in Figure 4.12c and d, respectively. For the three data points available, it is clear that the change in pitching moment effected by the SS actuators is augmented as the PS actuators are moved upstream. The effect on PS actuator performance is unclear. Practical considerations– specifically the difficulty associated with dismounting and remounting the PS actuators– prevented collection of further data points during this preliminary investigation. The airfoil profiles for the reference and optimal configurations are depicted schematically in Figure 4.12e.

The corresponding lift and pitching moment increments ΔC_{L} and $\Delta C_{\mathrm{M},c/4}$ (relative to $c/4$) are plotted in Figure 4.13 for all the available data (about 3,000 points) within the range $-1 \leq u_{\mathrm{f}} \leq 1$; $-2^\circ \leq \alpha \leq 10^\circ$; $0.83 \leq x_{SS}/c \leq 1$; $0.96 \leq x_{PS}/c \leq 1$. It is remarkable that the entire data set collapses on a single linear distribution with a slope of $\frac{\Delta C_{\mathrm{L}}}{\Delta C_{\mathrm{M},c/4}} = -3.2$. That different actuation effects, as manifested by changes in actuation position and actuation strengths at all angles of attack, collapse on a single curve, indicates that the increments in the lift and pitching moment are primarily affected by the strength of the trapped vorticity.

4.3 Effect of Actuation on the Time-Averaged Flow Field

The effects of actuation near the trailing edge of the stationary airfoil are assessed from time-averaged PIV measurements. The measurement domain is $0.84 < x/c < 1.07$ and $-0.07 < y/c < 0.12$ and includes the exit plane of the suction actuator jets [the trailing edge is located at $(x, y) = (c, 0)$]. The pressure side actuator jets are obscured by the shadow of the airfoil. First an angle sweep was conducted in which the evolution of the unforced flow and the flow in the presence of full SS actuation ($u_\mathrm{f} = 1$), and full PS actuation ($u_\mathrm{f} = -1$) was measured for $\alpha = -5°$, $-4°$, ..., $14°$, $15°$. Next a series of measurements were made for $\alpha = -5°$, $3°$, and $15°$ for which $-1 \leq u_\mathrm{f} \leq 1$ at increments of $\Delta u_\mathrm{f} = 0.1$. The instantaneous PIV measurements are used to compute the time-averaged velocity field $\overline{u}$, the Reynolds stresses $\overline{u'u'}$, $\overline{v'v'}$, and $\overline{u'v'}$ and the time-averaged spanwise vorticity (§ 2.3.2).

4.3.1 Time-Averaged Velocity and Vorticity Fields at the Trailing Edge

The effects of the actuation near the trailing edge of the stationary airfoil are assessed from raster plots of distributions of the time-averaged spanwise vorticity $\omega_z c/U_0$ and velocity vectors, as shown in Figure 4.14. Measurements are presented at $\alpha = -3°$, $3°$, $9°$, $15°$ for the unactuated flow (Figures 4.14a-d), full SS actuation ($u_\mathrm{f} = 1$, Figures 4.14e-h), and full PS actuation ($u_\mathrm{f} = -1$, Figures 4.14i-l).

In the absence of actuation (Figures 4.14a-d), the baseline flow separates locally over the downstream edge of the actuators for all α surveyed. The separated shear layer forms a clockwise (CW) trapped vortex within the closed recirculation domains between the actuator and the trailing edge. (Similarly, a counter-clockwise (CCW) vortex forms downstream of the PS actuator. Although the flow near the surface of the airfoil upstream of the trailing edge is not fully resolved, it is possible to identify CCW and CW vorticity layers near the suction and pressure surfaces, respectively, that are induced by the upstream flow. Naturally, for higher α, the airfoil boundary layer upstream of the suction side actuators thickens and the vorticity in the shear layer over the actuator becomes more diffuse and is displaced away form the surface.

Activation of the suction-side actuators (Figures 4.145e-h) reduces the thickness of the vorticity layer and consequently the characteristic scale of the trapped vortex, resulting in tilting of the flow downstream of the actuator towards the surface and in a reduction in the cross-stream width of the near wake. As discussed in §4.1.1, this downwash is accompanied by a pressure recovery downstream of the SS actuator as the flow attaches to the Coanda surface. While this reattachment is visible at all angles, the shear layer exhibits a bifurcation with increasing α (in particular, for $\alpha = 9^\circ$ and 15°, Figures 4.145g and h, respectively). These data show two distinct regions of high concentration CW vorticity downstream of the jet. The lower layer is attached to the wall while the upper layer is advected parallel to the ramp but exhibits a cross-stream diminution of the vorticity towards the surface. The beginning of this bifurcation is visible for $\alpha = 3^\circ$ (Figure 4.145e) in the slight CW vorticity depression at $(x, y)/c = (0.9, 0.05)$. These data suggest that at higher angles, the increased suction between the SS actuator and the trailing edge is insufficient to entrain the entire width of the shear layer to the surface. The vorticity layer near the surface is associated with the propagation of the jet flow and appears to diminish with increasing angle of attack.

Activation of the pressure-side actuators (Figures 4.145i-h) causes the CCW trapped vorticity layer on the pressure side to become somewhat thinner and leads to an upwash of the near wake that is associated with a reduction in the lift and a nose-up pitching moment (relative to the unactuated airfoil). While in the data presented here the flow on the pressure side of the airfoil is blocked by the laser shadow, separate measurements (not shown) confirm that PS actuation results in local attachment between the actuator and the trailing edge that is similar to the effect of the SS actuator. In addition, it is noteworthy that pressure-side actuation results in significant changes in the trapped vortex upstream of the trailing edge on the suction side of the airfoil, and in migration of the stagnation point in the cross-stream direction from $\mathbf{x}/c = (1.06, 0)$ when $u_\mathrm{f} = 0$ to $(1.06, 0.02)$ when $u_\mathrm{f} = -1$.

The vectoring of the wake as a result of the actuation input is more clearly demonstrated by the *residual velocity* or the difference between the time-averaged velocity fields of the actuated and unactuated flows. Figure 4.15 shows the residual velocity fields for full SS and PS actuation, respectively. For SS actuation (Figure 4.15a-d) flow control results in an increase in streamwise momentum downstream of the actuator as the flow is attached and higher-speed fluid is deflected into the region between the actuator and the trailing edge. Below the trailing edge (but still downstream of the laser shadow), the streamwise velocity is reduced relative to the unforced flow which, when taken in combination with the increased velocity on the suction side, indicates an increase in circulation about the airfoil resulting from SS actuation. The bifurcation in the SS-actuated shear layer discussed in connection with Figure 4.14 is evident in the residual velocity as well. Here this vorticity-deficit region is associated with the broad invariant cross-stream segments of the residual velocity profiles (for example, at $(x, y)/c = (0.91, 0.05)$ in Figure 4.15c). Although the vectoring of the velocity field due to operation of PS actuator is obstructed by the laser shadow, the decrease in lift and circulation are evident in the visible portion of the field. The residual velocity field associated with the PS actuation (Figures 4.15e-h) results in increased velocity within the lower edge of the wake and upward vectoring. It is noteworthy that the induced effect on the suction side results in slowing of the flow and consequently in a reduction of and an increase in the static pressures on the suction and pressure sides, respectively. The changes in the pressure are commensurate with the changes in the pitching moment (cf. Figure 4.2).

4.3.2 Vorticity Flux Distribution in the Near Wake

The vectoring of the wake is further quantified by the cross-stream distribution of vorticity flux through the wake. For each time-averaged flow field, the local vorticity flux is computed as the product of the streamwise velocity and spanwise vorticity (neglecting turbulent stresses): $\mathrm{f}_\omega = u\omega_z$. For $\alpha = -5°$, $3°$, and $15°$, the cross-stream distribution of f_ω is extracted at the streamwise station $x/c = 1.04$ for each forcing level $-1 < u_\mathrm{f} < 1$, $\Delta u_\mathrm{f} = 0.1$ (Figure 4.16). The traces on the graph are colored such that black corresponds to the unactuated flow and increasing levels of red (blue) correspond to increasing levels of SS (PS) actuation. Although the integrated time-averaged cross-stream vorticity flux vanishes for a steady flow in accordance with Kelvin's Theorem, the distribution of the integrand is instructive for assessing the effect of the actuation on the wake structure.

In the absence of actuation, the *wake width* as may be defined by the cross-stream distance between the positive and negative peaks of vorticity flux varies from $0.055c$ at $\alpha = -5°$ to $0.088c$ at $15°$ with an intermediate value of $0.062c$ at $\alpha = 3°$ (Figure 4.16). When $u_\mathrm{f} = 0$, at $y = 0$ (the cross-stream coordinate of the trailing edge), the flux of the unactuated flow exhibits a local maximum or minimum which correspond to reversed flow immediately downstream of the trailing edge for all angles. For $\alpha = 3°$ (Figure 4.16b) vorticity flux, $f_\omega c/U_\infty^2$ has peak values of -23 ($y/c = 0.036$) and 32 ($y/c = -0.022$) that are associated with the SS and PS boundary layers and demonstrate that the SS boundary layer is thicker.

When the SS actuators are operated at low power $0 < u_\mathrm{f} < 0.2$, for $\alpha = -5°$ and $3°$ (Figures 4.16a and b, light red), the wake exhibits a slight broadening in the cross-stream direction, which is accompanied by an increase in the flux magnitude from either side. As the actuation level continues to increase past $u_\mathrm{f} = 0.2$, the flux magnitudes decrease as the wake is continuously deflected downward. This deflection continues until $u_\mathrm{f} = 1$ at which point wake center is displaced approximately $-0.018c$ with respect to the unactuated case. It is noteworthy that this trend reverses about $u_\mathrm{f} = 0.2$ and is consistent with the measurement of the pitching moment (Figure 4.2f) where the sign of ΔC_M reverses at $u_\mathrm{f} = 0.2$. At $\alpha = 15°$ (Figure 4.16c) the change in flux distribution as a result of the SS actuation is much more subtle and is primarily limited to a slight increase in flux magnitude from both sides of the trailing edge but little displacement of the wake. These small changes are also consistent with the force measurements (Figure 4.2) in which operation of the SS actuators at high α was seen to have little or no effect.

Operation of the the PS actuators leads to an *upward* deflection of the wake compared to the unforced flow for all angles surveyed. This deflection increases monotonically with actuator power u_f and reaches maximum levels of $0.011c$, $0.013c$, and $0.02c$ for $\alpha = -5°$, $3°$, and $15°$, respectively (all occur at the maximum level actuation level, $u_\mathrm{f} = -1$). It was previously observed in connection with the force measurements (cf. Figure 4.18f) that PS actuation effect appeared to *saturate* at $\alpha = 15°$ for $u_\mathrm{f} < -0.5$. The flux data exhibit a similar trend in that the shear layer from the lower side of the airfoil is displaced by $0.018c$ for $0 > u_\mathrm{f} > -0.5$ of actuation input and only another $0.008c$ for $-0.5 > u_\mathrm{f} > -1$.

4.3.3 Turbulence and Reynolds Stress Estimates

The turbulent characteristics of the wake are significantly altered as a result of the actuation. The components of the Reynolds stress tensor $\overline{u'u'}$, $\overline{v'v'}$ and $\overline{u'v'}$ are computed from the instantaneous velocity fields and the time-averaged turbulent energy is approximated as

$k = \frac{1}{2}\left(\overline{u'u'} + \overline{v'v'}\right)$. In order to ensure statistical convergence, the time-averaged results presented in this section are computed from $N = 2500$ instantaneous velocity fields (in contrast to the typical $N = 200$ fields in all other PIV measurements).

In order to verify statistical convergence, an additional 7500 instantaneous vector fields were recorded for $u_\mathrm{f} = 0$ for a total of $N = 10,000$ image pairs. Incremental point estimates of $\overline{u}$, $\overline{v}$, $\overline{u'u'}$, $\overline{v'v'}$ and $\overline{u'v'}$ were computed for each $100 \leq N \leq 10,000$ at the location of maximum k in the wake ($x/c = 1.07$, $y/c = -0.006$). The resulting estimates are plotted as a function of N in Figure 4.17. For each point estimate, a 95% confidence interval was computed assuming appropriate statistical distributions[1]. For the mean velocity components (Figure 4.17a) the confidence intervals have width $0.023U_0$ and $0.025U_0$ for $\overline{u}$ and $\overline{v}$, respectively at $N = 2500$. The respective errors decrease to $0.010U_0$ and $0.013U_0$ at $N = 10,000$. For the Reynolds stresses (Figure 4.17b), the confidence interval widths for $\overline{u'u'}$, $\overline{v'v'}$ and $\overline{u'v'}$ at $N = 2500$ are $0.007U_0^2$, $0.012U_0^2$, and $0.005U_0^2$, respectively. These values decrease to $0.003U_0^2$, $0.006U_0^2$, and $0.003U_0^2$ at $N = 10,000$. The fact that the errors associated with measuring the cross-stream statistics ($\overline{v}$ and $\overline{v'v'}$) are approximately twice the errors associated with the streamwise statistics ($\overline{u}$ and $\overline{u'u'}$) is consistent with the fact that the magnitude of $\overline{v'v'}$ is approximately that of $\overline{u'u'}$. Nonetheless, it may be assessed from this analysis that all five statistics are well converged by $N = 2500$.

Distributions of k and $\overline{u'v'}$ are shown in Figure 4.18 for $\alpha = 3°$. For the unforced flow ($u_\mathrm{f} = 0$, Figure 4.18a,d) large concentrations of both k and $\overline{u'v'}$ are visible downstream of the trailing edge with peak values of $k/U_0^2 = 0.087$ and $|\overline{u'v'}|/U_0^2 = 0.048$ at $x/c = 1.07$. When the SS actuators are operated ($u_\mathrm{f} = 1$, Figure 4.18b,e) the turbulence level is substantially reduced throughout the wake with local maxima of $k/U_0^2 = 0.031$ and $|\overline{u'v'}|/U_0^2 = 0.021$ displaced slightly upstream (with respect to the $u_f = 0$ case) to $x/c = 1.05$. When the PS actuators are operated ($u_\mathrm{f} = -1$, Figure 4.18c,f), the turbulence level is also reduced (peak levels $k/U_0^2 = 0.044$ and $|\overline{u'v'}|/U_0^2 = 0.030$), however, in this case the peaks are displaced

---

[1] At each spatial location, the instantaneous velocity samples $(u, v)_i$ are assumed to be independent and identically-distributed random variables pairs. Thus, for large N, the time-averaged velocity components, $\overline{u}$ and $\overline{v}$, follow a Gaussian distribution and the diagonal Reynolds stresses, $\overline{u'u'}$ and $\overline{v'v'}$, follow a Chi-Squared distribution (Rice, 2006). The distribution of $\overline{u'v'}$ is estimated using Fisher's Transformation (Fisher, 1915).

slightly downstream to $x/c = 1.08$. This reduction in turbulent kinetic energy is consistent with enhanced mixing and subsequent dissipation effected by the high frequency actuation (see Vukasinovic *et al.*, 2010).

4.4 Phase-averaged Measurements of the Synthetic Jet Cycle

A series of phase-averaged PIV measurements were recorded in the domain immediately downstream of the SS actuator ($0.855 < x/c < 0.896$, $0.033 < y/c < 0.069$) when the airfoil was held at $\alpha = 3^\circ$ with the pitch servo. In order to minimize the portion of the image taken up by the airfoil model, the camera was rotated along the pitch axis by 7.2° so that the ramp is approximately parallel to the top and bottom edges of the image. The synthetic jet exit slot is located in the yz plane at the streamwise coordinate $x/c = 0.861$ and spans the cross-stream domain $0.055 < y/c < 0.057$. Phase-averaged velocity fields were measured at 18 equally-spaced phases during the jet cycle (i.e., $\phi = 0^\circ$, 20°, ..., 340°). The synthetic jet frequency is $f_{\mathrm{act}} = 2000$ Hz which corresponds to a Strouhal number $St_{\mathrm{act}} = \frac{f_{\mathrm{act}} c}{U_0} = 30.5$ or a cycle period of $0.033\,T_{\mathrm{conv}}$.

The time-averaged flow in the absence and presence of actuation is shown in Figure 4.19 in terms of vorticity (Figures 4.19a&c) and velocity magnitude (Figure 4.19b&d) contours with overlaid velocity vectors. These data show that the unforced flow separates off the actuator ramp and forms a shear layer which grows with increasing downstream distance from the end of the ramp. The fluid between the shear layer and airfoil surface (downstream of the actuator) is nearly stagnant corresponding to the locally constant pressure in Figure 4.1b. At the top of the measurement domain, the velocity magnitude slightly exceeds the free stream speed U_0 by $2 - 5\%$ ostensibly owing to blockage effect of the airfoil model. When flow control is engaged (Figures 4.19c&d), the flow attaches to the downstream side of the actuator as discussed in §4.3. The corresponding unsteady flow field is shown in Figure 4.20 for 18 phases during the synthetic jet cycle. The first and second columns of Figure 4.20 show contours of phase-averaged vorticity and velocity magnitude, respectively, with overlaid velocity vectors.

The sequence begins as the synthetic jet is completing the suction segment of the cycle and beginning the blowing segment. As a result of the suction, the boundary layer vorticity flowing over the ramp is pulled toward the jet orifice (Figure 4.20a). The strength of the entrainment is indicated by the high velocity fluid above and downstream of the actuator tip which takes a maximum value of $|\mathbf{u}|/U_0 = 1.39$ at $\mathbf{x}/c = (0.85, 0.06)$. Farther downstream, the vortex pair from the previous cycle is still visible at $\mathbf{x}/c = (0.88, 0.06)$. As the jet velocity out of the actuator increases, a counter-rotating vortex pair is formed at the orifice which is not initially resolved in these measurements. However, the new CW vortex (from the jet) merges with the CW vorticity concentration immediately downstream of the jet exit which begins to lift away from the surface and increases in size (Figures 4.20b-c). As the cycle continues, the CW vorticity concentration is pinched off of the boundary layer (Figures 4.20d-e) and ultimately forms a large discrete vortex (Figures 4.20f). During this process the local velocity immediately above the CW vortex reaches $1.4U_0$. As the blowing segment of the jet cycle diminishes (Figures 4.20g-h), the CW vortex begins to move downstream and a the CCW vortex becomes visible as it grows between the upstream boundary layer and the CW vortex. As the CCW vortex grows in size (Figures 4.20i-j), the upstream boundary layer once again begins to wrap around to tip of the ramp towards the jet exit. At this point, the jet transitions from blowing to suction and the CCW vortex reaches its maximum strength (Figures 4.20k). During the suction part of the cycle, the counter-rotating vortex pair advects downstream from the jet exit and the flow over the ramp accelerates to a peak velocity of $1.4U_0$ (Figures 4.20l-r). This flow turning around the tip of the ramp is apparently affected by the induced velocity field of the CCW vortex and the jet suction. By drawing this higher momentum flow into the region downstream of the actuator, the suction pressure on the Coanda and the airfoil surface recovers and the total circulation about the airfoil increases. The change in pressure field and global circulation result in the increased lift and nose-down pitching moment associated with operation of the SS actuator.

The effect of the actuation on the flow field immediately downstream of the SS actuator is assessed in terms of the change in local circulation Γ_{CV} in the measurement domain. Taking the flow domain depicted in Figures 4.19 and 4.20 as a “control volume”, the total circulation in the region is computed using the line integral $\Gamma_{\text{CV}} = \oint \mathbf{u} \cdot d\mathbf{l}$. In the absence of actuation, the circulation in this region is $-0.040U_0c$ (Figure 4.21, black dashed line). When actuation is applied the time-averaged, local circulation increases in magnitude to $-0.053U_0c$. This change in circulation is consistent with the attachment of the flow to the Coanda surface downstream of the actuator which results in enhanced CW vorticity. The variation in phase-averaged local circulation during the synthetic jet cycle is also shown in Figure 4.21. For $0 < \phi < 80°$, Γ_{CV} increases in magnitude above the time-averaged level due to the strong CW vorticity building up at the jet exit during the suction segment of the actuation cycle (cf. Figures 4.20a-e). Following a peak local circulation of $-0.055U_0c$ at $\phi = 80°$, this vortex pinches off and is advected downstream. As a CCW vortex develops between the first vortex and the jet exit, the local circulation decreases ($120° < \phi < 200°$) below the time-averaged value before recovering ($200° < \phi < 360°$) as the vortex pair flows out of the measurement domain.

The effects of voltage applied to the actuator disk (quantified by u_{f}), and the jet frequency on the unsteady unsteady flow field were characterized using a larger field of view of the SS actuator ($0.81 < x/c < 0.94$, $0.01 < y/c < 0.1$) at $\alpha = 3°$. Vorticity and velocity fields are shown for the time-averaged unforced flow (Figure 4.22a) and during a single phase of the phase-averaged velocity field ($\phi = 260°$) for $u_{\text{f}} = 0.25$, 0.5, 0.75, and 1 (Figures 4.22b-d, respectively).

Consider first the SS actuation case (Figure 4.22a), which corresponds approximately to the phase shown in (Figure 4.20d). Because of the larger field of view, three CW vortices are visible downstream of the actuator. In these phase-averaged measurements, the vortices appear to diffuse as they advect downstream, however, Jee (2010) demonstrated in a numerical study of this configuration that the flow between the SS actuator and the trailing edge is highly chaotic when the SS actuator is operating. Thus, the diffusion of phase-average vortices does not necessarily correlate to diffusion of instantaneous vortices. Nonetheless, coherent structures are visible both in the vorticity and velocity fields. Note that for $u_{\text{f}} = 1$ the shear layer downstream of the actuator is nearly parallel to the airfoil surface (flow angle $\beta = -17.6°$) indicating the strong turning of the flow as a result of the actuation. (Compare to the unforced case in Figure 4.22e where the flow separates at

$x/c = 0.86$ and the shear layer forms off the actuator ramp with a region of slowly rotating fluid at its low-speed side between the Coanda surface and the trailing edge.) As the jet strength decreases to $u_\mathrm{f} = 0.75$ and $u_\mathrm{f} = 0.5$ (Figures 4.22b and c, respectively), the individual vortices appear to be weaker but remain phase-locked to the actuation. Note that the streamwise spacing between successive vortices increases with actuation amplitude. At higher u_f the vortices advect downstream faster because of the local high speed flow entrained by the actuation. Another feature of the actuation amplitude is the turning of the flow around the actuator's edge. For $u_\mathrm{f} = 0.75$ and 0.25, the flow angle in the shear layer (measured at $\mathbf{x}/c = (0.92, 0.06)$ increases to $\beta = -15.8^\circ$ and -12.3°, respectively. For $u_\mathrm{f} = 0.25$ (Figure 4.22d), the first two discrete vortices are visible downstream of the jet, yet the actuation appears to have minimal effect on displacing the shear layer. In fact, the shear layer is deflected slightly *upward* ($\beta = -8.9^\circ$) with respect to the unforced case ($\beta = -9.2^\circ$). These observations are consistent with the force measurements presented in 4.2e and f, which indicate that the increase in lift and nose-down pitching moment are not present- and in some places reversed- for $u_\mathrm{f} < 0.25$.

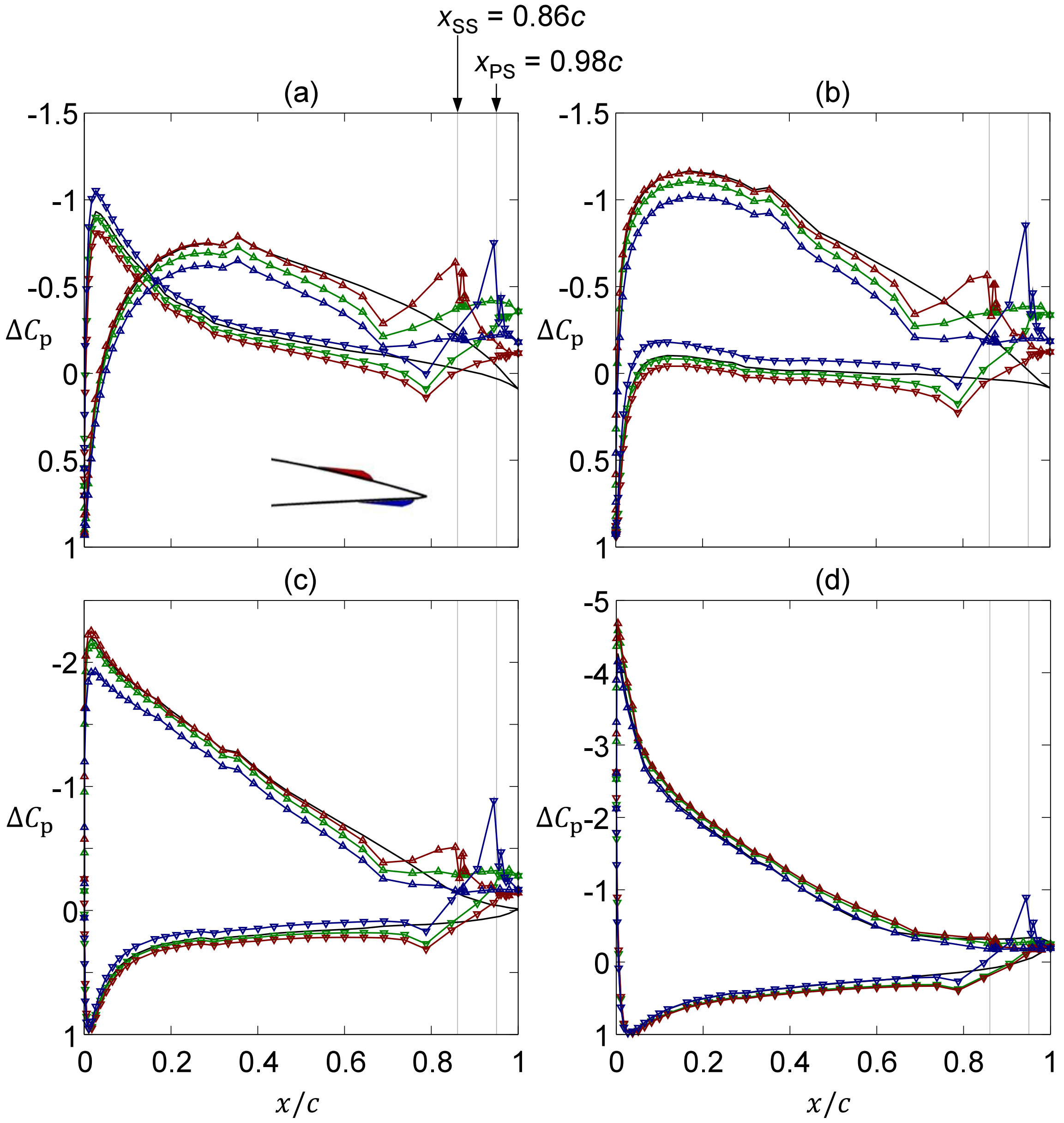

Figure 4.1: Distributions of static pressure C_p when the actuators are mounted at $[x_{SS} = 0.86c,\ x_{PS} = 0.95c]$ for $\alpha = -3°$ (a), $3°$ (b), $9°$ (c), and $15°$ (d), and actuation level $u_f = 0$ (▲), 1 (▲), and -1 (▲). Corresponding C_p for the smooth airfoil (▬).

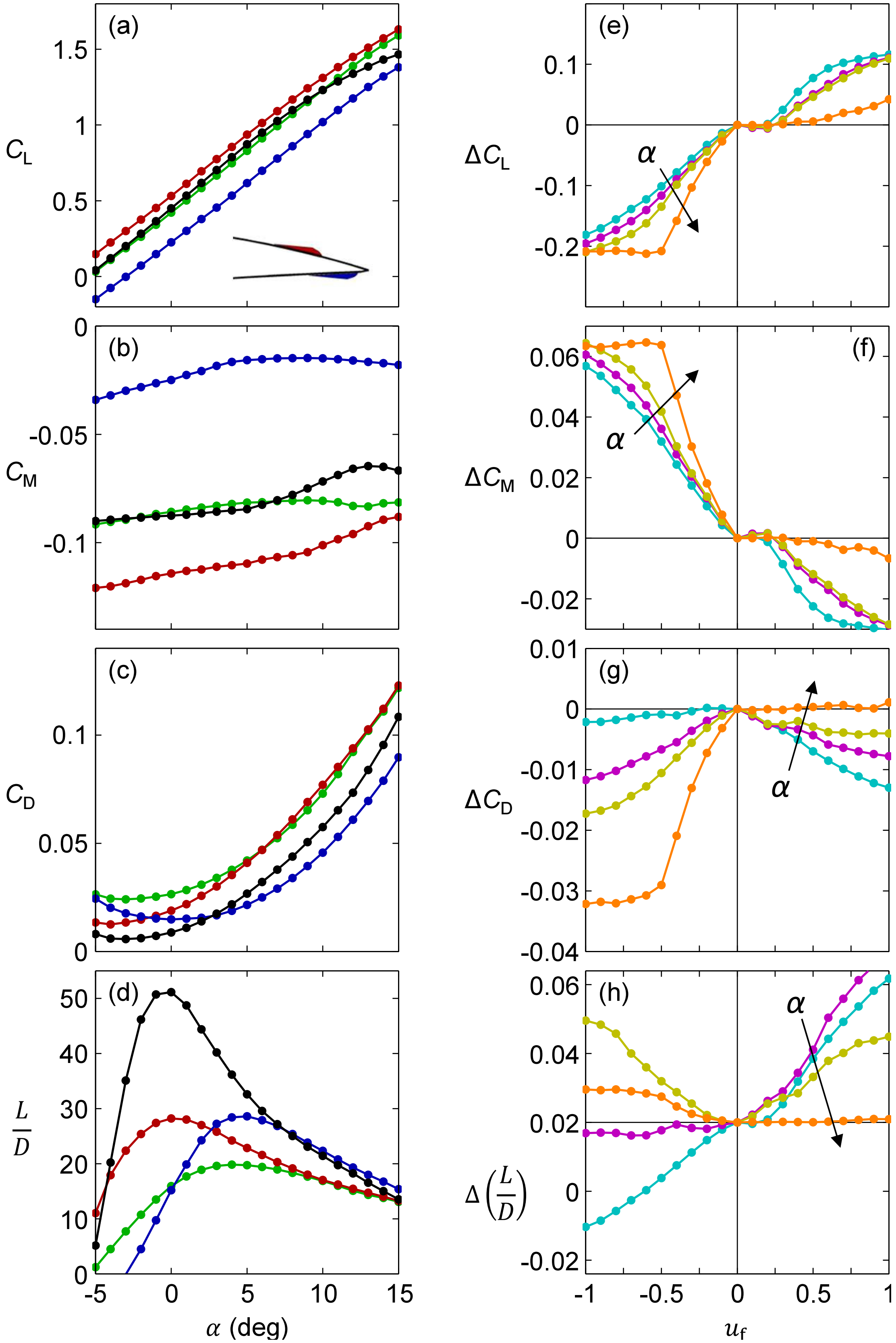

Figure 4.2: Variation of (a) C_L, (b) C_M, (c) C_D and (d) L/D with α for the smooth airfoil (—) and modified [$x_{SS} = 0.86c$, $x_{PS} = 0.95c$] airfoil with $u_\mathrm{f} = 0$ (●), 1 (●), and -1 (●). Variation of (e) ΔC_L, (f) ΔC_M, (g) ΔC_D and (h) $\Delta\left(L/D\right)$ with u_f $\alpha = -5°$ (●), 0° (●), 3° (●), and 15° (●).

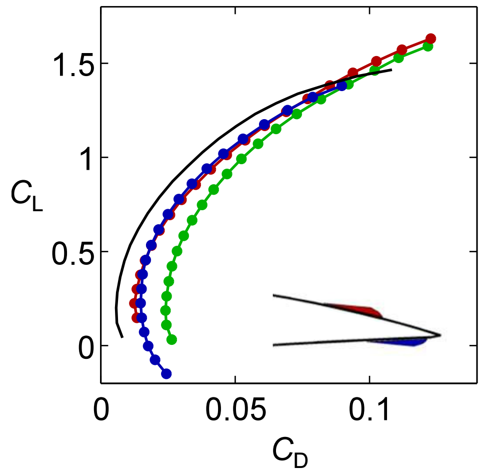

Figure 4.3: Drag polar for the smooth airfoil (▬) and modified [$x_{SS} = 0.86c$, $x_{PS} = 0.95c$] airfoil with $u_f = 0$ (●), 1 (●), and -1 (●).

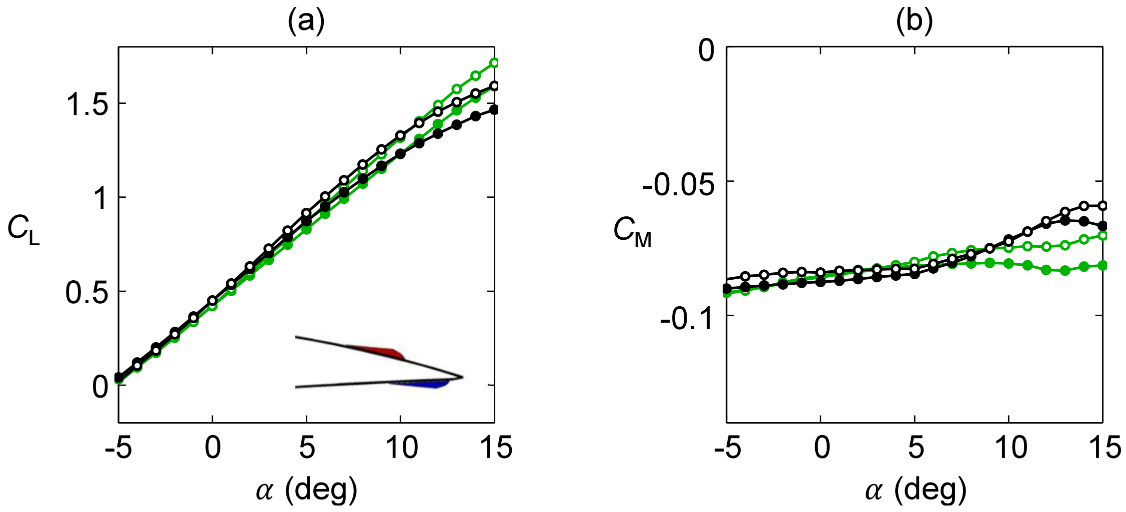

Figure 4.4: Comparison of sectional force coefficients (closed symbols) and global force coefficients (open symbols) for the smooth (▬) and modified [$x_{SS} = 0.86c$, $x_{PS} = 0.95c$] (▬) airfoil.

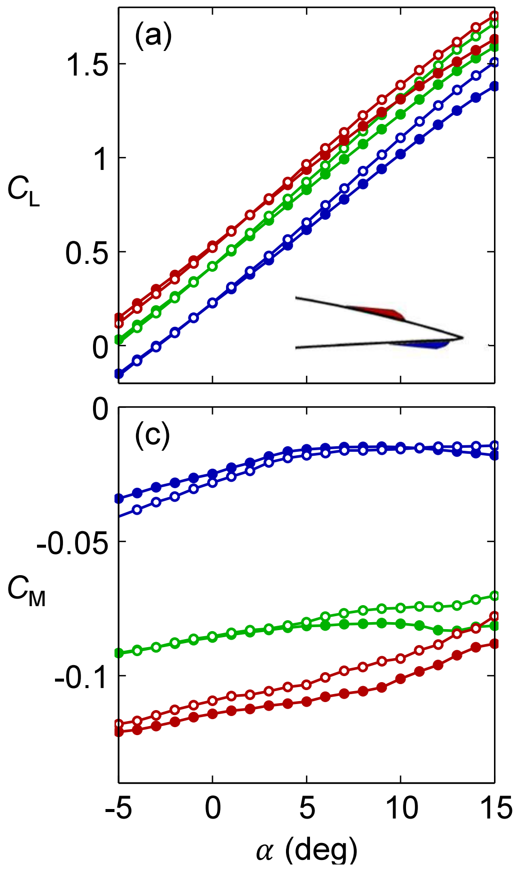

Figure 4.5: Comparison of sectional force coefficients (closed symbols) and global force coefficients (open symbols) for the modified $[x_{SS} = 0.86c,\ x_{PS} = 0.95c]$ airfoil. Colors as in Figure 4.2.

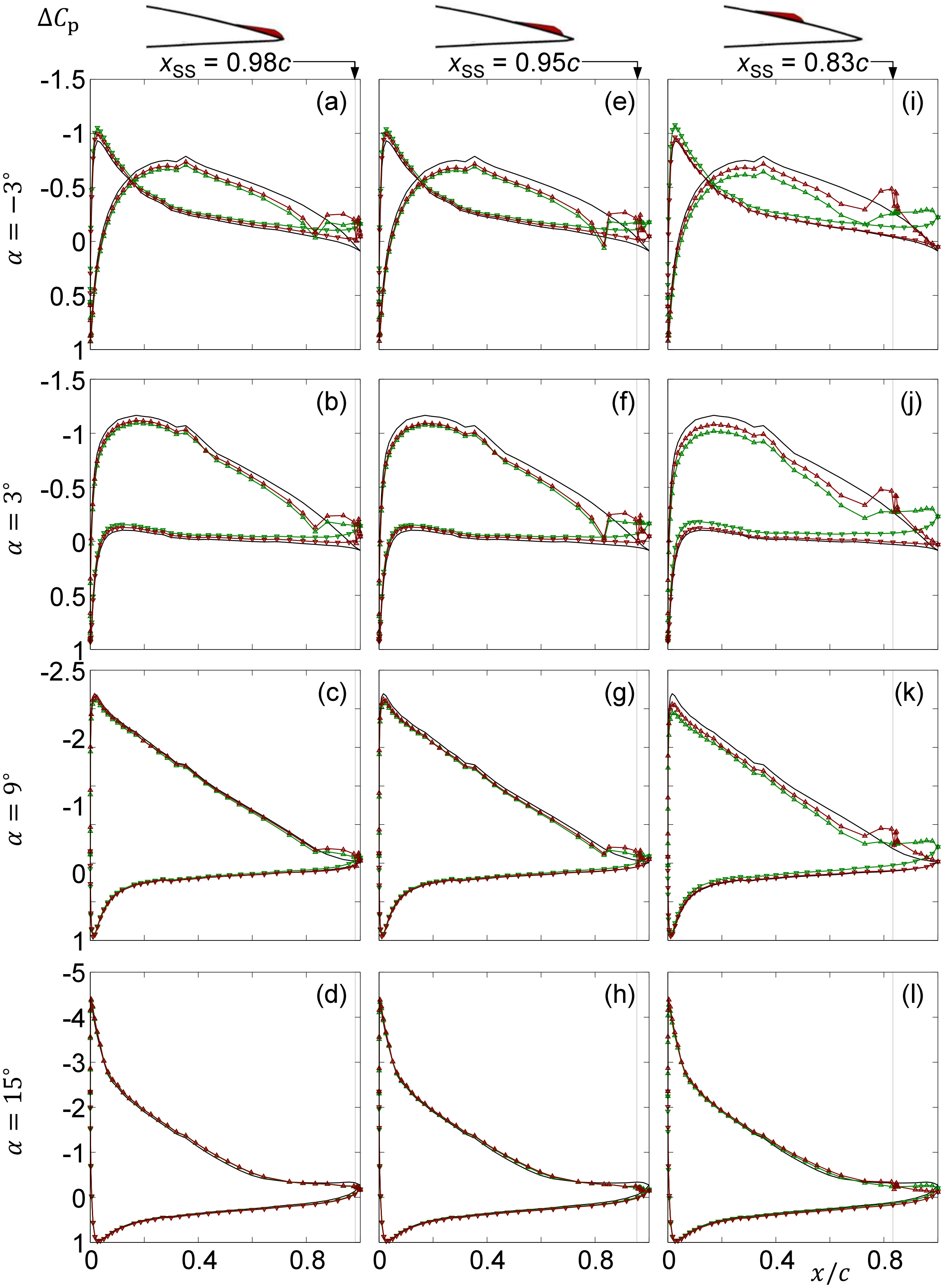

Figure 4.6: Distributions of static pressure C_p for when only the SS actuator is present and installed at $x_{SS}/c = 0.98$ (a-d), 0.95 (e-h), and 0.83 (i-l). Colors as in Figure 4.1.

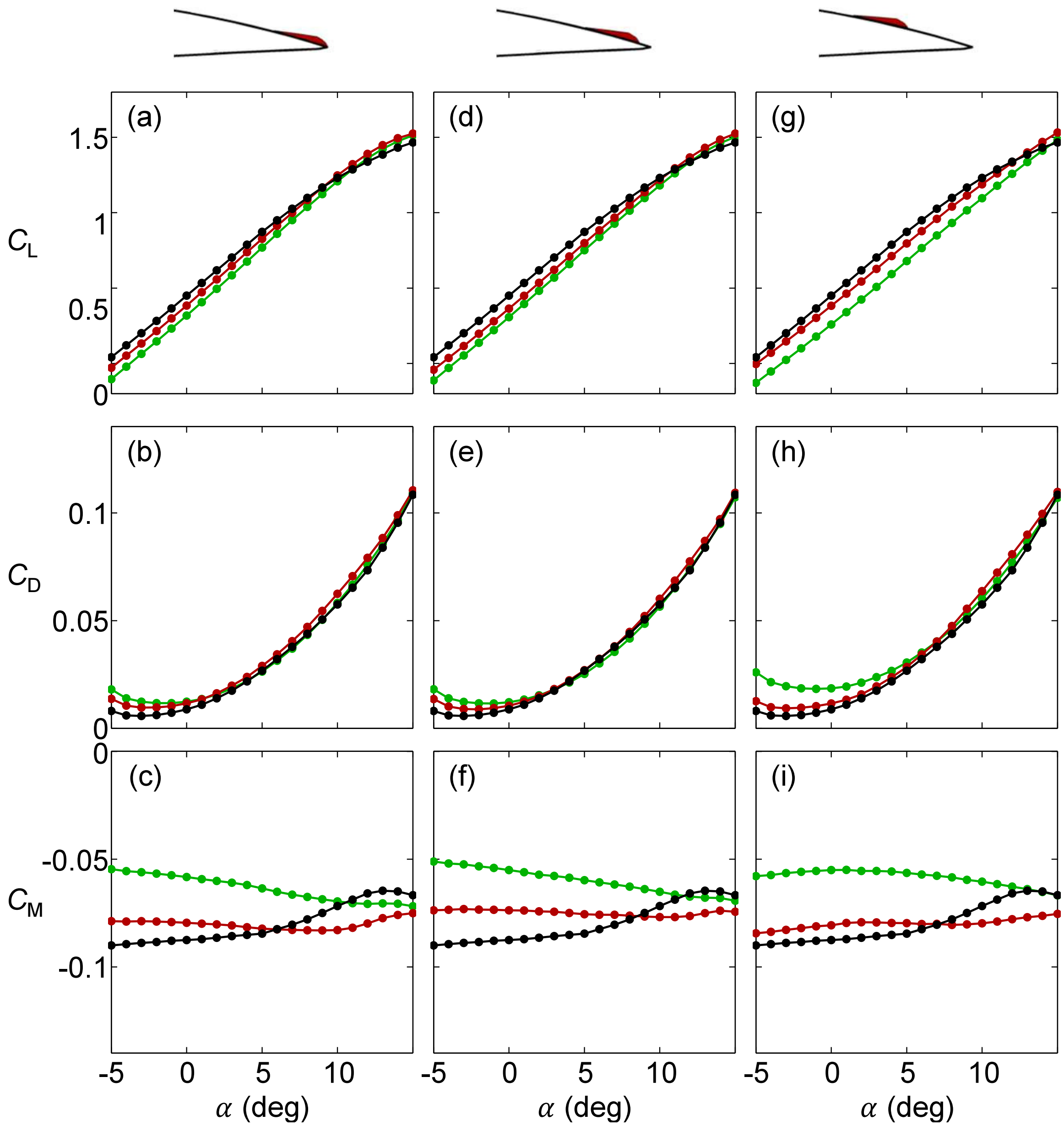

Figure 4.7: Variation of C_L (a,d,g), C_D (b,e,h), and C_M (c,f,i) when only the SS actuator is present and installed at $x_{SS}/c = 0.98$ (a-c) , 0.95 (d-f), and 0.83 (g-i). Colors as in Figure 4.2.

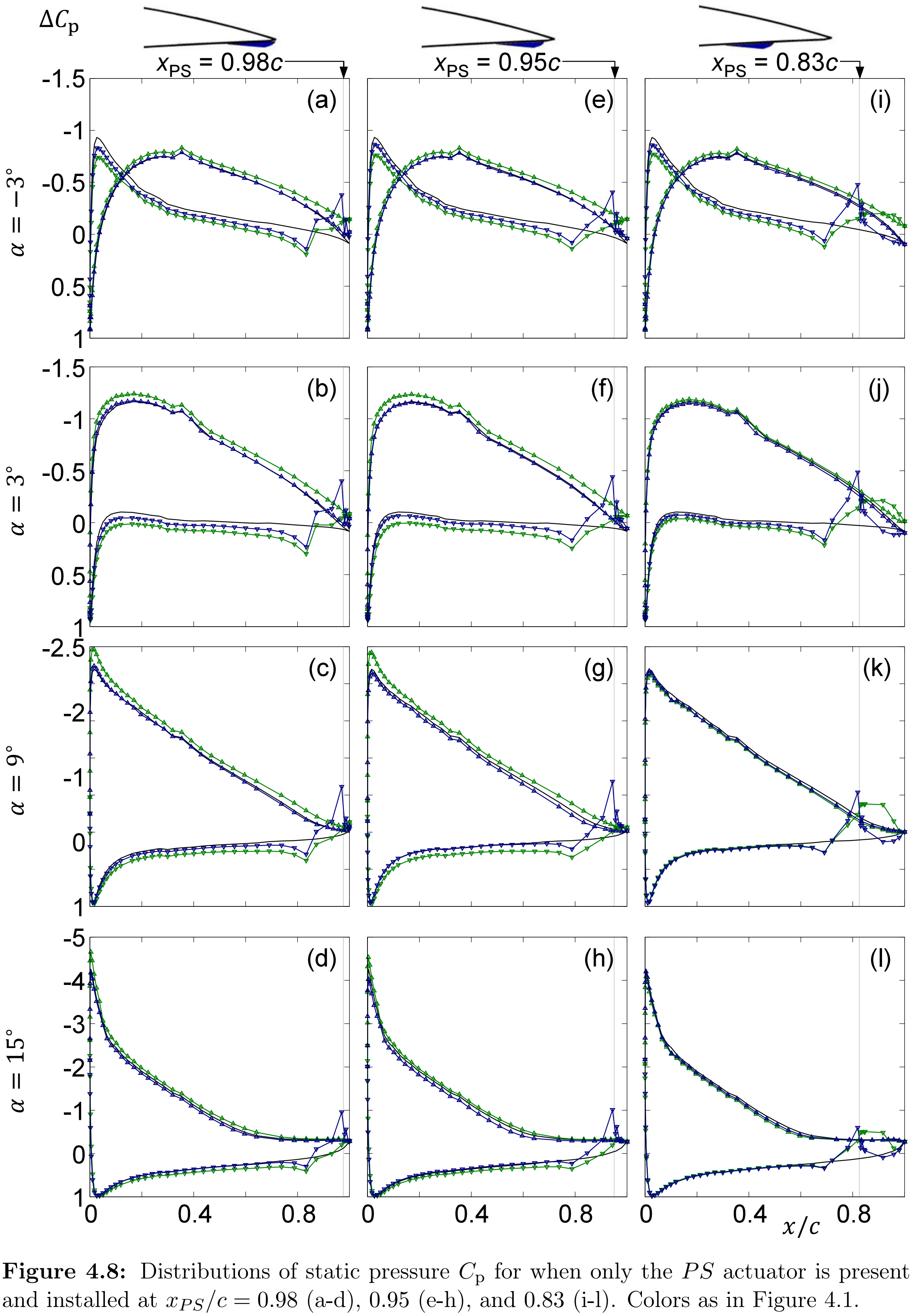

Figure 4.8: Distributions of static pressure C_p for when only the PS actuator is present and installed at $x_{PS}/c = 0.98$ (a-d), 0.95 (e-h), and 0.83 (i-l). Colors as in Figure 4.1.

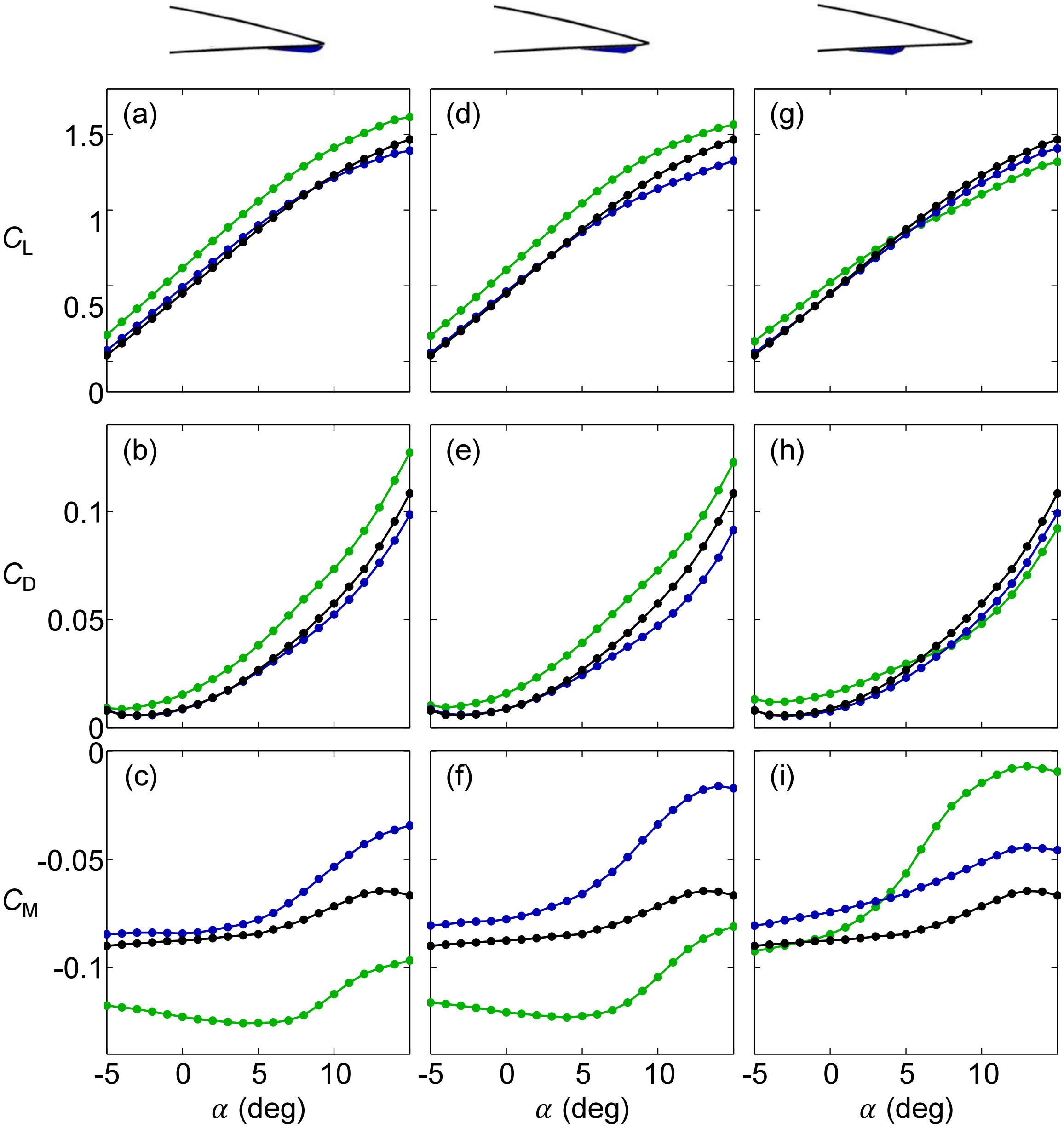

Figure 4.9: Variation of C_L (a,d,g), C_D (b,e,h), and C_M (c,f,i) when only the PS actuator is present and installed at $x_{PS}/c = 0.98$ (a-c), 0.95 (d-f), and 0.83 (g-i). Colors as in Figure 4.2.

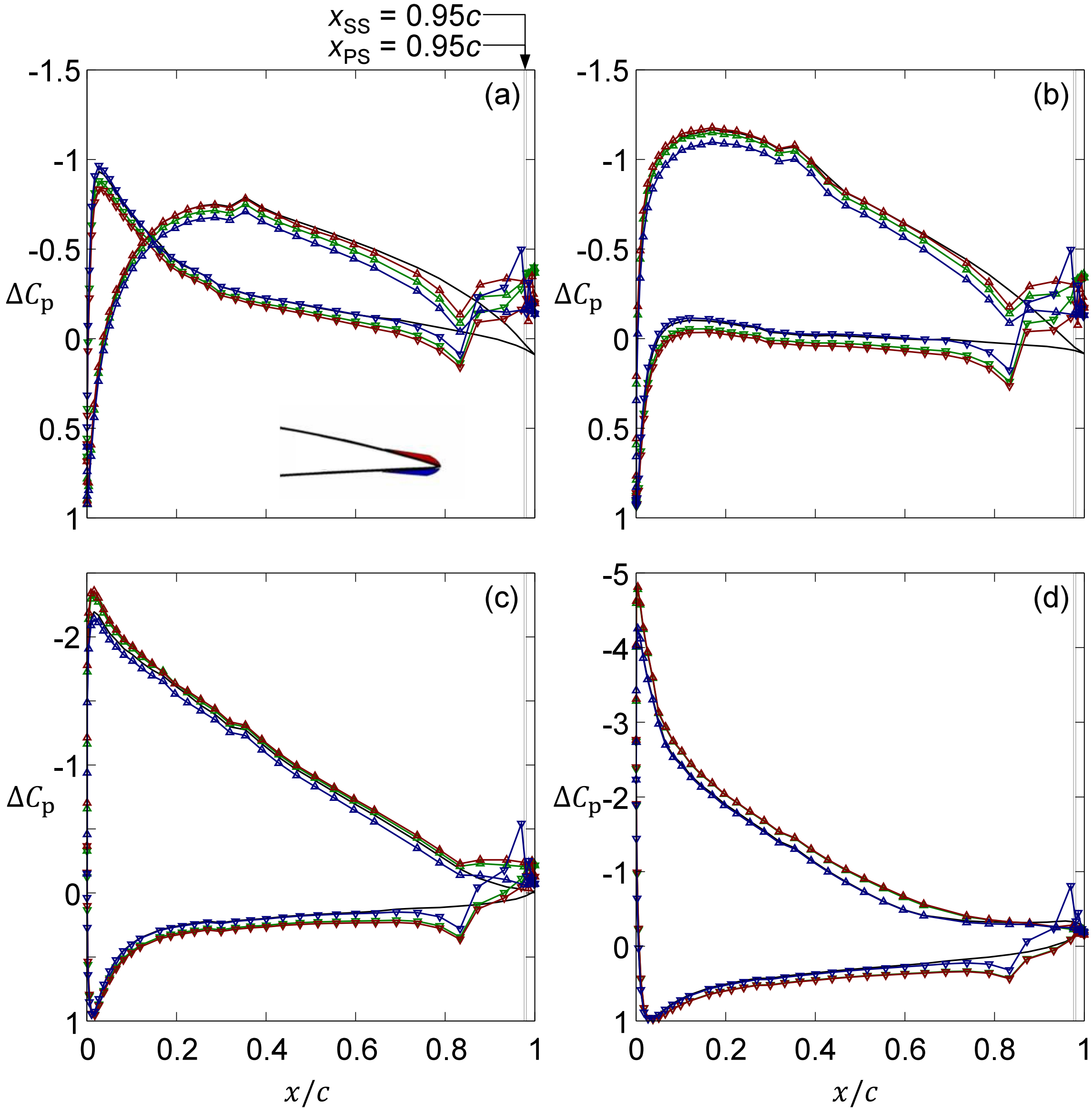

Figure 4.10: Distributions of static pressure C_p for the configuration in which both actuators are mounted flush with the trailing edge [$x_{SS} = 0.95c$, $x_{PS} = 0.95c$] for $\alpha = -3^\circ$ (a), 3° (b), 9° (c), and 15° (d), and actuation level $u_\mathrm{f} = 0$ (▲), 1 (▲), and -1 (▲). Corresponding C_p for the smooth airfoil (▬).

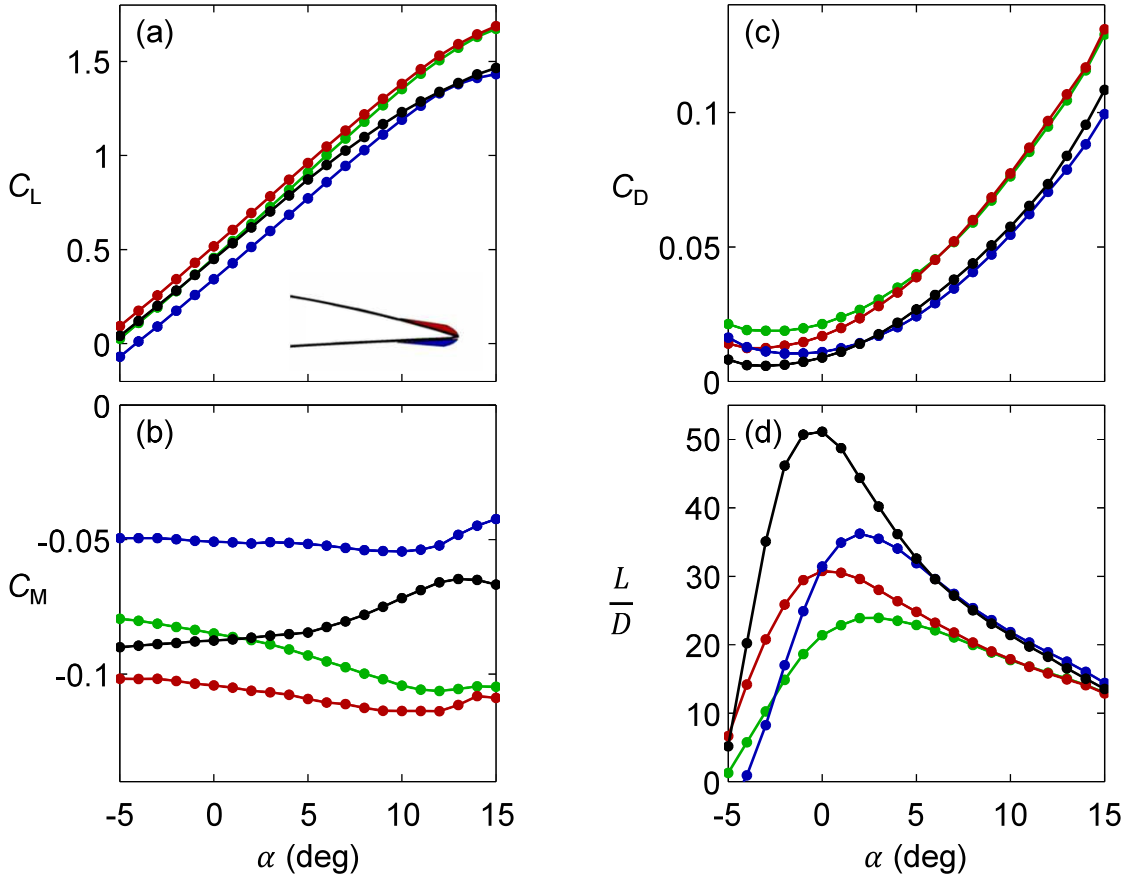

Figure 4.11: Variation of (a) C_L, (b) C_M, (c) C_D and (d) L/D with α for the smooth airfoil (━) and modified[$x_{SS} = 0.95c$, $x_{PS} = 0.95c$] airfoil with $u_f = 0$ (●), 1 (●), and -1 (●).

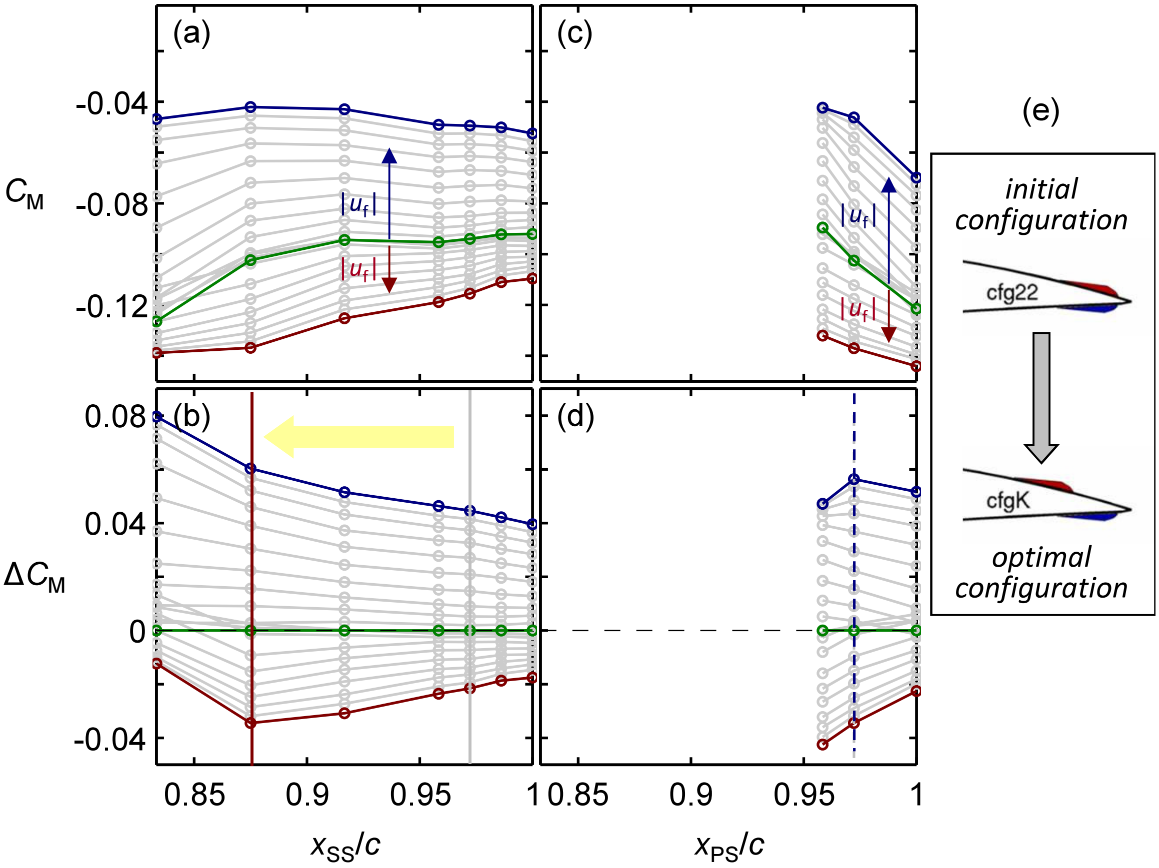

Figure 4.12: Variation of (a) C_M and (b) ΔC_M with x_{SS} for $x_{PS} = 0.98$. Variation of (c) C_M and (d) ΔC_M with x_{PS} for $x_{SS} = 0.88$. Colors as in Figure 4.2. (e) Schematic comparison of initial and optimal configurations.

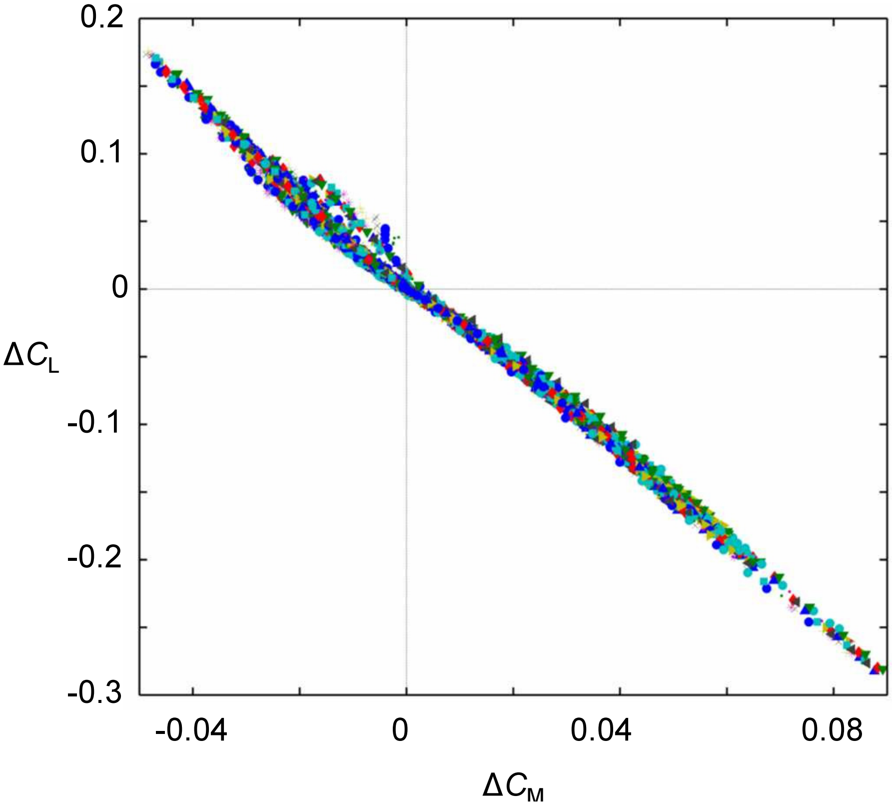

Figure 4.13: Variation of ΔC_L with ΔC_M for all recorded data: $0.83 < x_{SS} < 1$, $0.96 < x_{PS} < 1$, $-5^\circ < \alpha < 15^\circ$, and $-1 < u_\mathrm{f} < 1$.

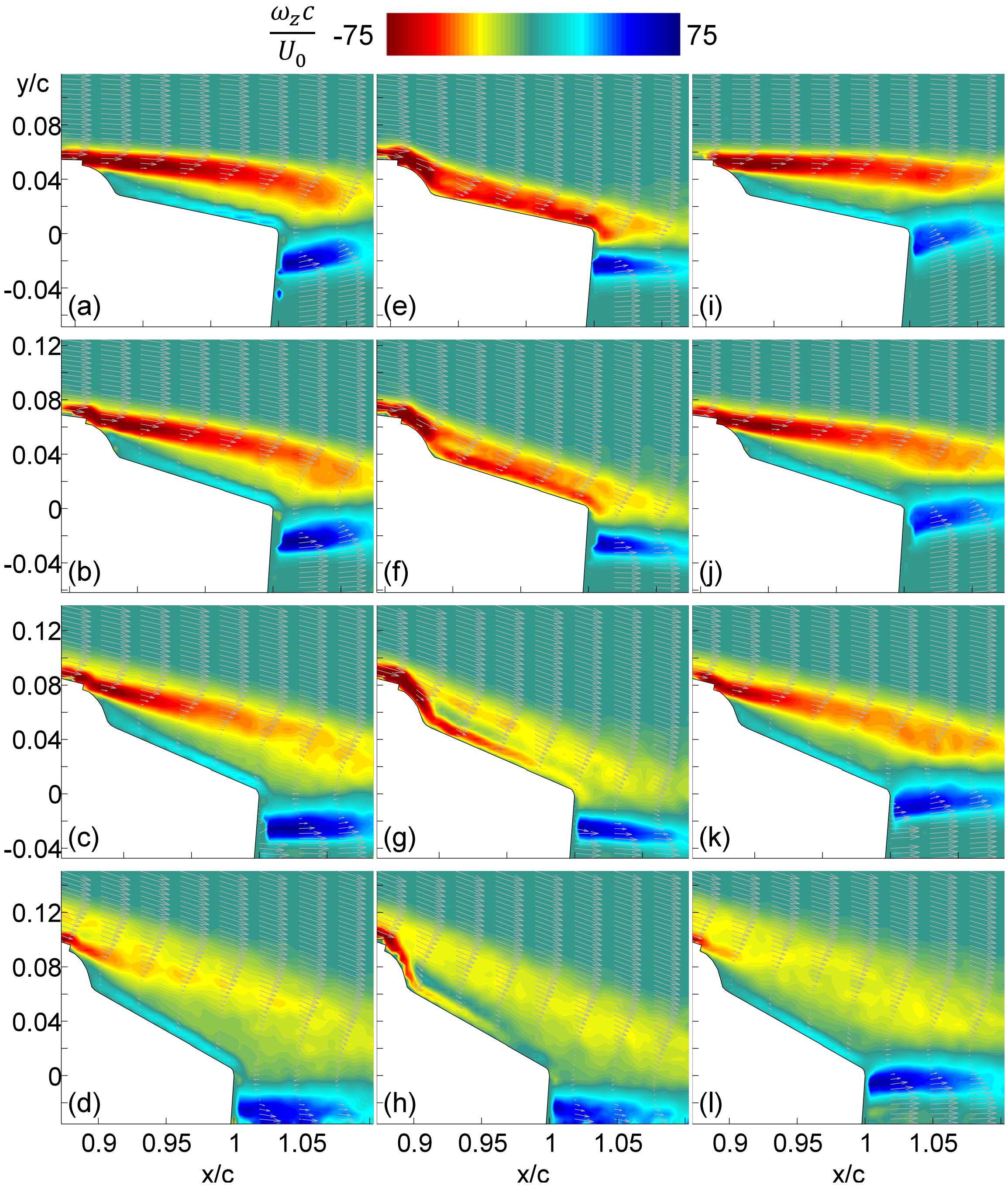

Figure 4.14: Raster plots of the time-averaged spanwise vorticity $\omega_z c/U_0$ at $\alpha = -3°$ (a,e,i), 3° (b,f,j), 9° (c,g,k), and 15° (d,h,l) with $u_\mathrm{f} = 0$ (a-d), 1 (e-h), and -1 (i-l).

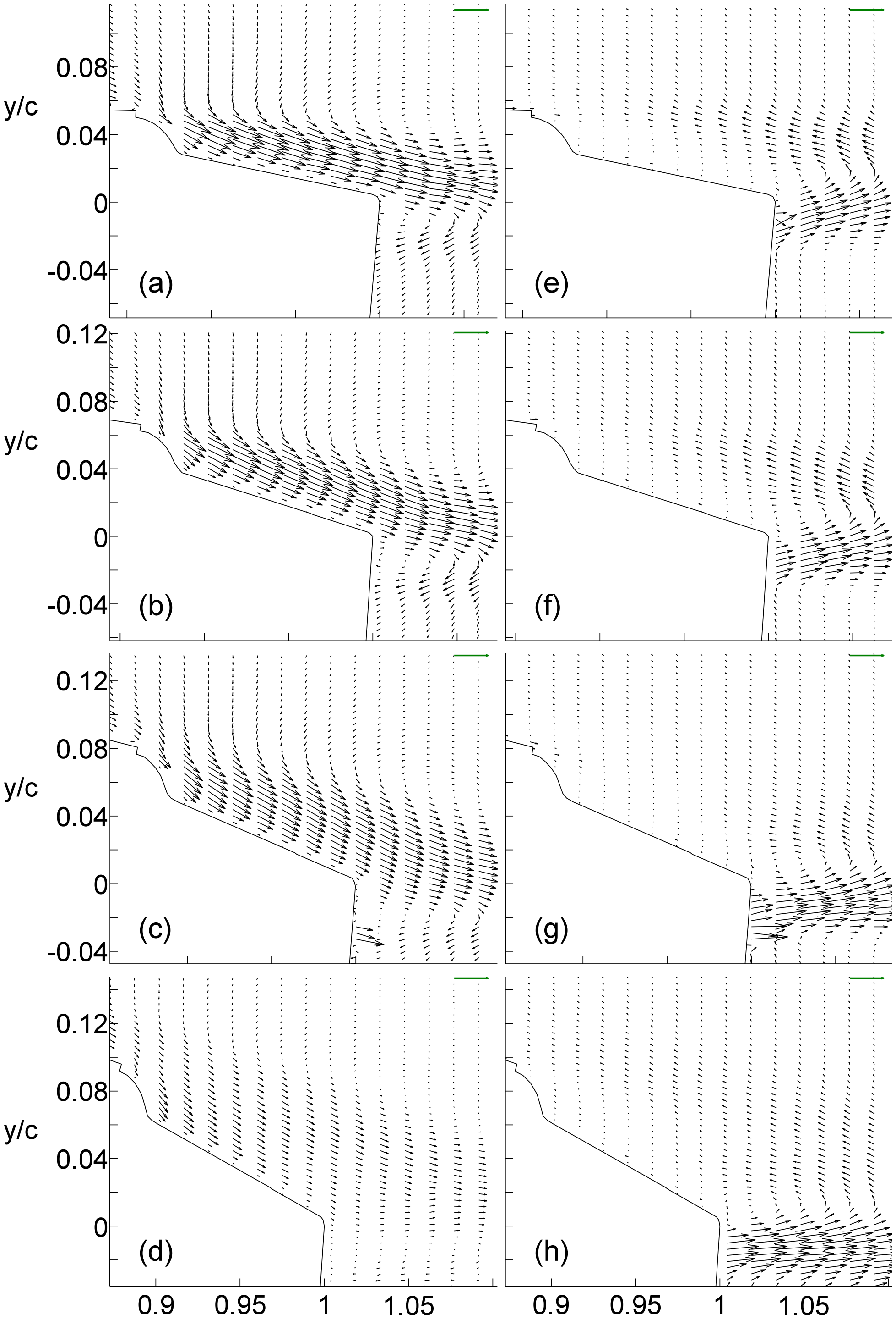

Figure 4.15: Maps of time-averaged residual velocity (vector difference between actuated and unactuated flows) at $\alpha = -3°$ (a,e), $3°$ (b,f), $9°$ (c,g), and $15°$ (d,h) with $u_{\mathrm{f}} = 1$ (a-d) and -1 (e-h).

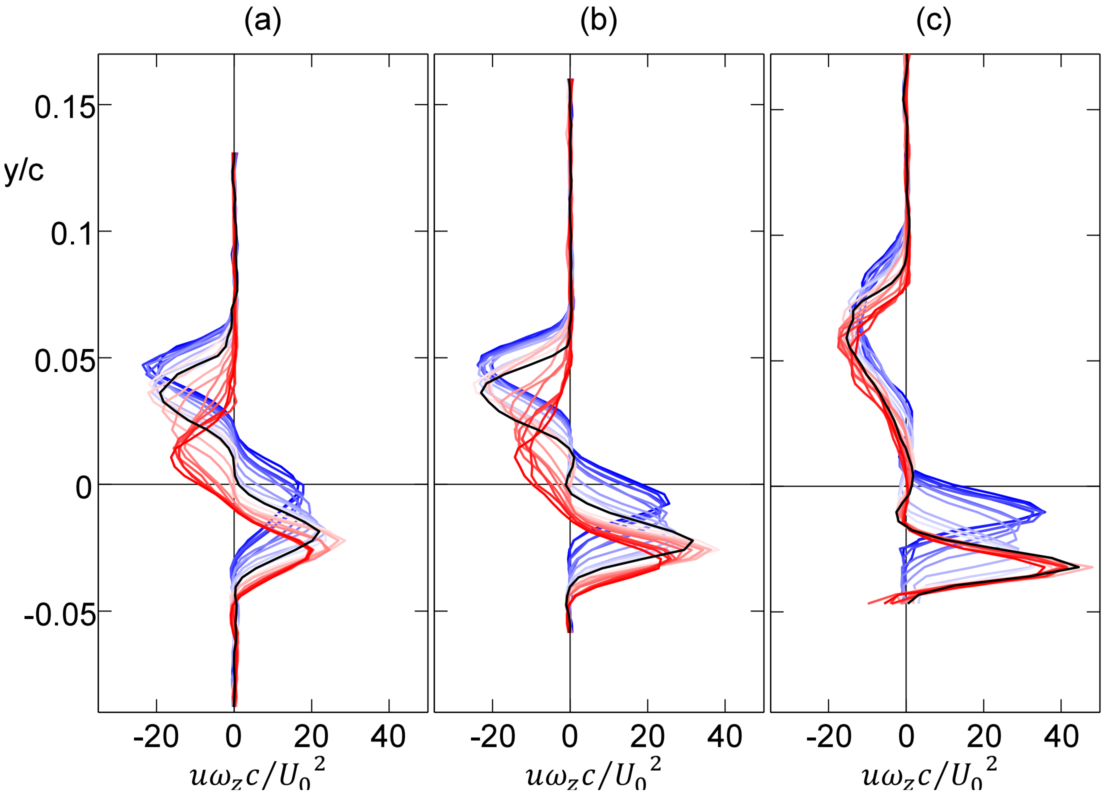

Figure 4.16: Time-averaged cross-stream distributions of vorticity flux in the wake ($x/c = 1.05$) for $-1 < u_\mathrm{f} < 1$ for static model at $\alpha = -5°$ (a), 3° (b), and 15° (c). The traces are colored such that black corresponds to the unactuated flow and increasing levels of red (blue) correspond to increasing levels of SS (PS) actuation.

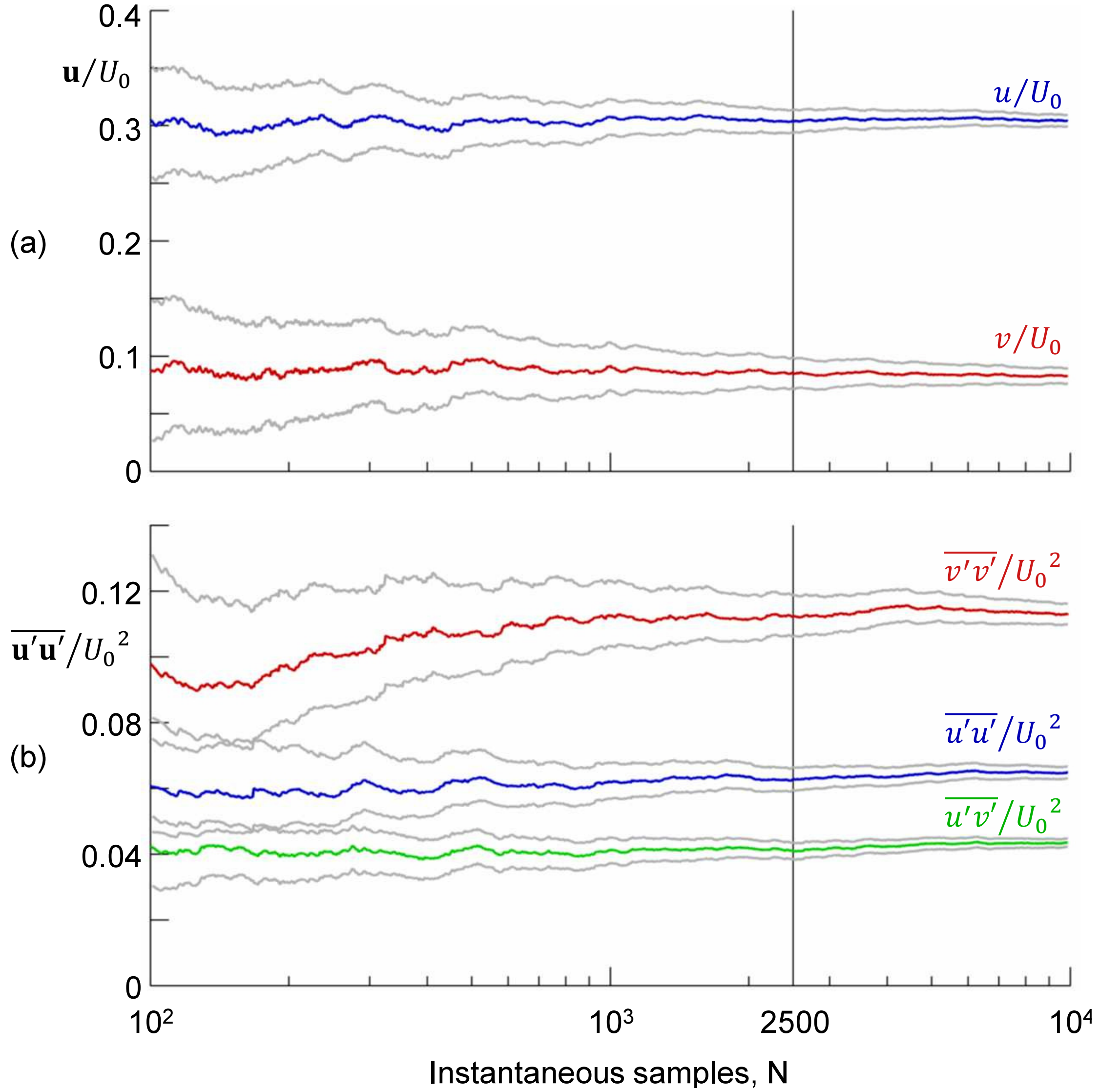

Figure 4.17: Statistical convergence of (a) time-averaged velocity components and (b) time-averaged Reynolds stresses at the point of maximum k in the wake for static airfoil at $\alpha = 3^\circ$ and $u_\mathrm{f} = 0$. The gray lines indicate 95% confidence intervals around the estimates.

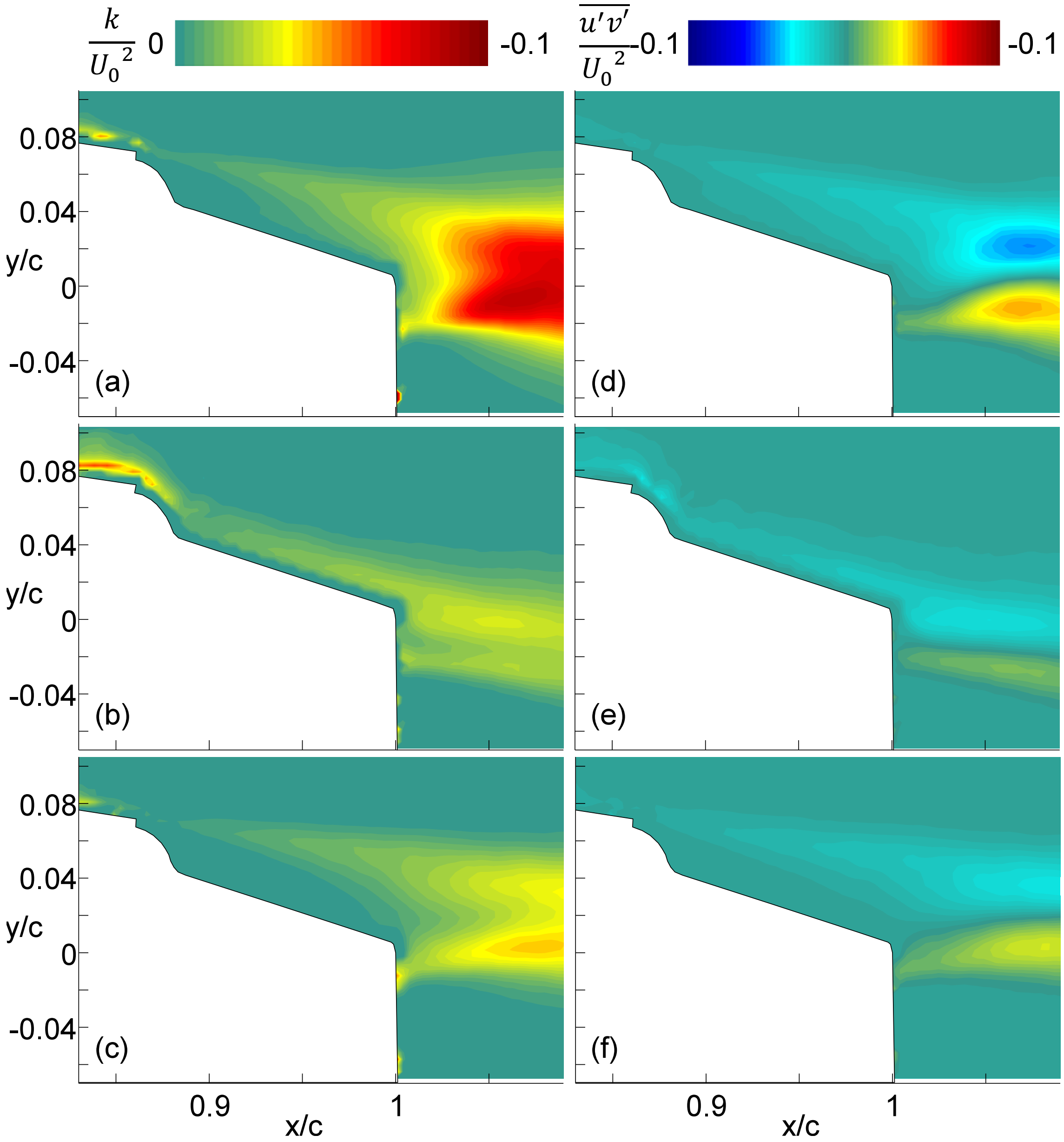

Figure 4.18: Raster plots of (a-c) time-averaged turbulent kinetic energy and (d-f) velocity correlation for static model at $\alpha = 3°$ with $u_\mathrm{f} = 0$ (a,d), 1 (b,e), and -1 (c,f).

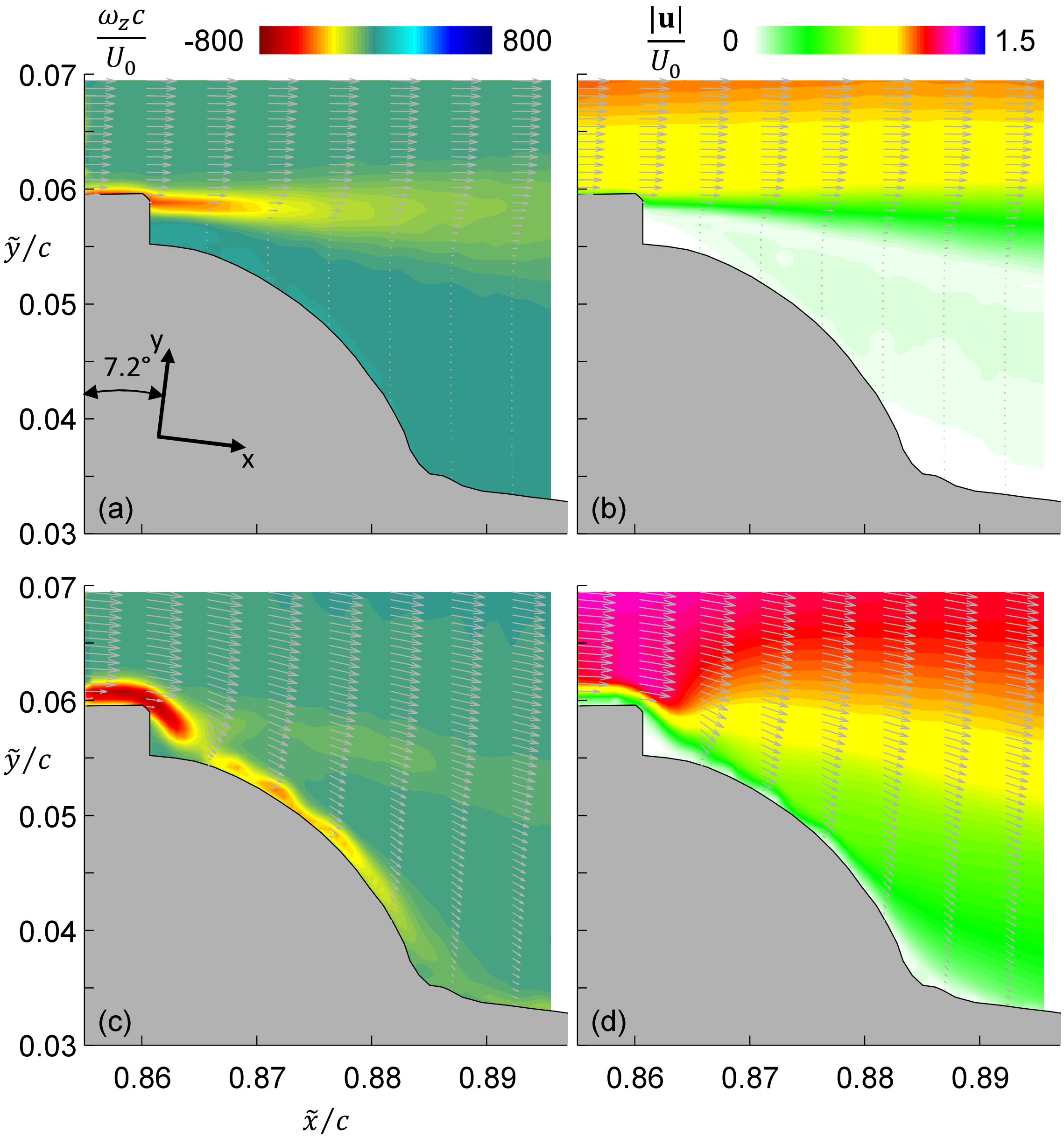

Figure 4.19: Raster plots of (a,c) time-averaged spanwise vorticity and (b,d) velocity magnitude for (a,b) the unforced flow and (c,d) full SS actuation in the region immediately downstream of the SS actuator. View is rotated (in the pitch axis) with respect to the wind tunnel frame by 7.2° as indicated.

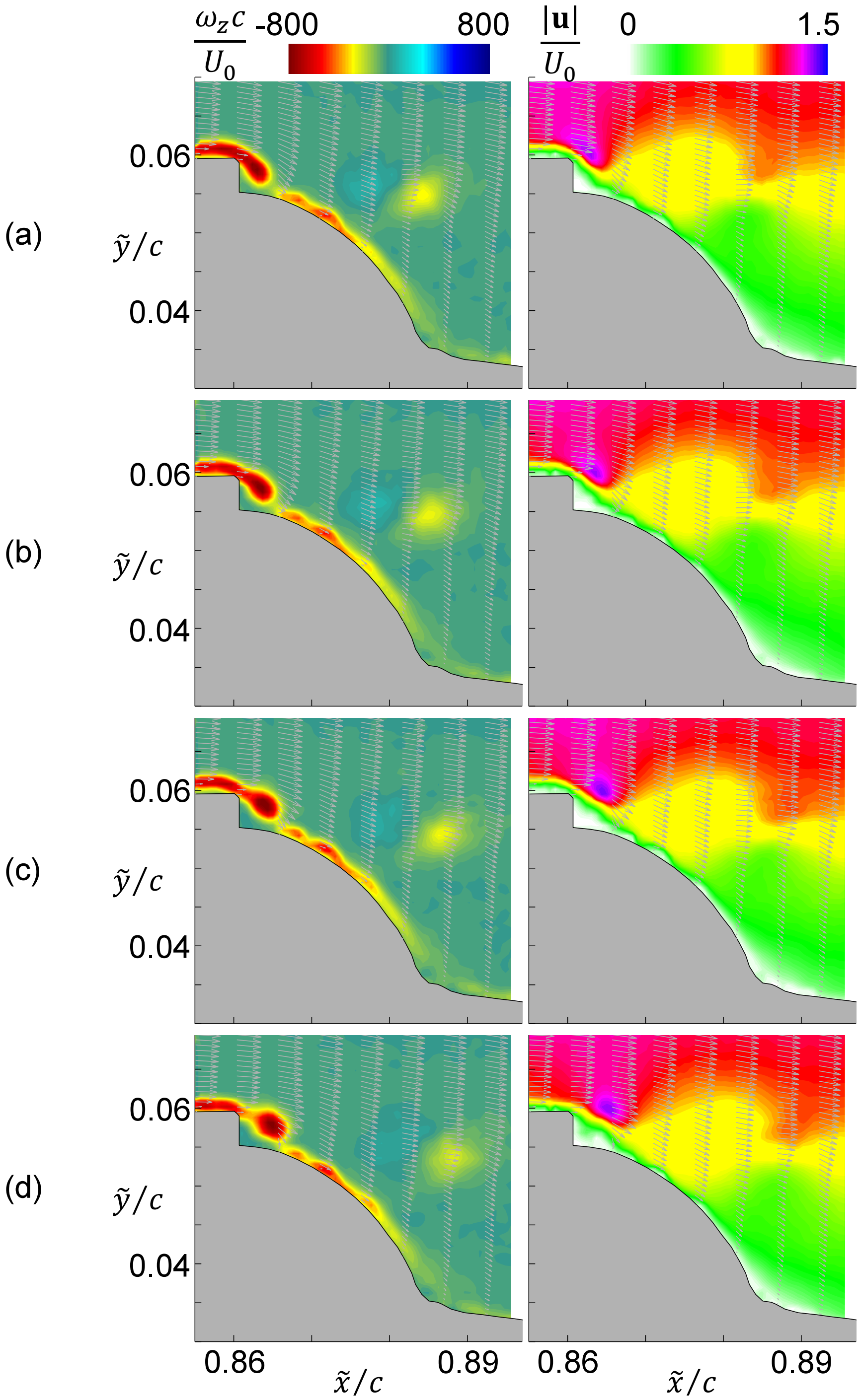

Figure 4.20: Raster plots of phase-averaged spanwise vorticity (left column), velocity magnitude (right column) for 18 equally-spaced phases during the synthetic jet cycle.

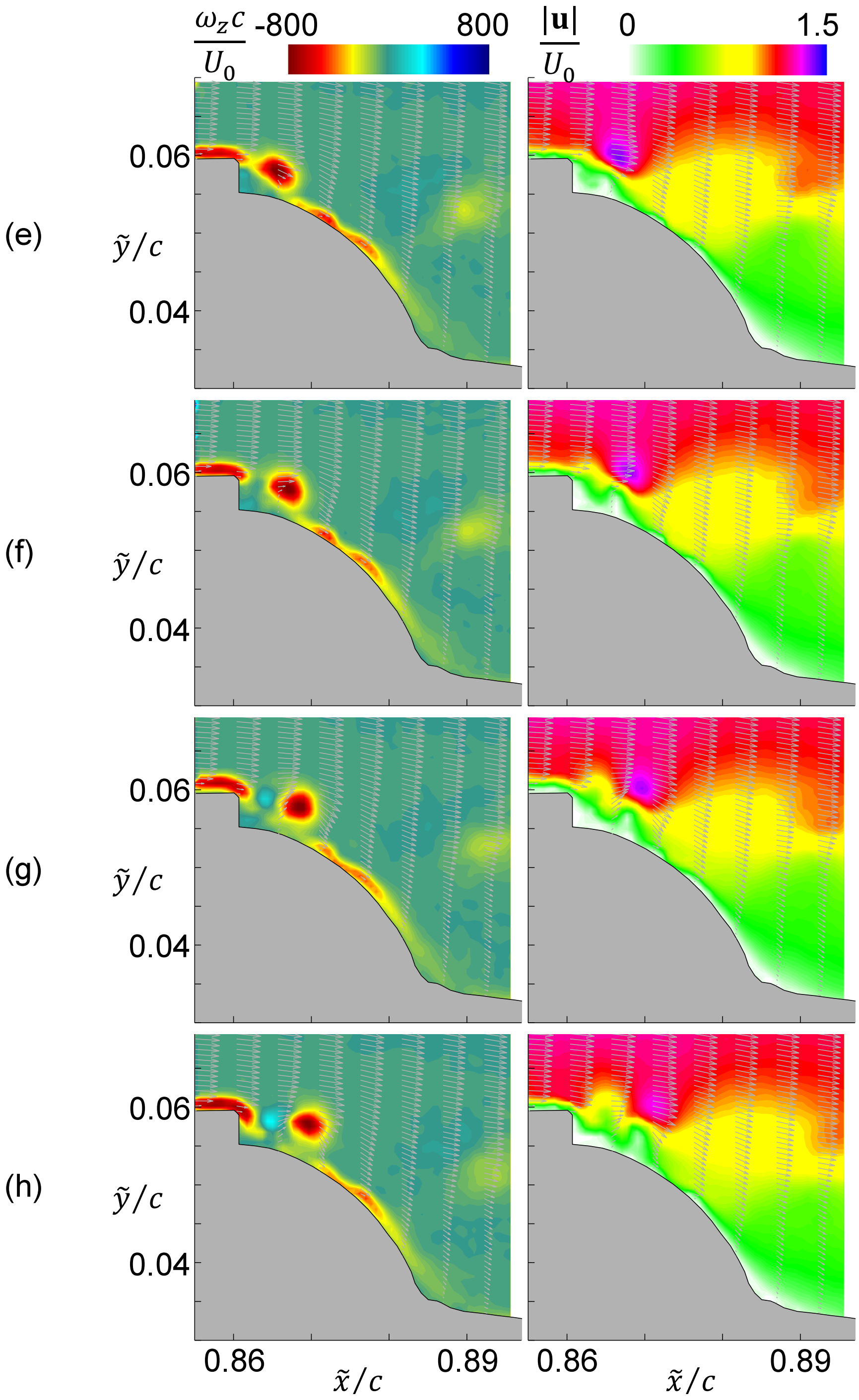

Figure 4.20: (continued)

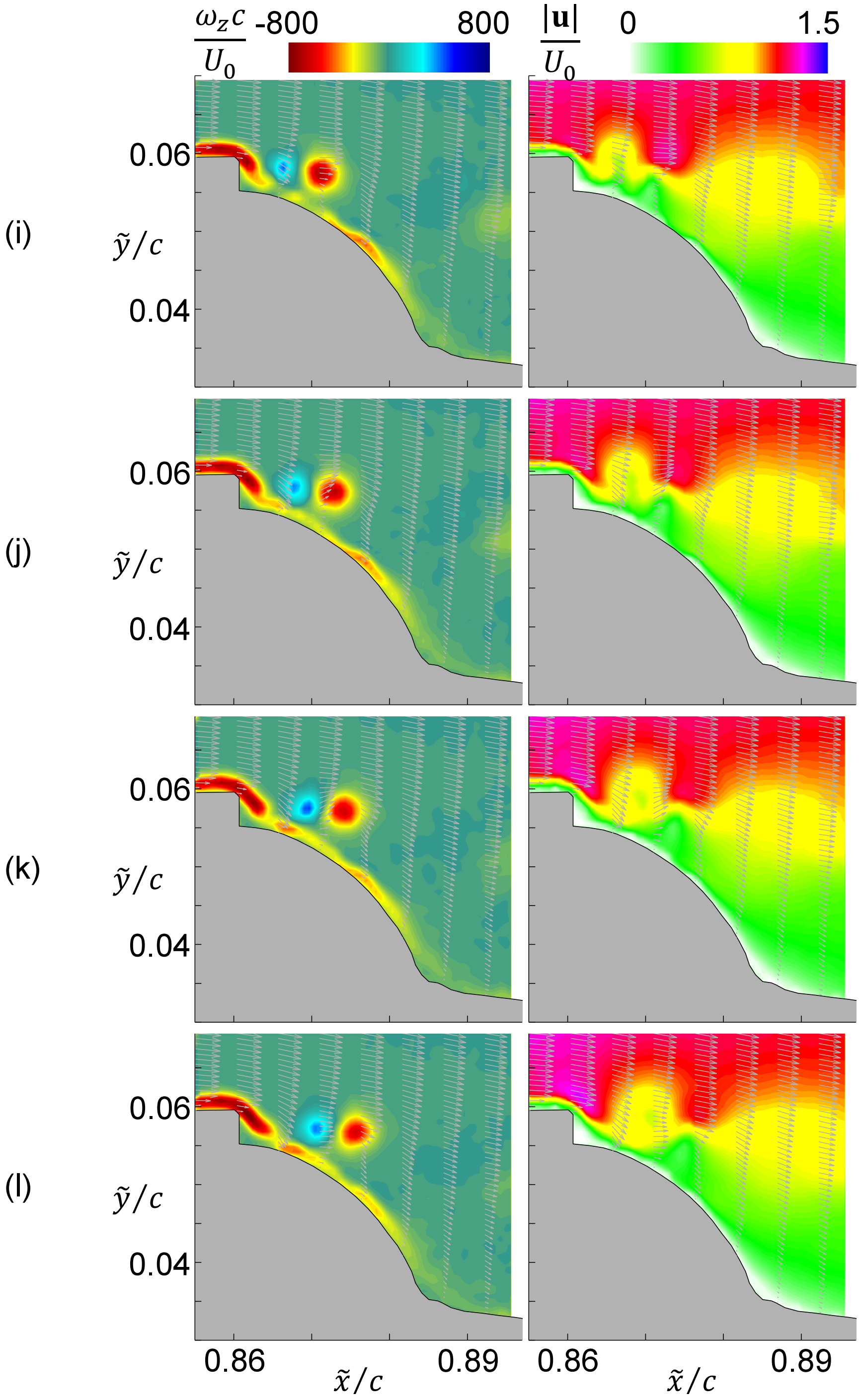

Figure 4.20: (continued)

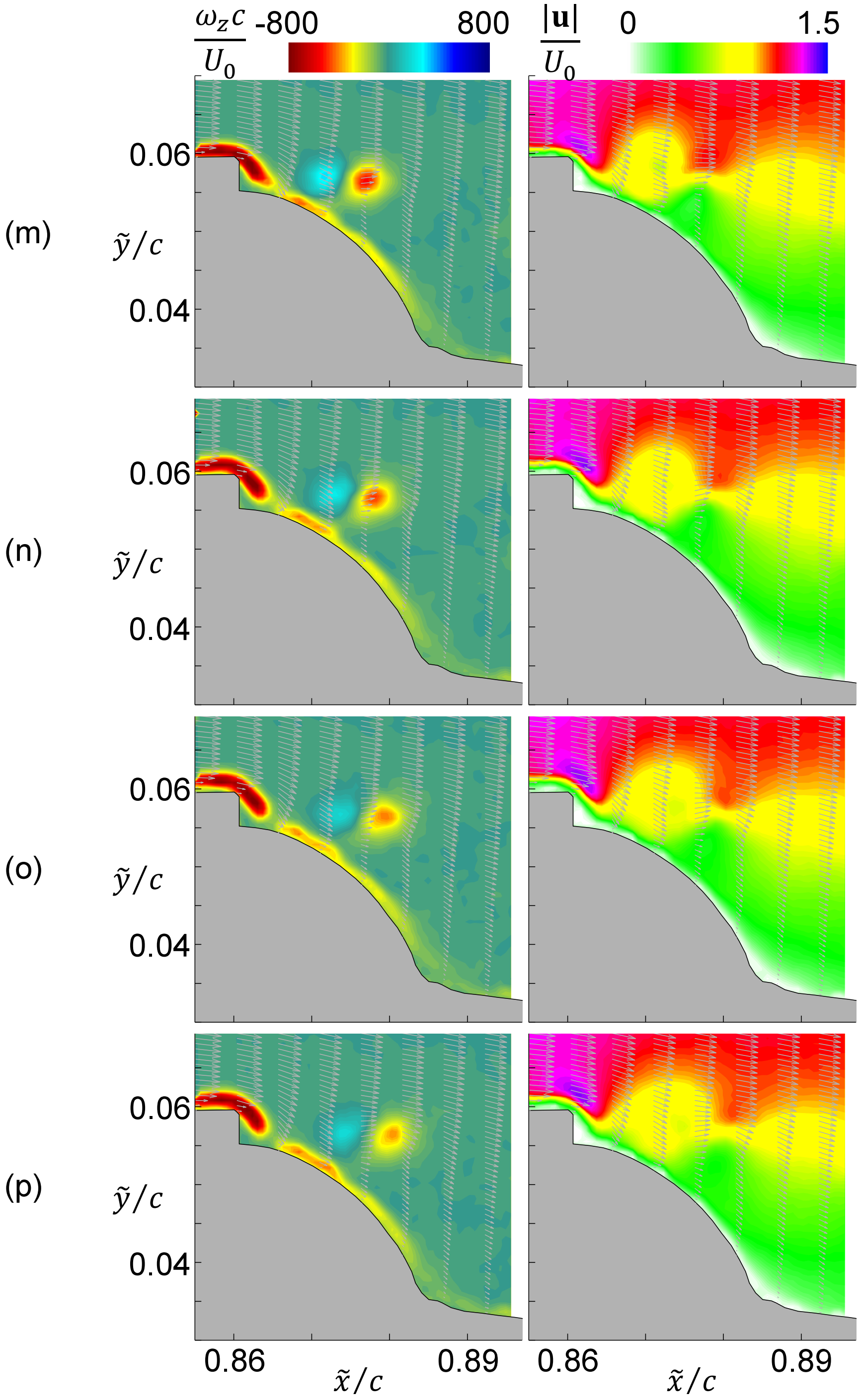

Figure 4.20: (continued)

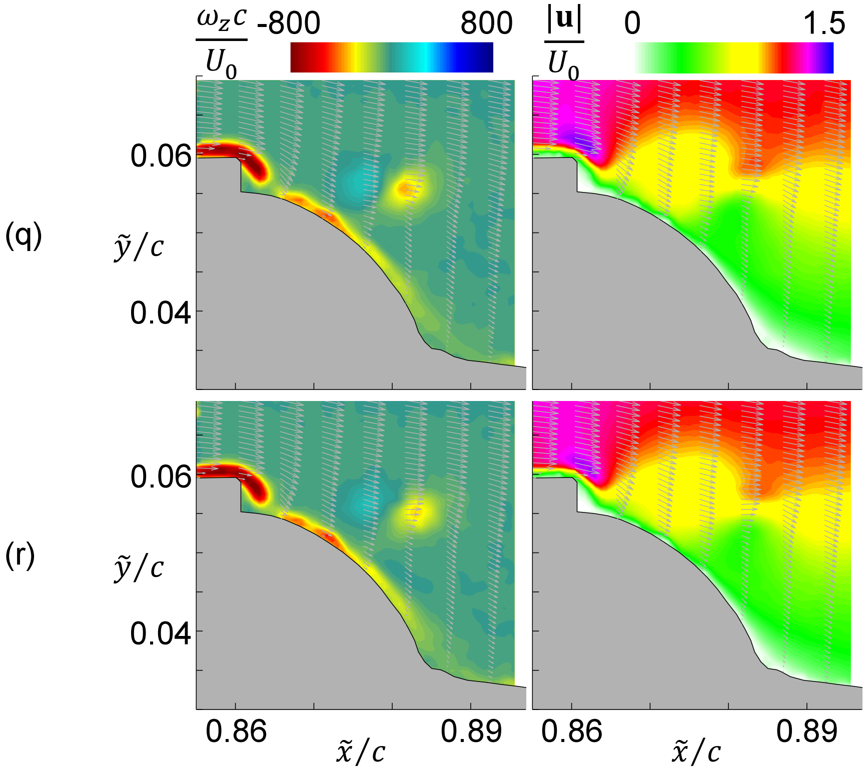

Figure 4.20: (continued)

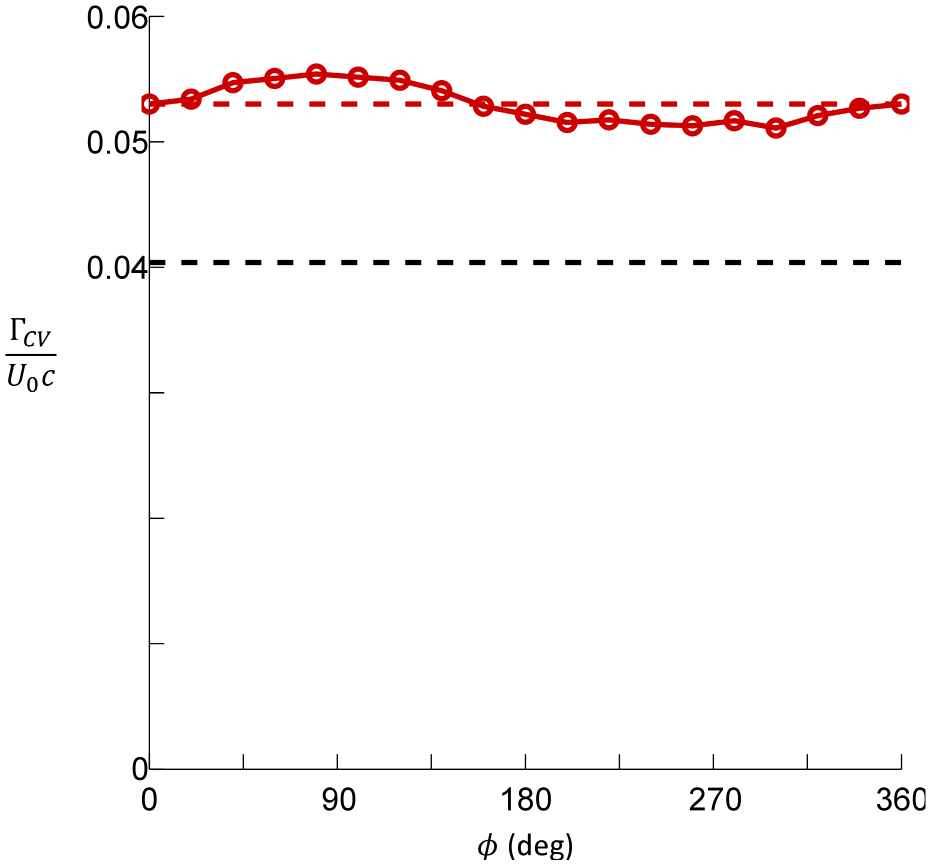

Figure 4.21: Time history of circulation within a volume immediately downstream of the *SS* actuator during the synthetic jet cycle. Dashed lines indicate time-averaged circulation when $u_\mathrm{f} = 0$ (black) and $u_\mathrm{f} = 1$ (red).

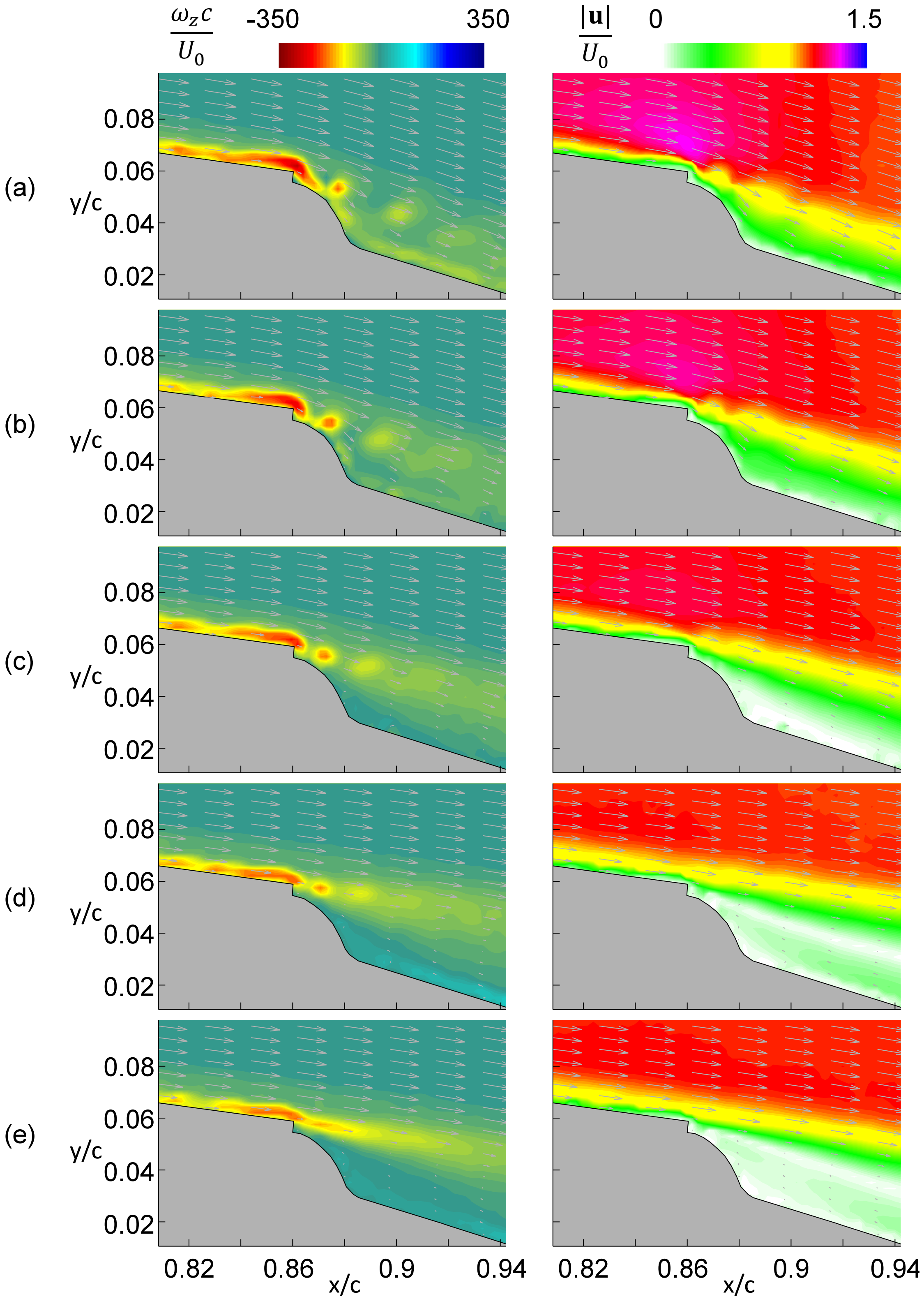

Figure 4.22: Raster plots of phase-averaged spanwise vorticity (left column) and velocity magnitude (right column) for $\phi = 260°$ during the synthetic jet cycle for $u_\mathrm{f} = 1$ (a) 0.75 (b), 0.5 (c), 0.25 (d), and 0 (e).

Chapter V

FLOW RESPONSE TO A STEP INPUT IN ACTUATION

The characteristic time scale associated with the response of the flow to actuation is a crucial parameter for the implementation of real-time control. This chapter discusses a series of experiments in which this time response is investigated using step transitions between the three actuation states, namely unforced ($u_\mathrm{f} = 0$), full SS actuation ($u_\mathrm{f} = 1$), and full PS actuation ($u_\mathrm{f} = -1$). The airfoil response is characterized both in terms of the flow dynamics and the resulting rigid body dynamics. For the former, phase-averaged PIV and surface pressure measurements were recorded following step transitions in actuation command. The PIV measurements were recorded phase-locked to- and at the same frequency as- the synthetic jet ($St_\mathrm{act} = 30.5$). The data are analyzed with an emphasis on vorticity transport and conservation of circulation in the flow. The time-history of aerodynamic forces resulting from the actuation is assessed from force/torque measurements as well as surface pressure data at select points along the airfoil. In addition to the actuation effectiveness, the motion of the airfoil naturally exhibits a strong dependence on the control system parameters which alter the system dynamics as discussed in §5.1.

5.1 Influence of Controller Gain Parameters

As open-loop flow control commands were issued to assess system response to actuation input, α was regulated by operating the pitch servo actuator in closed-loop (i.e., to prevent the model from "flying away" as a result of the flow control inputs). Naturally, as a result of the action of the pitch servo, the resultant time-dependent trajectory depends on the controller parameters. The torque applied to the servo during these maneuvers is given by:

$$\tau_s(t) = k_\mathrm{loop}\left[k_\mathrm{d}\dot{\alpha} + k_\mathrm{p}(\alpha - \alpha_0) + k_\mathrm{i}\int_0^t (\alpha - \alpha_0)\,dt\right] + k_\mathrm{a}\ddot{\alpha} \tag{5.1}$$

where $\alpha_0 = 3^\circ$ is the (constant) commanded pitch angle, k_loop is the "loop gain", $\{k_\mathrm{p}, k_\mathrm{i}, k_\mathrm{d}\}$ are the usual PID gains, and k_a is an acceleration feedback gain. As discussed in §3.2, acceleration feedback is used to compensate for the large inertia of the wind tunnel model. A series of experiments were conducted in which $SS \rightarrow PS$ and $PS \rightarrow SS$ flow control actuation transitions were issued in open loop for several values of k_{loop} and k_{a} (k_{p}, k_{i}, and k_{d} were kept constant).

Figure 5.1a shows the pitch trajectory following a $SS \rightarrow PS$ transition for the different controller gain combinations. For the “weakest” controller ($k_{\text{a}} = 0.5$, $k_{\text{loop}} = 5$), the pitch excursion is greater than 15° and the model is not settled back to α_0 even after $300T_{\text{conv}}$. In contrast, for the “stiffest” controller ($k_{\text{a}} = 0$, $k_{\text{loop}} = 80$), the excursion is kept to less than 1° and settles out within $200T_{\text{conv}}$. Similarly, Figure 5.1b shows a series of pitch trajectories following a $PS \rightarrow SS$ transition for the same range of controller gains. As in the previous case, the pitch excursion varies between 1° and 15° depending on the controller gains. For both the $SS \rightarrow PS$ and $PS \rightarrow SS$ transitions, at the highest loop gains, the pitch trajectory exhibits higher frequency oscillations having a period of $3T_{\text{conv}}$. These correspond to an instability in the system which is only visible with a very stiff controller.

Another detail of note in Figure 5.1 is that in all cases the airfoil motion occurs on the order of tens to hundreds of convective time scales. It is important to note that this time scale is entirely dependent on the large inertia of the experimental model relative to the pitching moment provided by the actuated flow. On an actual flight vehicle the inertia would be much lower. The crucial point, however, is that this response time is *not* caused by a limitation in the flow control- in fact, as demonstrated in the present chapter, the change in aerodynamic forces occurs in less than ten convective time scales.

In order to maximize the PIV data acquisition rate, it was necessary to make the recovery time as short as possible, which corresponds (as indicated in Figure 5.1) to setting $k_{\text{a}} = 0$ and k_{loop} as large as possible. However, the instability observed for the two highest values of k_{loop} was avoided in the interest of isolating the unsteady effect of the actuators from the controller dynamics as much as possible. Therefore, for all of the experiments discussed in the remainder of this chapter, the controller gains were set to the intermediate level, ($k_{\text{a}} = 0$, $k_{\text{loop}} = 30$), which corresponds to the cyan curves in Figure 5.1.

5.2 Transition from Unforced to Full Actuation (SS or PS)

5.2.1 Time Histories of α, C_L, C_M and p

This first section considers a step transition from the unforced state to and full actuation (either $u_\mathrm{f} = 1$ or $u_\mathrm{f} = -1$) and back to the unforced state. The four transitions are denoted as $0 \rightarrow SS$, $SS \rightarrow 0$, $0 \rightarrow PS$, and $PS \rightarrow 0$. In all cases, the controller is commanded to hold the airfoil steady at $\alpha_0 = 3°$ using the pitch servo actuator as the flow control actuation is applied in open loop. Starting with the stationary model at α_0 with $u_\mathrm{f} = 0$, actuation is applied at $t = 0$ and then terminated at $t = 328T_\mathrm{conv}$. The latter time was chosen to allow the model to return to steady state at α_0.

The resulting pitch trajectory $\alpha(t)$, lift increment $\Delta C_\mathrm{L}(t)$, and moment increment $\Delta C_\mathrm{M}(t)$ (all phase-averaged over 100 cycles) are shown in Figure 5.2 where the $0 \rightarrow SS/SS \rightarrow 0$ and $0 \rightarrow PS/PS \rightarrow 0$ transitions are indicated using red and blue lines, respectively. Corresponding levels of ΔC_L and ΔC_M for the same α for continuous actuation at the same u_f are obtained from a look up table and plotted (in black) on top of the unsteady results. Following the $0 \rightarrow SS$ transition, the airfoil experiences a sudden decrease in C_M (Figure 5.2c) which causes the airfoil to accelerate nose-down in pitch (Figure 5.2a). In response to this change in α, the controller applies a counteracting torque through the servo actuator to return the airfoil to the desired α_0. Upon termination of the SS actuation ($t = 328T_\mathrm{conv}$), the pitching moment on the airfoil increases to the unforced level and the model which is now trimmed by the servo actuator in response to $u_\mathrm{f} = 1$ accelerates nose-up before the controller once again returns the model to $\alpha = 0°$. It should be noted that the pitch excursions ($\pm 1°$) and the overall shape of the trajectory depend on the controller gains (cf. §5.1).

The changes in C_M resulting from the $0 \rightarrow SS/SS \rightarrow 0$ actuation are accompanied by changes in C_L (Figure 5.2b), both of which exhibit rapid adjustments to the actuation level followed by slower changes as a result of the induced changes in angle of attack. These variations are most significant for $0 < t/T_\mathrm{conv} < 100$ and $328 < t/T_\mathrm{conv} < 428$. It is important to note that while C_L varies almost linearly with α (cf. Figure 4.2a), C_M is only weakly dependent on α which is beneficial from the standpoint of closed-loop flow control (cf. Chapter 6).

The changes in α, ΔC_{L}, and ΔC_{M} for the transitions $0 \rightarrow PS/PS \rightarrow 0$ (blue curves) are similar to the changes associated with the $0 \rightarrow SS/SS \rightarrow 0$ transitions. However, PS actuation effects nose-up C_{M} and reduction in C_{L} and the effects are stronger than for the SS actuation (cf. Chapter 4). As a result of the larger ΔC_{M} effected by the PS actuators, the pitch excursion following the transient ($\Delta\alpha = 1.8°$) is larger than the corresponding change following the SS transition.

As noted in §2.5, the bandwidth of the C_{L} and C_{M} measurements is limited to approximately 20 Hz, which corresponds to a period of $3.3T_{\mathrm{conv}}$. In order to assess the transient response of the flow over the airfoil on such short time scales, surface pressure is monitored at four streamwise positions along the surface of the airfoil using high-frequency pressure sensors (cf. §2.4.2). Figure 5.3a-d show the time history of pressure changes ΔC_{p} (relative to the time-averaged pressure at $\alpha = \alpha_0$ and $u_{\mathrm{f}} = 0$) at the leading edge (5.3a), on the suction surface at $x/c = 0.39$ (5.3b), on the pressure surface at $x/c = 0.4$ (5.3c), and at the trailing edge (5.3d). As one would expect based the time histories of ΔC_{L} and ΔC_{M} during the transient actuation (cf. Figure 5.2), for all time except the first few T_{conv} following each transition, ΔC_{p} tracks the same trend as the corresponding static values. The slight offsets between the static and dynamic traces are caused by fluctuating pressure inside the airfoil cavity to which the sensors are referenced. The most dramatic unsteady effects are evident at the trailing edge sensor which exhibits suction peaks of $\Delta C_{\mathrm{p}} = -0.31$ and -0.37 following onset and termination, respectively, of the PS actuator (5.3d). These momentary suction peaks- which occur at $0.26T_{\mathrm{conv}}$ following the onset and and $0.4T_{\mathrm{conv}}$ following the termination- are consistent with the passage of the large vortical structures associated with the transients. The same peaks are not present for the SS actuator transitions, ostensibly because the SS actuator is located so far upstream from the trailing edge port ($0.14c$, compared to $0.05c$ for the PS actuator). While the trailing edge pressure converges to the quasi-steady value with in $1 - 2T_{\mathrm{conv}}$, for the upstream ports, convergence occurs over $2 - 4T_{\mathrm{conv}}$ following each transition.

Table 5.1: Phase-averaged PIV measurements were recorded during the transition time $0 < t/T_{\text{conv}} < 1.94$ with phase increments of $\Delta t = 0.033T_{\text{conv}}$.

sub-figure	t/T_{conv}	sub-figure	t/T_{conv}	sub-figure	t/T_{conv}
a	0	h	0.23	o	0.46
b	0.03	i	0.26	p	0.49
c	0.07	j	0.3	q	0.52
d	0.10	k	0.33	r	0.56
e	0.13	l	0.36	s	1.94
f	0.16	m	0.39		
g	0.2	n	0.43		

5.2.2 The Unsteady Trailing Edge Flow Field

The response of the flow to the transient actuation was further characterized with phase-locked PIV measurements in the near wake. Figures 5.4 and 5.5 show raster plots of the normalized spanwise vorticity $\hat{\omega} = \omega_z c/U_0$, and velocity magnitude $\hat{u} = |\mathbf{u}|/U_0$ following the transitions $0 \to SS$ and $SS \to 0$, respectively. The field of view is within the domain $0.85 < x/c < 1.07$ and $-0.09 < y/c < 0.13$ [the coordinate systems is defined such that the trailing edge is located at $(x/c, y/c) = (1, 0)$ when $\alpha = 3°$].

At the onset of the transition $0 \to SS$ ($t = 0$, Figure 5.4a), the flow nearly corresponded to the time-averaged unforced flow (Figure 5.5s). The slightest evidence of the oncoming actuation is evident in the necking of the shear layer immediately downstream of the jet exit at $\mathbf{x}/c = (0.87, 0.07)$. At $t = 0.03T_{\text{conv}}$, the shear layer pinches off (Figure 5.4b) and a CW vorticity concentration rolls up and is advected downstream (Figure 5.4c-e). Meanwhile the upstream portion of the shear layer attaches around the Coanda surface downstream of the jet exit. Because the PIV recording is phase-locked to the synthetic jet cycle, the individual vortices emanating from the jet are aliased and appear "frozen" downstream of the actuator. At $t = 0.13T_{\text{conv}}$, the first two synthetic jet vortices are clearly visible (Figure 5.4e). As the large CW vortex grows and passes the trailing edge, a shear layer reforms downstream of the actuator, as the flow attaches along the Coanda surface and the surface of the airfoil. By $t = 0.46T_{\text{conv}}$ (Figure 5.4o), the passage of the large vortex is complete and the flow transitions to the quasi-steady forced state ($t = 1.94T_{\text{conv}}$, Figure 5.4s). As noted in §4.4, the upper portion of the bifurcated shear layer actually results from the train of CW vortices emanating from the synthetic jet.

The transition $SS \to 0$ begins with $u_\mathrm{f} = 1$ (Figure 5.5a) in which the flow is attached to the downstream edge of the actuator and along the airfoil to the trailing edge. Following the termination of SS actuation, the vorticity layer passing over the jet exit begins to detach from the Coanda surface ($0.03 < t/T_\mathrm{conv} < 0.1$, Figure 5.5b-d). As this vorticity layer pulls off the surface, a region of stagnant fluid develops at the juncture between the actuator and the airfoil surface at $\mathbf{x}/c = (0.88, 0.04)$. Throughout this detachment process, pulses of CW vorticity are evident in the shear layer with spacing that is consistent with the characteristic period of the (now-inactive) synthetic jet. It appears that these structures are triggered by residual ringing of the piezo disk in the actuator cavity following termination of the actuation and persist though Figure 5.5l. The flow becomes fully separated at the trailing edge at $t = 0.43T_\mathrm{conv}$ (Figure 5.5n) and gradually relaxes to the unforced state as shown at $t = 1.96T_\mathrm{conv}$ (Figure 5.4s). The vorticity transport across the trailing edge is discussed in §5.4.

5.3 Transition Between SS and PS Actuation

5.3.1 Time Histories of α, C_L, C_M and p

Closed-loop flight control typically requires switching between the PS and SS actuation states. This operation often includes commands to switch from maximum nose-down moment ($u_\mathrm{f} = 1$) to maximum nose-up pitching moment ($u_\mathrm{f} = -1$) and vica versa. It is important to understand the flow phenomena associated with $PS \to SS$ and $SS \to PS$ transitions in order to maximize controller bandwidth and hence response time of the aircraft. To this end, measurements were recorded for these transitions following the same procedure as for the single actuator measurements discussed in §5.2. The controller is commanded to hold the airfoil still at $\alpha_0 = 3°$ with the pitch servo actuator. Starting with the model stationary at α_0 with $u_\mathrm{f} = -1$, the actuation input it switched to $u_\mathrm{f} = 1$ at $t = 0$ and then back to $u_\mathrm{f} = -1$ at $t = 328T_\mathrm{conv}$. The resulting pitch trajectory $\alpha(t)$, lift increment $\Delta C_\mathrm{L}(t)$, and moment increment $\Delta C_\mathrm{M}(t)$ (phase-averaged over $N = 100$ cycles) are shown in Figure 5.6 with corresponding steady values for ΔC_L and ΔC_M. The transitions $PS \to SS$

and $SS \rightarrow PS$ yield $\Delta C_{\mathrm{M}} = \pm 0.08$, which for this particular controller result in peak pitch displacements of $\alpha = \pm 5.8^{\circ}$. As with the single actuator transitions, for all but the shortest times following transition, the dynamic ΔC_{M} and ΔC_{L} are very close to the steady levels.

Figure 5.7 shows the phase-averaged pressure traces measured by the four sensors represented in Figure 5.3. Overall the transient variation of the pressure traces is consistent with the measurements for the single transitions. The trailing edge sensor (Figure 5.3d) and upstream sensors (Figure 5.3a-c) exhibit convergence to quasi-steady values within $1 - 2T_{\mathrm{conv}}$ and $2 - 4T_{\mathrm{conv}}$, respectively. Following the transition $PS \rightarrow SS$, a sharp suction peak ($\Delta C_{\mathrm{p}} = -0.63$) is evident at the trailing edge at $t = 0.33T_{\mathrm{conv}}$. Similar to the suction peak observed in connection with the transition $SS \rightarrow PS$ (cf. Figure 5.3), this transient occurs during the shedding of the large-scale vortex at the trailing edge, however the magnitude of this suction spike is more than twice what it was for the single transition.

Following the transition $SS \rightarrow PS$, a pressure peak ($\Delta C_{\mathrm{p}} = -0.45$) is evident at the trailing edge at $t = 0.5T_{\mathrm{conv}}$ (Figure 5.7d). Since this peak occurs immediately following the onset of SS separation at the trailing edge, this pressure spike is most likely associated with the sudden exposure to the slow fluid of the recirculation region downstream of the SS actuator when the jets are inactive. For the upstream sensors (Figure 5.7a-c), the same essentially monotonic convergence to steady state is seen as for the transition $PS \rightarrow SS$.

5.3.2 The Unsteady Trailing Edge Flow Field

Phase-averaged maps of spanwise vorticity $\hat{\omega}$ and velocity magnitude $\hat{u}$ following the transition $PS \rightarrow SS$ are shown in Figure 5.8 for $t/T_{\mathrm{conv}} = 0.3$, 0.33, and 0.36. Similar to the vorticity distributions in Figure 5.4, the vorticity layer downstream of the actuators appears to bifurcate into two branches due to the train of CW vortices emanating from the SS actuator. The CCW vortex which is visible on the right of Figure 5.8a at $\mathbf{x}/c = (1.03, 0)$ results from the PS shear layer breaking off at the trailing as the CW vortex associated with onset of the SS actuation passes above it. This stronger interaction between the SS and PS shear layers is due to the fact that at $t = 0.3T_{\mathrm{conv}}$ the PS shear layer is vectored upward due to the PS actuation. A comparison of Figures 5.8b and c with the corresponding times during the transition $0 \rightarrow SS$ (Figures 5.4k and l) reveals that this roll-up of the PS shear layer is present during the $0 \rightarrow SS$ transition but the size of the resulting CCW vortex is much smaller due to the larger distance between the upper and lower shear layers.

Phase-averaged maps of $\hat{\omega}$ and $\hat{u}$ following the $SS \rightarrow PS$ transition are shown in Figure 5.9 for $t/T_{\text{conv}} = 0.1$, 0.13, and 0.16. At $t/T_{\text{conv}} = 0.1$ (Figure 5.9a), a large CCW vortex is present below and just downstream of the trailing edge ($\mathbf{x}/c = (1.01, -0.02)$). This vorticity concentration results from the PS shear layer which was severed by the onset of PS actuation, rolled up and advected downstream. During $0.1 < t/T_{\text{conv}} < 0.16$, this vortex moves downstream to $\mathbf{x}/c = (1.05, -0.03)$ at an approximate speed of $0.63U_0$ (Figures 5.9b and c). Because the changes in the flow due to the termination of actuation have not propagated to the trailing edge by this time, there is little opportunity for the CCW vortices associated with the PS transition to interact with the SS shear layer.

5.4 Vorticity Flux and Circulation

The time scale associated with the actuation process is also assessed using a survey of the local vorticity flux $u\omega_z$ into the wake. Phase-averaged maps of $u\omega_z$ extracted from the PIV measurements at $x/c = 1.04$ are plotted as a function of y/c and t/T_{conv} for each of the four transitions presented in §5.2 and §5.3 (Figure 5.10). Considering first the transition $0 \rightarrow SS$ (Figure 5.10a), the flux profile a $t = 0$ corresponds to the unactuated case (cf. Figure 5.4a) in which the SS (CW) and PS (CCW) shear layers are separated by a cross-stream gap $\Delta y = 0.06c$ owing to the recirculation regions downstream of each actuator. The large CW vortex resulting from the severing of the CW shear layer (cf. Figures 5.4g-k) is evident for $0.2 < t/T_{\text{conv}} < 0.33$ at $0.03 < y/c < 0.09$. Following the passage of this vortex, there is momentary decrease in flux of CW vorticity from the suction surface ($0.33 < t/T_{\text{conv}} < 0.46$) as the circulation around the airfoil builds up. (SS actuation is associated with an increase in C_{L}.) Following this period of net CCW vorticity flux, the wake relaxes to the $u_{\text{f}} = 1$ state which is nearly complete by $t = 0.8T_{\text{conv}}$.

The transition $SS \rightarrow 0$ (Figure 5.10b) occurs over a slightly longer period. Starting from the $u_{\text{f}} = 1$ state at $t = 0$, the cross-stream width of the CW shear layer begins to diminish around $t = 0.4T_{\mathrm{conv}}$ which is about the time that the separation along the SS surface of the airfoil reaches the trailing edge (cf. Figure 5.5m). During $0.46 < t/T_{\mathrm{conv}} < 0.82$, the cross-stream width of the CCW (PS) shear layer diminishes as CW vorticity is transported into the wake and the circulation about the airfoil decreases. For $t > 0.82$, the CCW shear layer thickens to its unforced state and the CW shear layer is advected in the cross-stream direction to its unforced elevation which is nearly reached by $t = 1.4T_{\mathrm{conv}}$.

The vorticity flux map for the transition $PS \to SS$ is shown in Figure 5.10c. As noted in connection with Figure 5.8, the primary difference between $0 \to SS$ and $PS \to SS$ transitions is that in the latter there is more interaction between the CW and CCW shear layers because of their closer proximity during the initial state ($u_{\mathrm{f}} = -1$ $\Delta y = 0.05c$). Immediately following the passage of the large CW vortex from the suction surface ($0.3 < t/T_{\mathrm{conv}} < 0.43$), there is a period of strong CCW vorticity flux ($u\omega_z = 35U_0^2$) during which the airfoil gains significantly more lift than following the transition $0 \to SS$ ($\Delta C_{\mathrm{L}} = 0.34$ vs 0.14). A large contribution to this CCW vorticity flux is the large CCW vortex noted in connection with Figure 5.8.

Finally, the local vorticity flux distribution following the transition $SS \to PS$ is shown in Figure 5.10d. The large CCW vortex resulting from the severing of the CCW shear layer by the onset of PS actuation (cf. Figure 5.9) is evident at $-0.04 < y/c < -0.02$ for $0.1 < t < 0.2$. Following the passage of this vortex there is a period of diminished CCW vorticity flux from the PS side of the airfoil as the lift on the airfoil decreases by $\Delta C_{\mathrm{L}} = -0.34$ (i.e., the difference between $u_{\mathrm{f}} = 1$ and $u_{\mathrm{f}} = -1$). The process is complete by $t = 1.4T_{\mathrm{conv}}$ and for the remaining part of the record ($1.4 < t/T_{\mathrm{conv}} < 1.94$) the flux profile corresponds to $u_{\mathrm{f}} = -1$, which is characterized by a thinning of both the CW and CCW shear layers as well as an upward displacement of the latter.

The total vorticity flux from each side of the airfoil as well as the total net vorticity flux into the wake is computed at each time step by integrating in the cross-stream direction:

$$\begin{aligned}
\left(\frac{d\Gamma}{dt}\right)_{SS} &= \int_{y_{\text{wake}}}^{y_{\max}} u\omega_z dy \\
\left(\frac{d\Gamma}{dt}\right)_{PS} &= \int_{y_{\min}}^{y_{\text{wake}}} u\omega_z dy \\
\left(\frac{d\Gamma}{dt}\right)_{\text{total}} &= \left(\frac{d\Gamma}{dt}\right)_{SS} + \left(\frac{d\Gamma}{dt}\right)_{PS}
\end{aligned}$$

where $y_{\min}$ and $y_{\max}$ are the lower and upper edges of PIV domain and y_{wake} is the "wake center" defined by the vorticity zero-crossing at the streamwise survey point $x_0 = 1.04$. The extents of the PIV domain were selected such that ω_z vanished on both the upper and lower edges and thus these integrals converge. Note that the vorticity flux is averaged over a small streamwise domain ($\Delta x = 0.015c$) to improve measurement fidelity. Time histories of the normalized fluxes $\frac{1}{U_0^2}\left(\frac{d\Gamma}{dt}\right)_{SS}$, $\frac{1}{U_0^2}\left(\frac{d\Gamma}{dt}\right)_{PS}$, $\frac{1}{U_0^2}\left(\frac{d\Gamma}{dt}\right)_{\text{total}}$ are plotted in Figure 5.11 for each of the four transitions. As a general trend the largest fluctuations in vorticity flux are seen on the side of the airfoil undergoing actuation transition. For example, in Figures 5.11a and b, only the SS actuator is transitioned and accordingly the variations in $\left(\frac{d\Gamma}{dt}\right)_{SS}$ are twice as large as those in $\left(\frac{d\Gamma}{dt}\right)_{PS}$. In these cases the major changes in circulation about the airfoil are controlled by the intensification and diminution of vorticity flux from the transitioning side of the airfoil while the flux from the opposing side varies on a much smaller scale. The largest excursion of $\left(\frac{d\Gamma}{dt}\right)_{\text{total}}$ occurs during the transition $PS \rightarrow SS$ (Figure 5.11c) as a result of the large CW vortex from the suction side at $t = 0.23T_{\text{conv}}$ being immediately followed by the CCW vortex from the pressure side $t = 0.33T_{\text{conv}}$. As these vortices pass, $\frac{1}{U_0^2}\left(\frac{d\Gamma}{dt}\right)_{\text{total}}$ varies from -0.6 to 0.8.

The total vorticity flux $\left(\frac{d\Gamma}{dt}\right)_{\text{total}}$ for each of the four transitions is integrated forward in time to obtain the time-history of circulation change $\Delta\Gamma$ about the airfoil. Normalized circulation change $\frac{\Delta\Gamma}{U_0 c}$ about the airfoil is plotted in Figure 5.12 where a sign convention is adopted such that positive circulation corresponds to positive lift on the airfoil. Along with the transient $\Delta\Gamma$, the steady change in circulation corresponding to the change in lift measured by the load cells is plotted (solid line). For the transition $0 \rightarrow SS$ (Figure 5.12a), the airfoil experiences a slight decrease in circulation during $0.23 < t/T_{\text{conv}} < 0.3$ as the CW vortex passes followed by a monotonic increase to the steady state value for $t > 0.3T_{\text{conv}}$.

Conversely during the transition $SS \rightarrow 0$, the circulation first exhibits a slight increase ($0.26 < t/T_{\text{conv}} < 0.46$) followed by a monotonic decrease towards the steady state value (Figure 5.12b). The trend of $\Delta\Gamma$ for the transition $PS \rightarrow SS$ (Figure 5.12c) is qualitatively similar to that of the transition $0 \rightarrow SS$ however the initial decrease and subsequent increase in circulation are larger in magnitude owing to the larger fluxes of vorticity discussed in connection with (Figure 5.11c). However, the transition $SS \rightarrow PS$ exhibits a rather different $\Delta\Gamma$ trend than any of the other three cases (Figure 5.12d). Initially, $\Delta\Gamma$ exhibits a slight increase as the CCW vortex passes ($0.1 < t/T_{\text{conv}} < 0.16$). As the flux from the pressure side of the airfoil abates ($0.16 < t/T_{\text{conv}} < 0.23$), $\Delta\Gamma$ decreases to zero (Γ returns to its initial value). For $0.23 < t/T_{\text{conv}} < 0.49$, the diminished flux from the pressure side is approximately balanced by the diminished flux from the suction side and as a result $\Delta\Gamma$ nearly vanishes (cf. Figure 5.11d). Finally at $t = 0.5T_{\text{conv}}$, the vorticity flux from the suction side resumes and $\Delta\Gamma$ steadily decreases for $0.5 < t/T_{\text{conv}} < 0.9$. For $t > 0.9T_{\text{conv}}$, the flux from the suction side remains invariant while the flux from the pressure side increases until the total flux into the wake vanishes. Consequently, the circulation relaxes to the steady-state value.

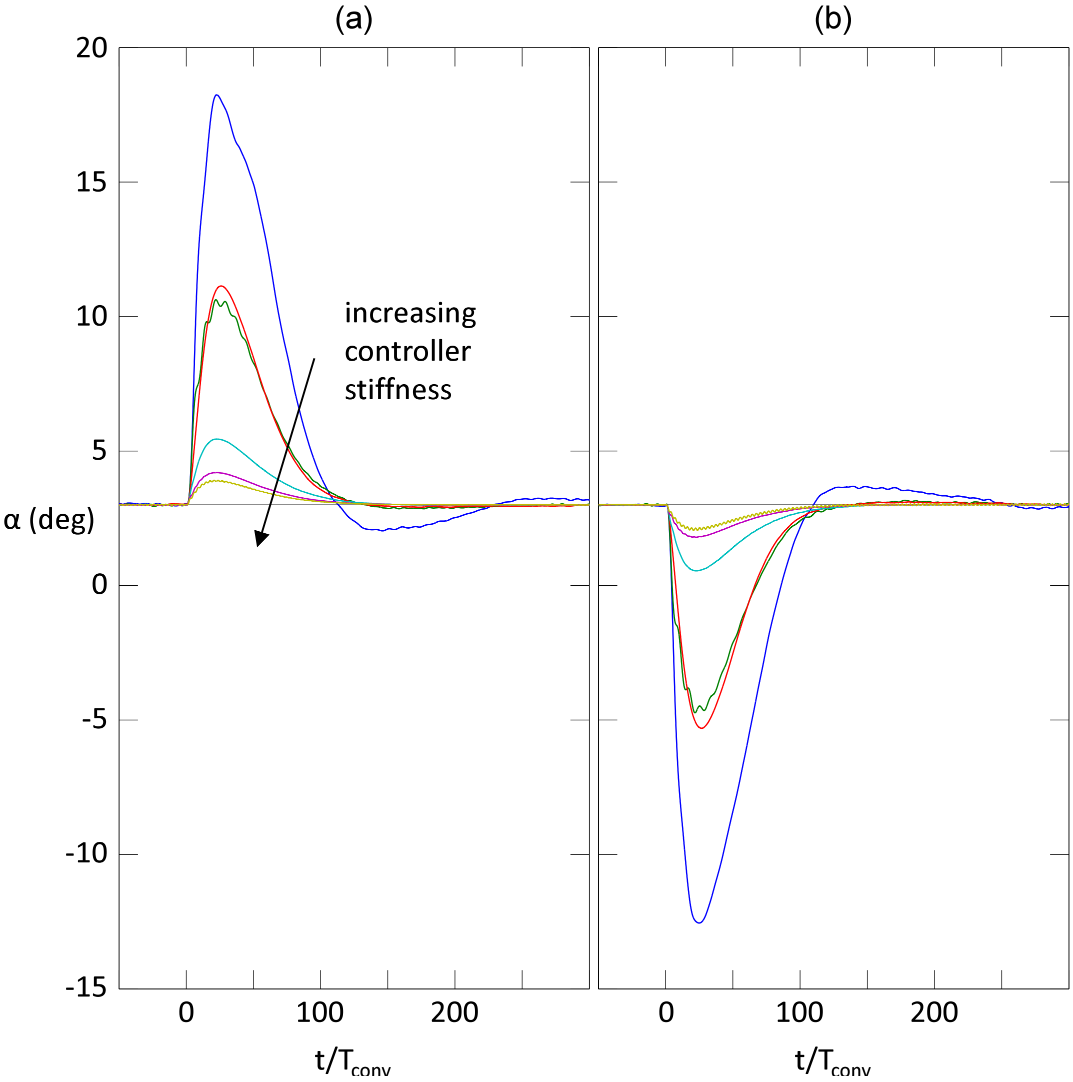

Figure 5.1: Time histories of α following transition from (a) $PS \rightarrow SS$ and (b) $SS \rightarrow PS$ for different controller stiffnesses.

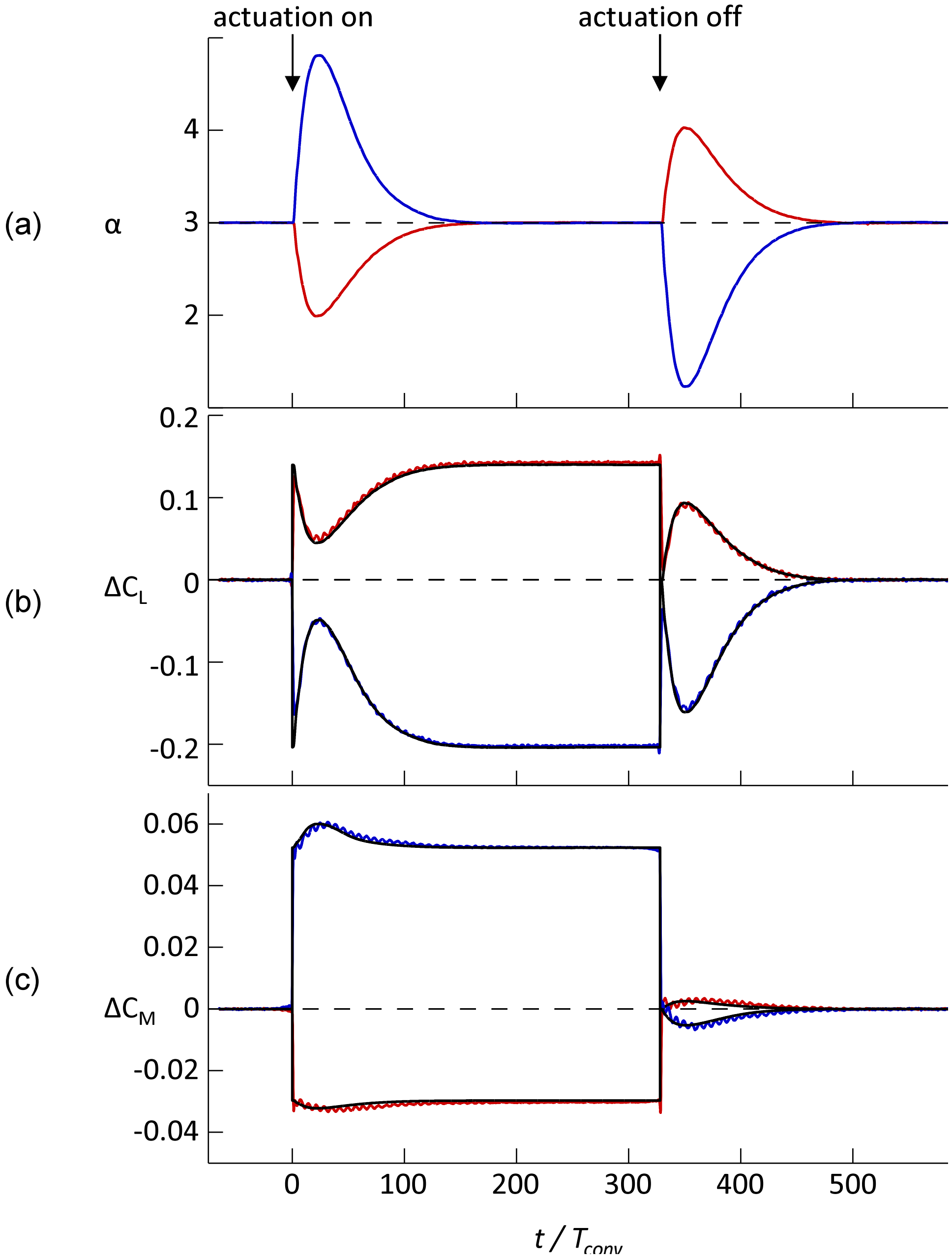

Figure 5.2: Time histories of (a) α, (b) ΔC_{L}, and (c) ΔC_{M} during step changes in actuation with the *SS* (▬) and *PS* (▬) actuators. Corresponding steady-state values (▬) based on a look up table using α and u_{f}.

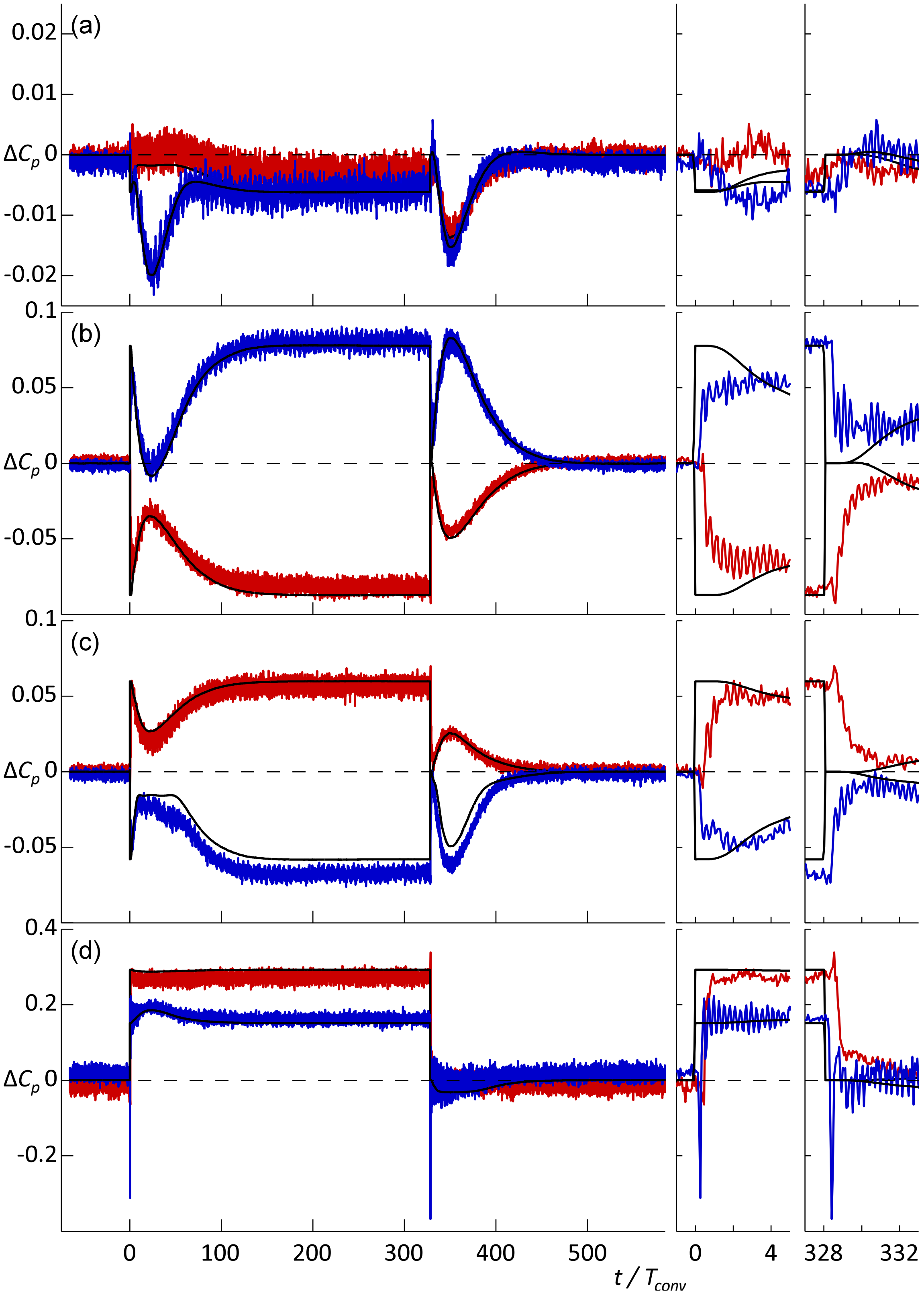

Figure 5.3: Time histories of ΔC_{p} at (a) the leading edge, (b) on the suction surface at $x/c = 0.39$, (c) on the pressure surface at $x/c = 0.4c$, and (d) at the trailing edge, with corresponding static values (▬). Colors as in Figure 5.2.

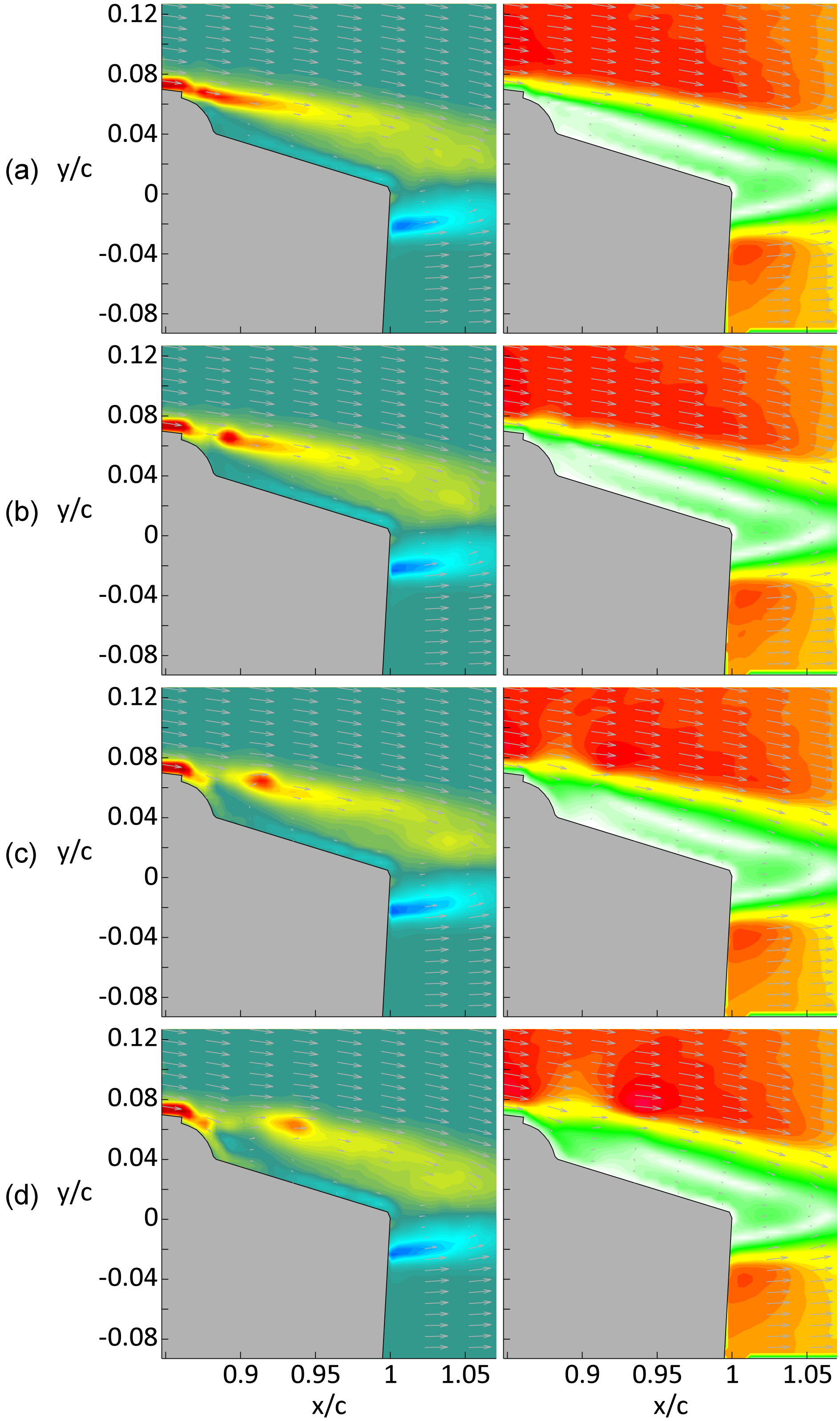

Figure 5.4: Phase-averaged maps of spanwise vorticity (first column) and velocity magnitude (second column) following the transition $0 \rightarrow SS$. Phase times t/T_{conv} are listed in Table 5.1.

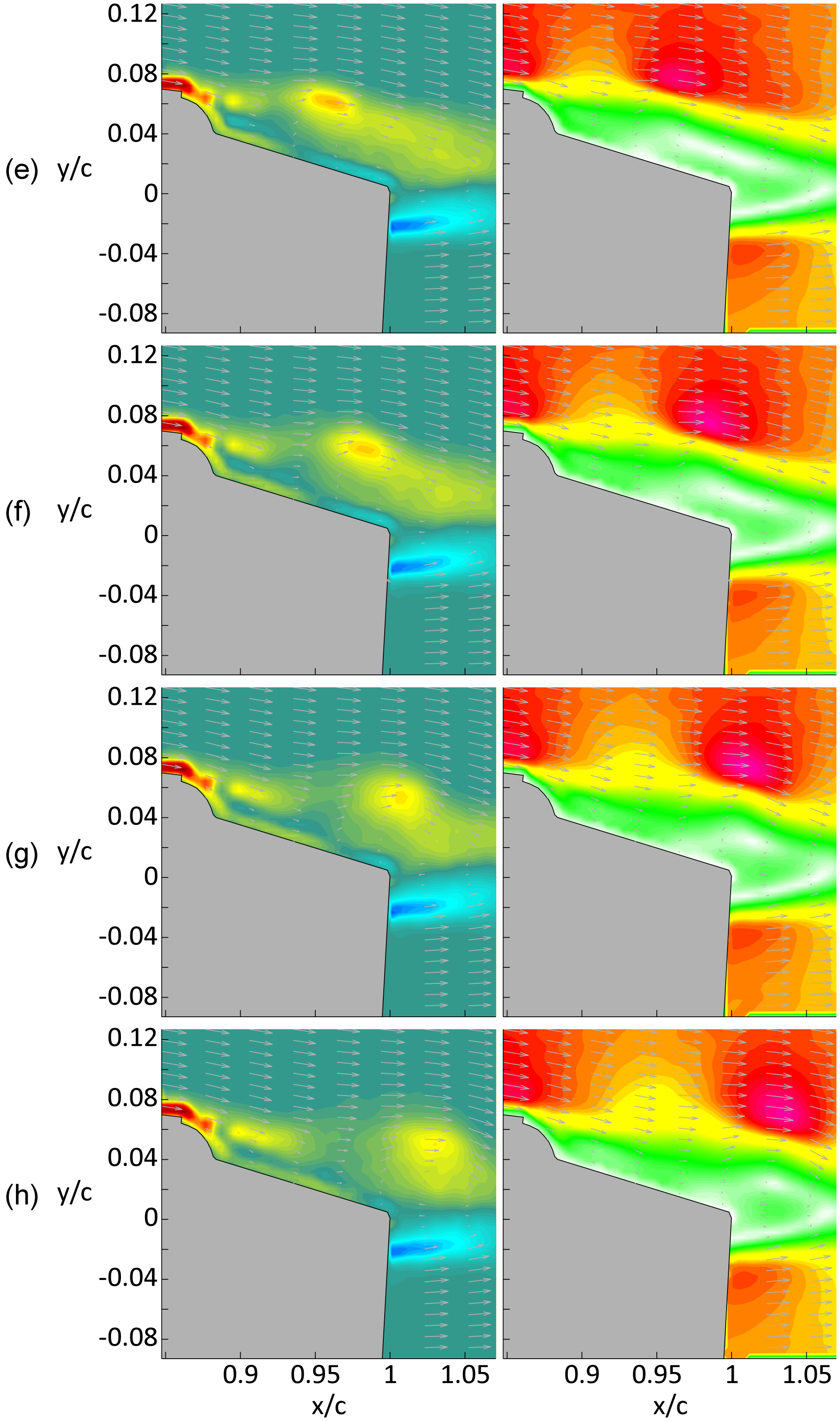

Figure 5.4: (continued)

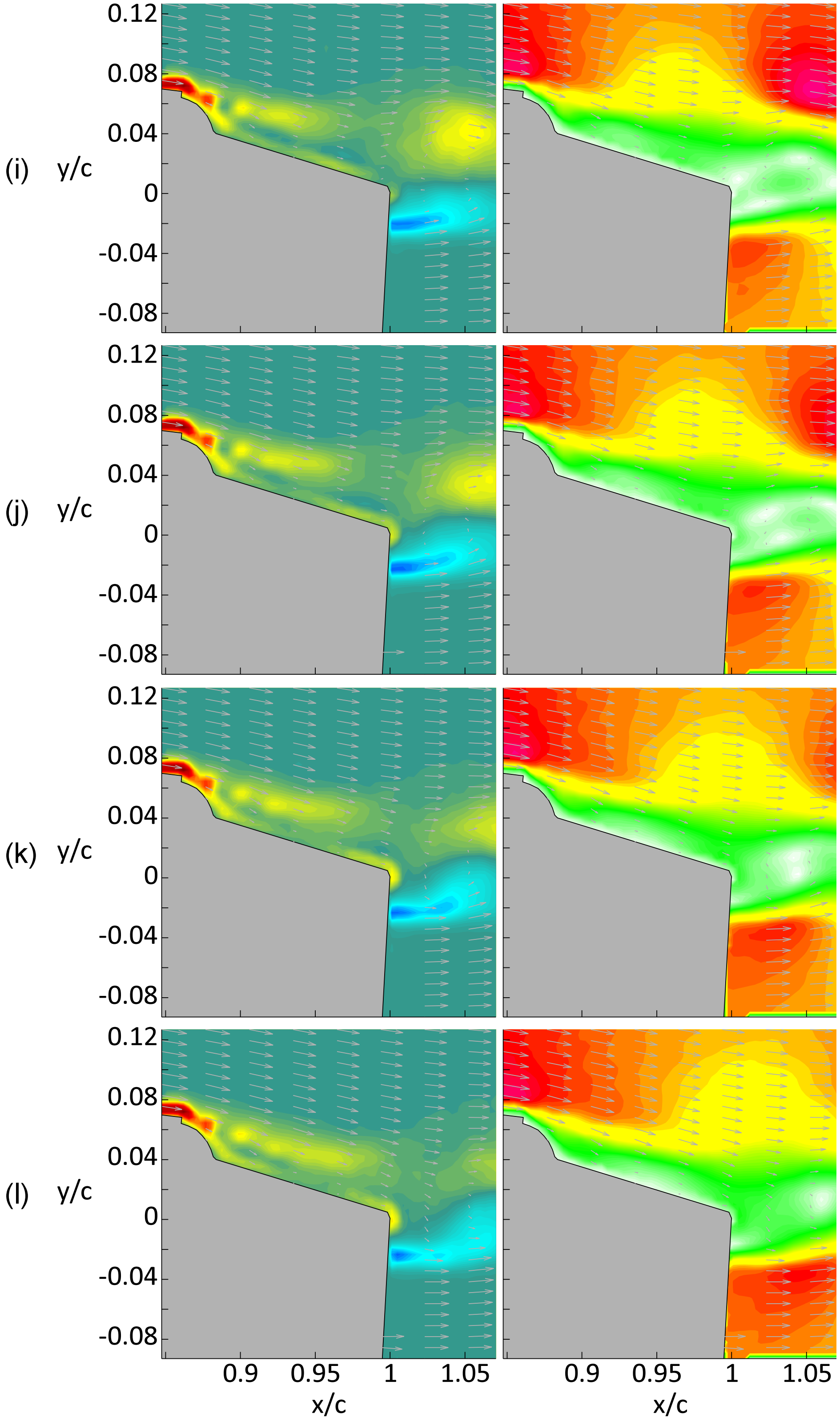

Figure 5.4: (continued)

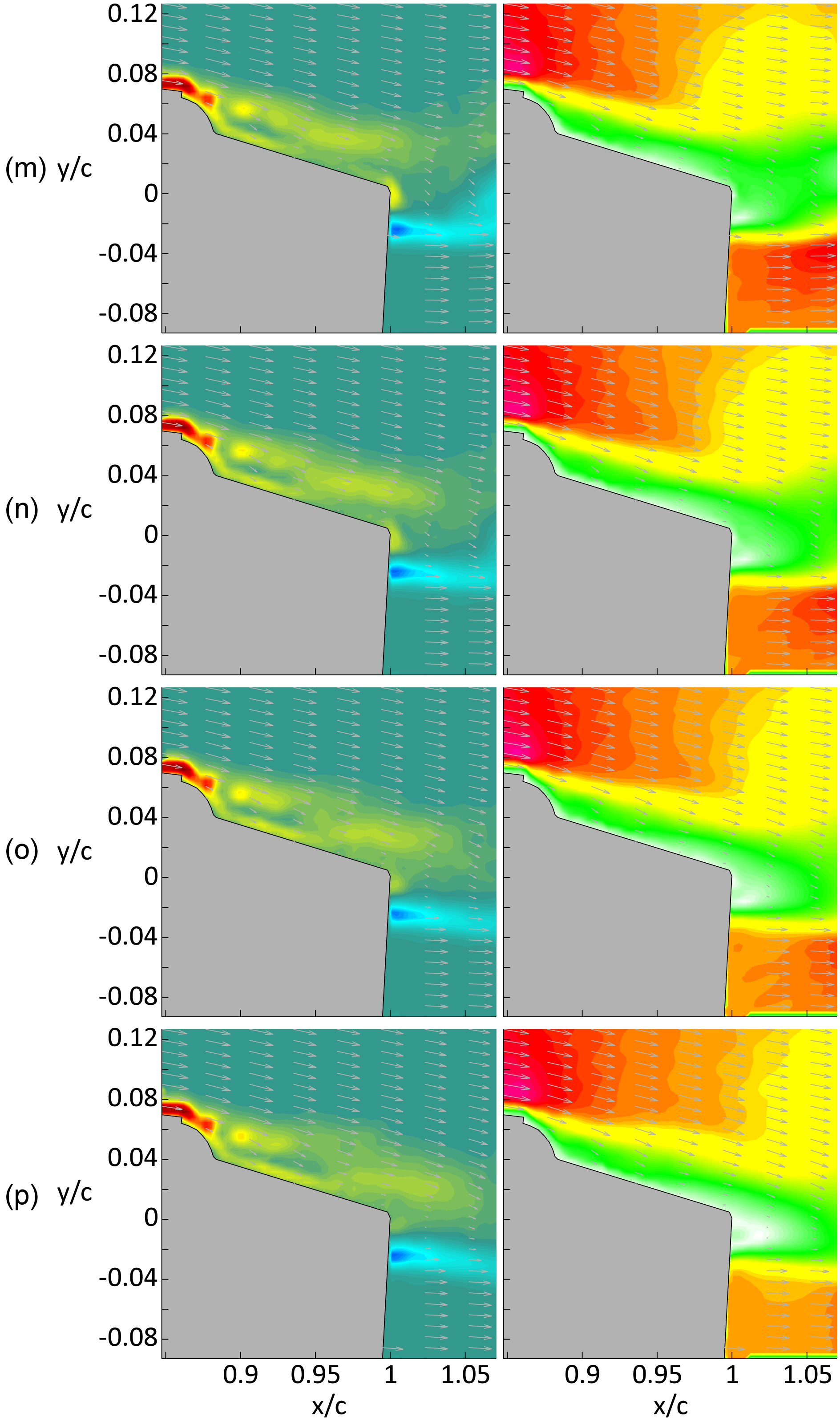

Figure 5.4: (continued)

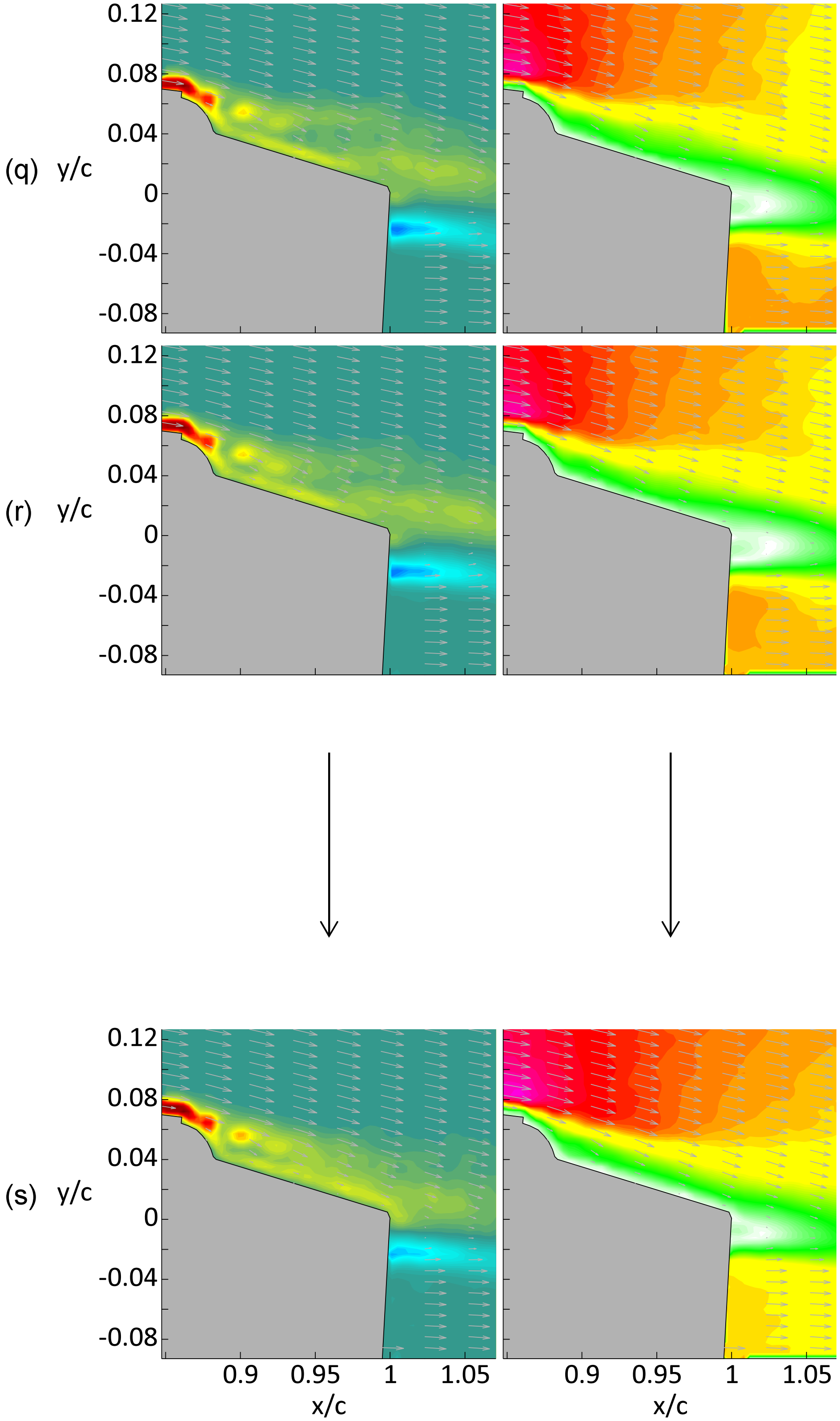

Figure 5.4: (continued)

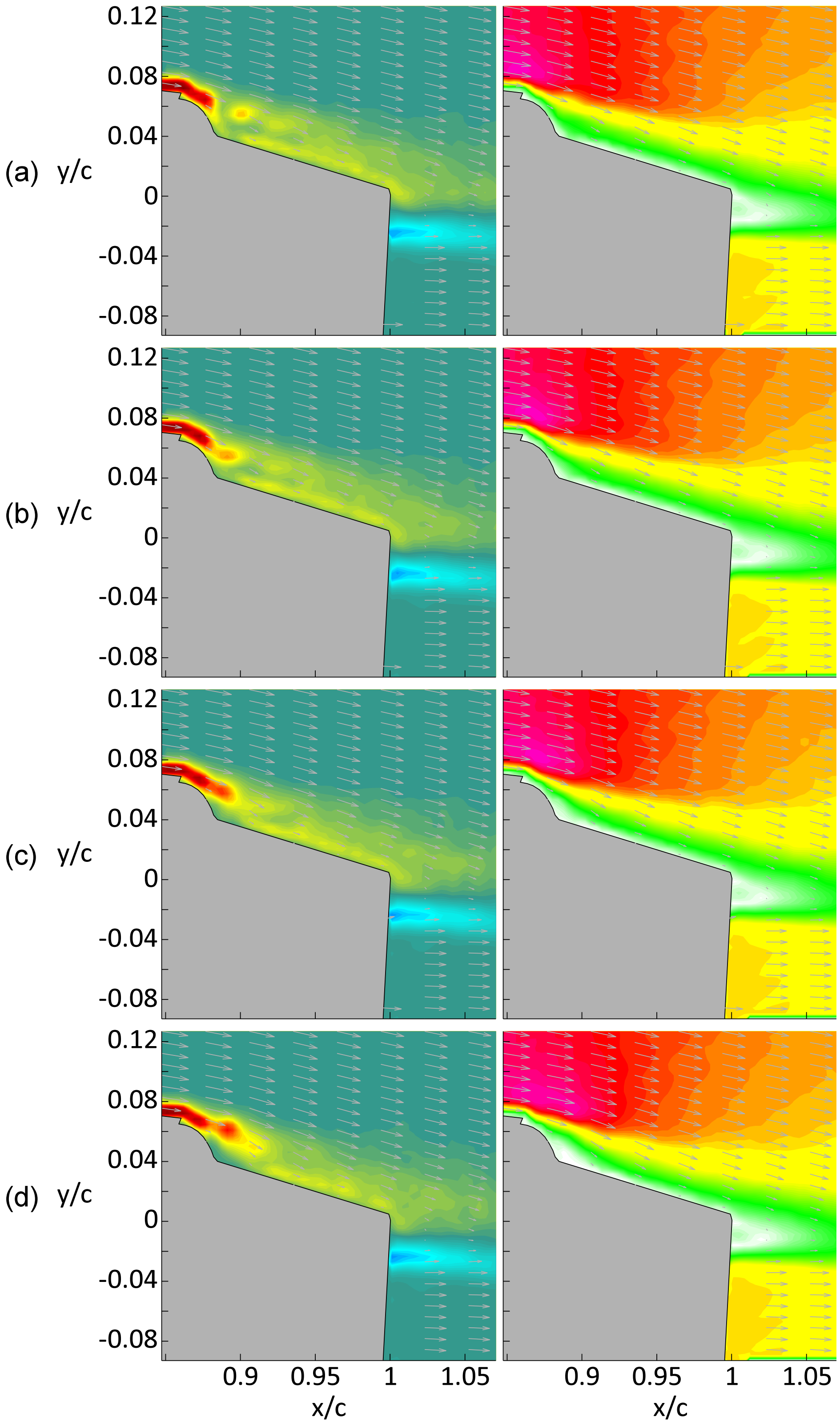

Figure 5.5: Phase-averaged maps of spanwise vorticity (first column) and velocity magnitude (second column) following the transition $SS \rightarrow 0$. Phase times t/T_{conv} are listed in Table 5.1.

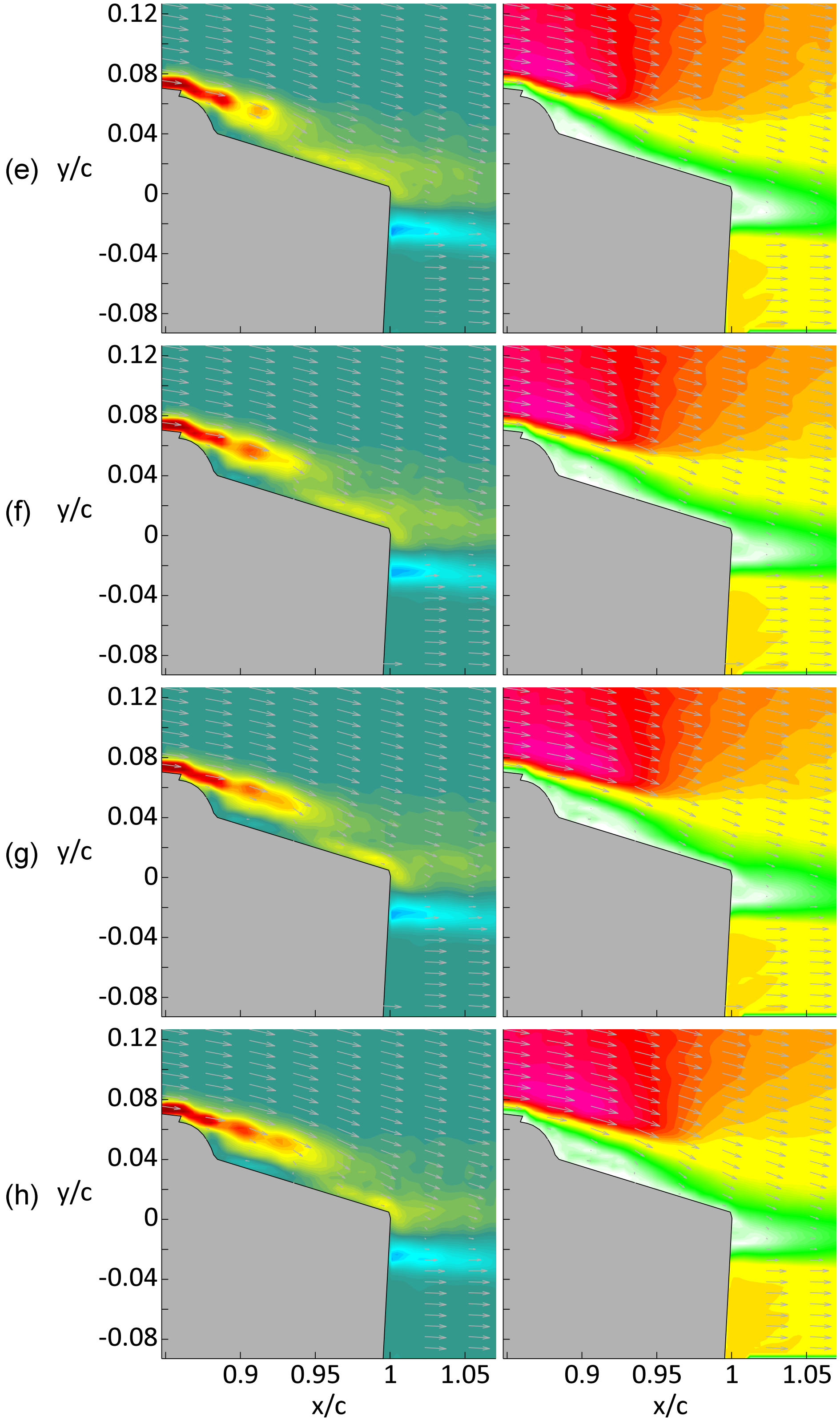

Figure 5.5: (continued)

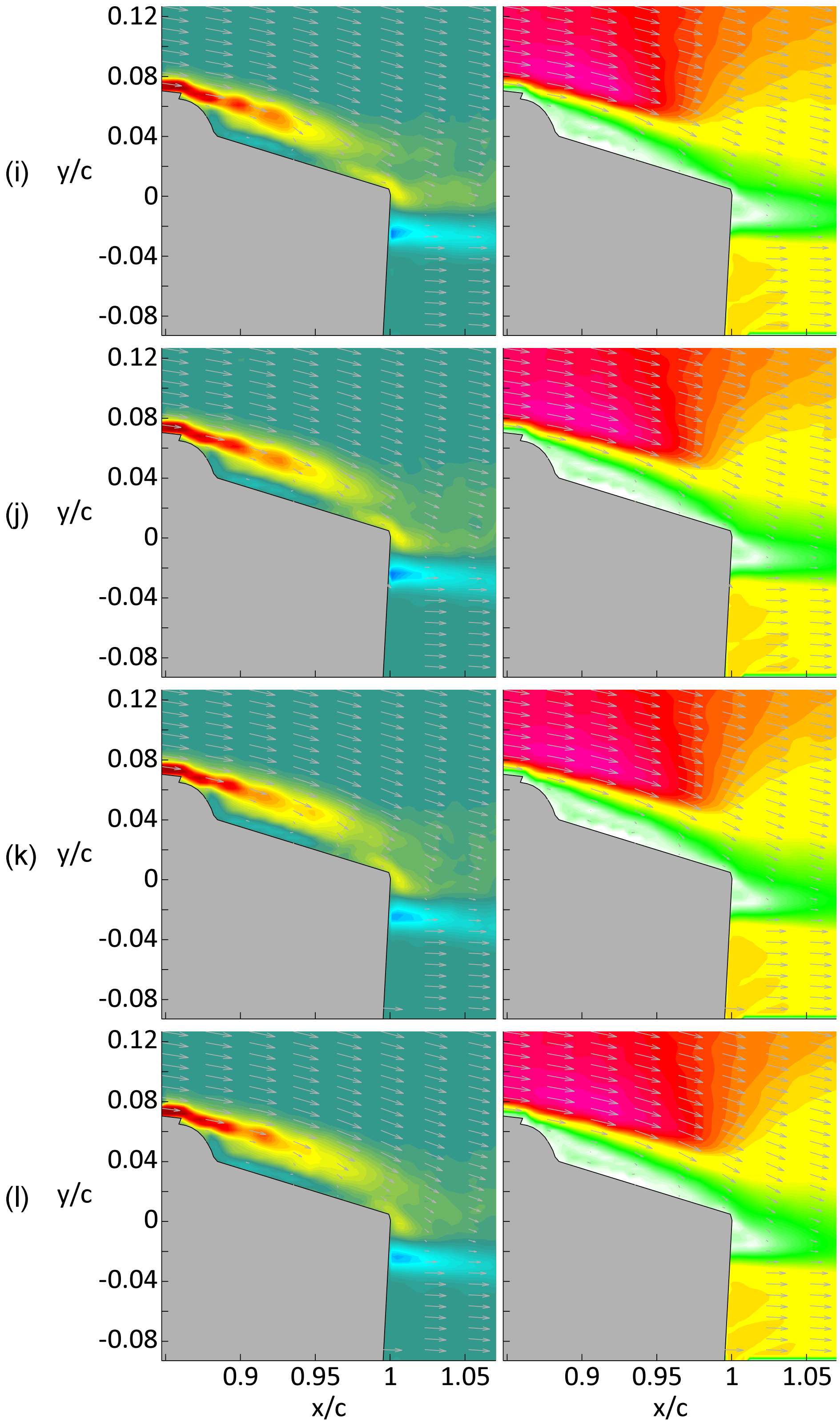

Figure 5.5: (continued)

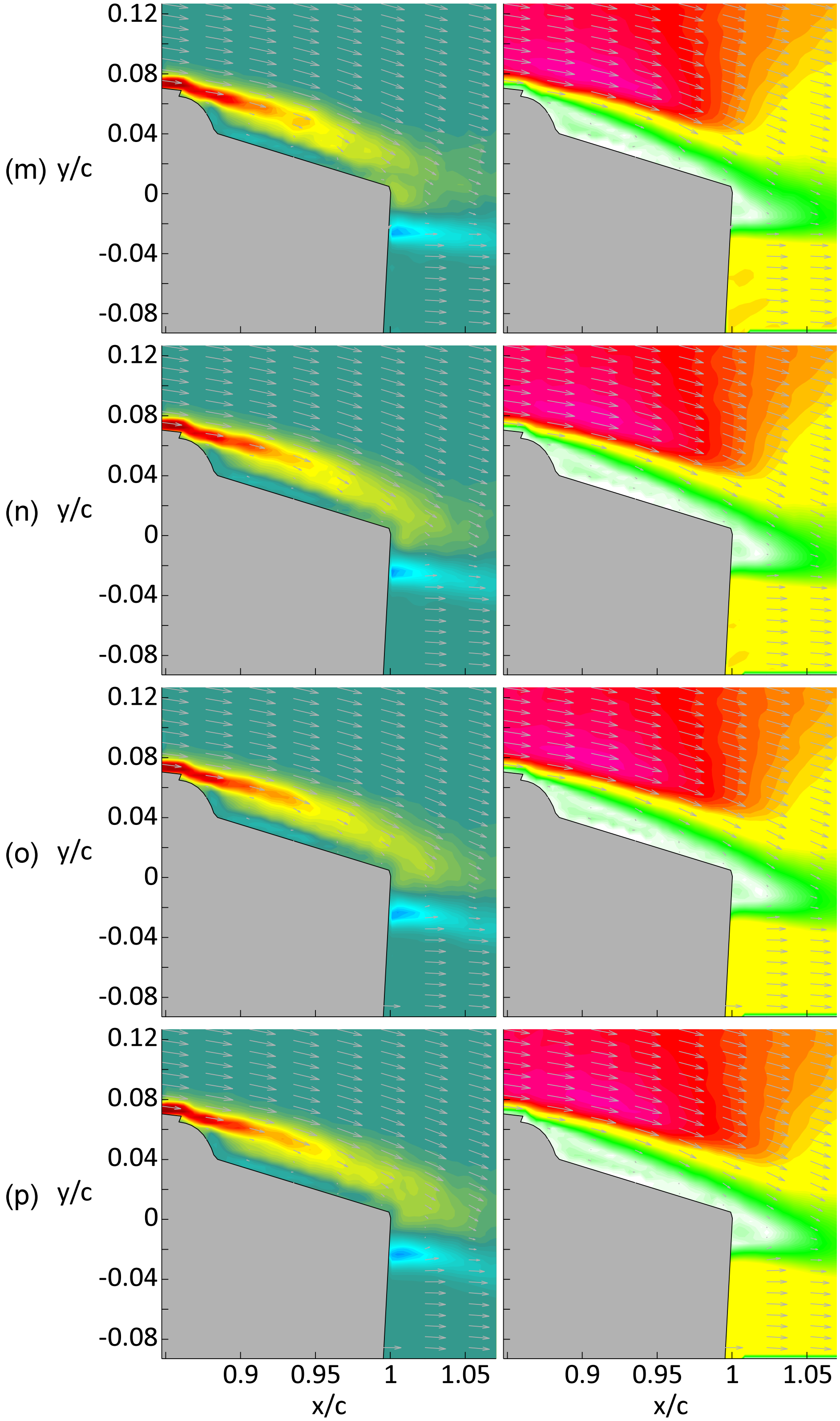

Figure 5.5: (continued)

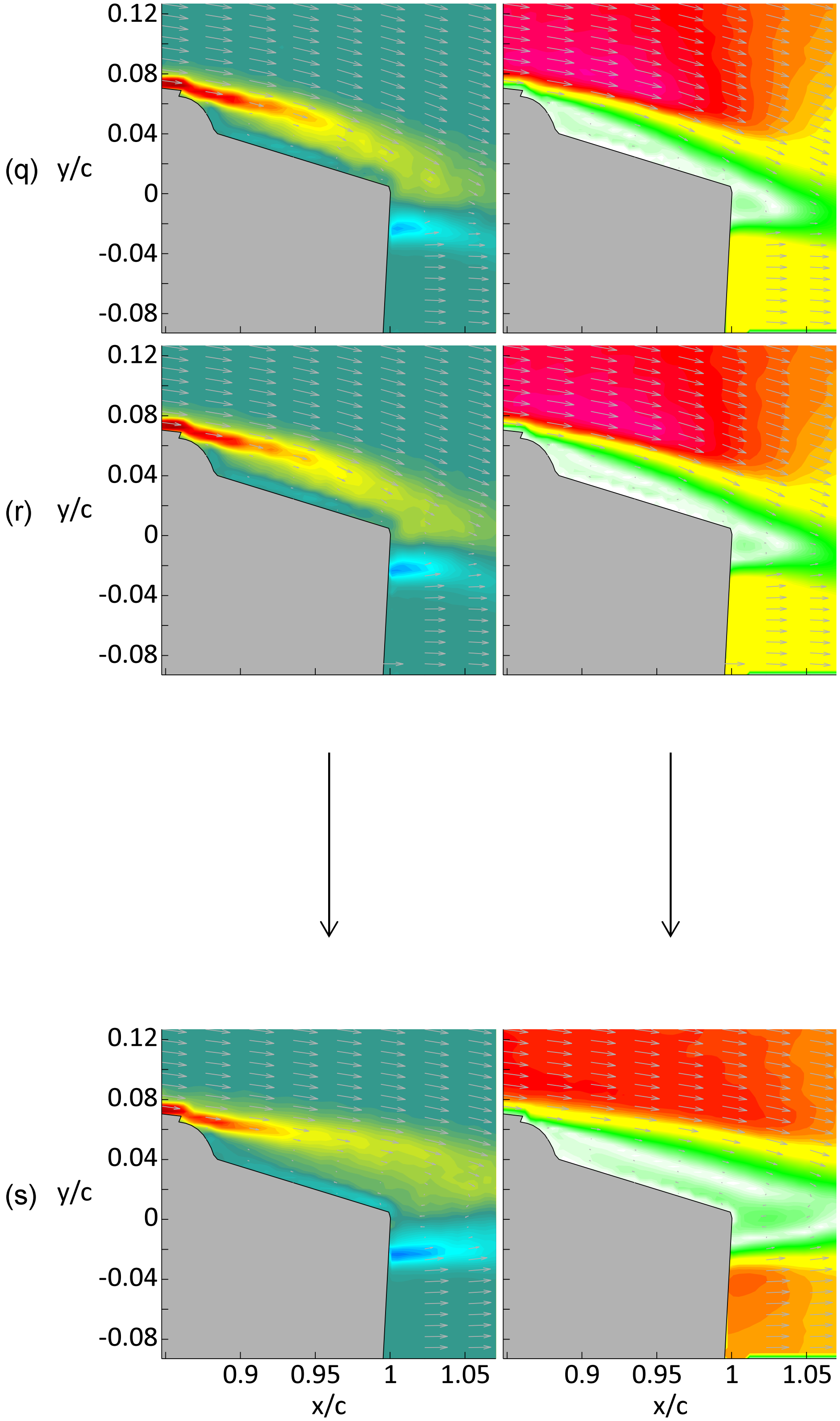

Figure 5.5: (continued)

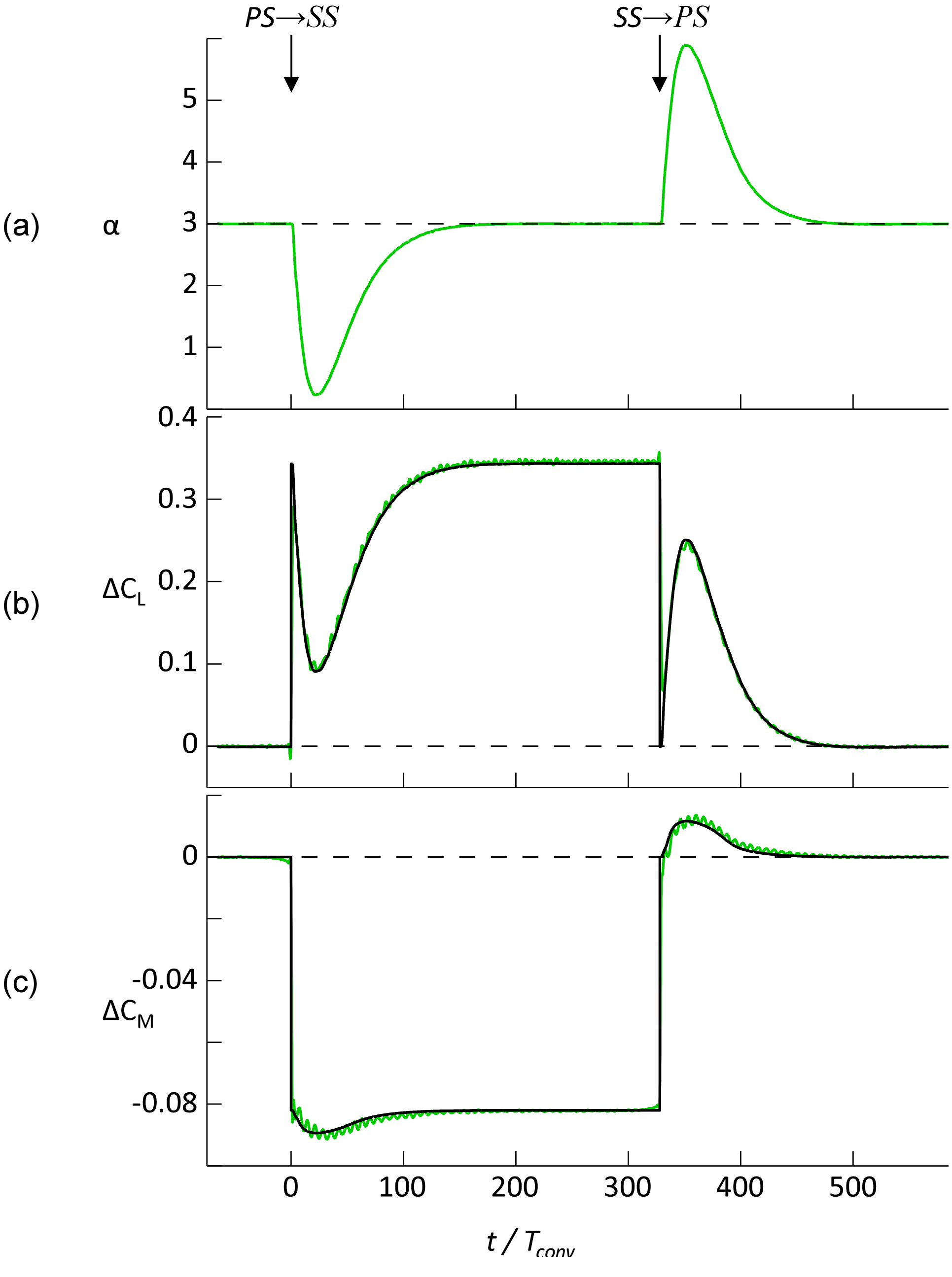

Figure 5.6: Time histories (🟩) of (a) α, (b) ΔC_{L}, and (c) ΔC_{M} during step changes in actuation between SS and PS actuators. Corresponding steady-state values (▬) based on a look up table using α and u_{f}.

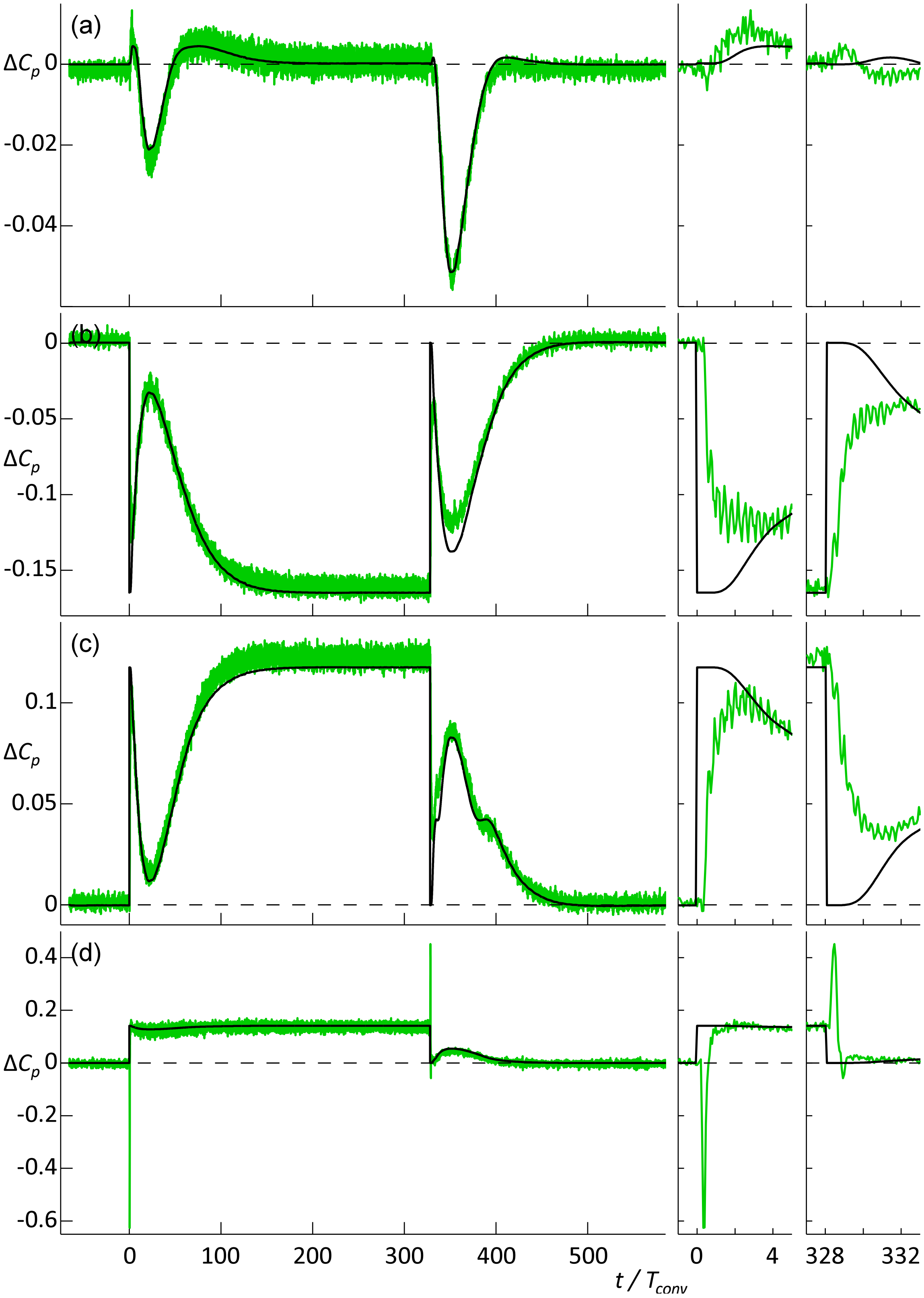

Figure 5.7: Time histories (🟩) of ΔC_p at (a) the leading edge, (b) on the suction surface at $x/c = 0.39$, (c) on the pressure surface at $x/c = 0.4c$, and (d) at the trailing edge, with corresponding static values (▬).

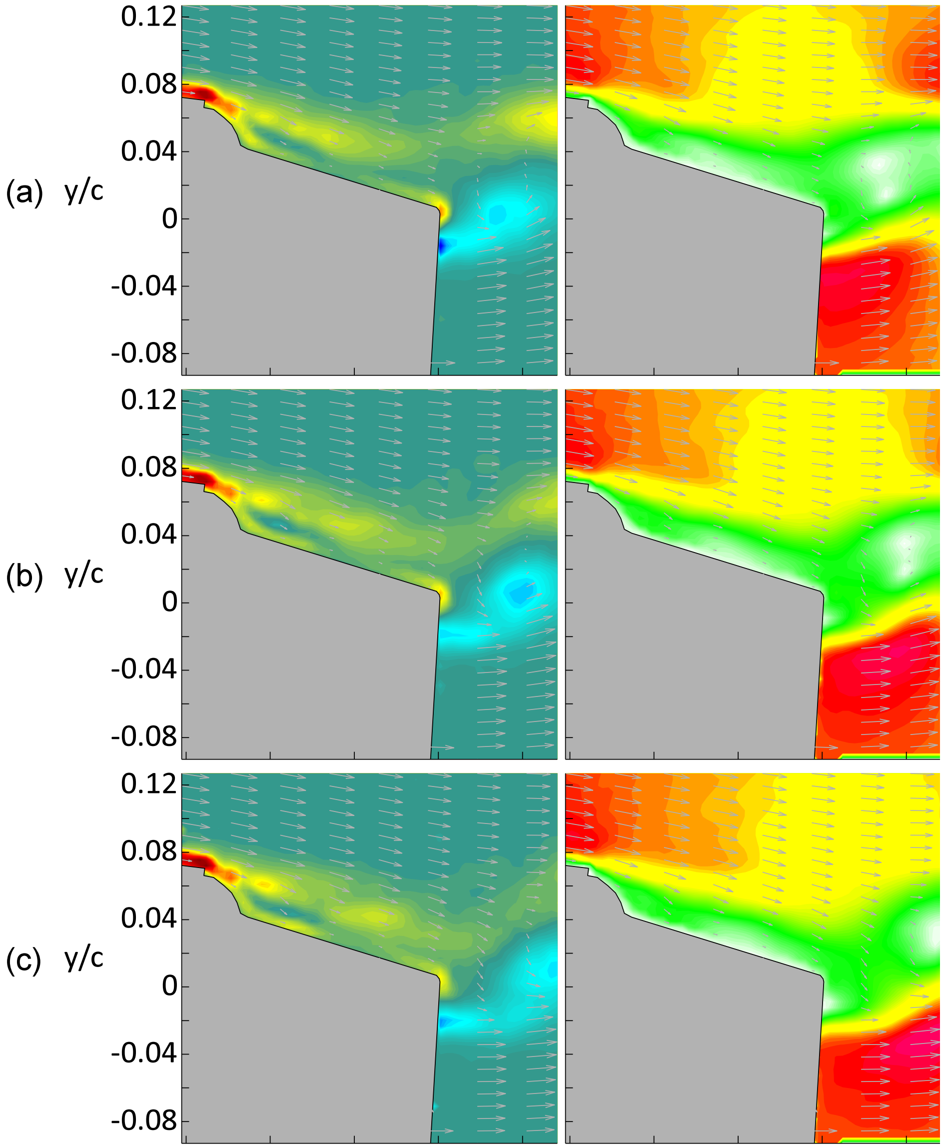

Figure 5.8: Raster plots of phase-averaged spanwise vorticity (left column) and velocity magnitude (right column) following the transition $PS \rightarrow SS$ at $t/T_{\text{conv}} = 0.3$ (a), 0.33 (b), and 0.36 (c).

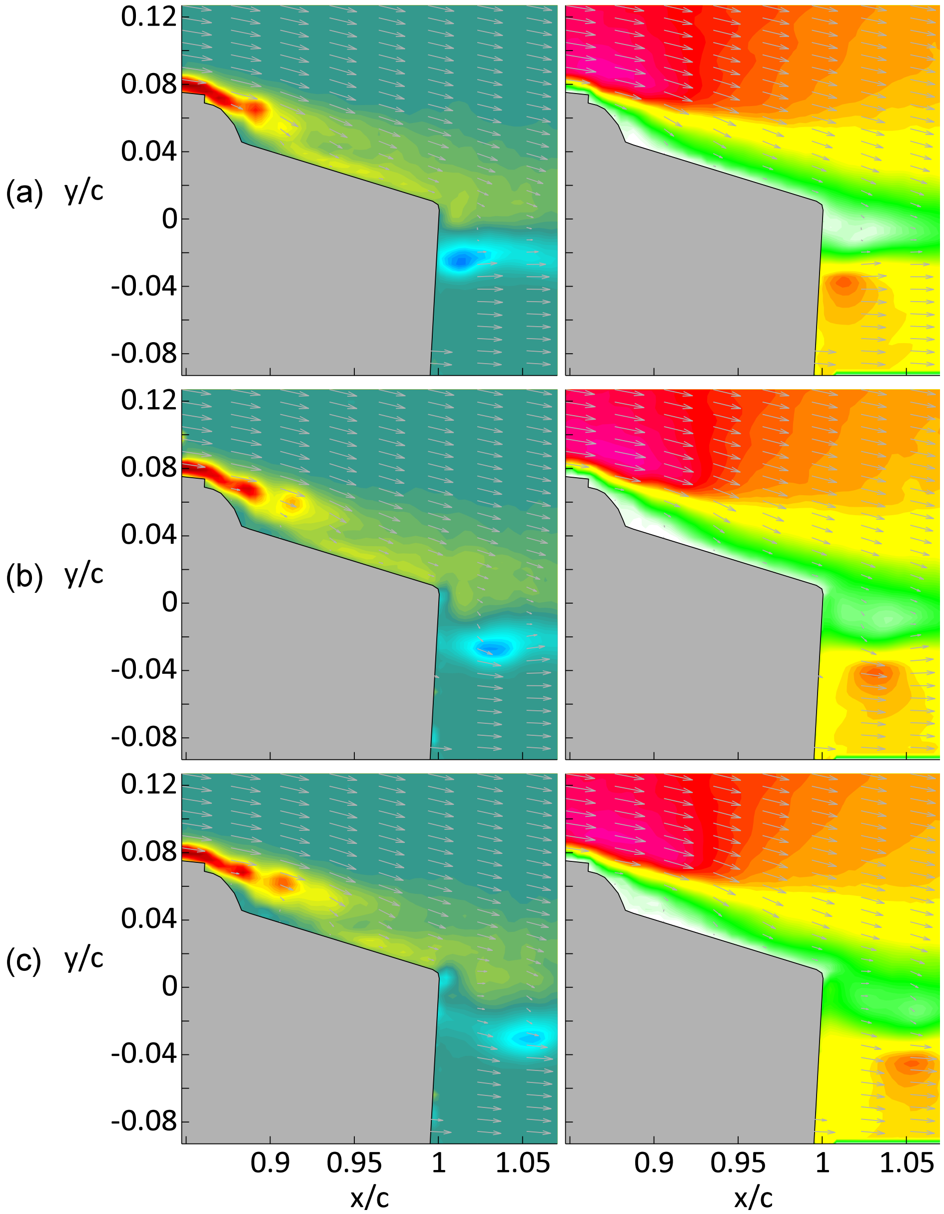

Figure 5.9: Raster plots of phase-averaged spanwise vorticity (left column) and velocity magnitude (right column) following the transition $SS \rightarrow PS$ at $t/T_{\mathrm{conv}} = 0.3$ (a), 0.33 (b), and 0.36 (c).

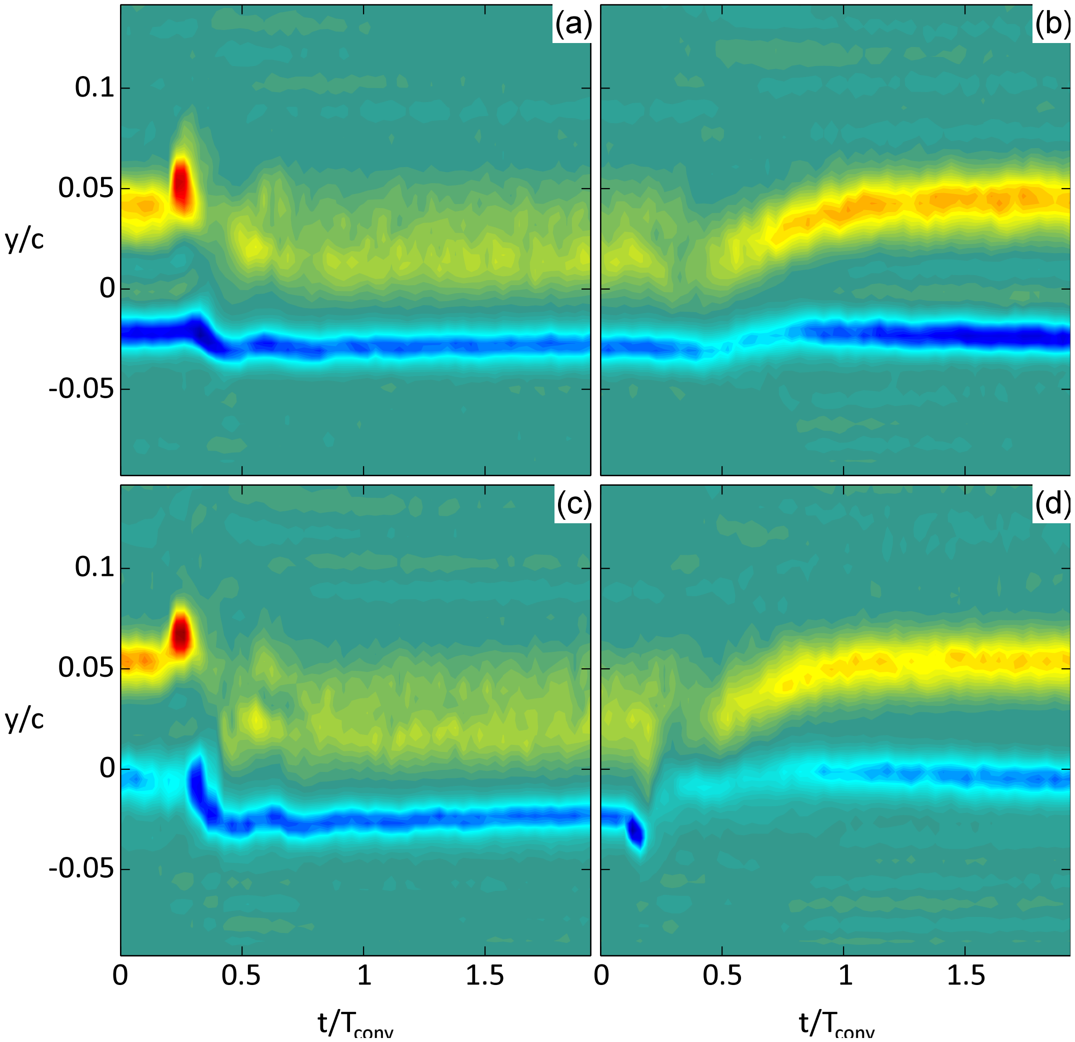

Figure 5.10: $y - t$ maps of vorticity flux at $x/c = 1.04$ following transition (a) $0 \rightarrow SS$, (b) $SS \rightarrow 0$, (c) $PS \rightarrow SS$, and (d) $SS \rightarrow PS$.

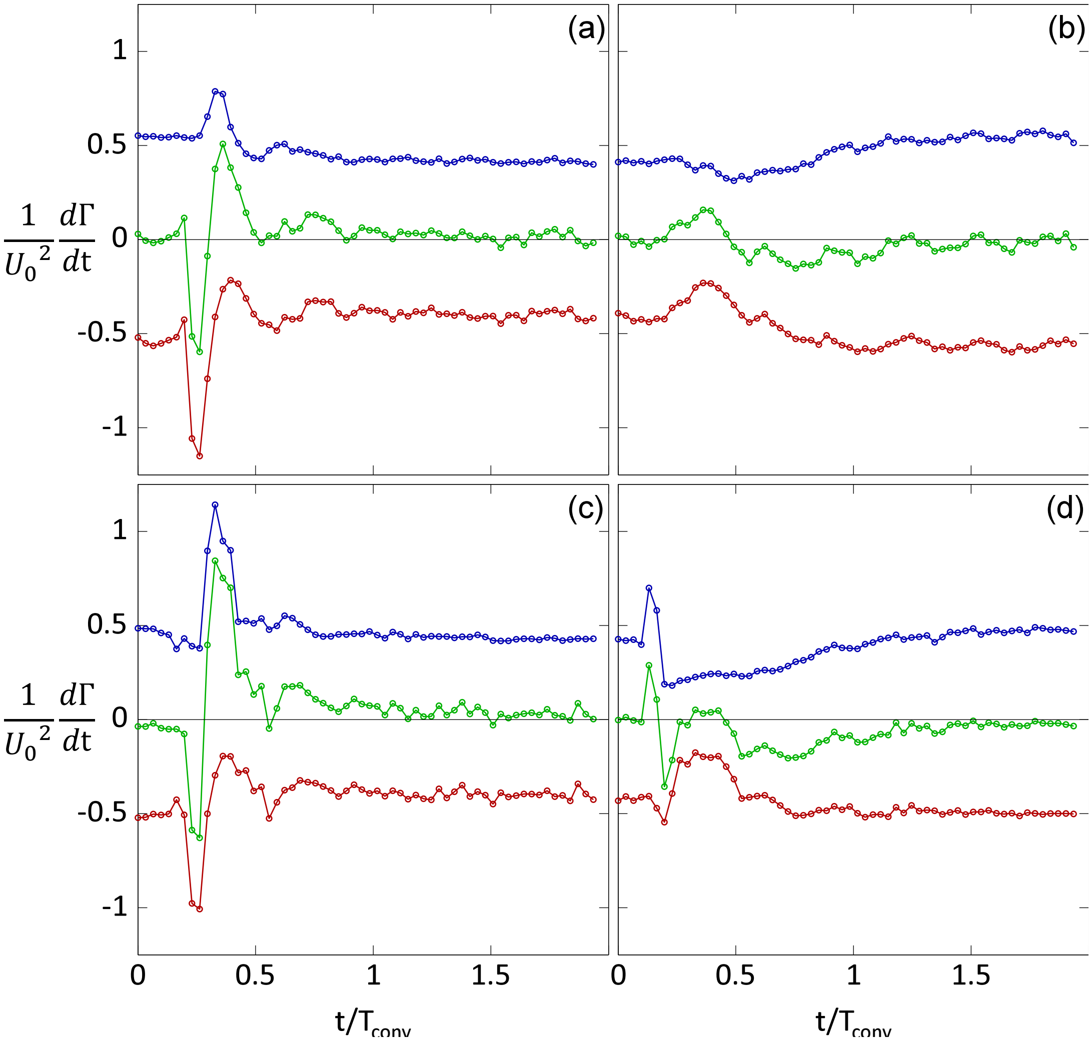

Figure 5.11: Time histories of vorticity flux corresponding to the four actuation transitions in Figure 5.10. Vorticity flux from suction (🟥) and pressure (🟦) sides of the airfoil is computed separately. The total flux (🟩).

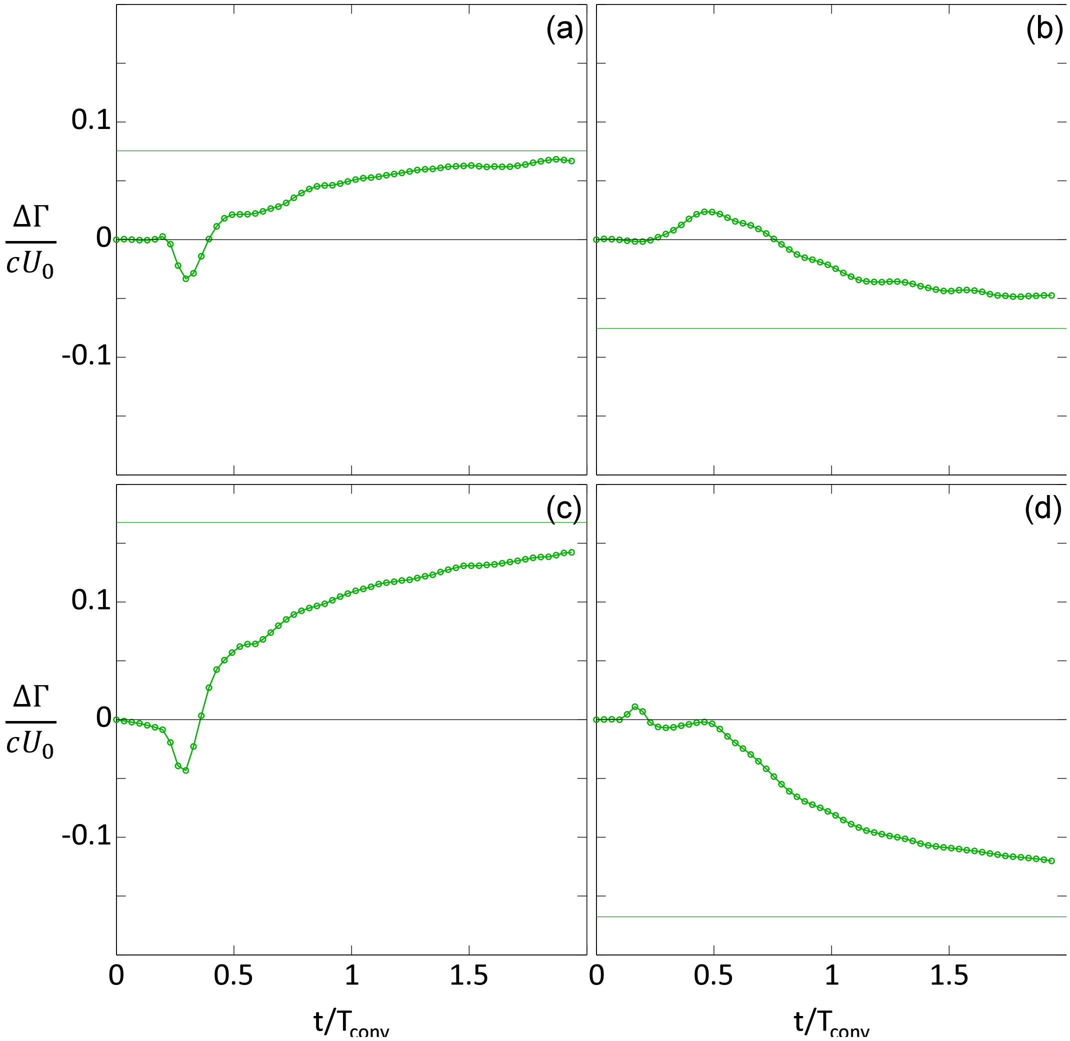

Figure 5.12: Time histories of circulation change about the airfoil corresponding to the four actuation transition in Figure 5.10.

Chapter VI

CLOSED-LOOP CONTROL OF PITCH AND PLUNGE

One of the goals of the present work is to explore the coupling between the unsteady flow field created by the flow control actuators and the induced airfoil motion. To this end, three maneuvers are investigated in which the motion of the airfoil is regulated via closed-loop flow control. In the first maneuver, the airfoil is constrained to move in pitch only and the controller tracks step changes in α (§6.1). In subsequent maneuvers, the airfoil is free to move in pitch and plunge and flow control is used to regulate plunge position (§6.2)- first by tracking step changes in plunge (§6.2.1) and then by tracking a constant altitude in presence of vertical force disturbances (i.e., "disturbance rejection", §6.2.2).

6.1 Closed-Loop Control of Pitch

6.1.1 Tracking Step Changes in α with Flow Control and Servo Control

A series of maneuvers were recorded when the airfoil was constrained to move in pitch only and the control system was operated in 1DOF pitch tracking mode (§3.3). First, the model was trimmed at $\alpha = 3°$ by adjusting the servo torque u_{m} until the airfoil held its pitch angle with approximately zero mean flow control input ($\overline{u_{\mathrm{f}}} \approx 0$). Then, the controller was issued a series of step commands (Figure 6.1a, black) from $\alpha = 0°$ to $6°$. The phase-averaged trajectory of the model over 100 cycles is shown in Figure 6.1a (blue), and the time-history of the flow control input u_{f} is shown in Figure 6.1b. Following the pitch-up command at $t = 0$, the controller activates the SS actuators ($u_{\mathrm{f}} = -1$) for $0 < t/T_{\mathrm{conv}} < 6.4$ in order to generate the necessary nose-up pitching moment. By $t = 6.5T_{\mathrm{conv}}$ the model has pitched up to $\alpha = 2.2°$ and the controller activates the SS actuators ($u_{\mathrm{f}} = 1$) over $6.5 < t/T_{\mathrm{conv}} < 8$ in order to slow the pitch rate. The model overshoots the $\alpha = 6°$ target at $t = 11T_{\mathrm{conv}}$ and the SS actuators remain engaged until $t = 22T_{\mathrm{conv}}$ when $\alpha = 7.8°$ (following a peak of 8.4° at $t = 18.5T_{\mathrm{conv}}$). For $22 < t/T_{\mathrm{conv}} < 50$, the actuation command oscillates several times before bringing the model to rest at $\alpha = 6°$ at which point the actuation command settles to a time-invariant level that is required to balance the pitching moment C_{M} at that angle. It should be noted that the overshoot in α (about $2.4°$) is associated with the diminished effectiveness of the SS actuators as the angle of attack increases.

The plunge-down command from $\alpha = 6°$ to $0°$ (Figure 6.1a) is issued at $t = 131T_{\mathrm{conv}}$. The pitch trajectory and u_{f} history following the step command are similar to the pitch-up transition, though with inverted u_{f} input as shown in Figure 6.1b. For $131 < t/T_{\mathrm{conv}} < 140$, SS actuation ($u_{\mathrm{f}} = 1$) is applied to effect a nose-down pitching moment which accelerates the model towards the target $\alpha = 0°$. At $t = 141T_{\mathrm{conv}}$, the pitch angle decreases to $2°$ and u_{f} switches sign engaging PS actuation to slow the model. The flow control state $u_{\mathrm{f}} = 1$ persists through $146T_{\mathrm{conv}}$ where $\alpha = -0.6°$. As in the pitch-up transition, the airfoil overshoots slightly (reaching $\alpha = -0.9°$ at $148T_{\mathrm{conv}}$). This overshoot is not as large for the pitch-down transition (as it was for pitch-up) since PS actuation is more effective at lower α. However, the lower effectiveness of the SS actuation is evident in the rise time of $\Delta t = 13T_{\mathrm{conv}}$ for the pitch-down transition compared to $11T_{\mathrm{conv}}$ during pitch-up.

The small variations in the servo torque u_{m} during the maneuver (Figure 6.1c) stabilize the bending of the wind tunnel model. When the traverse is configured in 1DOF mode (i.e., the vertical displacement of airfoil support bar is held fixed at either end of the tunnel as discussed in §3.3), an unstable coupling is set up between the actuation input u_{f} and the first bending mode of the airfoil model. Without any correction, unsteady actuation inputs excite the bending mode with an oscillation amplitude which grows large enough to damage the system components. This coupling was mitigated by feeding back to the pitch servo actuator the first derivative of the load cell mounted opposite the pitch servo. It is important to note, however, that no pitch information is fed to the servo- the tracking is entirely effected by the flow control actuators.

The pitch tracking maneuver discussed above was also executed when the controller was operated in servo control mode as discussed in (§3.2). In order to facilitate comparison between flow control and servo control, the servo output was regulated using software such that the controller exhibited the same nonlinear gain and α dependence as the flow control actuators. The resulting pitch trajectory α and normalized servo torque u_{m} are shown in

Figures 6.1a and c, respectively (red). In these figures, u_{m} is normalized by $\frac{1}{2}\rho U_0^2 c^2$ (i.e., consistent with the pitching moment coefficient C_{M}). The successful matching of the servo torque (by adjusting the controller gain as described above) to the flow-control-provided torque is evident in the nearly identical rise times following the step transitions at $t = 0$ and $131T_{\mathrm{conv}}$. The trends of u_{m} and u_{f} are similar in that the pitch servo first applies torque to accelerate the model and then an opposing torque to slow it down near the target α. Note, however, that u_{m} does not saturate like u_{f}, (e.g., $0 < t/T_{\mathrm{conv}} < 6$), but varies with α according to the gain look up table which adjusts the available torque for a given α.

For both step-up and step-down, the overshoot is smaller when the model is controlled by the pitch servo (Figure 6.1b). This may be explained by considering the time-history of the aerodynamic pitching moment in Figure 6.2a which shows the change in phase-averaged aerodynamic pitching moment ΔC_{M} during the maneuver (blue) along with the corresponding static change $\Delta C_{\mathrm{Ms}}(\alpha, u_{\mathrm{f}})$ (green). These data show that ΔC_{M} tracks ΔC_{Ms} reasonably well within the bandwidth of the force measurements. However, as discussed in Chapter 5, the onset and termination of flow control actuation takes place over a period of several convective time scales, whereas the torque provided by the pitch servo is realized on $O(0.1T_{\mathrm{conv}})$ following the command.

The more important features, however, of ΔC_{M} and ΔC_{L} (Figure 6.2a and b, respectively) are the magnitudes of the changes in aerodynamic forces during the flow-controlled maneuver: C_{M} varies over ± 0.05 under flow control, compared to ± 0.01 under servo control and $\Delta C_{\mathrm{L}} = 0.5$ due to the change in α for both actuation modes. Note that the transients under flow control ($-0.2 < \Delta C_{\mathrm{L}} < 0.9$) are larger than under servo control ($0 < \Delta C_{\mathrm{L}} < 0.7$).

6.1.2 The Trailing Edge and Near-Wake Flow Fields

The flow field near the trailing edge of the airfoil was investigated using PIV measurements which were phase-locked to the α command. Figure 6.3 shows raster plots of spanwise vorticity concentration with overlaid velocity vectors when the airfoil is at $\alpha = 5°$ during pitch-up (Figure 6.3a,b), static model (c,d), and during pitch-down (e,f). The left and right columns correspond to flow and servo control, respectively. Figure 6.3 is acquired $9.5T_{\mathrm{conv}}$

following the pitch-up and pitch-down commands at $t = 0$ and $137T_{\mathrm{conv}}$, respectively. This particular time during the maneuver was selected in order to exclude transient effects and focus on the effect of the unsteady motion of the model compared to steady actuation on the stationary model. As noted in connection with Figure 6.1, unlike the servo control command, the flow control actuation command u_{f} is saturated at 1 for $8 < t/T_{\mathrm{conv}} < 22$. During flow control actuation on the moving model (Figures 6.3a&e), the vorticity layer along the airfoil surface (between the downstream edge of the Coanda and the trailing edge) is considerably thicker than when the airfoil is stationary (Figure 6.3c). The features of the vorticity concentrations in the unsteady flow during the pitch-up (Figure 6.3a) and pitch-down (Figure 6.3e) motion are similar even though the airfoil is pitching in opposite sense. This indicates that the motion probably affects the boundary layer on the suction surface of the airfoil (upstream of the actuator) but the attached flow is insensitive to the sense of the pitch. Although the changes in the aerodynamic lift and pitching moment that are induced by servo control are similar in magnitude to the changes induced by flow control, the unsteady flow field in the presence of servo control is vastly different from the flow under flow control. Figures 6.3b&d show that under servo control the flow downstream of the SS actuator is separated with significant recirculation within the separated domain as evidenced by the CCW vorticity layer near the surface. Furthermore at this pitch angle, the (CCW) vorticity layer from the pressure side protrudes farther up into the wake which appears to be vectored up compared to the flow controlled by the jet actuators. The flow in the presence of servo control appears to be insensitive to the sense of the pitch and is similar to the flow about the static airfoil at the same angle of attack. The similarity of the flow images over the pitching airfoil to the flow over the stationary airfoil indicates (as confirmed by Figure 6.2) that, with the exception of the flow transients that are associated with the onset and termination of the top hat trajectory, the motion does not alter the static forces.

Unsteady effects are evident in the presence of flow control during the actuation onset immediately following the top hat command. Raster plots of spanwise vorticity with overlaid velocity vectors are shown in Figure 6.4 for $0.13 < t/T_{\mathrm{conv}} < 0.66$ following the pitch-up command. At $t = 0.13T_{\mathrm{conv}}$ (Figure 6.4a), the airfoil is at rest at $\alpha = -0.28°$ as the actuation command transitions from the trim level of $u_\mathrm{f} = 0.05$ to $u_\mathrm{f} = -1$ in response to the pitch command. As the PS actuators are engaged, the CCW shear layer is pinched to form a large CCW vortex which is advected into the near wake (Figures 6.4b-f). This shedding is accompanied by a momentary reduction in lift which is evident in 6.4b. The CCW vortex appears to induce the formation of a CW vortex which is located at $x = 1.08c$ at $t = 0.33T_\mathrm{conv}$ (Figure 6.4d). As this vortex advects out of the flow domain (Figures 6.4g-i), it is followed by another CCW vortex (Figures 6.4g-i).

A similar transient is visible following the pitch-down command (Figure 6.5). For convenience, let $t' = t - 131T_\mathrm{conv}$ be the time which has passed since the pitch-down command. The airfoil is initially at rest at 6° with $u_\mathrm{f} = 0.26$ (Figure 6.5a-b). The thick ($\Delta y \approx 0.7c$) CCW vorticity layer is a feature of the higher angle of attack noted in §4.3. At $t' = 0.26T_\mathrm{conv}$, a CW vortex appears at the upstream edge of the field of view ($1 < x/c < 1.02$) which is rolled-up by the severing of the suction side vorticity layer as discussed in (Figure 6.5c) for $\alpha = 3°$. This CW vortex continues to grow in circulation as it moves downstream (Figures 6.5d-e) with a peak vorticity of $\omega_z c/U_0 = 43$ at $x/c = 1.09$ and $t' = 0.39T_\mathrm{conv}$ (Figure 6.5e). As the CW vortex advects downstream, it induces a rolling-up of a CCW vortex behind it (Figures 6.5f-g) that is advected downstream (Figures 6.5h-i).

To facilitate study of the wake dynamics for longer times, the local vorticity flux $u\omega_z$ into the wake is extracted from the PIV measurements at $x/c = 1.05$. Phase-averaged maps of $u\omega_z$ are plotted as a function of y/c and t/T_conv following the pitch-up and pitch-down commands in Figures 6.6a and b, respectively. Considering first the pitch-up maneuver (Figure 6.6a), following the passage of the CCW (blue) and CW (red) vortices at $t = 0.20$ and 0.26, respectively (cf. Figures 6.4b and c), vortices of alternating sign continue to shed from the trailing edge as long as $u_\mathrm{f} = -1$ (i.e., through $t = 6T_\mathrm{conv}$). The period of this vortex shedding is $0.26T_\mathrm{conv}$ which corresponds to a reduced frequency $St_\mathrm{wake} = 3.8$. This is comparable to the value 5.1 computed by Lopez *et al.* (2011) in a numerical investigation of a similarly modified NACA 4415. The same organized shedding is not evident following the transition $0 \rightarrow SS$ in response to the pitch-down command (Figure 6.6b).

Vorticity flux maps for the duration of the PIV measurements ($0 < t/T_\mathrm{conv} < 49$) are shown in Figure 6.7 for both the flow-controlled and servo-controlled maneuvers. Note again the separation of time scales between the actuation dynamics and the airfoil motion $O(T_{\text{conv}}) = 1$ and 10, respectively. These wake surveys also highlight the fact that in the flow-controlled cases (Figures 6.7a-b), the C_{M} required to move the airfoil is generated by modifying the flow field about the airfoil, the evidence of which is naturally washed into the wake. In contrast, when the motion of the airfoil is controlled by the servo motor, the wake dynamics essentially amount to a shifting of the wake in the cross-stream direction corresponding to the motion of the trailing edge.

6.2 Closed-Loop Control of Pitch and Plunge

An important objective of the present work is the demonstration of 2DOF closed-loop control in pitch (α) and plunge (y) by using the flow control actuators. In these experiments, the airfoil is free to maneuver in both degrees-of-freedom while the vertical forces that are applied at each spanwise end of the model are regulated by the force controller (§3.4.1). Maneuvering of the airfoil in 2DOF is accomplished using a longitudinal flight controller (discussed in §3.4.1) which operates independently of the force controller and utilizes flow control actuation to achieve a desired trajectory of the airfoil. Effective 2DOF control is demonstrated first by tracking a commanded plunge trajectory (§6.2.1) and then by maintaining a fixed vertical elevation in the presence of a force disturbance in lift (§6.2.2).

6.2.1 Tracking Step Changes in Plunge

Trajectory tracking in two degrees-of-freedom is demonstrated when the longitudinal flight controller is given step changes in plunge from $y = -0.2c$ to $0.2c$ (Figure 6.8a). Initially, the actuation command is at a trim value of $u_{\text{f}} = 0.2$ (Figure 6.8c). The pitch servo torque is deliberately trimmed to a slight nose-up moment, requiring the SS actuators to be partially engaged in order to maintain steady level flight. This low-level of actuation helps stabilize the otherwise unsteady flow between the SS actuator and the trailing edge which can cause the controller to fall into limit cycles in pitch and plunge.

Following the plunge up command at $t = 0$, u_{f} decreases to -0.27 in order to generate the necessary nose-up pitching moment to accelerate the model in α (Figure 6.8b). As α

increases, ΔC_{L} increases which accelerates the airfoil in plunge. In order to keep α within an operational range, for $6.4 < t/T_{\mathrm{conv}} < 22$, u_{f} is increased to 0.6 to generate a nose-down moment, slowing the airfoil's pitch rate. At $t = 23$, the model has risen to $y = -0.18c$ with $\alpha = 6.7°$. At this point α begins to decrease, which decreases ΔC_{L} and thereby slows the plunge rate. The pitch angle continues to decrease to $\alpha = 1.5°$ at $t = 56T_{\mathrm{conv}}$ at which point ΔC_{L} reaches a minimum level of -0.19 (Figures 6.9b). For $56 < t/T_{\mathrm{conv}} < 120$, y continues to increase ultimately reaching a maximum height of $y = 0.22c$ before leveling out to $y = 0.21c$ ($120 < t/T_{\mathrm{conv}} < 328$). A similar process is evident following the step down transition at $t = 328T_{\mathrm{conv}}$.

The time histories of ΔC_{M} and ΔC_{L} are shown in Figures 6.9a and b, respectively. Following the decrease in u_{f} over $0.6 < t/T_{\mathrm{conv}} < 6.3$, ΔC_{M} increases to 6.8 providing the necessary moment to start the positive acceleration in α (Figures 6.9a). For $6.3 < t/T_{\mathrm{conv}} < 21$, ΔC_{M} decreases to -0.023, which first slows the airfoil to rest at $\alpha = 6.7°$ ($t = 23T_{\mathrm{conv}}$) and then causes the airfoil to pitch back down, ultimately reaching 1.5° at $56T_{\mathrm{conv}}$. Throughout the maneuver, the trend of ΔC_{M} follows very closely that of u_{f}, as the pitching moment is largely independent of α In contrast, ΔC_{L} (Figures 6.9b) varies almost linearly with α and thus the time-history of ΔC_{L} closely follows that of α. However, the evidence of flow control is directly visible in the lift as well. For example, immediately following the plunge-up command at $t = 0$, a small decrease (0.05) in ΔC_{L} occurs for $0 < t < 8$ as α essentially remains constant. This decrease in lift directly results from the modification of the pressure distribution on the airfoil by the actuation. Similarly, a slight increase in ΔC_{L} is evident over $328 < t/T_{\mathrm{conv}} < 338$ for the same reason.

6.2.2 Disturbance Rejection

An important aspect of the present work is the ability to demonstrate controlled rejection of momentary aerodynamic disturbances (e.g., gust) that is accomplished exclusively by flow control actuation. In the present experiments this capability is demonstrated using an external momentary force which is applied using the force controller asynchronously with the longitudinal flight controller to simulate a sudden gust. The applied disturbance

C_{Fcmd} (Figure 6.10a, black line) corresponds to a momentary change in lift $\Delta C_{\text{L}} = 0.43$ (corresponding to a static change in angle of attack of $\Delta\alpha = 4.8°$) with a nominal duration of $10T_{\text{conv}}$. The disturbance waveform is generated by applying a second order low pass filter with a natural frequency of 25 rad/sec to a square-wave type pulse with the desired amplitude and duration. The peak force applied by the force controller ($C_{\text{Fcmd}} = 0.43$) is delayed by approximately $4T_{\text{conv}}$ relative to the disturbance command. The actual disturbance force C_{F} realized by the force controller is plotted in blue (Figure 6.10a).

The response of the wind tunnel model to the disturbance is shown in Figures 6.10b-d along with the corresponding ΔC_{L} and ΔC_{M} (Figures 6.10e and f). As the model begins to accelerate upwash as a result of the disturbance force (Figure 6.10b), the flight controller (Figure 6.10d) responds by commanding $u_{\text{f}} = 0.87$ at $t = T_{\text{conv}}$ to effect nose-down pitching moment (Figure 6.10e). For $1 < t/T_{\text{conv}} < 10$, the model pitches down from $\alpha = 2.8°$ to $1.1°$. During this time u_{f} changes sign several times but is on average positive. These oscillations in control signal correspond to a frequency of 16 Hz and result from the flow control coupling with the spanwise bending of the wind tunnel model. These oscillations are also evident (although much less prominently) in the time history of α (Figure 6.10c). At $t = 16.5$, the airfoil reaches a minimum in pitch ($\alpha = -0.27°$) which corresponds to the minimum $\Delta C_{\text{L}} = -0.42$. (Note this is approximately equal to the magnitude of the initial disturbance.) The maximum plunge excursion of $y = 0.036c$ occurs at $t = 19T_{\text{conv}}$. As y decreases back towards zero ($20 < t/T_{\text{conv}} < 40$), the controller applies increasing levels of u_{f} to pitch the airfoil up. Ultimately both α and y settle out by $t = 100T_{\text{conv}}$.

The 2DOF controller is also tested in the presence of a downwash disturbance (Figure 6.11). The disturbance magnitude $C_{\text{Fcmd}} = -0.43$ (Figure 6.11a) is equal and opposite to the upwash disturbance. Following the simulated gust, the controller regulates u_{f} (Figure 6.11d) to vary the pitch angle over $1.6° < \alpha < 5.6°$ (Figure 6.11c). The plunge excursion is limited to $|\Delta y| = 0.026c$. As with the upwash disturbance, the maximum ΔC_{L} generated during the recovery is approximately equal in magnitude to the disturbance force.

The most remarkable feature of the disturbance rejection maneuver is the rapid response time of the flow control to the disturbance. To illustrate this, C_{F}, u_{f}, and the angular acceleration of the airfoil $\ddot{\alpha}$ are plotted in Figures 6.12a-c, respectively for the first $5T_{\mathrm{conv}}$ following the maneuver for the upwash and downwash disturbances. Consider first the upwash disturbance (blue). At $t = 0.85T_{\mathrm{conv}}$, the disturbance input has reached approximately 30% of its final value ($C_{\mathrm{F}} = 0.12$, Figure 6.12a) and the controller applies $u_{\mathrm{f}} = 0.87$ (Figure 6.12b) to generate the necessary nose-down pitching moment to decrease α as discussed above. The model, which begins to accelerate up in pitch at $t = 0.79T_{\mathrm{conv}}$, reaches its maximum acceleration of $\ddot{\alpha}c^2/U_0^2 = 1.5 \cdot 10^{-3}$ at $t = 2.7T_{\mathrm{conv}}$ indicating that the flow control is effecting the maximum nose-down pitching moment. Note that the time scale associated with the generation of these aerodynamic forces is so short that they cannot be resolved by the traverse sensors (cf. 2.5). Nonetheless, the angular acceleration provides concrete evidence of the change in pitching moment.

The response is even faster for the downwash disturbance owing to the larger maximum pitching moment available from the *PS* actuators. As for the upwash disturbance, actuation reaches the full level (here, $u_{\mathrm{f}} = -1$) at $t = 0.98T_{\mathrm{conv}}$ which causes the model to begin accelerating in pitch at $t = 1.1T_{\mathrm{conv}}$. While the airfoil reaches its peak acceleration by $t = 2.6T_{\mathrm{conv}}$ (similar to the $2.7T_{\mathrm{conv}}$ for the upwash disturbance), the acceleration magnitude is $\ddot{\alpha}c^2/U_0^2 = 2.7 \cdot 10^{-3}$. The larger acceleration magnitude is indicative of the larger pitching moment effected by the *PS* actuators. Because of the higher acceleration, the airfoil more quickly reaches the target α and consequently generates the required lift force necessary to recover from the gust.

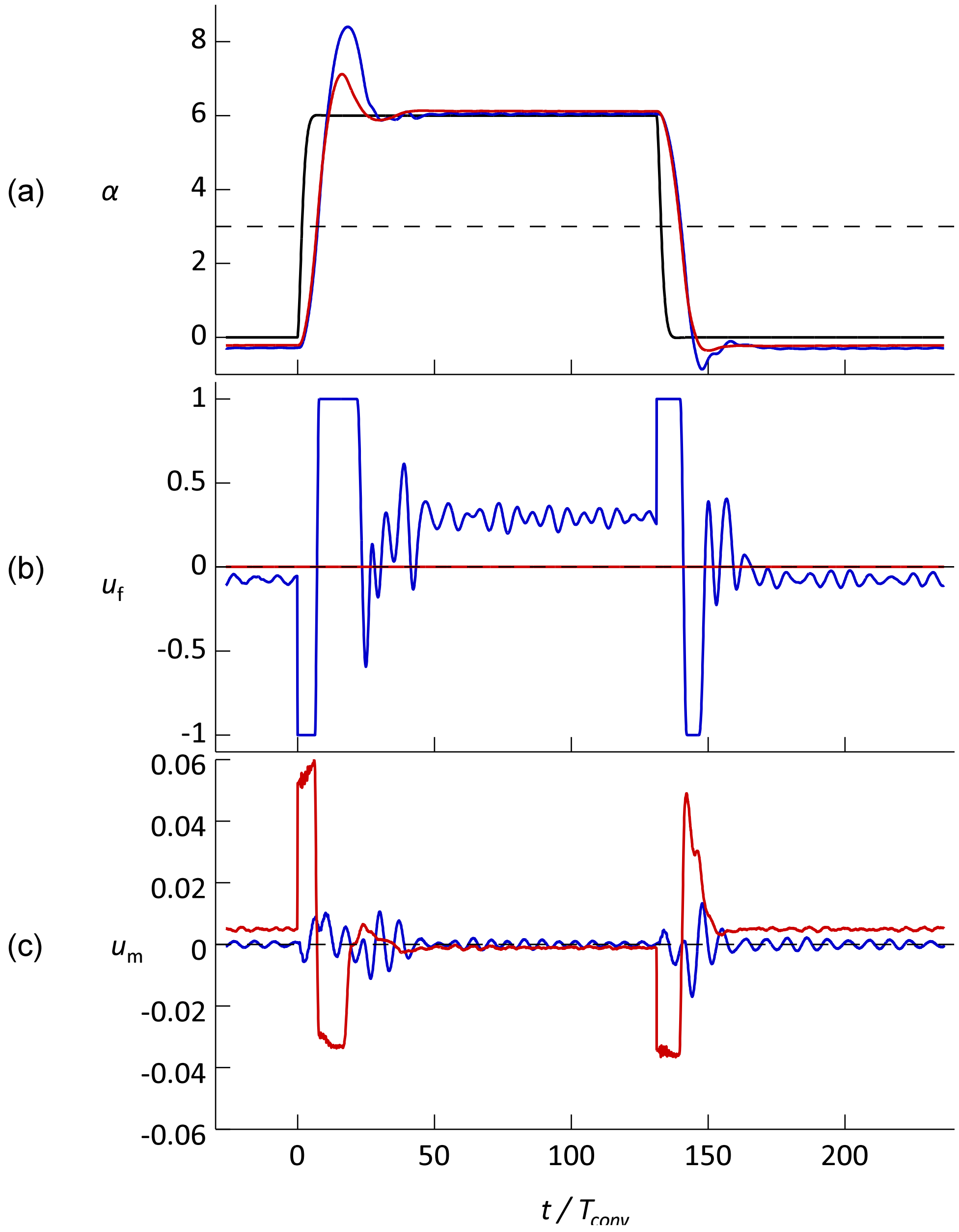

Figure 6.1: Time histories of (a) α , (b) u_f, and (c) u_m when the controller is commanded to track a top hat trajectory in α (▬) using the flow control actuators (▬) and the pitch servo actuator (▬).

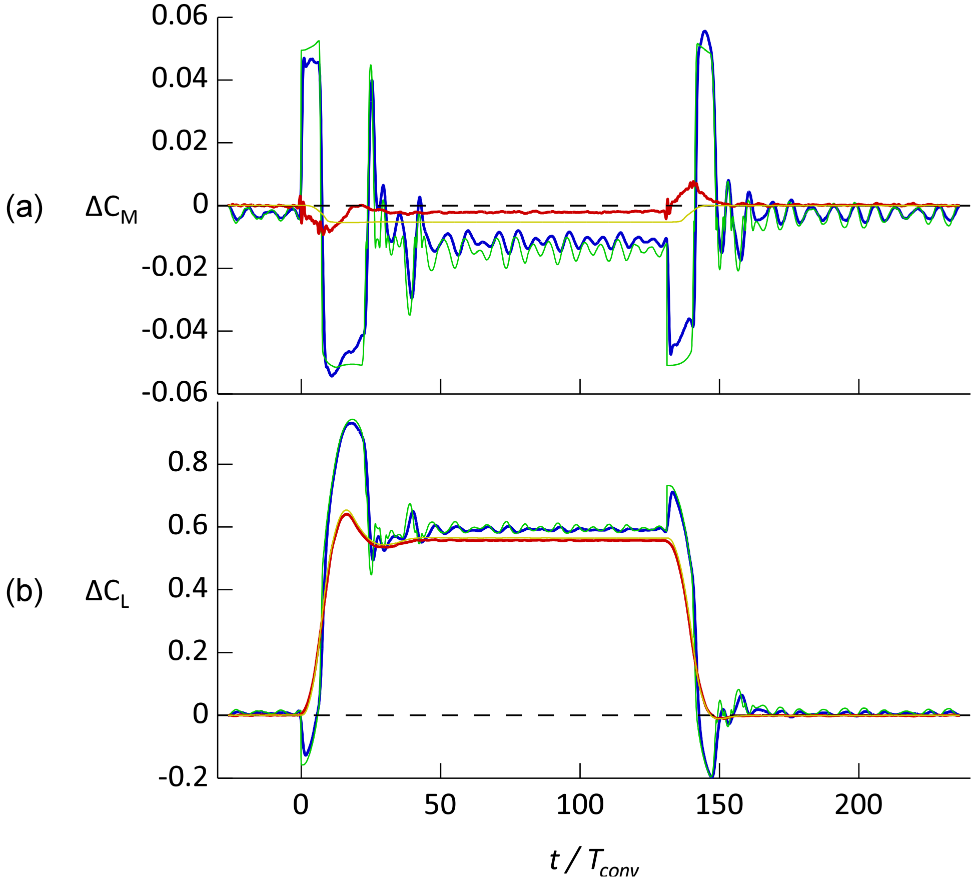

Figure 6.2: Time histories of (a) ΔC_{M} and (b) ΔC_{L} when the controller is commanded to track a top hat trajectory in α (⬛) using the flow control actuators (🟦) and the pitch servo actuator (🟥). Corresponding steady-state values based on a look up table using α and u_{f} for flow control (🟩) and servo control (🟨).

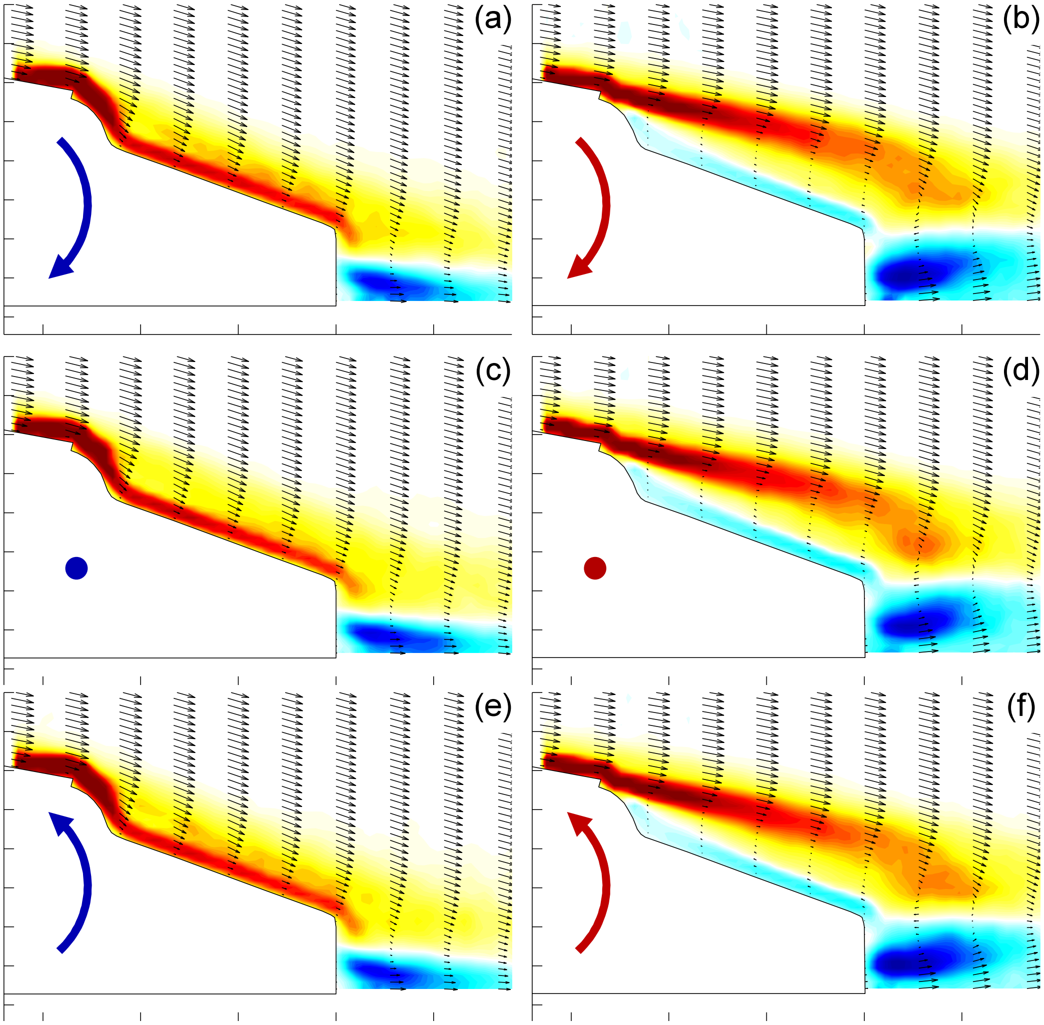

Figure 6.3: Raster plots of phase-averaged spanwise vorticity ω_z with overlaid velocity vectors when the model is driven by (a,e) the flow control actuators and (b,d) the pitch servo during (a,b) pitch-up and (e,f) pitch-down past $\alpha = 5°$ along with the corresponding fields for the static model (c and d, respectively).

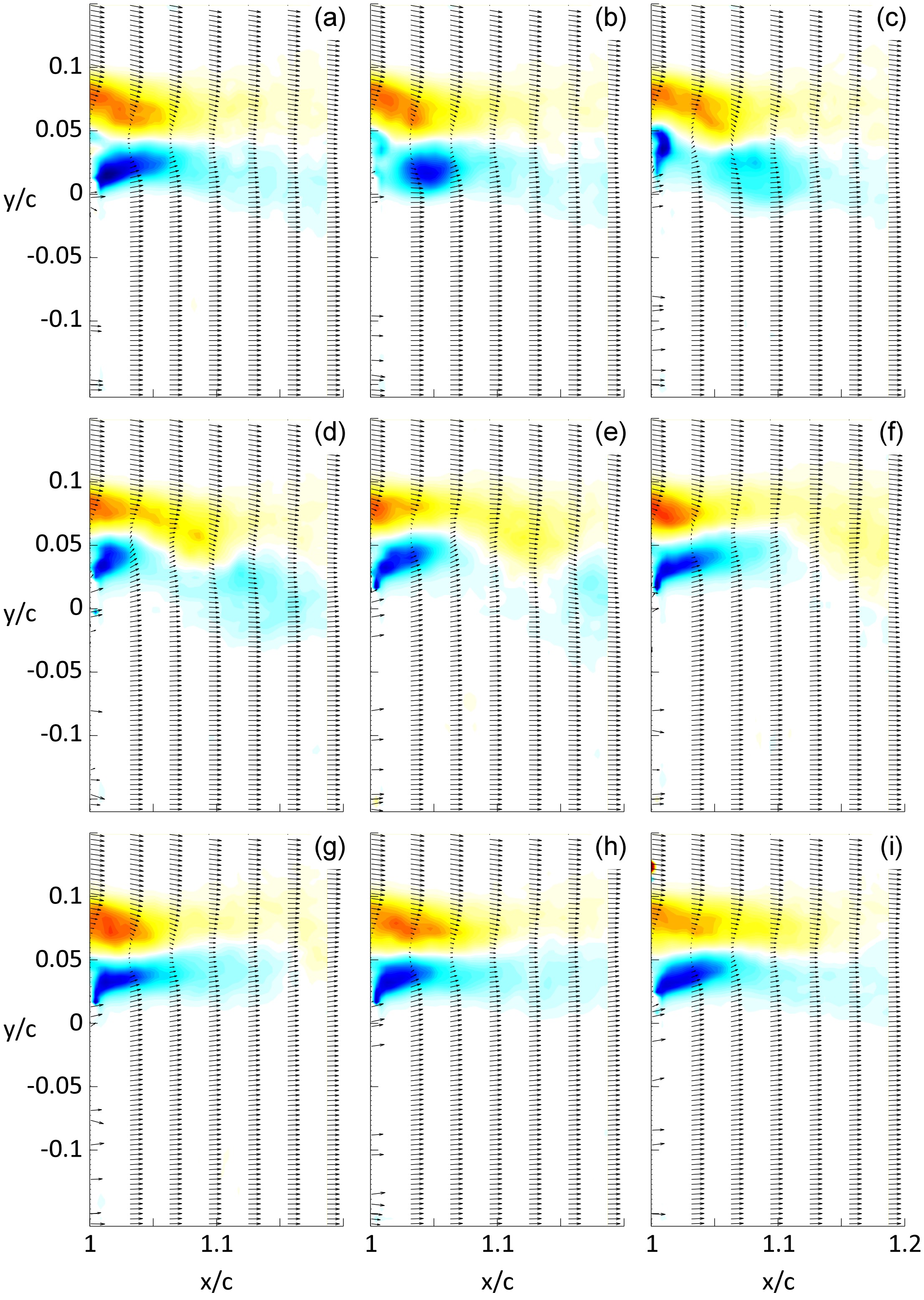

Figure 6.4: Raster plots of phase-averaged spanwise vorticity ω_z with overlaid velocity vectors immediately following a pitch-up command from $\alpha = 0^\circ$ to 6° when the model is driven in pitch by the flow control actuators.

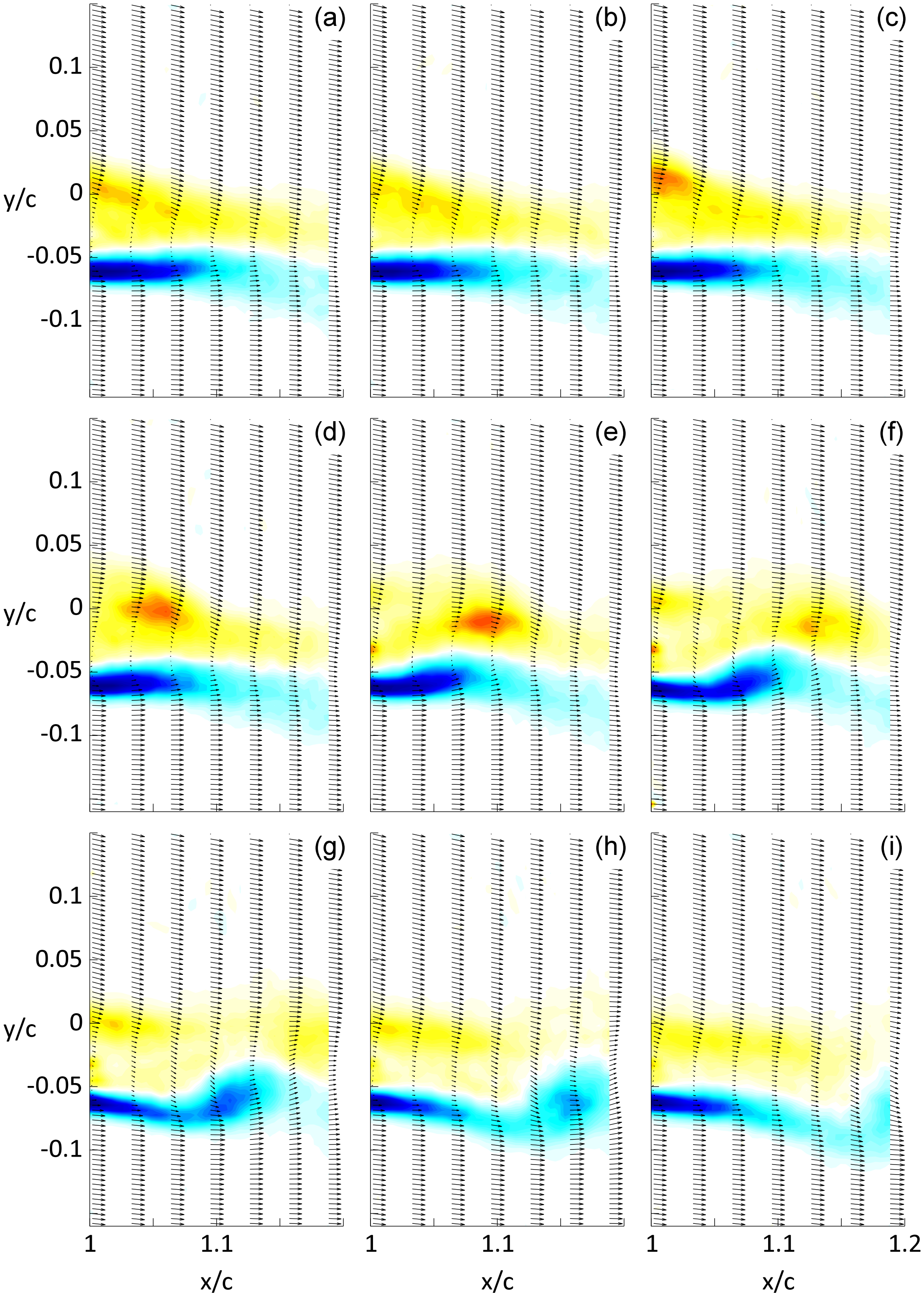

Figure 6.5: Raster plots of phase-averaged spanwise vorticity ω_z with overlaid velocity vectors immediately following a pitch-down command from $\alpha = 6°$ to $0°$ when the model is driven by the flow control actuators.

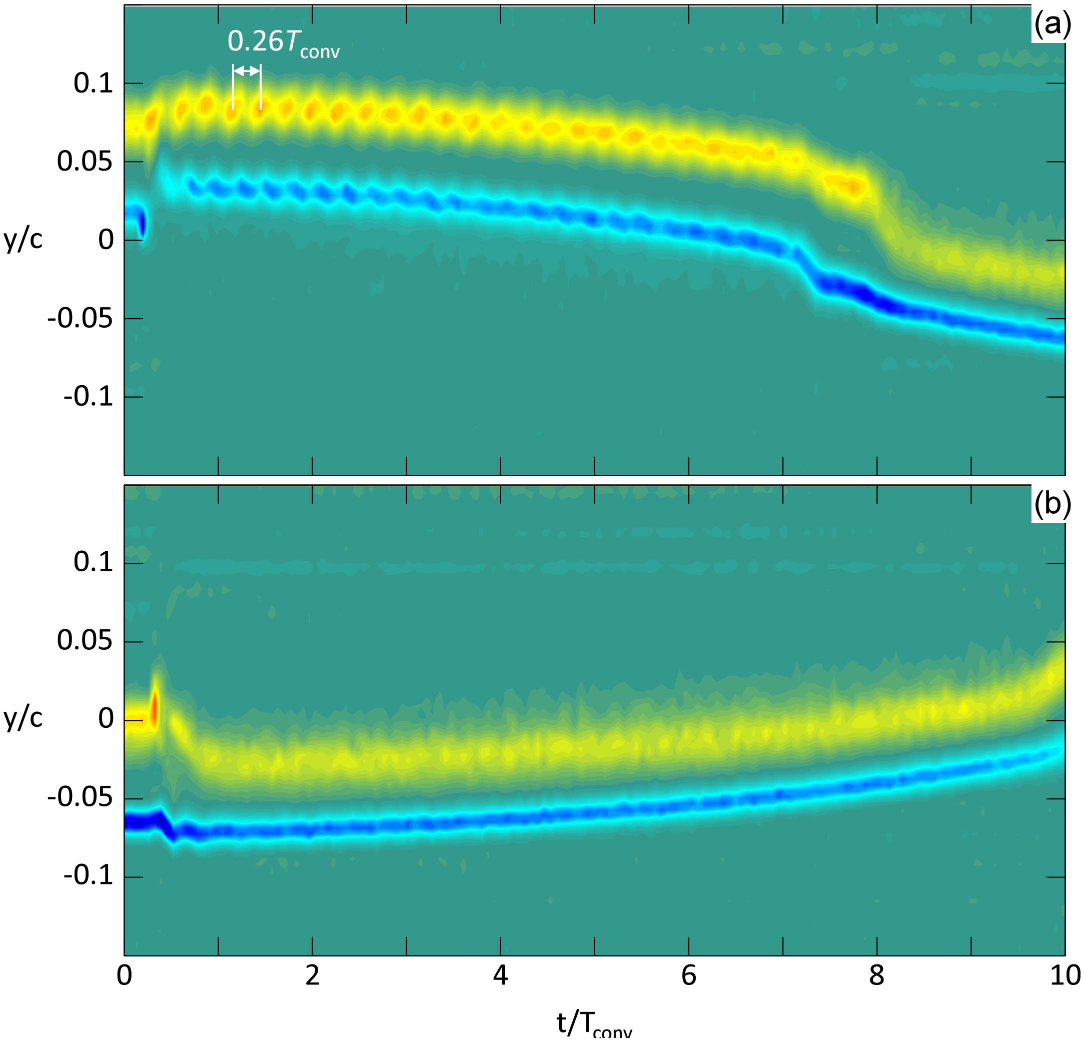

Figure 6.6: $y - t$ maps of vorticity flux at $x/c = 1.05$ for $t < 10T_{\text{conv}}$ following a (a) pitch-up and (b) pitch-down command when the model is driven by flow control.

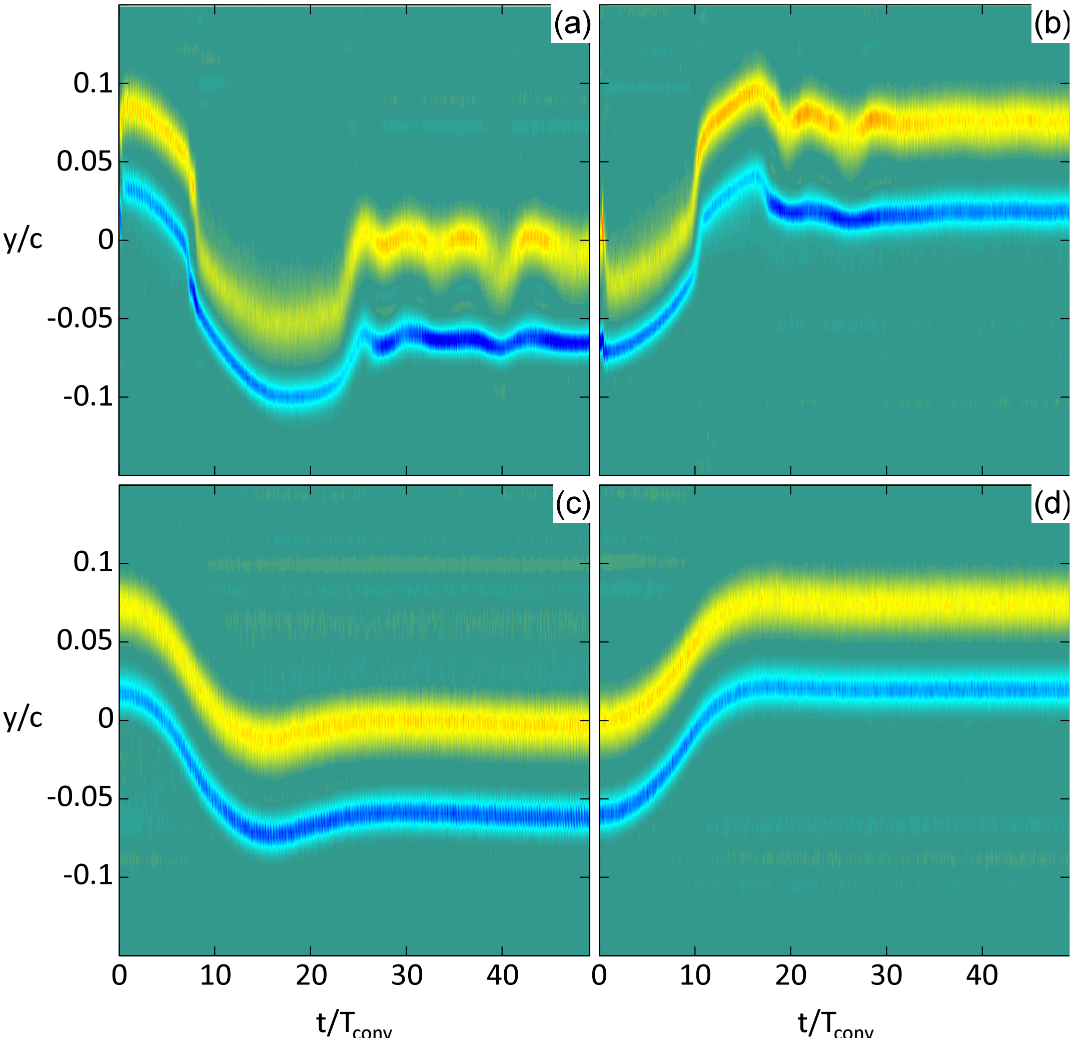

Figure 6.7: $y - t$ maps of vorticity flux at $x/c = 1.05$ following a (a,c) pitch-up and (b,d) pitch-down command when the model is driven by (a,b) flow control and (c,d) servo control.

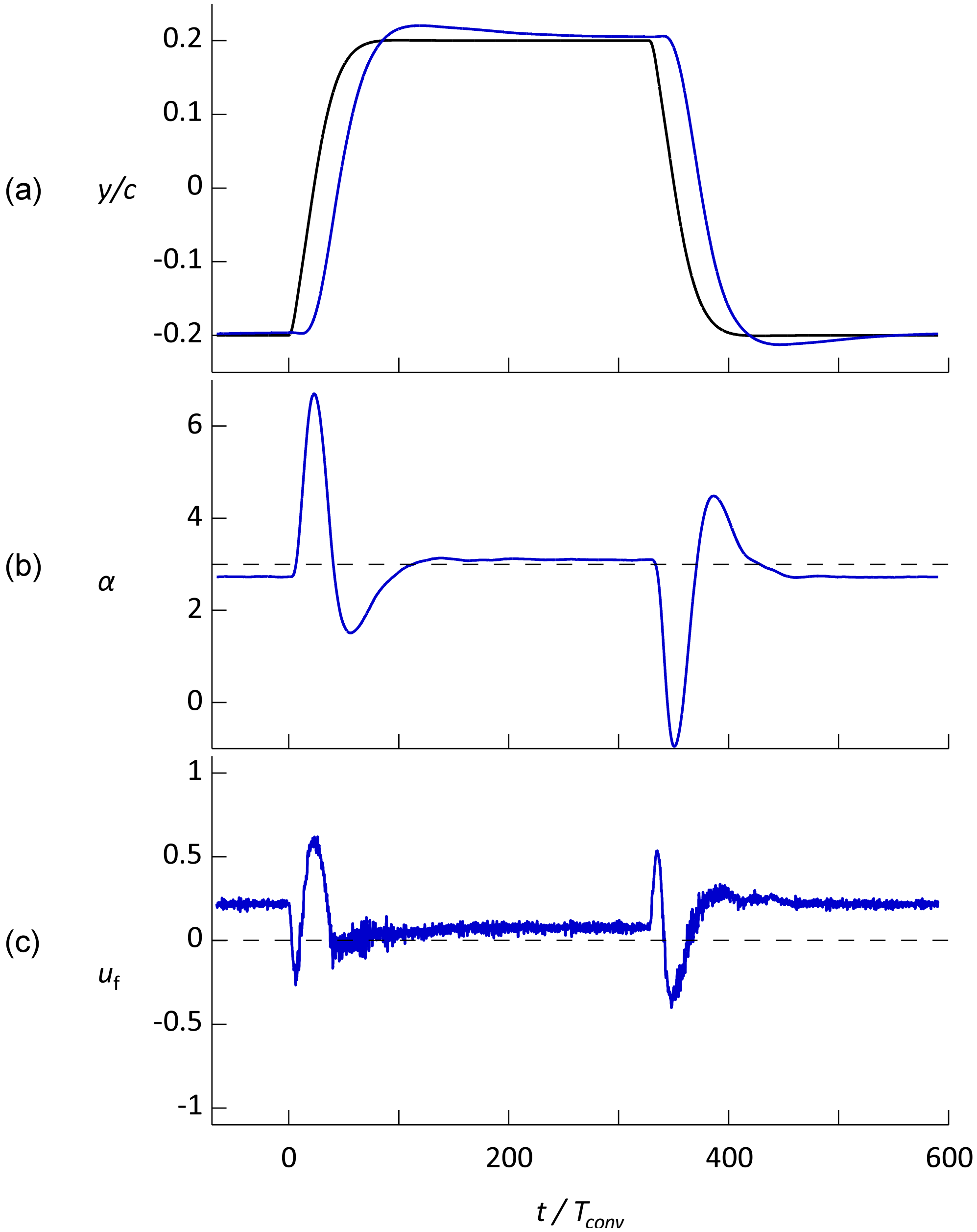

Figure 6.8: Time histories of (a) y/c, (b) α, and (c) u_f when the controller is commanded to track the square wave trajectory (▬) in plunge with the flow control actuators.

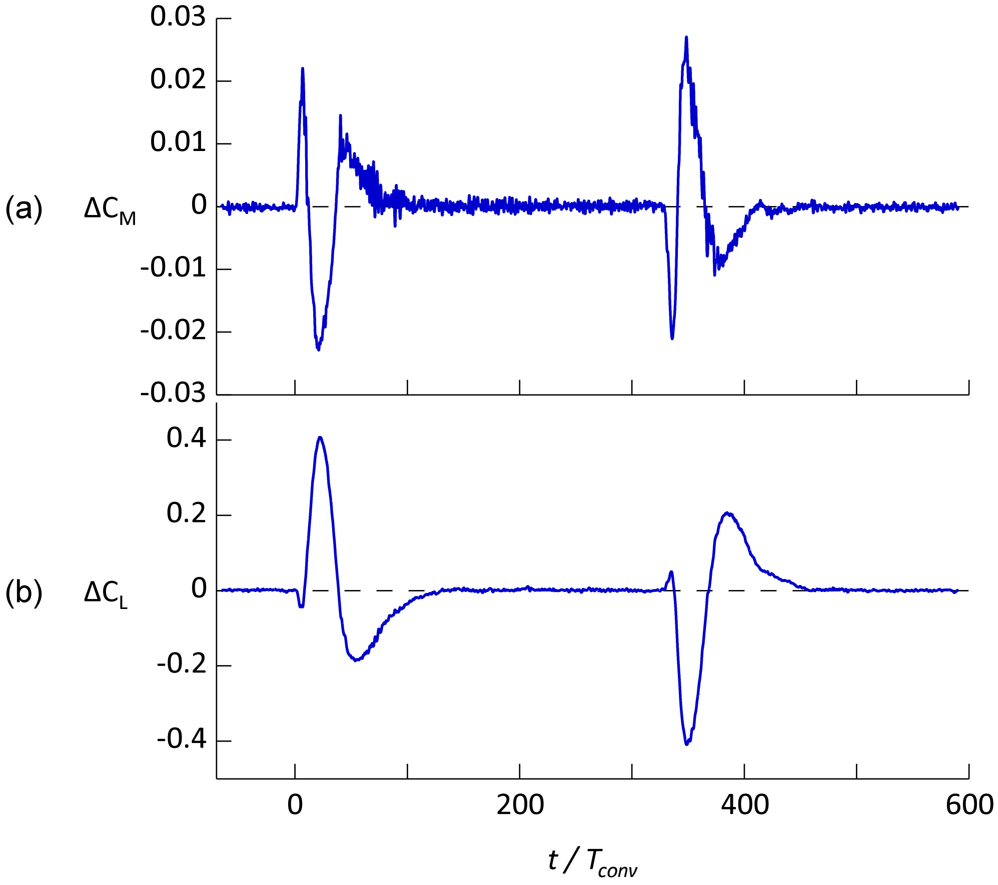

Figure 6.9: Time histories of (a) ΔC_{M} and (b) ΔC_{L} when the controller is commanded to track a square wave trajectory in plunge using the flow control actuators.

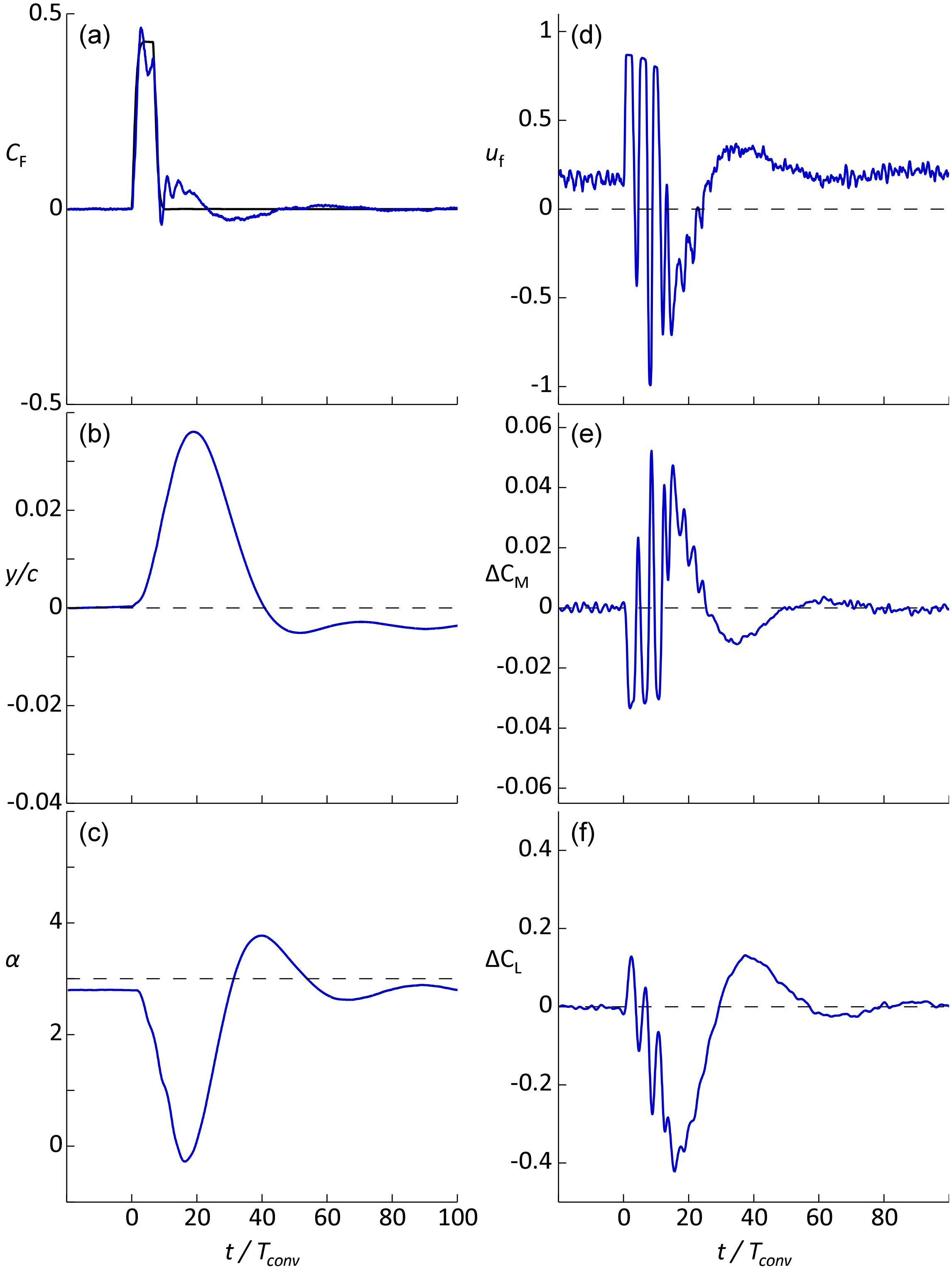

Figure 6.10: Time histories of (b) y/c, (c) α, (d) u_f, (e) ΔC_M, and (f) ΔC_L following (a) an upwash force disturbance C_F.

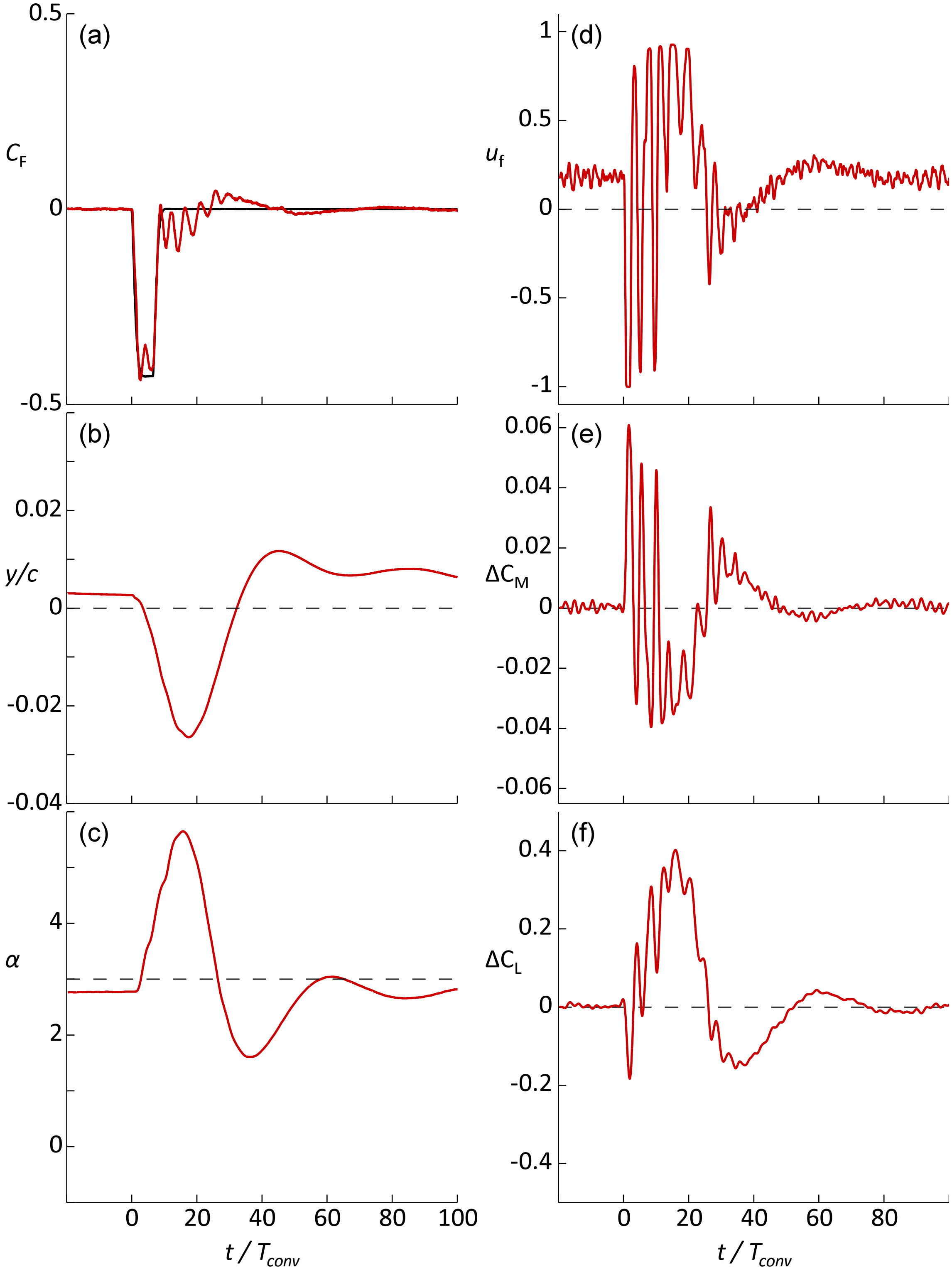

Figure 6.11: Time histories of (b) y/c, (c) α, (d) u_f, (e) ΔC_M, and (f) ΔC_L following (a) an downwash force disturbance C_F.

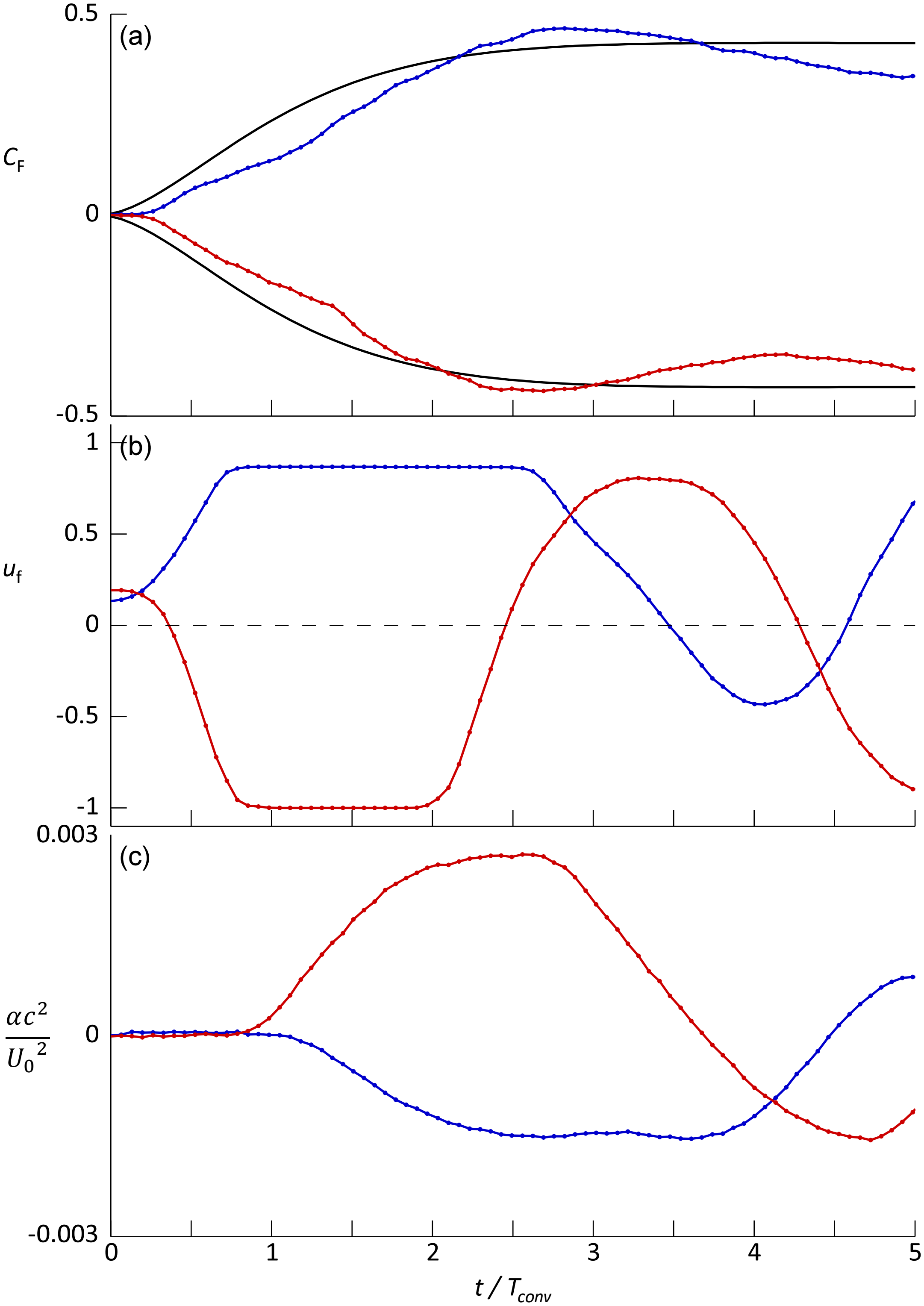

Figure 6.12: Time histories of (a) C_{F}, (b) u_{f}, and (c) $\ddot{\alpha}c^2/U_0^2$ for $0 < t/T_{\mathrm{conv}} < 5$ following an upwash (▬) and downwash (▬) disturbance.

Chapter VII

EXPERIMENTAL VALIDATION OF REDUCED-ORDER VORTEX MODEL

A reduced order model (ROM) for the controlled flow over the airfoil was developed by Tchieu & Leonard (2011). The model was developed to describe the state of the controlled flow using ordinary-differential equations which are suitable for an adaptive control architecture for dynamic flight maneuvering. An additional attribute of the ROM is that it can provide insight into the fluid dynamic processes during unsteady two-dimensional maneuvers effected and, in particular, estimates of the unsteady lift force and pitching moment on the airfoil on relatively short time scales (i.e, $T_{\text{conv}} \sim O(1)$) Muse *et al.* (2009) employed a linearized version of the ROM consisting of only three flow states. These states included the circulation of a control vortex, and the circulation and streamwise position and circulation of a single wake vortex propagating at the free stream speed and having the instantaneous circulation necessary for momentum conservation. This model was integrated into an adaptive control architecture which was used to track commanded trajectories in pitch and plunge. The authors demonstrated an marked improvement in the controller performance relative to a controller based on a static actuator model.

As part of the present investigation, the fidelity of the ROM model was enhanced by Tchieu and Leonard by including a continuous vortex sheet following the analysis of von Kármán & Sears, 1938. The structure of this vortex sheet (and the lift imparted onto the airfoil) are computed both from the vorticity flux into the wake (measured experimentally using PIV) and the time-rate of change of the bound circulation. In the previous chapters, the lift force and pitching moment were measured directly using the sensors of the 2DOF traverse. While this method of estimating the unsteady lift and pitching moment gives excellent results, it is clearly limited by the bandwidth of the traverse to about 20 Hz. However the ROM can be used to measure the changes in aerodynamic forces on shorter time scales which are on the order of (or ideally less than) the convective time over the airfoil T_{conv} (approximately 15 msec). In the present work, the ROM is used in conjunction with flow measurements to assess instantaneous the aerodynamic force and moment that result from time-dependent flow control in the wind tunnel.

7.1 Overview of the Modified ROM

The airfoil is modeled as a 2D thin flat plate having chord c that is undergoing small amplitude motions in pitch and plunge about an axis located a distance a upstream of the midchord (Figure 7.1). The pitch angle α and plunge coordinate y (measured at quarter-chord) are prescribed functions of time. The lift and pitching moment on the airfoil result from four contributions by the (i) the quasi-steady (qs) motion, (ii) flow control (fc) actuation, (iii) the additional apparent mass (am), and (iv) the wake vorticity (w):

$$C_{\mathrm{L}} = \underbrace{C_{\mathrm{Lqs}} + C_{\mathrm{Lfc}}}_{C_{\mathrm{Lb}}} + C_{\mathrm{Lam}} + C_{\mathrm{Lw}} \tag{7.1}$$

$$C_{\mathrm{M}} = C_{\mathrm{Mqs}} + C_{\mathrm{Mfc}} + C_{\mathrm{Mam}} \tag{7.2}$$

The sum of the quasi-steady lift and the lift due to flow control is also the total lift due to bound vorticity, C_{Lb}, which is used later in estimating the wake vorticity. Also there is no contribution to the pitching moment from the wake vorticity because the net force of the wake vorticity acts at quarter chord.

The *quasi-steady* lift is the component of circulatory lift due to the instantaneous pitch/plunge state of the airfoil and thus depends on the instantaneous angle of attack α, the angular rate $\dot{\alpha}$ and the plunge rate $\dot{y}$. The quasi-steady lift and corresponding pitching moment (adapted from Tchieu & Leonard, 2011) are:

$$C_{\mathrm{Lqs}} = C_{\mathrm{Ls}}(\alpha) + 2\pi\left(\frac{3}{4}\frac{c\dot{\alpha}}{U_0} - \frac{\dot{y}}{U_0}\right) \tag{7.3}$$

$$C_{\mathrm{Mqs}} = C_{\mathrm{Ms}}(\alpha) + \frac{\pi}{4}\frac{c\dot{\alpha}}{U_0} \tag{7.4}$$

While classic thin airfoil theory gives $C_{\mathrm{Ls}}(\alpha) = 2\pi\alpha$ and $C_{\mathrm{Ms}}(\alpha) = 0$, here they are left as general functions to account for thickness and camber (e.g., of the present NACA 4415 model). The form and calibration of these functions is described below.

The *additional apparent mass* contribution to the lift and moment expressions arises from the fact that the airfoil must do work to accelerate the surrounding fluid as it changes pitch rate and plunge rate (Tchieu & Leonard, 2011):

$$C_{\mathrm{Lam}} = \frac{\pi}{8}\frac{c^2\ddot{\alpha}}{U_0^2} - \frac{\pi}{2}\frac{c\ddot{y}}{U_0^2} \tag{7.5}$$

$$C_{\mathrm{Mam}} = \frac{3\pi}{64}\frac{c^2\ddot{\alpha}}{U_0^2} - \frac{\pi}{8}\frac{c\ddot{y}}{U_0^2} \tag{7.6}$$

The effect of the flow control is modeled as a *trapped vortex* having strength (circulation) Γ_{C} centered about a chordwise location ξ_{C} which was selected based on the actuator geometry. The effect of this trapped vortex is twofold. First it contributes to the bound circulation directly (by an amount Γ_{C}). Second, as indicated by measurements on a stationary airfoil (discussed below) the trapped vortex also displaces the trailing edge stagnation point and thereby modifies the Kutta condition. This effect is modeled with a parameter κ which is a fractional increment in lift. Thus the flow control contributes to the lift and pitching moment as (Tchieu & Leonard, 2011):

$$C_{\mathrm{Lfc}} = -(1+\kappa)\frac{2\Gamma_{\mathrm{C}}}{U_0^2} \tag{7.7}$$

$$C_{\mathrm{Mfc}} = -\left(\frac{\xi_{\mathrm{C}}}{c} + \frac{1+\kappa}{4}\right)\frac{2\Gamma_{\mathrm{C}}}{U_0^2} \tag{7.8}$$

In earlier publications that used this ROM, the control vortex strength Γ_{C} was taken to be a direct function of the actuation command u_{f} thereby neglecting any transients associated with the development and decay of trapped vorticity concentrations on the airfoil as a result of the actuation (Tchieu *et al.*, 2008; Muse *et al.*, 2009; Tchieu & Leonard, 2011). This is a reasonable assumption for the time scales associated with flight control, which are typically an order of magnitude greater than the time scales associated with the flow dynamics. However as noted above, the present work focuses on flow dynamics and forces on time scales that are equal to or shorter than T_{conv}. Thus calculation of the control vortex strength is extended with a dynamic model. First the variation of the strength (circulation) of the static control vortex Γ_{Cs} with the actuation command u_{f} is determined over a range of static angles of attack (as discussed in §7.2). The dynamic variation of the strength of the dynamic control vortex $\Gamma_{\mathrm{C}}(t)$ is computed by using a heuristic model described by the ODE,

$$\frac{1}{\omega_{\mathrm{n}}^2}\ddot{\Gamma}_{\mathrm{C}} + \frac{2}{\omega_{\mathrm{n}}}\dot{\Gamma}_{\mathrm{C}} + \Gamma_{\mathrm{C}} = \frac{1}{\omega_0}\dot{\Gamma}_{\mathrm{Cs}}\left(t - t_0\right) + \Gamma_{\mathrm{Cs}}\left(t - t_0\right), \tag{7.9}$$

which was developed based on transitory measurements of the vorticity flux into the near wake in response to a step change in the actuation. As discussed in §7.3.2 below, the response of the control vortex to the actuation can be modeled by a critically- or over-damped second order system which describes the dynamic evolution of the control vortex quite well. The second order ODE depends on the variation of the control vortex for the static airfoil $\Gamma_{\mathrm{Cs}}$for a given angle of attack $\alpha(t)$ and control input $u_{\mathrm{f}}(t)$. The ODE has three parameters: the natural frequency ω_{n}, a frequency parameters ω_0 controlling the initial buildup of circulation of opposite sign on the airfoil following a transition, and a characteristic time delay $t_0$corresponding to the duration from application of control input to vorticity flux change in the wake.

As discussed by von Kármán & Sears (1938), the wake of an airfoil in unsteady motion exerts a net force on the airfoil which results in a low-pass filtering effect of the quasi-steady lift. That is, the lift resulting from higher frequency components of the pitch/plunge motion is attenuated with respect to the corresponding quasi-steady lift according to Theodorsen's function (Theodorsen, 1935). For an arbitrary wake vortex sheet with instantaneous span-wise vorticity distribution $\gamma\left(x\right)$, the wake lift is computed by applying Biot Savart's Law:

$$C_{\mathrm{Lw}} = -\frac{1}{U_0}\int_{\frac{c}{2}}^{\infty} \frac{\gamma\left(\xi\right) d\xi}{\sqrt{\xi^2 - \frac{c^2}{4}}} \tag{7.10}$$

(note that in this notation the origin of the coordinates is taken to be at half-chord so the trailing edge is at $x = c/2$). Since the wake vorticity distribution is not known in general, it must be estimated from available data. In the following analysis the form of the wake vortex sheet is approximated using two methods.

The first method, following the analysis of Tchieu & Leonard, (2010, private communication), the wake vortex sheet is computed from the vorticity flux $\frac{d\Gamma}{dt}$ past the trailing edge using flow measurements (PIV). Assuming that the wake vorticity is advected uniformly at

Table 7.1: Static model parameters

Parameter	**Description**
$C_{\mathrm{Ls}}(\alpha)$	static lift curve in the absence of actuation (measured)
$C_{\mathrm{Ms}}(\alpha)$	static pitching moment in the absence of actuation (measured)
$\Gamma_{\mathrm{Cs}}(u_{\mathrm{f}}, \alpha)$	control vortex strength (available from look up table for α and u_{f}
ξ_{C}	control vortex position (constant for each actuator)
κ	Kutta condition parameter (constant for each actuator)

the free stream speed ($\frac{d\xi}{dt} = U_0$), the wake lift is:

$$C_{\mathrm{Lw,measured}}(t) \quad = \quad -\int_{-\infty}^{t} \frac{dt'}{U_0^2\sqrt{(t-t')^2 + \frac{c}{U_0}(t-t')}} \left(\frac{d\Gamma}{dt'}\right) \tag{7.11}$$

Here, the spatial integral over the wake is replaced with a time integral over the vorticity flux with a suitable kernel function.

The second method for computing the wake lift is taken from classic unsteady airfoil theory. Here the unsteady wake vortex sheet is computed from the time history of the bound vorticity by using Kelvin's Theorem. The resulting wake lift may be written as function of the lift due to the bound vorticity $C_{\mathrm{Lb}}(t)$ (Wagner, 1925):

$$C_{\mathrm{Lw,theory}}(t) = -\frac{1}{2}C_{\mathrm{Lb}}(t) + \int_{-\infty}^{t} C_{\mathrm{Lb}}(t')\,\phi'(t-t')\,dt' \tag{7.12}$$

where $\phi'(t)$ is the time derivative of Wagner's lift deficiency function. The expression gives the classic result in which a step change in the bound circulation causes a step change in the wake lift which is of the opposite sense and is initially equal to half the magnitude of the lift due to bound circulation. As the transient passes, the wake lift decays to zero.

7.2 Application of the ROM to Experimental Data

The model described in §7.1 contains several free parameters and functional relationships which can be used to generate and optimal fit to the experimental data. These parameters are listed in Table 7.1. All model parameters are computed from a static test matrix in which the lift and pitching moment were measured over a range $-5° \leq \alpha \leq 15°$ (increments of 1°) and $-1 \leq u_{\mathrm{f}} \leq 1$ ($\Delta u_{\mathrm{f}} = 0.1$). The static lift and moment in the absence of actuation,

C_{Ls} and C_{Ms}, are obtained from measurements (Figure 7.2a and b). The position of the control vortex in the presence of SS and PS actuation are assigned as $\xi_{\mathrm{C},SS} = 0.38c$ and $\xi_{\mathrm{C},PS} = 0.40c$ based on the location of the downstream edge of the actuator (relative to the midchord). The parameters κ_{SS} and κ_{PS} are computed based on the formulation of Tchieu and Leonard. First the lift and moment increments as a result of actuation, ΔC_{L} and ΔC_{M} are computed for all data points (Figure 7.2c&d). Next the slopes $\left(\frac{\Delta C_{\mathrm{M}}}{\Delta C_{\mathrm{L}}}\right)_{SS}$ and $\left(\frac{\Delta C_{\mathrm{M}}}{\Delta C_{\mathrm{L}}}\right)_{PS}$ are computed respectively for the SS an PS actuators (Figure 7.2e). The parameters κ_{SS} and κ_{PS} are:

$$\kappa_{SS} = \frac{\xi_{\mathrm{C},SS}}{\left(\frac{\Delta C_{\mathrm{M}}}{\Delta C_{\mathrm{L}}}\right)_{SS} - \frac{c}{4}} - 1 \qquad \kappa_{PS} = \frac{\xi_{\mathrm{C},PS}}{\left(\frac{\Delta C_{\mathrm{M}}}{\Delta C_{\mathrm{L}}}\right)_{PS} - \frac{c}{4}} - 1$$

and the strength of the control vortex is computed from a look up table:

$$\Gamma_{\mathrm{Cs}}\left(u_{\mathrm{f}}, \alpha\right) = \frac{\Delta C_{\mathrm{M}}}{\xi_{\mathrm{C}} + \frac{c}{4}\left(1+\kappa\right)}$$

where the appropriate values of ξ_{C} and κ are substituted depending on the active actuator. The results of the calibration, shown as solid lines in Figures 7.2a-d and f, demonstrate adequate fidelity.

The kinematic states describing the airfoil trajectory as well as the flow control command $u_{\mathrm{f}}(t)$ are extracted from the controller data which includes the plunge positions of the 2DOF traverse front and back gimbals, $y_1(t)$ and $y_2(t)$ as well as estimates of the the pitch angle $\alpha(t)$, pitch rate $\dot{\alpha}(t)$ and angular acceleration $\ddot{\alpha}(t)$ using a Kalman filter (cf. §3.2).

The plunge state of the quarter chord point of the airfoil is computed from the measured gimbal positions, $\{y_1, y_2\}$, along with the output of the Kalman filter, $\{\alpha, \dot{\alpha}, \ddot{\alpha}\}$. For the ROM analysis, the bending of the model about the chordwise axis is neglected, and the vertical position of the axis of rotation is taken to be $y_a = \frac{1}{2}\left(y_1 + y_2\right)$. The plunge rate and plunge acceleration of the axis of rotation, $\dot{y}_a$ and $\ddot{y}_a$ are computed by spectral differentiation (i.e., computation of the derivative in Fourier space) over the time-periodic phase-averaged motion. The plunge state at the quarter chord is computed using the pitch and the plunge states of the axis of rotation as:

$$\begin{aligned} y &= y_a + \left(a - \frac{c}{4}\right)\sin\alpha \\ \dot{y} &= \dot{y}_a + \left(a - \frac{c}{4}\right)\dot{\alpha}\cos\alpha \\ \ddot{y} &= \ddot{y}_a + \left(a - \frac{c}{4}\right)\left(\ddot{\alpha}\cos\alpha - \dot{\alpha}^2\sin\alpha\right) \end{aligned}$$

where $a = 0.1244$ m is the distance from the leading edge to the axis of rotation.

The actuation command $u_{\mathrm{f}}(t)$ recorded by the controller represents the dimensionless RMS voltage which the control system is *commanding* to the piezoelectric disks in the flow control actuators, which in turn corresponds approximately linearly to the RMS jet exit velocity of the actuators.

As mentioned above, the contribution of the wake vorticity to the lift is calculated using the time history of vorticity flux into the wake, $\frac{d\Gamma}{dt}$. For each maneuver, the vorticity flux is computed from phase-averaged PIV measurements in the wake- just downstream of the trailing edge of the airfoil (cf. §2.3). For given streamwise station, x_0, the vorticity flux is computed as the product of the streamwise velocity u and spanwise vorticity ω_z integrated across the full height of the measurement domain such that the vorticity vanishes outside of the the wake:

$$\frac{d\Gamma}{dt}(x_0, t) = \int_{-\infty}^{\infty} u(x_0, y, t)\,\omega_z(x_0, y, t)\,dy$$

Ideally this integral would be evaluated at the airfoil's trailing edge ($x_0/c = 0.5$), however, because of the shadow of the laser sheet, the velocity field is below the trailing edge is not visible. Therefore it is necessary to evaluate this integral at $x_0/c = 0.55$. Note that the vorticity flux is averaged over a small streamwise domain ($\Delta x = 0.03c$) to reduce fluctuations. It is noteworthy that computing the flux downstream of the trailing edge introduces an inherent time delay which is on the order of $\Delta t = 0.03T_{\mathrm{conv}}$ that is deemed negligible.

7.3 Validation of the ROM

The unsteady lift and pitching moment are computed for five unsteady maneuvers of the wind tunnel model using the reduced order model described above. These maneuvers are selected to highlight different aspects of the model's motion in 1DOF (pitch only) and 2DOF in the absence and presence of actuation. The ROM estimates of lift and pitching moment are compared to the force and moment estimated from direct measurements of forces, torque and acceleration (cf. §2.5).

7.3.1 Unsteady Motion in the Absence of Actuation

The fidelity of the ROM is first discussed for the unsteady motion in pitch (1DOF) using the servo motor in the absence of flow control actuation. For this maneuver, the airfoil tracks a nose-down step change in pitch from $\alpha = 4^\circ$ to $\alpha = 2^\circ$. From the pitch trajectory $\alpha(t)$ (Figure 7.3a) it can be seen that the airfoil reaches the halfway point $\alpha = 3^\circ$ at $t = 2.5T_{\text{conv}}$. The trajectory command is issued to the controller through a 2^{nd} order command filter having damping ratio 0.9 and natural frequency 60 rad/s ($0.9T_{\text{conv}}^{-1}$). The parameters of the command filter are chosen to limit the trajectory commands to those inside the performance envelope of the pitch axis (which is primarily determined by the torque limit of the pitch servo). During the maneuver the airfoil reaches a peak angular acceleration of $|\ddot{\alpha}|_{\max} = 9 \times 10^{-3}T_{\text{conv}}^{-2}$ at $t = T_{\text{conv}}$, followed by a peak angular rate of $|\dot{\alpha}|_{\max} = 1.4 \times 10^{-2}T_{\text{conv}}^{-1}$ at $t = 2.7T_{\text{conv}}$. Note that in this case the airfoil is constrained to move about the pitch axis, and small excursions in plunge result from the offset of the axis of rotation relative to quarter-chord.

The quasi-steady lift (Figure 7.3b) decreases from the initial value of $C_{\text{Lqs}} = C_{\text{Lb}} = 0.56$ to 0.38 at $t = 3.5T_{\text{conv}}$ ($\Delta C_{\text{Lb}} = -0.18$ as a result of the pitch-down). In the absence of actuation, the variation of C_{Lb} tracks the changes in α. As the airfoil pitches down (and consequently loses lift), a slight negative flux of vorticity is evident for $0 < t/T_{\text{conv}} < 5$(Figure 7.3c) which is consistent with the decrement in C_{Lb}. As the airfoil's pitch rate slows ($5 < t/T_{\text{conv}} < 10$), the flux in the wake returns to zero. The wake lift estimated from vorticity flux $C_{\text{Lw,measured}}$ exhibits a rapid onset of positive lift with a local peak at $t/T_{\text{conv}} = 2$ (Figure 7.3d). This is in good agreement with the wake lift $C_{\text{Lw,theory}}$ which is computed from C_{Lb} as discussed in §7.1. Note that for an step change in C_{Lb} of this magnitude Wagner's theory predict an initial wake lift of $C_{\text{Lw}} = -\frac{1}{2}\Delta C_{\text{Lb}} = 0.09$ compared to 0.06 here.

The total lift coefficient C_{L} is shown in Figure 7.3e for both methods of computing C_{Lw} along with the C_{L} estimate obtained from the external traverse sensors (i.e., load cells, pitch servo and accelerometers discussed in §2.5). The sum C_{Lb} and C_{Lw} results in a total lift which changes more slowly than C_{Lb} which highlights the time required for the flow about the airfoil to adjust to the change in external flow conditions (i.e., the smaller incidence angle). Both lift estimates obtained from the ROM track the measured values up to the resolution of the latter ($\Delta t = 50\,\mathrm{msec} = 3T_{\mathrm{conv}}$). Namely, the oscillations exhibited in the measured lift over $0 < t/T_{\mathrm{conv}} < 5$ are at the edges of the bandwidth of the force measurement.

The corresponding pitching moment C_{M} and constituent terms for this maneuver are shown in Figure 7.3f. Since there is no flow control in this case and no wake contribution to C_{M}, the only dominant term is C_{Mqs}. (Strictly speaking there is a slight contribution from C_{Mam}, but this term is an order of magnitude smaller than C_{Mqs}.) In contrast to C_{Lqs}, the primary contribution to C_{Mqs} arises from the pitch rate $\dot{\alpha}$ which peaks at $t/T_{\mathrm{conv}} = 2.7$ (cf. Figure 7.3a). During the period of rapid nose-down pitching ($1 < t/T_{\mathrm{conv}} < 4$) the airfoil experiences a slight decrease in (nose-down) pitching moment. As with the externally measured C_{L}, the resolution in measured C_{M} is limited to $\Delta t = 3T_{\mathrm{conv}}$ and as a result is not possible to resolve the transient behavior during pitch-down.

7.3.2 Unsteady Actuation on a Stationary Airfoil

The ROM performance for a transitory (step) actuation input is assessed when the airfoil is held nominally stationary at $\alpha_0 = 3^\circ$ using the servo motor. Two cases are analyzed: (i) a step transition from an unforced ($u_{\mathrm{f}} = 0$) state to a state in which the SS actuators are operated continuously at full power ($u_{\mathrm{f}} = 1$) and (ii) a step transition from the latter back to an unforced state.

The transition from $u_{\mathrm{f}} = 0$ to $u_{\mathrm{f}} = 1$(Figure 7.4a) occurs at $t = 0$. The control signal plotted in the figure depicts a step over a single controller period of $\Delta t_{\mathrm{controller}} = 1\,\mathrm{msec} = 0.065T_{\mathrm{conv}}$, however in order to protect the AC signal amplifiers, the actual command is rate-limited to $\Delta u_{\mathrm{f}} = 0.2$ per controller cycle. Consequently the true rise time of the actuator command is $5\Delta t_{\mathrm{controller}} = 0.33T_{\mathrm{conv}}$. Following the onset of actuation, the airfoil experiences a small (nose-down) acceleration in pitch with a maximum $|\ddot{\alpha}| = 0.0018T_{\text{conv}}^{-2}$ at $t = 1.1T_{\text{conv}}$ (not shown) which is indicative of the characteristic onset time of the actuation. Since the only relevant dynamic terms of the ROM for this case are the flow control input and the wake effect, following Equations 7.1 and 7.2, the lift and moment are:

$$C_{\text{L}} = \underbrace{C_{\text{Ls}}(\alpha_0)}_{C_{\text{Lqs}}} \underbrace{- (1+\kappa)\frac{2\Gamma_{\text{C}}}{U_0^2}}_{C_{\text{Lfc}}} + C_{\text{Lw}} \tag{7.13}$$

$$C_{\text{M}} = \underbrace{C_{\text{Ms}}(\alpha_0)}_{C_{\text{Mqs}}} \underbrace{+ \left(\frac{\xi_{\text{C}}}{c} + \frac{1+\kappa}{4}\right)\frac{2\Gamma_{\text{C}}}{U_0^2}}_{C_{\text{Mfc}}} \tag{7.14}$$

The lift due to bound vorticity C_{Lb} (Figure 7.4c) is equal to the sum of C_{Lqs}, which is essentially constant over the interval shown (due to the absence of motion), and C_{Lfc} which is computed from $u_{\text{f}}(t)$ using the dynamic actuator model (Equation 7.9). The model coefficients are fitted to the measured wake data as described below.

The vorticity flux following the transition (Figure 7.4c) shows negative flux commences following a delay of $0.19T_{\text{conv}}$ for $0.21 < t/T_{\text{conv}} < 0.3$ as a result of the shedding of CW vorticity into the wake as the local separation downstream of the actuator collapses (cf. §5). This is followed by a period of positive flux ($0.3 < t/T_{\text{conv}} < 0.77$) as the CW trapped vorticity concentration of the control vortex builds up (in the absence of a change in α, the effect of the actuation is to alter the strength of the control vortex). Note that the effect of the actuation leads to a stationary increase in lift and therefore the vorticity flux becomes vanishingly small for large times. The step response indicates that the characteristic settling time for the actuation is T_{conv}.

The wake lift estimated from PIV measurements of the vorticity flux $C_{\text{Lw,measured}}$ is shown in Figure 7.4d. For $t/T_{\text{conv}} < 0.21$, the estimated wake lift is essentially zero because the vorticity flux up to that point is essentially zero. For $0.21 < t/T_{\text{conv}} < 0.32$, there is a brief increase in C_{Lw}that reaches a peak value of 0.13 at $t/T_{\text{conv}} = 0.26$ due to the shedding of the CW vortex described above indicating an initial *decrease* in lift as can be seen in the distribution of C_{Lb} (Figure 7.4b). For $t/T_{\text{conv}} > 0.32$, the wake vortex sheet imparts a downward force on the airfoil with a nominal value of $C_{\text{Lw}} = -0.1$ following the buildup of the trapped vorticity (i.e., control vortex) during $0.3 < t/T_{\text{conv}} < 0.5$. This contribution indicates that the steady-state lift due to flow control is $C_{\mathrm{Lfc}} = 0.2$. However, the actual increment in measured steady-state lift due to full SS actuation at this angle is $C_{\mathrm{Lfc}} = 0.14$ (this number is obtained from load cell measurements before and after the transient). This over-prediction of the wake vortex strength by the PIV measurements is ostensibly a result of the fact that the PIV data were recorded along the centerline of a synthetic jet and reflects the largest change in sectional lift.

The theoretical estimate of the wake lift C_{Lwk} (Figure 7.4) is computed from $C_{\mathrm{Lb}} = C_{\mathrm{Lqs}} + C_{\mathrm{Lfc}}$ following Equation 7.12. Since C_{Lfc} depends on Γ_{C} (Equation 7.7) which in turn depends on the undetermined parameters ω_{n}, ω_0, and t_0 of the dynamic actuator model (Equation 7.9), these model parameters are solved for iteratively such that $C_{\mathrm{Lw,theory}}$ follows the same trend as the wake lift computed from the PIV measurements (allowing for the offset due to known over-prediction of the wake lift in the PIV). The time shift was set to $t_0 = 0.19T_{\mathrm{conv}}$ which corresponds to the time delay between the onset of actuation and the first change in the measured vorticity flux. The frequency parameters $\omega_{\mathrm{n}} = 28T_{\mathrm{conv}}^{-1}$ and $\omega_0 = -8T_{\mathrm{conv}}^{-1}$ reflect the transient response of the trapped vorticity system. Note that $\omega_0 < 0$ corresponds to the observation that immediately following the onset of actuation, the bound circulation decreases relative to its ultimate steady state level.

The total lift for this case is plotted in Figure 7.4e using both the measured and theoretical C_{Lw}, and, as noted in connection with Figure 7.4b, the lift due to bound vorticity is computed using the dynamic model for Γ_{C}. The lift predicted using the wake measurements is almost flat due to the fact that $C_{\mathrm{Lw,measured}}$ very nearly cancels out C_{Lb}. This result is not surprising given the previous observation that the wake lift computed directly from the PIV measurements is over-predicted. However, the lift is computed using a the more realistic wake lift provided by the dynamic model, predicts a brief transient for $0.2 < t < 0.5$ at the end of which the increase in lift has reached 50% of the steady-state value. The pitching moment (Figure 7.4f) for this case is the sum of C_{Mqs} and C_{Mfc}, the former of which is constant. Thus the pitching moment for this case is directly a function of the dynamically predicted control vortex strength.

The second case presented here is the transition from full SS actuation ($u_{\mathrm{f}} = 1$) to the unforced state ($u_{\mathrm{f}} = 0$). The actuator command input $u_{\mathrm{f}}(t)$ is show in Figure 7.5a, where as in the previous case the command is issued over one controller period, but rate-limited such that the transition occurs over $0.33T_{\mathrm{conv}}$. As above, the lift due to bound vorticity C_{Lb} (Figure 7.5b) is the sum of C_{Lqs} (constant) and C_{Lfc}, a linear function of Γ_{C} which is determined by fitting the undetermined parameters ω_{n}, ω_0, and t_0 of the dynamic actuator model. The vorticity flux $\frac{d\Gamma}{dt}$ measured in the wake during the transient is shown in Figure 7.5c. Following the transition from $u_{\mathrm{f}} = 1$ to $u_{\mathrm{f}} = 0$ at $t = 0$, there is a period of positive vorticity flux ($0.21 < t/T_{\mathrm{conv}} < 0.47$) which is primarily a result of the decrease in CW vorticity flux from the top surface. The flux peak of $\frac{d\Gamma}{dt} = 0.11U_0^2$ at $t = 0.34T_{\mathrm{conv}}$ is followed by a transition from positive to negative flux (during $0.11 < t/T_{\mathrm{conv}} < 0.54$). The flux remains negative throughout the remainder of the recorded data ($0.54 < t/T_{\mathrm{conv}} < 2$) as the airfoil's total circulation decreases to the unactuated level. Given this time history of vorticity flux following actuation termination, it is clear that the dynamic actuator model parameters computed for the actuation onset transition are not appropriate for this case. Thus, a second set of coefficients was determined to model the decay of the trapped vorticity following the termination of actuation. The time shift was again set $t_0 = 0.19T_{\mathrm{conv}}$, but the frequency parameters were decreased to $\omega_0 = 5T_{\mathrm{conv}}^{-1}$ and $\omega_0 = -3T_{\mathrm{conv}}^{-1}$ to reflect the slower transient associated with actuation termination.

The wake lift $C_{\mathrm{Lw}}$is shown in Figure 7.5d as computed directly from the wake measurements (blue) and theoretically from C_{Lb} (green). As in the actuation case of actuation onset, the overall magnitude of $C_{\mathrm{Lw,measured}}$ is larger (by a nearly constant factor of 2) than $C_{\mathrm{Lw,theory}}$ because the former only reflects vorticity flux measured at jet center whereas the latter is constrained to give the same total change in circulation implied by the change in lift measured by the load cells. $C_{\mathrm{Lw,theory}}$ first exhibits a slight increase having peak magnitude of 0.03 at $t = 0.35T_{\mathrm{conv}}$. Following this peak, the lift decreases below the initial value with the decrement reaching half of the steady-state value at $t = 1.2T_{\mathrm{conv}}$.

In order to apply the dynamic actuator model to an arbitrary actuation input, it was necessary to reconcile the two sets of parameters, namely $(\omega_{\mathrm{n}}, \omega_0) = (28, -8)\, T_{\mathrm{conv}}$for actuation onset and $(\omega_{\mathrm{n}}, \omega_0) = (5, -3)\, T_{\mathrm{conv}}$ for actuation termination. The decision was made to use a variable-coefficient ODE model in which the parameters would take on one set of values during actuation onset and a second during decay. Here actuation onset is formally defined as a state in which the magnitude of the control vortex is less than the magnitude of the steady-state value corresponding to the current actuation command, or $|\Gamma_{\mathrm{C}}| < |\Gamma_{\mathrm{Cs}}|$. Clearly actuation termination is the converse. This variable-coefficient ODE was solved numerically in Matlab using the `ode113` solver for non-stiff systems of equations.

7.3.3 Closed-Loop Pitch Tracking

The previous sections discussed (i) unsteady motion in the absence of flow control actuation and (ii) unsteady actuation on a rigid airfoil. In this section, these two phenomena are brought together in a case where the airfoil executes a pitch-down maneuver effected entirely with the flow control actuators. The maneuver discussed here is one in which the the flow control actuators are used to track a step down in pitch from $\alpha = 6°$ to $\alpha = 0°$, a transition which spans approximately $25T_{\mathrm{conv}}$ (Figure 7.6). At $t = 0$, the *pitch down* command is issued to the controller, which responds by immediately applying full SS actuation from $0.1 < t < 8.7$ (Figure 7.6d). During this time the pitch accelerates in pitch at a nearly constant rate (Figure 7.6c) to maximum nose-down angular velocity of $\dot{\alpha} = -0.014T_{\mathrm{conv}}^{-1}$ at $t = 11$ (Figure 7.6b). As the pitch angle approaches the target $\alpha = 0°$ (Figure 7.6a), control input is shifted from the SS actuators to the PS actuators ($9 < t < 11$) to provide a pitch-up moment to slow the airfoil (Figure 7.6d). Nonetheless, the airfoil overshoots the target at $t = 13.8$ and continues to $\alpha = -0.44°$ before reversing direction at $t = 16.5$ (Figure 7.6a). For $t > 16.5$, the pitch angle slowly relaxes to $\alpha = 0°$.

The unsteady lift for this maneuver is a balance between C_{Lqs}, C_{Lfc} and C_{Lw} all three of which are on the same order of magnitude during the transient. The quasi-steady lift varies from it's static value of $C_{\mathrm{Lqs}} = C_{\mathrm{Ls}} = 0.8$ at $t = 0$ to a final value of 0.2 at $t = 30T_{\mathrm{conv}}$ in a nearly monotonic fashion (Figure 7.6e). Because the time scale of the maneuver is an order of magnitude larger than the transient time scale associated with the onset of actuation (reflected in the parameters of the dynamic actuator mode), the lift contribution from flow control C_{Lfc} is essentially a linear function of u_{f}. Specifically, the top actuators cause an increase in the steady-state lift and the bottom actuators cause a decrease.

The more interesting component of the unsteady lift, however, arises from the wake vorticity (Figure 7.6f). Recall that the wake vorticity acts in such a manner as to retard the changes in the circulatory lift. For example, when the actuation switches from full SS to full PS at $t = 5T_{\mathrm{conv}}$, a period of CW vorticity flux is observed ($5 < t/T_{\mathrm{conv}} < 7$) in the wake as the circulatory lift decreases. The CW vorticity shed into this wake during the transition exert a net upward force on the airfoil whose magnitude decreases as these vortices advect downstream. Consequently, both sharp changes in actuation state ($u_{\mathrm{f}} = 0$ to $u_{\mathrm{f}} = 1$ at $t = 0$ and $u_{\mathrm{f}} = 1$ to $u_{\mathrm{f}} = -1$ at $t = 5T_{\mathrm{conv}}$, cf. Figure 7.6d) are accompanied by a flux of vorticity into the wake which exert a vertical force on the airfoil opposite in direction to the steady-state force provided by the actuators. It is interesting to note that the large changes in wake vorticity flux are almost exclusively associated with the flow control actuation- as opposed to, for example, the dynamic changes in angle of attack. This is due to the fact that the changes in actuation occur much more rapidly than the changes in pitch angle. As a result, the shed vorticity into the wake following a change in actuation is much more concentrated and imposes a larger force on the airfoil than a more gradual change such as the change in α.

The wake lift C_{Lw} (Figure 7.6g) is again computed both directly from the vorticity flux measurements (blue) and from C_{Lb} using Wagner's theory (green). Note that in this case, unlike in the unsteady actuation cases discussed in §7.3.2, $C_{\mathrm{Lw,theory}}$ is computed entirely independent from the wake measurements. (The quantity is computed from $\alpha(t)$, $u_{\mathrm{f}}(t)$ and model parameters fit to separate cases.) Given the independent nature of the two estimates, there is a remarkable similarity between $C_{\mathrm{Lw,measured}}$ and $C_{\mathrm{Lw,theory}}$. In fact, the only discrepancy between the two predictions is the apparent over-prediction of the wake lift from the PIV measurements following the large changes in u_{f} which is consistent with the observations noted in §7.3.2. Consequently, both of the total lift predictions (Figure 7.6h) track reasonably well with the measured lift, however it could be argued that total lift predicted using the theoretical wake vorticity more closely follows the trend of the measured lift.

In contrast to the lift, the pitching moment (Figure 7.6i) is almost solely dependent on the actuation state. Apart from the fact that there is no contribution from the wake vorticity, the static change in pitching moment with angle of attack is not nearly as substantial for the pitching moment as it is for the lift. In fact, the small changes which *are* present in the quasi-steady term appear to result from the pitch rate.

7.3.4 Closed-Loop Plunge Tracking

In all the maneuvers discussed up to this point (in the present chapter), the airfoil has been constrained to move in one degree-of-freedom only. (As noted above the small excursions in y, $\dot{y}$, and $\ddot{y}$ were a result of the fact that the plunge position is measured about quarter chord which is some distance upstream from the axis of rotation.) The final maneuver presented combines the elements of unsteady actuation, unsteady pitch motion and unsteady plunge motion. Here the airfoil tracks a step change in plunge elevation from $y = 0$ to $y = -0.44c$ which is effected entirely via the flow control actuators (Figure 7.3.4).

The *plunge down* command is issued at $t = 0$ at which time the controller begins to energize the SS actuator (Figure 7.3.4d) in order to generate a nose-down pitching moment (Figure 7.3.4i). The actuation command exhibits a relatively slow rise time ($\Delta t = 7T_{\text{conv}}$) with respect to the previous cases as a result of the low gain controller employed for 2DOF maneuvers. (The low controller gains are necessary to keep the motion of the model within the operational bandwidth of the force controller). The airfoil begins to pitch downward ($0 < t/T_{\text{conv}} < 23$) reaching a maximum nose-down pitch rate of $\dot{\alpha} = -0.007T_{\text{conv}}^{-1}$ at $t = 13.3T_{\text{conv}}$ (Figure 7.3.4a). As the airfoil pitches down, it experiences a reduction in lift (Figure 7.3.4h) which causes it to begin to descend around $t = 10T_{\text{conv}}$. Interesting, after the SS actuators are engaged but before the airfoil has pitched down significantly, there is a momentary *increase* in lift ($5 < t/T_{\text{conv}} < 9$) as a result of the activation of the top actuators which causes the airfoil to ascend slightly by an almost imperceptible amount before it begins to descend (Figure 7.3.4c). The airfoil begins to descend at $t = 10T_{\text{conv}}$ and continues to accelerate downward through $t = 25T_{\text{conv}}$. During $10 < t/T_{\text{conv}} < 15$ the flow control command is gradually switched from SS actuation to PS actuation and by $t = 18.5T_{\text{conv}}$ the *PS* actuators have reached their maximum value of this maneuver of $u_{\text{f}} = 0.43$ (Figure 7.3.4d). The airfoil reaches its minimum pitch angle of $\alpha = 0.9°$ at $t = 23T_{\text{conv}}$ (Figure 7.3.4a)- and accordingly its minimum lift during the maneuver. For $23 < t/T_{\text{conv}} < 36$ the airfoil continues to accelerate in pitch (in the nose-up sense) and it begins to recover lift, slowing the downward plunge acceleration. At $t = 36T_{\text{conv}}$ the airfoil is pitching upward at a peak rate of $\dot{\alpha} = 0.004T_{\text{conv}}^{-1}$. For $36 < t/T_{\text{conv}} < 44$ the plunge rate begins to level off and the airfoil reaches a maximum downward velocity of $\dot{y} = 0.01U_0$ at $t = 44T_{\text{conv}}$. The PIV measurements end before the maneuver is complete at $t = 46T_{\text{conv}}$ with airfoil less than halfway to its target plunge position and pitching upward at nearly its maximum rate as the controller attempts to recover lift to slow down the downward acceleration in plunge as it approaches the target plunge position $y = -0.1c$.

As with the previous cases discussed above, the unsteady lift is dominated by C_{Lqs}, C_{Lfc}, and C_{Lw} (Figure 7.3.4h). The quasi-steady term (Figure 7.3.4e) accounts for the overall shape of the lift curve which decreases from $C_{\text{L}} = 0.5$ before motion starts ($t = 0$) to a minimum value of $C_{\text{L}} = 0.15$ at $t = 23T_{\text{conv}}$ when the airfoil is at its minimum pitch angle. As the data record terminates at $t = 46T_{\text{conv}}$, both the C_{Lqs} and C_{L} have recovered past the initial value generating a net lift force which is larger than the *trim* lift in order to decelerate the plunging model. C_{Lfc} reflects the relatively small excursions in actuation state reaching extreme values of 0.08 and -0.09 at $t = 8T_{\text{conv}}$ and $19T_{\text{conv}}$, respectively (Figure 7.3.4e). As observed in previous cases, the wake term computed from PIV measurements $C_{\text{Lw,measured}}$ appears to be nearly equal and opposite the flow control term, effectively *canceling it out* throughout the maneuver (Figure 7.3.4g). For this reason the total lift estimated from the theoretical wake agree much better with the measured lift (Figure 7.3.4h).

The pitching moment terms (Figure 7.3.4i) are not surprising given the previous cases. C_{Mfc} has a similar structure C_{Lfc}, both of which are easy to relate back to the u_{f}. As with the closed-loop pitch tracking case above, the downward pitch rate during the maneuver is strong enough to cause deviations in C_{M} on the order of $C_{\text{Mqs}} = 0.01$. However, as before, C_{Mfc} dominates the C_{M}, which contributes to the particular effectiveness of this type of flow control in regulating $\alpha(t)$.

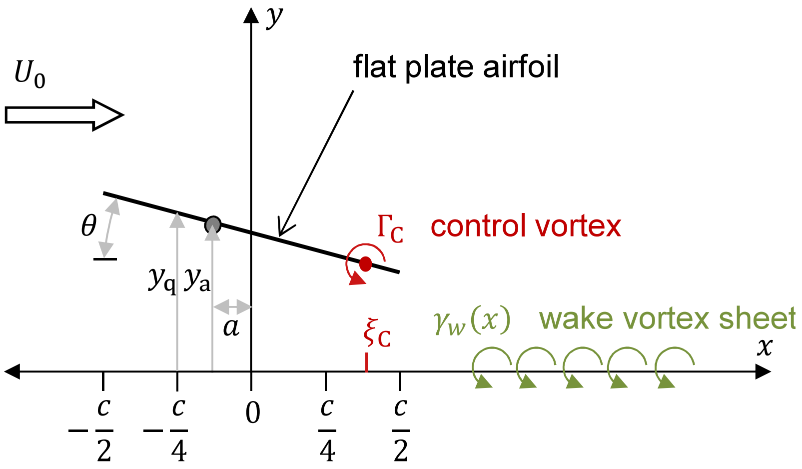

Figure 7.1: Schematic of the ROM. Note that the vortex dynamics are modeled as propagating in one dimension (along the x-axis).

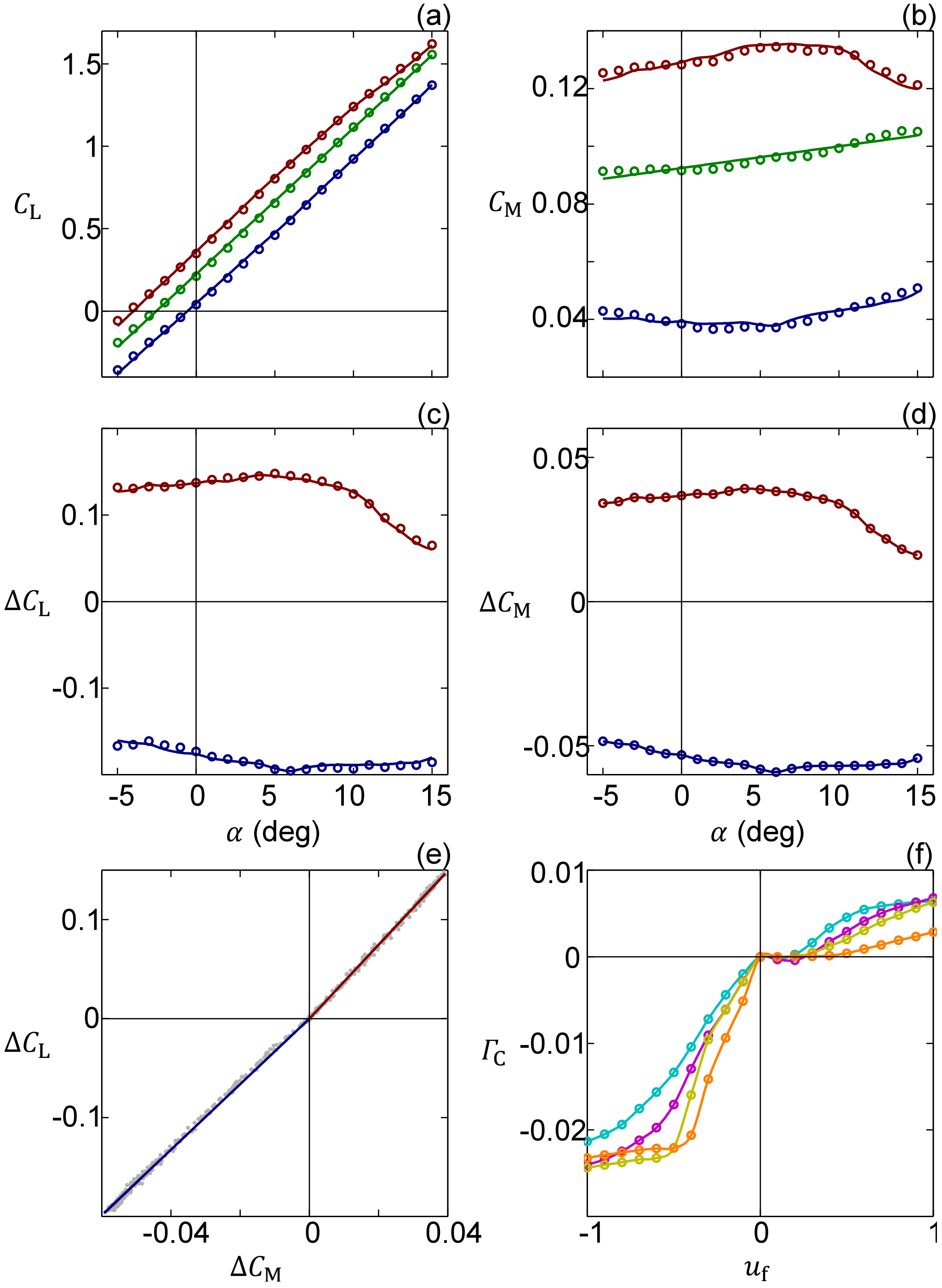

Figure 7.2: Static calibration of the ROM using time-averaged measurements during steady-state actuation conditions at static angles-of-attack. Variation of (a) C_L, (b) C_M, (c) ΔC_L, (d) ΔC_M with α for $u_f = -1$ (▬), 0 (▬), 1 (▬). (e) Variation of ΔC_L with ΔC_M for all cases. (f) Variation of control vortex strength Γ_C with actuation input u_f for $\alpha = -3°$ (▬), 3° (▬), 9° (▬), 15° (▬). Symbols are data points; solid lines are cubic polynomial fits.

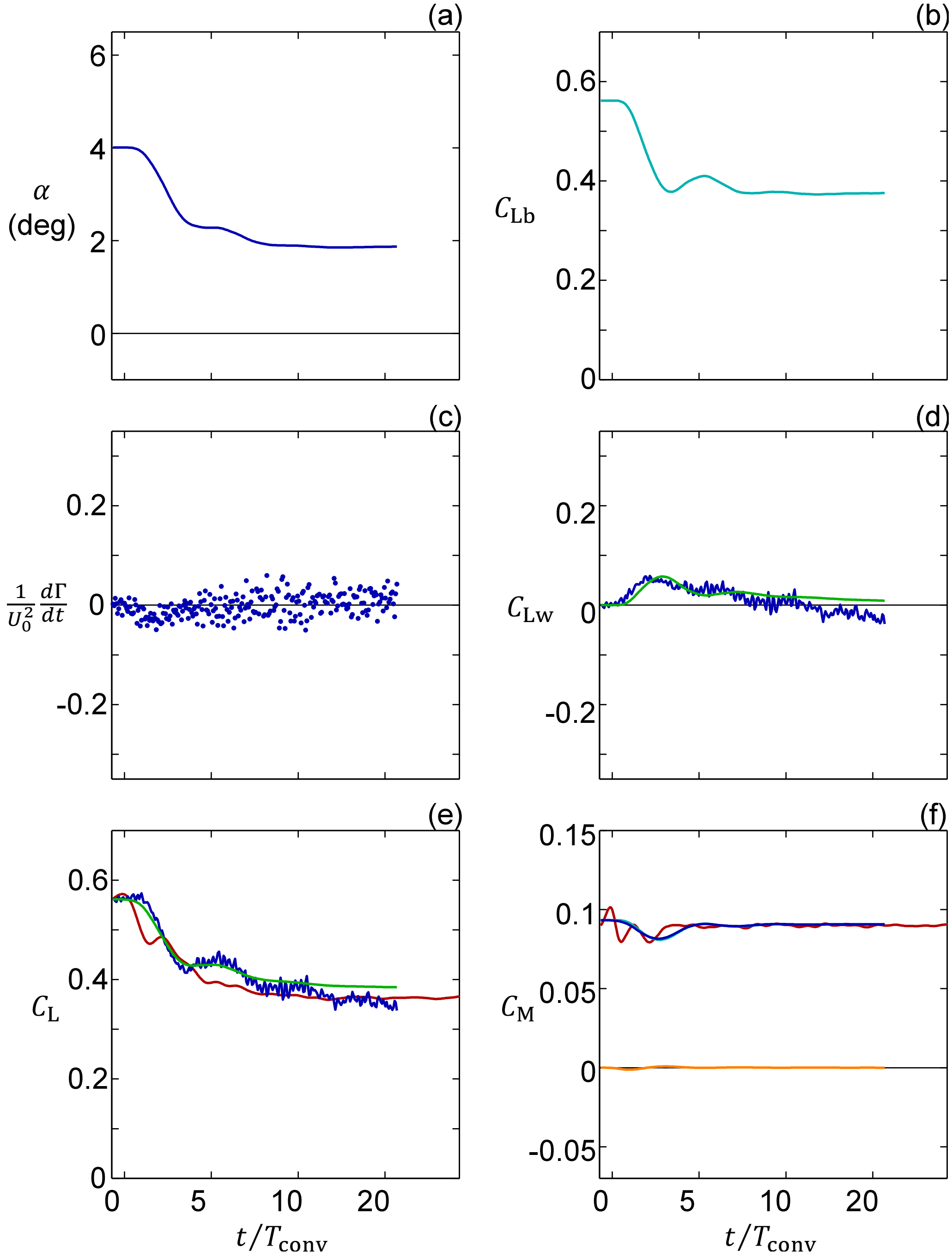

Figure 7.3: Time histories of (a) α; (b) C_{Lqs}; (c) $d\Gamma/dt$; (d) $C_{\mathrm{Lw,measured}}$ (—) and $C_{\mathrm{Lw,theory}}$ (—); (e) total C_{L} computed using both wake measurements (—) and theory (—); and (f) C_{Mam} (—), C_{Mqs} (—), and total C_{M} (—); during a maneuver in which the airfoil model executed a nose-down step change in pitch effected by the pitch servo. C_{L} and C_{M} measured externally using the traverse sensors (—) are included in (e) and (f).

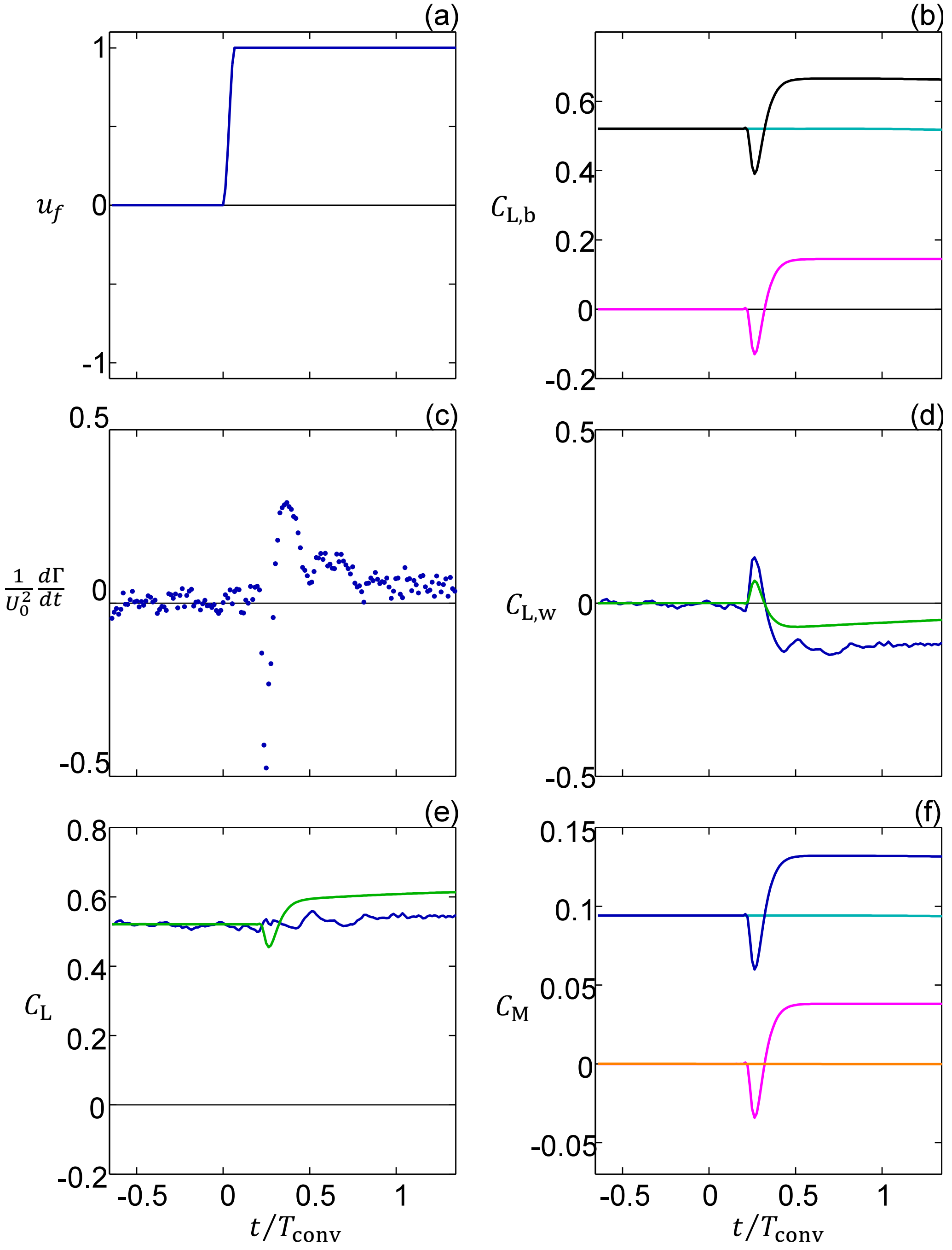

Figure 7.4: Time histories of (a) u_{f}; (b) C_{Lqs} (—), C_{Lfc} (—), and C_{Lb} (—); (c) $d\Gamma/dt$; (d) $C_{\mathrm{Lw,measured}}$ (—) and $C_{\mathrm{Lw,theory}}$ (—); (e) total C_{L} computed using both wake measurements (—) and theory (—); and (f) C_{Mam} (—), C_{Mqs} (—), and total C_{M} (—); following a step transition in actuation from $u_{\mathrm{f}} = 0$ to 1.

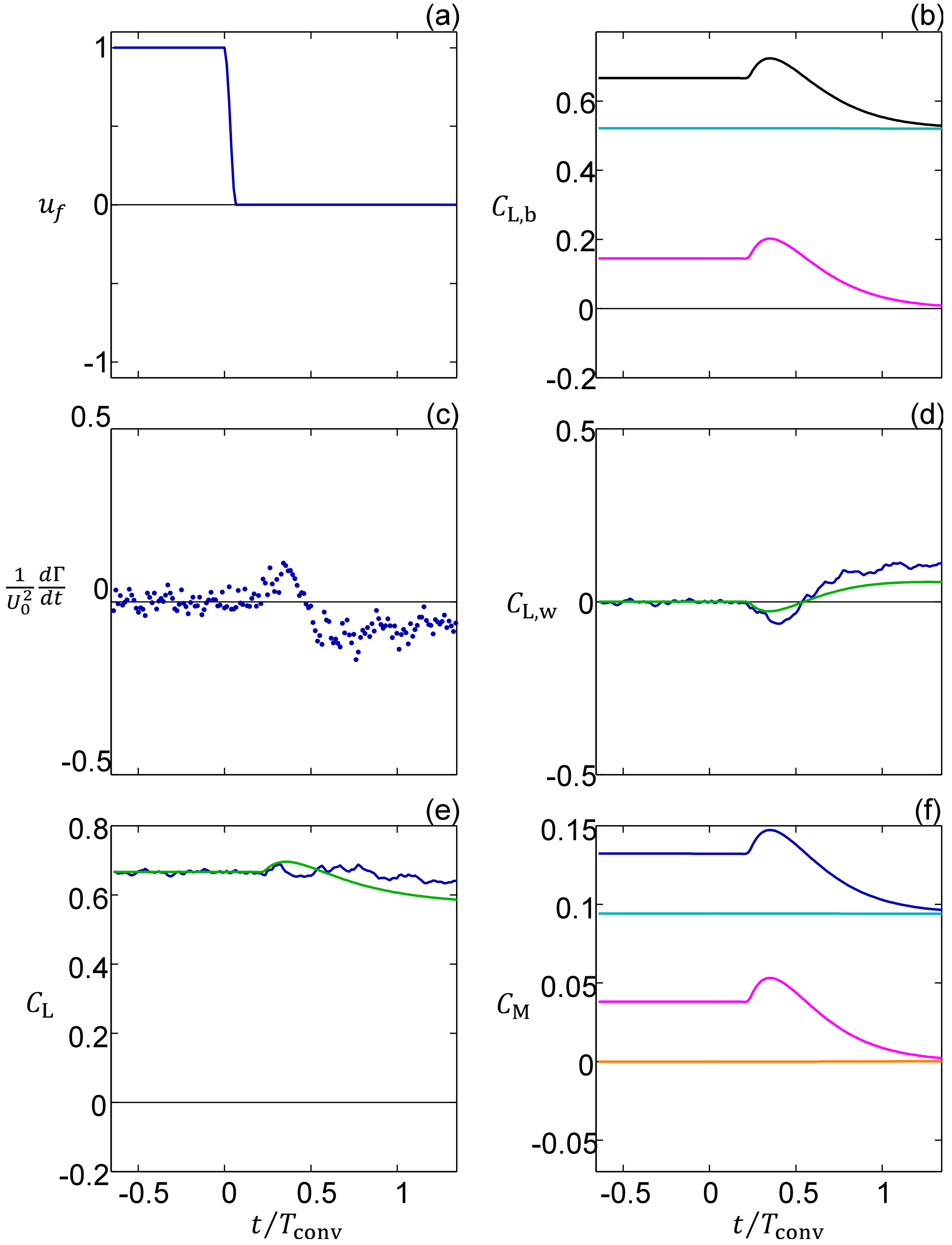

Figure 7.5: Time histories of (a) u_{f}; (b) C_{Lqs} (—), C_{Lfc} (—), and C_{Lb} (—); (c) $d\Gamma/dt$; (d) $C_{\mathrm{Lw,measured}}$ (—) and $C_{\mathrm{Lw,theory}}$ (—); (e) total C_{L} computed using both wake measurements (—) and theory (—); and (f) C_{Mam} (—), C_{Mqs} (—), and total C_{M} (—); following a step transition in actuation from $u_{\mathrm{f}} = 1$ to 0.

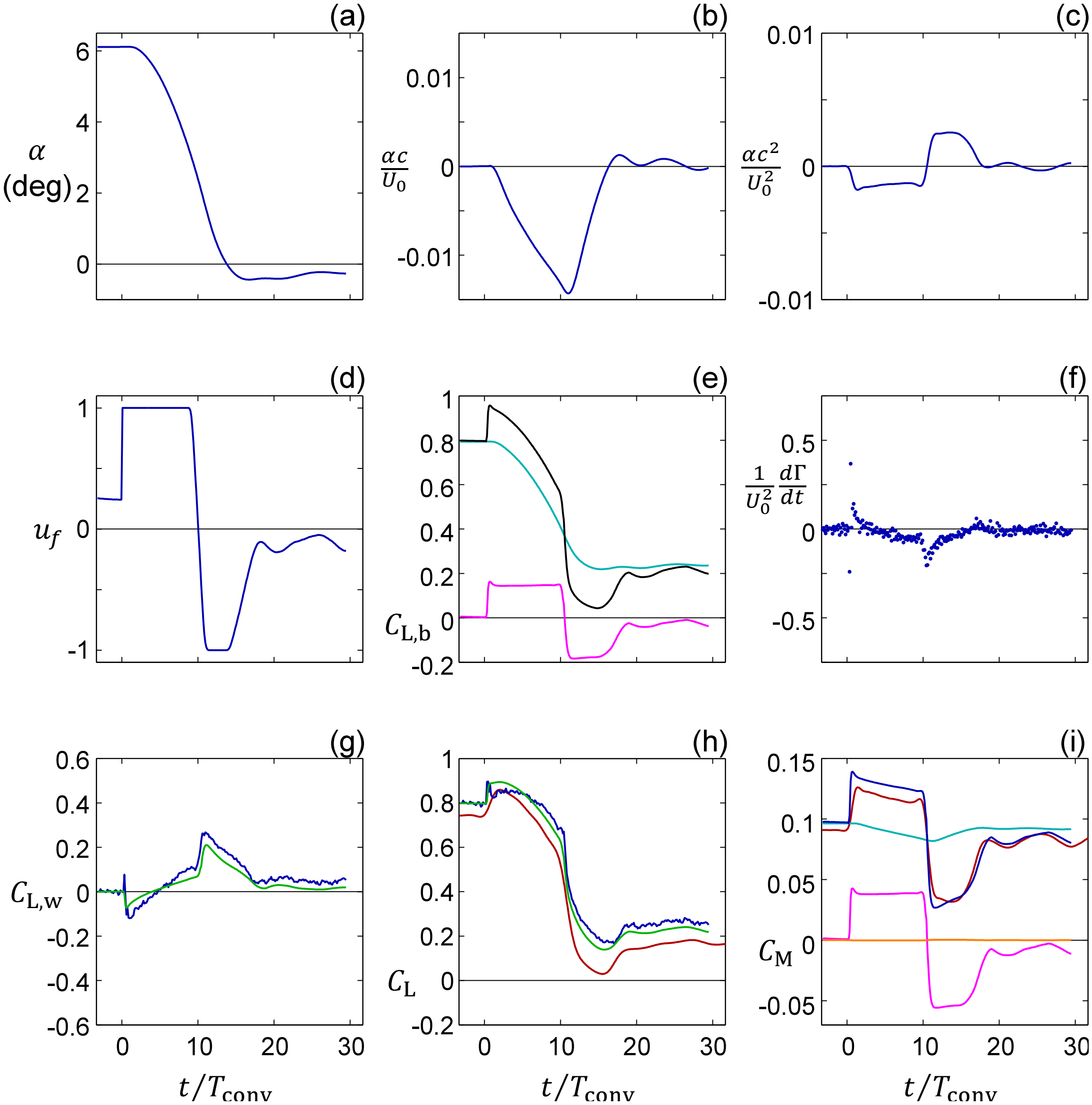

Figure 7.6: Time histories of (a) α; (b) $\dot{\alpha}$; (c) $\ddot{\alpha}$; (d) u_{f}; (e) C_{Lqs} (▬), C_{Lfc} (▬), and C_{Lb} (▬); (f) $d\Gamma/dt$; (g) $C_{\mathrm{Lw,measured}}$ (▬) and $C_{\mathrm{Lw,theory}}$ (▬); (h) total C_{L} computed using both wake measurements (▬) and theory (▬); and (i) C_{Mam} (▬), C_{Mqs} (▬), and total C_{M} (▬); during a maneuver in which the airfoil model executed a nose-down step change in pitch effected by flow control. C_{L} and C_{M} measured externally using the traverse sensors (▬) are included in (h) and (i).

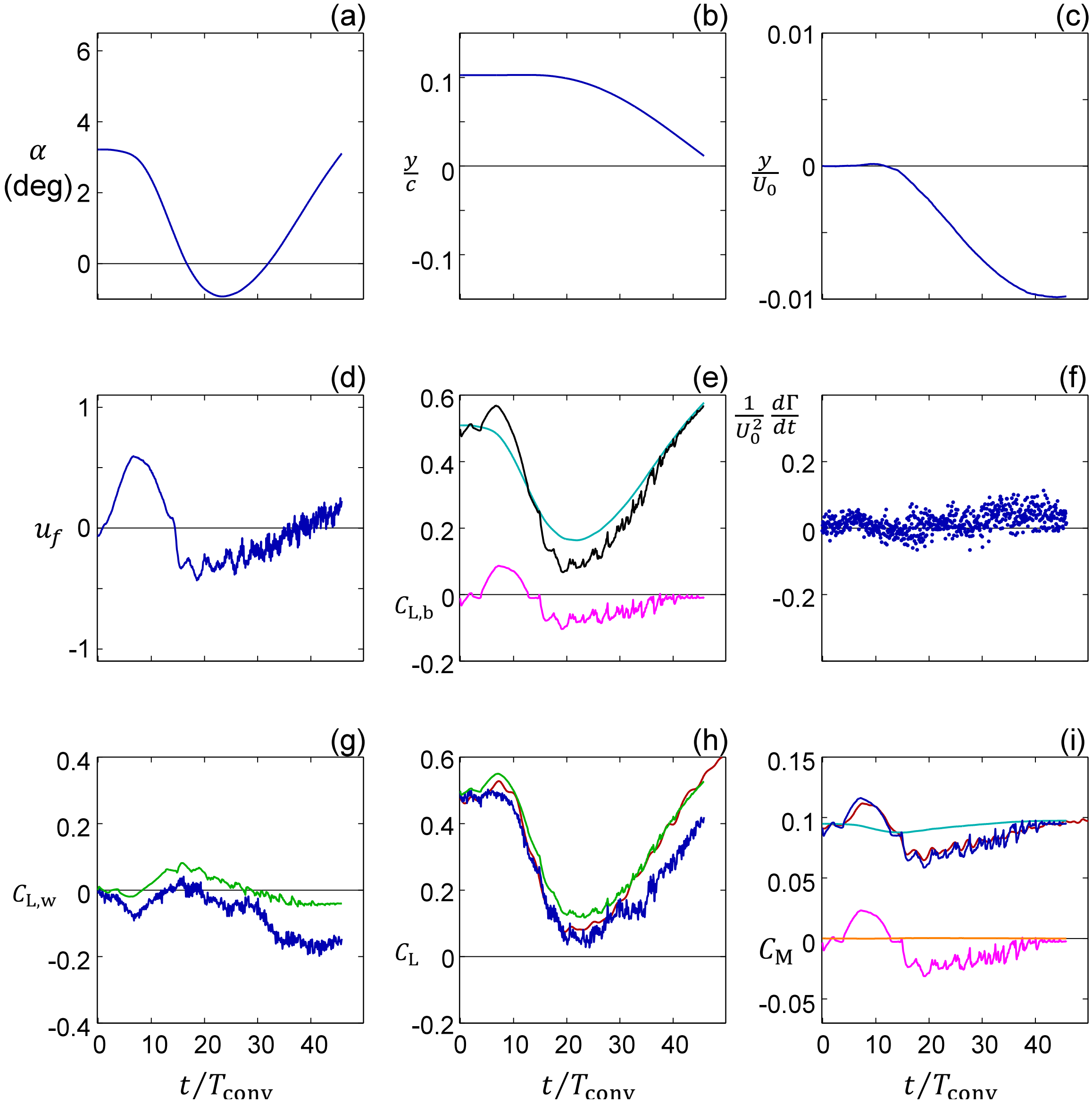

Figure 7.7: Time histories of (a) α; (b) y; (c) $\dot{y}$; (d) u_{f}; (e) C_{Lqs} (—), C_{Lfc} (—), and C_{Lb} (—); (f) $d\Gamma/dt$; (g) $C_{\mathrm{Lw,measured}}$ (—) and $C_{\mathrm{Lw,theory}}$ (—); (h) total C_{L} computed using both wake measurements (—) and theory (—); and (i) C_{Mam} (—), C_{Mqs} (—), and total C_{M} (—); during a maneuver in which the airfoil model executed a nose-down step change in plunge effected by flow control. C_{L} and C_{M} measured externally using the traverse sensors (—) are included in (h) and (i).

Chapter VIII

CONCLUDING REMARKS

8.1 Summary of Investigations

The dynamic control of aerodynamic forces on a moving airfoil using active flow control was investigated experimentally using an airfoil model integrated with spanwise arrays of synthetic jet actuators on the pressure and suction surfaces (PS and SS, respectively) upstream of the trailing edge. Aerodynamic control was effected by bi-directional variation of the pitching moment, through alternate operation of the SS and PS actuators, to induce nose-down or nose-up changes in angle of attack and thereby decrease or increase the lift. In these investigations, the airfoil model was mounted on a 2DOF traverse mechanism which allowed for commanded arbitrary pitch/plunge motions under direct flow control in the wind tunnel test section. The rigid body and fluid dynamics were characterized using force/torque measurements, surface pressure measurements, and particle image velocimetry (PIV).

First, the effects of quasi-steady actuation on a stationary airfoil were characterized to assess the induced changes in time-averaged pressure distributions and resulting aerodynamic forces and moments by the hybrid trailing edge actuation. These investigations were conducted over broad ranges of SS and PS actuator location ($0.83 < x/c < 1$), pitch angle ($-5 < \alpha < 15$), and actuation level ($-1 < u_\mathrm{f} < 1$). The findings were compared with the performance of the baseline airfoil and in the absence of active actuation. Time-averaged PIV measurements about the trailing edge of the airfoil were used to elucidate the underlying actuation mechanisms.

Next, the transient response of the flow to time-dependent (step) modulation of the actuation waveform was investigated to determine the characteristic time scales that are associated with the onset and termination of the actuation. Time-resolved, surface pressure measurements were recorded following transitions from three states, namely, unactuated ($u_\mathrm{f} = 0$), full SS actuation ($u_\mathrm{f} = 1$), and full PS actuation ($u_\mathrm{f} = -1$). It was shown that the onset or change in the state of the actuation is accompanied by global changes in the circulation about the airfoil that are accompanied by complex, transitory changes in vorticity and the shedding of trains of vorticity concentrations into the wake. The transient vortex dynamics for several of the transitions were recorded using PIV phase-locked to the actuation waveform. Following these open-loop investigations, closed-loop control of the airfoil's motion in pitch and plunge was demonstrated in several maneuvers where the motion of the model was effected exclusively by flow control. The phase-locked velocity field near the trailing edge was compared with the effects of the actuation on the static airfoil (for a given angle of attack and actuation level), when the airfoil moved in pitch only while the controller tracked commanded changes in α, during pitch-up and -down under flow control, and during pitch and plunge. The plunge motion was regulated by a longitudinal flight control system that generated the necessary vertical forces by pitching the airfoil using flow control, while the vertical force on the model was regulated by a dedicated force controller that allowed the airfoil to "fly" in the tunnel. The efficacy of this control strategy was demonstrated first by tracking step changes in plunge and then by tracking a desired (fixed) altitude in presence of vertical force disturbances (which were applied by the force controller).

Finally, a reduced order vortex model (ROM) for the controlled flow over the airfoil was validated against the experimental data. The vortex model developed by Tchieu & Leonard (2011) was extended in the present investigations to improve model fidelity for short times following actuation transients. The ROM predictions of C_L and C_M were computed for the 1DOF and 2DOF controlled maneuvers in which the wake contribution to C_L was calculated directly from the measured $d\Gamma/dt$ and from the quasi-steady lift using the classical unsteady thin airfoil theory of Wagner (1925) and Theodorsen (1935).

8.2 Main Findings

8.2.1 Continuous, Quasi-Steady Actuation

The flow control actuation methodology at the trailing edge that was originally developed by DeSalvo & Glezer (2007) was improved through detailed investigations of the primary flow parameters, and it was found that for the present airfoil the performance of the PS and SS

actuators could be optimized to effect changes in pitching moment as large as $\Delta C_{\mathrm{M}} = -0.05$ (nose-down) and 0.09 (nose-up). This range corresponds to 140% of the baseline $C_{\mathrm{M}} = -0.1$ of the smooth airfoil at $\alpha = 3°$. The present investigations also demonstrated that despite the close streamwise proximity of the SS and PS actuators on (opposite sides) of the airfoil upstream of the trailing edge, the operation of each actuator was almost independent of the presence of the opposite actuator.

The flow mechanisms associated with the quasi steady operation of each actuator were investigated in detail, and it was shown that operation of either actuator over a range of momentum coefficients resulted in partial or full attachment of the separating shear layer downstream of the actuator along the airfoil surface to the trailing edge. The effects of this attachment which significantly modifies the vorticity concentrations downstream of the actuator are manifested by a decrease in the local static pressure distribution, that is associated with the changes in the pitching moment and to a lesser extent in the lift. Furthermore, the collapse of the separated domain leads to vectoring of the flow downstream of the actuator and significant changes in the Kutta conditions as manifested by the migration of the stagnation point from the near wake onto the surface of the airfoil.

The present investigations have also demonstrated that the modification of vorticity concentrations downstream of the actuators does not apply exclusively to "trapped" concentrations adjacent to the flow boundary downstream of the actuator. In fact, substantial control authority of the pitching moment was observed when the downstream edges of both actuators were mounted flush with the trailing edge, and the "trapped vorticity" was essentially "bound" within the flow in the near wake.

8.2.2 Transitory Actuation

Time-resolved measurements of surface pressure on the airfoil were used to assess the progression of transitory effects following the onset of actuation. It was found that in all cases, the surface pressure near the trailing edge adjusts to the quasi-steady value of continuous actuation within one to two convective time scales, while the pressure at ports that are closer to the leading edge ($0 < x/c < 0.4$) reach the quasi-steady levels within $2 - 4T_{\mathrm{conv}}$

($T_{\text{conv}} = c/U_0 = 15$ ms). These observations indicate that the effects of the actuation are established considerably faster than with conventional (mechanical) control surfaces. From the standpoint of a flight control system, the present measurements indicate an operational bandwidth of about 16 Hz.

The transient dynamics of vorticity concentrations following the onset and termination of actuation were documented using phase-locked PIV measurements. During the onset of actuation, the first counter-rotating vortex pair formed by the synthetic jet causes the separated shear layer to roll up into a large vortex (nominally $0.03c$) which is advected into the wake. For the step-modulated transition from unforced flow to full SS actuation ($0 \rightarrow SS$), this vortex has clockwise (CW) sense and corresponds to a momentary decrease in C_{L} (as the total circulation about the airfoil decreases) and increase in C_{M}. Following the shedding of this vortex, the upstream shear layer becomes attached to the Coanda surface downstream of the jet exit. During this attachment, the vorticity flux from the suction surface of the airfoil is temporarily abated indicating accumulation and eventual increase in circulation (and lift). For the corresponding transition $0 \rightarrow PS$, counter-clockwise (CCW) vorticity is initially shed from the pressure side of the airfoil, and the total circulation about the airfoil momentarily increases above the initial circulation (in the absence of actuation). This is followed by a period of net CW vorticity flux as the flow attaches around the PS actuator and the total circulation around the airfoil decreases to a value which corresponds to the C_{L} decrease associated with the PS actuators.

When actuation is terminated, the vorticity layer on the surface of the airfoil slowly lifts off the surface (over a period of $0.5T_{\text{conv}}$), starting at the juncture between the downstream edge of the actuator and the surface of the airfoil. The lift-off process is accompanied by a momentary reduction in vorticity flux from the same side of the airfoil. For example, during the transition $0 \rightarrow SS$ there is a momentary increase in circulation about the airfoil, and, consequently, in C_{L}. However, once the separation progresses to the trailing edge, the vorticity flux changes sign because much of the vorticity associated the previously-attached surface layer is shed into the wake. It is remarkable that for both onset and termination of actuation, the changes in vorticity flux are almost exclusively confined to the actuated surface of the airfoil.

8.2.3 Closed-Loop Control

Effective closed-loop tracking in 1DOF (pitch) was demonstrated using flow control. Within the range of angles of attack of interest (when the baseline flow is fully attached), the characteristic response time of the wind tunnel model (which includes effects of system inertia that would not be present on a much lighter UAV of similar scale) was quite fast. For example, the respective rise times for a step change in pitch-up and -down of $\Delta\alpha = 6^\circ$ were about $11T_{\text{conv}}$ and $13T_{\text{conv}}$, respectively (the difference is attributed to the slightly higher effectiveness of PS actuation owing to the camber of the airfoil). In fact, it was demonstrated that the primary limiting factor for the rise time was the inertia of the airfoil and not the time response of the flow control, and that for a vehicle having lower inertia, it would be possible to push these times closer to the characteristic response time of the flow control actuation ($4T_{\text{conv}}$ for the present model). Phase-locked PIV measurements were recorded during pitch tracking maneuvers and compared to time-averaged measurements on a static airfoil at the same α and u_{f}. These data showed that while the resulting flow field of the maneuvering airfoil exhibited strong dependence on α and u_{f} (consistent with the static measurements), the corresponding flow fields were nearly invariant in the presence of airfoil motion (i.e., pitch-up and -down) indicating that the airfoil motion at these pitch rates ($\dot{\alpha} = 0.01T_{\text{conv}}^{-1}$) does not significantly affect the interaction between the actuation and the cross flow.

Closed-loop tracking using flow control was also demonstrated over a range of 2DOF maneuvers (pitch and plunge). Of particular note is the controller response to asynchronous, momentary downwash and upwash disturbances simulating the effects of a sudden gust. It was shown that the actuation-induced changes in C_{M} to overcome these upwash and downwash disturbances were evident in the model's angular acceleration as early as $1.1T_{\text{conv}}$ and $0.8T_{\text{conv}}$, respectively. The controller was able to completely suppress the effects of the disturbance within $100T_{\text{conv}}$ (in the absence of the controller, the model would become unstable and crash).

8.2.4 Reduced Order Modeling

The vortex model developed by Tchieu & Leonard (2011) was extended and validated against the experimental results. In order to improve model fidelity for short times following actuation transients, the static actuator model of these authors was replaced with a new dynamic actuator model which uses a second order ordinary differential equation to capture the transient changes in the bound circulation in the first several T_{conv} following the actuation. The result of this model is an improved estimate for the instantaneous lift due to bound circulation L_{b} in the presence of unsteady actuation. With this improved estimate of L_{b}, the total unsteady lift may be computed by convolution with Wagner's function. In other words, once the dynamic actuator model is calibrated, the instantaneous unsteady lift and pitching moment may be calculated in real time without any flow field measurements.

The parameters of the dynamic actuator model were calibrated from PIV measurements of vorticity flux into the wake and the time rate of change of circulation about the airfoil following the transitions $0 \to SS$ and $SS \to 0$. (For the purposes of the model, the time constants associated with the PS actuator dynamics were assumed to be the same as those measured for SS actuator.) The fitted model was validated on unsteady data in which the airfoil was driven in pitch and plunge by flow control. The lift and pitching moment estimated by the modified ROM tracked the lift force and pitching moment measured directly using the sensors of the 2DOF traverse within an error bound of 10%. It is also noteworthy that in the validation cases, that the estimates of L_{w} computed by the dynamic actuator model were in overall good agreement with the wake lift estimates computed directly from the measured wake vorticity flux.

8.3 Applications and Recommendations

The most direct application of this work is closed-loop flight control on a meter-scale unmanned aerial vehicle (UAV) such as the DragonEye. Flight maneuvering effected by flow control offers the potential for agile maneuvering as a result of the rapid onset of aerodynamic forces. Furthermore, the present investigations indicate that this flow control approach may be scaleable to larger flight platforms. In addition to maneuvering in the absence of (or significantly simplified) mechanical control surfaces, this flow control approach has the potential to enable novel wing designs that might be limited by conventional maneuvering capabilities.

It is clear that the next step in transitioning this technology to a flight platform is to address the integration of actuators into the wing. In the present configurations, the hybrid actuators were specifically designed to be surface-mounted so that their placement could be easily investigated and optimized. However, the presence of the inactive actuators could result in drag penalty. Therefore it is desired to develop methodologies for integration of the actuators into the skin of the airfoil so that they pose minimal drag penalty.

In addition to the promising application of the current technology, this research lays the groundwork for future investigations of the flow physics of trailing edge flow control actuation. In particular, the effects of segmented actuation and the formation of streamwise vorticity (single vortices, and counter-rotating vortex pairs) can lead to significant enhancements in their interaction with the cross flow and their performance by exploiting three-dimensional effects. Furthermore, spanwise arrays of discrete actuation jets would lower the required overall momentum and reduce the actuation power. By adjusting the spanwise segmentation, it may be possible to optimize the induced changes in aerodynamic forces per unit power input to the actuators for a desired maneuver. It is anticipated that such contributions will enable the development of advanced flow control technologies for a broad range of external and internal aerodynamic flows.

REFERENCES

Abbott, I. H. & von Doenhoff, A. E. 1959 *Theory of Wing Sections*. Dover Publications.

Ahuja, K. H. & Burrin, R. H. 1984 Control of flow separation by sound. In *9th AIAA/NASA Aeroacoustics Conference*, pp. AIAA–84–2298. Williamsburg, VA.

Aiyar, A., Song, C., Kim, S.-H. & Allen, M. G. 2009 An all polymer air-flow sensor array using a piezoresistive composite elastomer. In *22nd IEEE Int. Conf. Micro Electro Mechanical Systems (MEMS 2009)*, pp. 447–451. Sorrento, Italy.

Amitay, M. & Glezer, A. 1999 Aerodynamic flow control of a thick airfoil using the synthetic jet actuators. In *3rd ASME/JSME Joint Fluids Engineering Conference*. San Francisco, CA.

Amitay, M. & Glezer, A. 2002*a* Controlled transients of flow reattachment over stalled airfoils. *International Journal of Heat Transfer and Fluid Flow* **23**, 690–699.

Amitay, M. & Glezer, A. 2002*b* Role of actuation frequency in controlled flow reattachment over a stalled airfoil. *AIAA Journal* **40**, 209–216.

Amitay, M. & Glezer, A. 2006 Flow transients induced on a 2d airfoil by pulse-modulated actuation. *Experiments in Fluids* **40**, 329–331.

Amitay, M., Horvath, M., Michaux, M. & Glezer, A. 2001 Virtual aerodynamic shape modification at low angles of attack using synthetic jet actuators. In *31st AIAA Fluid Dynamics Conference and Exhibit*, pp. AIAA–2001–2975. Anaheim, CA.

Barnard, P. 2005 Software development principles applied to graphical model development. In *AIAA Modeling and Simulation Technologies Conference*, pp. AIAA–2005–5888. San Francisco.

Ben-Dov, G., Pearlstein, A. J., Brzozowski, D. P. & Glezer, A. 2009 Frequency-domain proper orthogonal decomposition of synthetic-jet actuated flow for airfoil control.

Talk at 62nd Annual Meeting of the American Physical Society Division of Fluid Dynamics, Minneapolis, Minnesota.

Brzozowski, D. P. & Glezer, A. 2009 Rapid modification of the flow field about a free moving airfoil by controlled, trapped vorticity conventrations. In *The 6th International Symposium on Turbulence and Shear Flow Phenomena*. Seoul, Korea.

Brzozowski, D. P., Woo, G. T. K., Culp, J. R. & Glezer, A. 2010 Transient separation control using pulse-combustion actuation. *AIAA Journal* **48**, 2482–2490.

Cater, J. E. & Soria, J. 2002 The evolution of round zero-net-mass-flux jets. *Journal of Fluid Mechanics* **472**, 167–200.

Chatlynne, E., Rumigny, N., Amitay, M. & Glezer, A. 2001 Virtual aero-shaping of a clark-y airfoil using synthetic jet actuators. In *39th Aerospace Sciences Meeting and Exhibit*, pp. AIAA–2001–0732. Reno, NV.

Colonius, T. & Williams, D. R. 2011 Control of vortex shedding on two- and three-dimensional aerofoils. *Philosophical Transactions of the Royal Society of London - Series A* **369**, 1525–1539.

Crittenden, T. & Glezer, A. 2006 A high-speed, compressible synthetic jet. *Physics of Fluids* **18**, 017107.

Crittenden, T., Glezer, A., Funk, R. & Parekh, D. E. 2001 Combustion-driven jet actuators for flow control. In *31st AIAA Fluid Dynamics Conference and Exhibit*, pp. AIAA–2001–2768. Anaheim, California.

Crittenden, T., Shlyubsky, D. & Glezer, A. 2004 Combustion-driven jet actuators in reversed flow configurations. In *2nd AIAA Flow Control Conference*, pp. AIAA–2004–2689. Portland, Oregon.

Dandois, J., Garnier, E. & Sagaut, P. 2006 Unsteady simulation of a synthetic jet in a crossflow. *AIAA Journal* **44**, 225–238.

Darabi, A. & Wygnanski, I. 2004*a* Active management of naturally separated flow over a solid surface. part 1. the forced reattachment process. *Journal of Fluid Mechanics* **510**, 105–129.

Darabi, A. & Wygnanski, I. 2004*b* Active management of naturally separated flow over a solid surface. part 2. the separation process. *Journal of Fluid Mechanics* **510**, 131–144.

DeSalvo, M. E., Amitay, M. & Glezer, A. 2002 Modification of the aerodynamic performance of airfoils at low angles of attack: Trailing edge trapped vortices. In *1st AIAA Flow Control Conference*, pp. AIAA–2002–3165. St. Louis, Missouri.

DeSalvo, M. E. & Glezer, A. 2004 Aerodynamic performance modification at low angles of attack by trailing edge vortices. In *2nd AIAA Flow Control Conference*, pp. AIAA–2004–2118. Portland, Oregon.

DeSalvo, M. E. & Glezer, A. 2005 Airfoil aerodynamic performance modification using hybrid surface actuators. In *43rd AIAA Aerospace Sciences Meeting and Exhibit*, pp. AIAA–2005–0872. Reno, Nevada.

DeSalvo, M. E. & Glezer, A. 2006 Aerodynamic control at low angles of attack using trapped vorticity concentrations. In *44th AIAA Aerospace Sciences Meeting and Exhibit*, pp. AIAA–2006–0100. Reno, Nevada.

DeSalvo, M. E. & Glezer, A. 2007 Control of airfoil aerodynamic performance using distributed trapped vorticity. In *45th AIAA Aerospace Sciences Meeting and Exhibit*, pp. AIAA–2007–0708. Reno, Nevada.

Dore, B. D. 1966 The unsteady forces on finite wings in transient motion. Reports and Memoranda 3456. Ministry of Aviation - Aeronautical Research Council.

Duraisamy, K. & Baeder, J. 2002 Active flow control concepts for rotor airfoils using synthetic jets. In *1st AIAA Flow Control Conference*, pp. AIAA–2002–2835. St. Louis, Missouri.

Englar, Robert J. 1975 Circulation control for high lift and drag generation on stol aircraft. *Journal of Aircraft* **12**, 457–463.

Fisher, R. A. 1915 Frequency distribution of the values of the correlation coefficient in samples of an indefinitely large population. *Biometrika* **10**, 507–521.

Florea, R. & Wake, B. 2003 Parametric analysis of directed-synthetic jets for improved dynamic-stall performance. In *41st AIAA Aerospace Sciences Meeting and Exhibit*, pp. AIAA–2003–216. Reno, Nevada.

Fung, Y. C. 1993 *Thery of Aeroelasticity*. Dover Publications.

Funk, R., Parekh, D. E., Crittenden, T. & A., Glezer 2002 Transient separation control using pulse actuation. In *1st AIAA Flow Control Conference*, pp. AIAA–2002–3166. St. Louis, Missouri.

Gallas, Q., Holman, R., Nishida, T., Carroll, B., Sheplak, M. & Cattafesta, L. 2003 Lumped element modeling of piezoelectric-driven synthetic jet actuators. *AIAA Journal* **41**, 240–247.

Gilarranz, J. L., W., Traub L. & Rediniotis, O. K. 2005 A new class of synthetic jet actuators- part ii: Application to flow separation control. *Journal of Fluids Engineering* **127**, 377.

Glezer, A., Amitay, M. & Honohan, A. M. 2005 Aspects of low- and high-frequency actuation for aerodynamic flow control. *AIAA Journal* **43**, 1501–1511.

Greenblatt, D. 2006 Managing flap vortices via separation control. *AIAA Journal* **44**, 2755–2764.

Greenblatt, D. & Washburn, A. E. 2008 Influence of finite span and sweep on active flow control efficacy. *AIAA Journal* **46**, 1675–1694.

Greenblatt, D. & Wygnanski, I. 2003 Effect of leading-edge curvature on airfoil separation control. *Journal of Aircraft* **40**, 473–481.

Greenblatt, D. & Wygnanski, I. J. 2001 Use of periodic excitation to enhance airfoil performance at low reynolds numbers. *Journal of Aircraft* **38**, 190–192.

Hildebrand, D. 1992 An architectual overview of qnx. In *Proceedings of the Workshop on Micro-kernels and Other Kernel Architectures*, pp. 113–126. Berkeley, California.

Honohan, A. M. 2003 he interaction of synthetic jets with cross flow and the modification of aerodynamic surfaces. PhD thesis, Georgia Institute of Technology.

Honohan, A. M., Amitay, M. & Glezer, A. 2000 Aerodynamic control using synthetic jets. In *AIAA Fluids 2000 Conference nd Exhibit*, pp. AIAA–2000–2401. Denver, CO.

Hsiao, F.-B., Liu, C.-F. & Shyu, J.-Y. 1990 Control of wall-separated flow by internal acoustic excitation. *AIAA Journal* **28**, 1440–1446.

Jabbal, M. & Zhong, S. 2008 The near wall effect of synthetic jets in a boundary layer. *International Journal of Heat and Fluid Flow* **29**, 119–130.

Jabbal, M. & Zhong, S. 2010 Particle image velocimetry measurements of the interaction of synthetic jets with a zero-pressure gradient laminar boundary layer. *Physics of Fluids* **22**, 063603.

Jee, S. K. 2010 Flow control simulation with synthetic and pulsed jet actuator. PhD thesis, University of Texas At Austin.

Jee, S. K., Lopez, O., Moser, R. D., Kutay, A. T., Muse, J. A. & Calise, A. J. 2009 Flow simulation of a controlled airfoil with synthetic jet actuators. In *19th AIAA Computational Fluid Dynamics*, pp. AIAA–2009–3673. San Antonio, Texas.

Jones, R. T. 1940 The unsteady lift of a wing of finite aspect ratio. TR 681. NACA.

von Kármán, T. & Sears, W. R. 1938 Airfoil theory for non-uniform motion. *Journal of Aeronautical Sciences* **5**, 379–390.

Kotapati, R. B., Mittal, R. & Cattafesta, L. N. 2007 Numerical study of a transitional synthetic jet in quiescent external flow. *Journal of Fluid Mechanics* **581**, 287–321.

Küssner, H. G. 1936 Züsammenfassender bericht über den instationaeren auftrieb von flügeln. *Luftfahrtforschung* **13**, 410–424.

Kutay, A. T., Calise, A. J. & Muse, J. A. 2006 A 1-dof wind tunnel experiment in adaptive flow control. In *AIAA Guidance, Navigation, and Control Conference and Exhibit*, pp. AIAA–2006–6430. Keystone, Colorado.

Lee, C. Y. & Goldstein, D. B. 2002 Two-dimensional synthetic jet simulation. *AIAA Journal* **40**, 510–516.

Liddle, S. C. & Wood, N. J. 2005 Investigation into clustering of synthetic jet actuators for flow separation control applications. *The Aeronautical Journal* **109**, 35–44.

Liebeck, Robert H. 1978 Design of subsonic airfoils for high lift. *Journal of Aircraft* **15**, 547–561.

Lopez, O.D., Moser, R. D., Brzozowski, D. P. & Glezer, A. 2011 Effects of trailing-edge synthetic jet actuation on an airfoil. *AIAA Journal* **49**, 1763–1777.

Lopez, O. D., Moser, R. D., Brzozowski, D. P. & Glezer, A. 2009 Aerodynamic performance of airfoils with tangential synthetic jet actuators close to the trailing edge. In *19th AIAA Computational Fluid Dynamics*, pp. AIAA–2009–3674. San Antonio, Texas.

Lorber, P.F., McCormick, D.C., Anderson, T.J., Wake, B.E, D.G., MacMartin, Pollack, M.J., Corke, T.C. & Breuer, K. 2000 Rotorcraft retreating blade stall control. In *Fluids 2000 Conference and Exhibit*, pp. AIAA–2000–2475. Denver, Colorado.

Lorber, P. F., McCormick, D., Wake, B. & Florea, R. 2002 Separation control for rotorcraft. *Tech. Rep.* 2002-5.200.0015-5. UTRC Final Progress Report.

Mane, P., Mossi, K. & Bryant, R. 2008 Experimental design and analysis for piezoelectric circular actuators in flow control applications. *Smart Materials And Structures* **17**, 1–12.

Margalit, S., Greenblatt, D., Seifert, A. & Wygnanski, I. 2005 Delta wing stall and roll control using segmented piezoelectric fluidic actuators. *Journal of Aircraft* **42**, 698–709.

Mathis, R., Lebedev, A. & Collin, E. 2009 Experimental study of transient forced turbulent separation and reattachment on a bevelled trailing edge. *Experiments in Fluids* **46**, 131–146.

Milanovic, I.M. & Zaman, K.B.M.Q 2003 Synthetic jets in cross-flow. In *Proceedings of the 33rd AIAA Fluid Dynamics Conference and Exhibit*, pp. AIAA–2003–3715. Orlando, Florida.

Milne-Thomson, L. M. 1973 *Theoretical Aerodynamics*. Dover Publications.

Muse, Jonathan 2010 An h_∞ norm minimization approach for adaptive control. PhD thesis, Georgia Institute of Technology Department of Aerospace Engineering.

Muse, J. A., Kutay, A. T. & Calise, A. J. 2008*a* Experimental trapped vorticity flight control using an augmenting error minimization adaptive law. In *AIAA Guidance, Navigation and Control Conference and Exhibit*, pp. AIAA–2008–6962. Honolulu, Hawaii.

Muse, J. A., Kutay, A. T. & Calise, A. J. 2008*b* A novel force control traverse for simulating uav flight in a wind tunnel. In *AIAA Atmospheric Flight Mechanics Conference and Exhibit*, pp. AIAA–2008–6714. Honolulu, Hawaii.

Muse, J. A., Tchieu, A. A., Kutay, A. T., Chandramoham, R., Calise, A. J. & Leonard, A. 2009 Vortex model based adaptive flight control using synthetic jets. In *AIAA Guidance, Navigation, and Control Conference*, pp. AIAA–2009–5761. Chicago, Illinois.

Nagib, H., Kiedaisch, J., Reinhard, P. & Demanett, B. 2006 Control techniques for flows with large separated regions: A new look at scaling parameters. In *3rd AIAA Flow Control Conference*, pp. AIAA–2010–0863. San Francisco, CA.

National Research Council 2006 *Decadal Survey of Civil Aeronautics: Foundation for the Future*. National Academy Press.

Neuberger, D. & Wygnanski, I. 1987 The use of a vibrating ribbon to delay separation on two dimensional airfoils. In *Proceedings of the Air Force Academy Workshop in Unsteady Separated Flow*, pp. Research Lab Report TR–88–0004. Colorado Springs, CO: ed. Seiler, F.J.

Perkins, C.D. & Hazen, D. 1953 Some recent advances in boundary layer and circulation control. In *Proceedings of the 4th Anglo-American Aeronautical Conference*. London, U.K.

Pinier, J. T., Ausseur, J. M., Glauser, M. N. & Higuchi, H. 2007 Proportional closed-loop feedback control of flow separation. *AIAA Journal* **45**, 181–190.

Raffel, M., Willer, C. E., Wereley, S. T. & Kompenhans, J. 2007 *Particle Image Velocimetry*. Springer.

Raju, R., Mittal, R. & Cattafesta, L. 2008 Dynamics of airfoil separation control using zero-net mass-flux forcing. *AIAA Journal* **46**, 3103–3115.

Rathnasingham, R. & Breuer, K. S. 2003 Active control of turbulent boundary layers. *Journal of Fluid Mechanics* **495**, 209–2333.

Rehman, A. & Kontis, K. 2006 Synthetic jet control effectiveness on stationary and pitching airfoils. *Journal of Aircraft* **43**, 1782–1789.

Rice, John A. 2006 *Mathematical Statistics and Data Analysis*. Duxbury Press.

Rizzetta, D. P., Visbal, M. R. & Stanek, M. J. 1999 Numerical investigation of synthetic-jet flowfields. *AIAA Journal* **37**, 919–927.

Roshko, A. 1993 Perspectives on bluff body aerodynamics. *Journal of Wind Engineering and Industrial Aerodynamics* **49**, 79–100.

Schatz, M., Thiele, F., Petz, R. & Nitsche, W. 2004 Separation control by periodic excitation and its application to a high-lift configuration. In *2nd AIAA Flow Control Conference*, pp. AIAA–2004–2507. Portland, OR.

Sears, W. R. 1940 Operational methods in the theory of airfoils in non-uniform motion. *Journal of the Franklin Institute* **230**, 95–111.

Sears, W. R. 1941 Some aspects of non-stationary airfoil theory and its practical application. *Journal of Aeronautical Sciences* **8**, 104–108.

Seifert, A., Bachar, T., Koss, D., Shepshelovich, M. & Wygnanski, I. 1993 Oscillatory blowing: A tool to delay boundary-layer separation. *AIAA Journal* **31**, 2052–2060.

Seifert, A. & Pack, L. G. 1999 Oscillatory control of separation at high reynolds numbers. *AIAA Journal* **37**, 1062–1071.

Shmilovich, A. & Yadlin, Y. 2006 Flow control for the systematic buildup of high lift systems. In *3rd AIAA Flow Control Conference*, pp. AIAA–2006–2855. San Francisco, CA.

Shuster, J. M. & Smith, D. R. 2007 Experimental study of the formation and scaling of a round synthetic jet. *Phy* **19**.

Siauw, W.L., Bonnet, J., Tensi, J. & Cattafesta, L. 2009 Physics of separated flow over a naca 0015 airfoil and detection of flow separation. In *47th AIAA Aerospace Sciences Meeting*, pp. AIAA–2009–144. Orlando, Florida.

Smith, B. L. & Glezer, A. 1998 The formation and evolution of synthetic jets. *Physics of Fluids* **10**, 2281–2297.

Smith, D. M., Dickey, E. & VonKlein, T. 2006 The advint program. In *3rd AIAA Flow Control Conference*, pp. AIAA–2006–2854. San Francisco, CA.

Smith, D. R. 2002 Interaction of a synthetic jet with a crossflow boundary layer. *AIAA Journal* **40**, 2277–2288.

Song, C., Aiyar, A. R., Kim, S.-H. & Allen, M. G. 2009 Exploitation of aeroelastic effects for drift reduction in an all-polymer air flow sensor. In *Tech. Dig. Int. Solid-State Sensors, Actuators and Microsystems Conference, 2009*, pp. 1545–1548. Denver, Colorado.

Tang, H. & Zhong, S. 2007 A static compressible flow model of synthetic jet actuators. *Aeronautical Journal* **111**, 421–431.

Tchieu, A. A., Kutay, A. T., Muse, J. A., Calise, A. J. & Leonard, A. 2008 Validation of a low-order model for closed-loop flow control enable flight. In *4th Flow Control Conference*, pp. AIAA–2008–3863. Seattle, Washington.

Tchieu, A. A. & Leonard, A. 2011 A discrete-vortex model for the arbitrary motion of a thin airfoil with fluidic control. *Journal of Fluids and Structures* **in press**, in press.

Tchieu, A. A. & Leonard, T. 2010 Integral kernel for force estimation. Private communication.

Theodorsen, T. 1935 General theory of aerodynamic instability and the mechanism of flutter. TR 496. NACA.

Timor, I., Ben-Hamou, E., Guy, Y. & Seifert, A. 2004 Maneuvering aspects and 3d effects of active airfoil flow control. In *2nd AIAA Flow Control Conference*, pp. AIAA–2004–2614. Portland, OR.

Vukasinovic, B., Rusak, Z. & Glezer, A. 2010 Dissipative small-scale actuation of a turbulennt shear layer. *Journal of Fluid Mechanics* **656**, 51–81.

Wagner, H. 1925 Über die enstehung des dynamischen auftriebes con tragflügeln (on the generation of lift on airfoils). *Zeitschrift für Angewandte Mathematik und Mechanik* **5**, 17–35.

Wake, B.E. & Lurie, E.A. 2001 Computational evaluation of directed synthetic jets for dynamic stall control. In *57th Annual Forum of the American Helicopter Society*.

Watson, M., Jaworski, A. J. & Wood, N. J. 2007 Application of synthetic jet actuators for the modification of the characteristics of separated shear layers on slender wings. *The Aeronautical Journal* **111**, 519–529.

Woo, G., Crittenden, T. & A., Glezer 2008 Transitory control of a pitching airfoil using pulse combustion actuation. In *4th AIAA Flow Control Conference*, pp. AIAA–2008–4324. Seattle, Washington.

Woo, G., Crittenden, T. & A., Glezer 2009 Transitory separation control over a stalled airfoil. In *39th AIAA Fluid Dynamics Conference*, pp. AIAA–2009–4281. San Antonio, Texas.

Woo, G. & Glezer, A. 2010 Transient control of separating flow over a dynamically-pitching airfoil. In *48th AIAA Aerospace Sciences Meeting*, pp. AIAA–2010–861. Orlando, FL.

Woods, L. C. 1954 The lift and moment acting on a thick aerofoil in unsteady motion. *Philosophical Transactions of the Royal Society of London - Series A* **247**, 131–162.

Wu, J.-Z., Lu, X.-Y., Denny, A. G., Fan, M. & Wu, J.-M. 1998 Post stall flow control on an airfoil by local unsteady forcing. *Journal of Fluid Mechanics* **371**, 21–58.

Yamaleev, N.K. & Carpenter, M.H. 2006 Quasi-one-dimensional model for realistic three-dimensional synthetic jet actuators. *AIAA Journal* **44**, 208–216.

Yao, C.S., Chen, F. J., Neuhart, D. & Harris, J. 2004 Synthetic jets in quiescent air. In *Langley Research Center Workshop - CFD Validation of Synthetic Jets and Turbulent Separation Control*. Williamsburg, Virginia.

Yehoshua, T. & Seifert, A. 2006 Active boundary layer tripping using oscillatory vorticity generator. *Aerospace Science and Technology* **10**, 175–180.

You, D., Ham, F. & Moin, P. 2008 Discrete conservation principles in large-eddy simulation with application to separation control over an airfoil. *Physics of Fluids* **20**, 101515.

Zhang, M. M., Cheng, L. & Zhou, Y. 2004 Closed-loop-controlled vortex shedding and vibration of a flexibly supported square cylinder under different schemes. *Physics of Fluids* **16**, 1439–1448.

Zhong, S., Millet, F. & Wood, N. J. 2005 The behaviour of circular synthetic jets in a laminar boundary layer. *The Aeronautical Journal* **109**, 461–470.

VITA

Daniel Brzozowski grew up in Swampscott, Massachusetts with his parents, Paul and Mary Beth, and his sister, Maureen. In 1999, he began his undergraduate studies at Johns Hopkins University, where a class with Prof. Charles Meneveau inspired his passion for fluid dynamics. Dan finished in 2004 with both a B.S. and an M.S. in Mechanical Engineering, and his master's thesis, "CFD Modeling and Analysis of an Axial-Flow Turbomachine", was under the direction of Prof. Meneveau. Dan joined Ari Glezer's Fluid Mechanics Research Laboratory at the Georgia Institute of Technology in 2004 and is currently an Aerodynamics Engineer with The Boeing Company. He lives in the St. Louis area with his wife, Amanda, and their two fantastic cats, Sammy and Yodel.